

Light-induced Pulsed Dipolar Spectroscopy and other Electron Spin Resonance studies of photogenerated paramagnetic species

Arnau Bertran

A thesis submitted for the degree of Doctor of Philosophy

Inorganic Chemistry Laboratory, Department of Chemistry

and

Lincoln College

University of Oxford

Michaelmas Term 2022

Abstract

Light-induced Pulsed Dipolar Spectroscopy and other Electron Spin Resonance studies of photogenerated paramagnetic species

A thesis submitted for the degree of Doctor of Philosophy by

Arnau Bertran

This thesis is concerned with the development of new methodologies in the field of Light-induced Pulsed Electron Spin Resonance Dipolar Spectroscopy (LiPDS), with the aim of applying them to the structural investigation of complex biological macromolecular systems with endogenous or artificially-added chromophores that can be photoexcited to form triplet states.

The orientational effects in previously reported LiPDS techniques and how to exploit them to extract additional molecular conformational information are explored in Chapter 2. The ReLaserIMD and LiDEER techniques are combined to fully characterise the relative orientation of the two spin centres in porphyrin-nitroxide model peptides, and a new two-dimensional LiPDS technique (frequency-correlated ReLaserIMD) is introduced to capture the complete orientational dependence of the dipolar interaction with a single experiment. These novel methodologies are extended to non-porphyrin chromophores

Chapter 3 goes a step further to tackle the challenge of measuring the dipolar interaction between two photogenerated triplets, removing the need for having any permanent spin centre in LiPDS. The new Light-Induced Triplet-Triplet Electron Resonance spectroscopy (LITTER) technique is developed using bis-porphyrin model peptides and an in-depth conformational study of a spectroscopic molecular ruler is performed exploiting the orientational effects. LITTER is also compared to conventional DEER spectroscopy, showing superior results, and is applied to the structural study of a dimeric heme protein and a supramolecular porphyrin tetramer.

Chapter 4 addresses some of the limitation of the LITTER technique

by using non-identical chromophores and two-colour photoexcitation in bis-labelled model peptides, improved performance and direct combination with Förster Resonance Energy Transfer.

This thesis constitutes an important step forward in the knowledge and development of the novel field of LiPDS, by introducing new triplet spin labels, improving existing techniques, developing new experiments and analysis methods, and combining them with other experimental tools for integrative structural biology.

Acknowledgements

My first and biggest thank you goes to Dr. Alice Bowen, for her very active supervision and help throughout this DPhil, despite having to spend most of her time delocalised between Oxford and Manchester. For patiently teaching me how to run ESR experiments in the lab and how to analyse the data, and for always being available for a late-night call when things were not going well in those long measurement days. My second thank you goes to Prof. Christiane Timmel, for her guidance and mentoring during the last four years, and especially for taking me under her wing as one of her own after Alice moved to Manchester.

This thesis relied heavily on complex instrumentation, which had a tendency to fail at the least appropriate moment. I give a big thank you to our ESR and laser gurus Dr. William Myers and Dr. Kevin Henbest for always coming to the rescue, and also for their advice and help in the development of the experimental setups for the novel spectroscopic techniques presented in this thesis.

Experimental science nowadays is no longer a one-person job, but a collective effort, and the work presented in this thesis would have not been possible without the multiple collaborators involved. I thank Prof. Marilena di Valentin for her involvement in the design of new light-induced ESR experiments since the first year of my DPhil, and for fruitful discussions and collaborative work with her and members of her group at the University of Padova (Daniele Panariti, Susanna Ciuti and Dr. Maria Giulia dal Farra), and Prof. Antonio Barbon for insightful conversations about optical setups and polarisation. I thank Prof. Marta de Zotti and Prof. Marina Gobbo from the University of Padova, and the members of their groups, for synthesising all the model peptide systems studied in this thesis, which were instrumental in the development of the new spectroscopic techniques. I also thank Prof. Marina Gobbo for hosting me in her laboratory in Padova for several months and patiently teaching me the art of peptide synthesis, which has given me

a much better understanding of the synthetic side of this research and has allowed me to interact smoothly with the synthetic collaborators. *Grazie per queste collaborazioni.*

Model peptides are great for method development, but eventually one aims to study more complex systems of real interest. I thank Prof. Edvinas Orentas and his group at the University of Vilnius for providing the tetraporphyrin cage samples studied in this thesis, and Jack Sawyer, Dr. Derren Heyes and Prof. Sam Hay form the University of Manchester for providing the myoglobin samples and for doing the FRET work on the model systems. I also thank Jack Sawyer and Ciarán Rogers for the copper protein experiments.

This DPhil has gone through many ups and downs (more downs than ups, I would say), including a global pandemic with several months-long laboratory closures and remote working, and many many instrumental failures. Facing this alone would drive anyone insane. Thankfully, I am part of the friendly and supportive community that is the Timmel group, and the daily interaction with them, the relaxed chats in the group office, beyond scientific topics, and the social activities helped to put things into perspective and to realise that life goes on regardless of the outcome of your experiments. I am grateful to all the current and former members of the group for this.

Pursuing a scientific career is not an easy path, and requires lots of time and effort that are often difficult to balance with a personal life. I am immensely fortunate to have someone by my side who understands and appreciates this, and that unconditionally supports me in this journey. *Merci pour ton existence.*

Finally, I would like to dedicate this thesis to my family, who have always encouraged me to pursue my own interests and have always supported my choices. *Gràcies pel vostre suport.*

Statement of authorship

Parts of this thesis have been reproduced or adapted from publications where I am not the sole author. The author contributions to these publications are stated below and have been clearly acknowledged in the relevant sections of the thesis.

- Bertran, A.; Barbon, A.; Bowen, A. M.; Di Valentin, M. Light-induced pulsed dipolar EPR spectroscopy for distance and orientation analysis, in Advances in Biomolecular EPR, ed. R. D. Britt, Elsevier Inc., 1st edn., 2022, Methods in Enzymology vol. 666, ch. 7, pp. 171–231.

  DOI: 10.1016/bs.mie.2022.02.012

  [Included in Chapters 1 and 4]

  I performed the experiments, analysed the data and made the figures for the novel work presented in this publication. Figures from published work have been reproduced/adapted with permission. I wrote the sections of the text included in the thesis, with input from A.B., A.M.B. and M.D.V.

- Bowen, A. M.; Bertran, A.; Henbest, K. B.; Gobbo, M.; Timmel, C. R.; Di Valentin, M. Orientation-Selective and Frequency-Correlated Light-Induced Pulsed Dipolar Spectroscopy. The Journal of Physical Chemistry Letters 2021, 12, 3819–3826.

  DOI: 10.1021/acs.jpclett.1c00595

  [Included in Chapter 2]

  The molecules were synthesised by M. G. I performed the experiments together with A.M.B. as training at the beginning of my DPhil, with the assistance of K.B.H. A.M.B. analysed the data. I carried out the density functional theory calculations and made the figures. A.M.B. and I wrote the text. C.R.T. and M.D.V. provided feedback on the

manuscript.

- Bertran, A.; Morbiato, L.; Aquilia, S.; Gabbatore, L.; De Zotti, M.; Timmel, C. R.; Di Valentin, M.; Bowen, A. M. Erythrosin B as a new photoswitchable spin label for light-induced pulsed EPR dipolar spectroscopy. Molecules 2022, 27, 7526.

  DOI: 10.3390/molecules27217526

  [Included in Chapter 2]

  The molecules were synthesised by L.M., S.A. and L.G., under the supervision of M.D.Z. I performed the experiments, quantum chemical calculations and simulations, analysed the data, made the figures and wrote the first draft of the text with contributions from other authors. M.D.Z., C.R.T., M.D.V. and A.M.B. provided feedback and edited the final manuscript.

- Bertran, A.; Panariti, D.; Ciuti, S.; Rogers, C. J.; Gobbo, M.; Wang, H.; Zhao, J.; Timmel, C. R.; Barbon, A.; Di Valentin, M.; Bowen, A. M. I2BODIPY as a new photoswitchable spin label for orientation-resolved light-induced pulsed ESR dipolar spectroscopy exploiting magnetophotoselection effects, *in preparation*.

  [Included in Chapter 2]

  The chromophore was synthesised by H.W., under the supervision of J.Z. The molecule used in the experiments was synthesised by M.G. D.P. (master's student under my day-to-day supervision) and I performed the experiments and analysed the data for the part of the manuscript included in the thesis. S.C., C.J.R. A.B. and A.M.B. contributed to a part of the manuscript not included in the thesis. I made the figures and wrote the initial draft of the text with contributions from other authors. C.R.T., A.B., M.D.V. and A.M.B. provided feed-

back and edited the final manuscript.

- Bertran, A.; Henbest, K. B.; De Zotti, M.; Gobbo, M.; Timmel, C. R.; Di Valentin, M.; Bowen, A. M. Light-Induced Triplet–Triplet Electron Resonance Spectroscopy. The Journal of Physical Chemistry Letters 2021, 12, 80–85.

  DOI: 10.1021/acs.jpclett.0c02884

  [Included in Chapter 3]

  The molecules were synthesised by M.D.Z. and M.G. I performed the experiments with the assistance of K.B.H. and A.M.B. A.M.B. and I analysed the data. I carried out the quantum chemical calculations, made the figures and wrote the first draft of the text with contributions from other authors. C.R.T., M.D.V. and A.M.B. provided feedback and edited the manuscript.

- Bertran, A.; De Zotti, M.; Timmel, C. R.; Di Valentin, M.; Bowen, A. M. Conformational information from orientation-selective Light-Induced Triplet–Triplet Electron Resonance spectroscopy. Chemistry – A European Journal, *under review.*

  [Included in Chapter 3]

  The molecules were synthesised by M.D.Z. I performed the experiments, quantum chemical calculations and simulations, analysed the data, made the figures and wrote the initial draft of the text with contributions from other authors. C.R.T., M.D.V. and A.M.B. provided feedback and edited the final manuscript.

- Bertran, A.; Sawyer, J.; Rogers, C. J.; Heyes, D. J.; De Zotti, M.; Timmel, C. R.; Di Valentin, M.; Hay, S.; Bowen, A. M. Photoexcitable endogenous groups allow nanoscale distance measurements in

unlabelled proteins by light-induced pulsed dipolar ESR spectroscopy, *in preparation.*

[Included in Chapter 3]

J.S. prepared the proteins, performed the mass spectrometry and carried out the docking calculations with the assistance of D.J.H. and under the supervision of S.H. and A.M.B. I performed the light-induced experiments in the presence of J.S. J.S. and C.J.R. performed the dark experiments under the supervision of A.M.B. I carried out the quantum chemical calculations, simulations and data analysis. I made the figures and wrote the first draft of the text with contributions from other authors. C.R.T., M.D.V., S.H. and A.M.B. provided feedback and edited the final manuscript.

- Jozeliūnaitė, A.; Neniškis, A.; Bertran, A.; Bowen, A. M.; Di Valentin, M.; Raišys, S.; Baronas, P.; Kazlauskas, K.; Vilčiauskas, L.; Orentas, E. Fullerene Complexation in Hydrogen-Bonded Porphyrin Cavitands via Induced-Fit: Cooperative Action of Tautomerization and C−H$\cdots\pi$ Interactions. Journal of the American Chemical Society 2023, *in press.*

  DOI: 10.1021/jacs.2c10668

  [Included in Chapter 3]

  I contributed with the ESR section of the manuscript, which is the only part included in the thesis. I performed the ESR experiments and the corresponding quantum chemical calculations and simulations, analysed the ESR data, made the ESR figures and wrote the first draft of the text of the ESR section of the manuscript with contributions from other authors. A.M.B. and M.D.V. provided feedback on this part of the manuscript. The non-ESR figures from this manuscript included in the thesis were prepared by E.O and other co-authors.

- Bertran, A.; Dalla Torre, C.; Sawyer, J.; Morbiato, L.; Heyes, D.; Hay, S.; Timmel, C. R.; Di Valentin, M.; De Zotti, M.; Bowen, A. M. Light-Induced Triplet–Triplet Electron Resonance Spectroscopy with Orthogonal Chromophores allows Pulsed ESR Distance Measurements between FRET Labels. Journal of the American Chemical Society, *submitted*.

  [Included in Chapter 4]

  The molecules were synthesised by C.D.T. and L.M., under the supervision of M.D.Z. J.S. performed the FRET experiments and analysis with the assistance of D.J.H. and S.H. I performed all the other experiments and calculations, analysed the data, made the figures and wrote the first draft of the text with contributions from other authors. C.R.T., M.D.V. M.D.Z., S.H. and A.M.B. provided feedback and edited the final manuscript.

Contents

Abstract 1

Acknowledgements 3

Statement of authorship 5

Contents 13

List of symbols, abbreviations and acronyms 14

1 Introduction **19**

1.1 Electronic spin and the spin Hamiltonian 20

1.1.1 Zeeman interaction 21

1.1.2 Hyperfine interaction 22

1.1.3 Zero-field splitting interaction 23

1.1.4 Electron-electron dipolar interaction 26

1.2 Electron spin resonance (ESR) spectros-copy 27

1.2.1 Continuous-wave ESR 28

1.2.2 Pulsed ESR 33

1.3 Relaxation 38

1.3.1 Spin-lattice or longitudinal relaxation 39

1.3.2 Spin-spin or transverse relaxation 41

1.4 Pulsed dipolar spectroscopy (PDS) 42

1.4.1 The dipolar spectrum 42
1.4.2 Double electron-electron resonance (DEER) 44
1.4.3 Orientational effects 50
1.4.4 Multi-spin effects 51
1.4.5 Analysis of PDS traces 53
1.4.6 Biological applications of PDS 60
1.5 Light-induced PDS (LiPDS) 62
1.5.1 The photogenerated triplet state 62
1.5.2 LiPDS techniques - State of the art 66
1.5.3 Biological applications of LiPDS - State of the art . . . 82
1.6 The structure of this thesis 88

2 Orientational effects in LiPDS 90
2.1 Orientationally selective porphyrin-nitroxide LiPDS 91
2.1.1 Characterisation of the model system 92
2.1.2 Orientationally selective ReLaserIMD 94
2.1.3 Frequency-correlated ReLaserIMD 99
2.1.4 Orientationally selective LiDEER 102
2.1.5 Conclusions 104
2.2 Orientationally selective LiPDS with non-porphyrin chromophores 106
2.2.1 Characterisation of the model systems 109
2.2.2 Orientationally selective ReLaserIMD 113
2.2.3 High-temperature LiPDS 121
2.2.4 Conclusions 124
2.3 Methods 125

3 Light-induced triplet-triplet electron resonance (LITTER) spectroscopy 130

3.1 Development of the technique 131

3.1.1 Characterisation of the model system 132

3.1.2 Proof-of-concept experiments 136

3.1.3 Optimisation of experimental conditions 144

3.1.4 Conclusions 148

3.2 Conformational information from orientationally selective LITTER 150

3.2.1 Spectroscopic ruler study 151

3.2.2 Comparison to Cu-Cu DEER 156

3.2.3 Orientation-independent analysis 161

3.2.4 Conclusions 164

3.3 Application to a protein system: Zn(II) myoglobin dimer . . . 166

3.3.1 LITTER on a ZnTPP-ZnTPP model peptide 168

3.3.2 LITTER on Zn-myoglobin dimer 171

3.3.3 Complementary experiments and simulations 174

3.3.4 Conclusions 177

3.4 Application to multiporphyrin supramolecular nanostructures 178

3.4.1 Characterisation of the system 178

3.4.2 PDS study 182

3.4.3 Conclusions 187

3.5 Analytical treatment of LITTER 187

3.5.1 Density-operator description 188

3.5.2 Modulation depth analysis 192

3.6 Limitations and advantages of the technique 197

3.7 Conclusions . . . 199
3.8 Methods . . . 201

4 Two-colour LITTER with non-identical chromophores 207

4.1 Identification of suitable chromophores for two-colour LITTER 208
4.1.1 Desirable qualities of a photoswitchable triplet spin label 209
4.1.2 Triplet chromophore characterisation . . . 210
4.1.3 Selection of chromophore pairs . . . 217
4.2 Two-colour LITTER . . . 219
4.2.1 Characterisation of the model systems . . . 220
4.2.2 Two-colour LITTER . . . 222
4.2.3 Direct comparison to FRET . . . 228
4.3 Conclusions . . . 230
4.4 Methods . . . 232

5 Conclusions and outlook 236

Appendices 250

I. Instrumentation . . . 251
I.1. ESR instrumentation . . . 251
I.2. Laser instrumentation . . . 251
I.3. Optical spectroscopy instrumentation . . . 254
II. Supplementary data . . . 256
II.1 Supplementary data for Chapter 2 . . . 256
II.2 Supplementary data for Chapter 3 . . . 259
II.3 Supplementary data for Chapter 4 . . . 263
III. Photoswitchable radical labels for PDS . . . 266

List of symbols, abbreviations and acronyms

$\mathbf{A}$: hyperfine coupling tensor

a_{iso} : isotropic hyperfine coupling constant

AO : Acridine Orange

AT : ATTO Thio12

AWG : Arbitrary Waveform Generator

α : Tikhonov regularisation parameter

α, β, γ : Euler angles

B : background factor

$\mathbf{B}_0$: externally applied static magnetic field

$\mathbf{B}_1$: microwave magnetic field

B_{mod} : magnetic field modulation amplitude

I_2BODIPY : 4,4-difluoro-diiodo-1,3,5,7,8-pentamethyl-4-bora-3a,4a-diaza-s-indacene

β : flip angle of a microwave pulse

β_e : electronic Bohr magneton

β_n : nuclear Bohr magneton

cryo-EM : cryogenic Electron Microscopy

CuCAAC : Cu-Catalised Azido-Alkyne Cycloaddition

CV : Crystal Violet

cwESR : continuous-wave Electron Spin Resonance

$\mathbf{D}$: zero-field splitting tensor

$\mathbf{d}$: nucleus-nucleus coupling tensor

D : zero-field splitting parameter

DAF : Delay After Flash

DEER : Double Electron-Electron Resonance

DFT : Density Functional Theory

DQC : Double-Quantum Coherence

Δ : dipolar modulation depth

ΔB_{pp} : peak-to-peak linewidth

e : elementary charge

E : zero-field splitting parameter

EB : Erythrosin B

ENDOR : Electron-Nuclear DOuble Resonance

EO : Eosin Y

ESEEM : Electron Spin-Echo Envelope Modulation

ESR : Electron Spin Resonance

EZ : Electronic Zeeman

e_1, e_2 : photoexcitation efficiencies of lasers 1 and 2

F : form factor

f : reduced form factor

FC : Frequency-Correlated

FRET : Förster Resonance Energy Transfer

$\mathbf{g}$: g-tensor

g : g-value

g_e : free electron g-value

g_{iso} : isotropic g-value

$\hat{H}$: Hamiltonian operator

HF : Hyperfine

$\hbar$: reduced Planck constant

$\hat{\mathbf{I}}$: total nuclear spin operator

I : nuclear spin quantum number

IR : InfraRed

ISC : InterSystem Crossing

J : overlap integral in FRET

LaserIMD : Laser-Induced Magnetic Dipolar

LiDEER : Light-induced Double Electron-Electron Resonance

LiPDS : Light-induced Pulsed Dipolar Spectroscopy

LiRIDME : Light-induced Relaxation-Induced Dipolar Modulation Enhancement

LITTER : Light-Induced Triplet-Triplet Electron Resonance

$\mathbf{M}$: magnetisation

MB : Methylene Blue

m_e : mass of the electron

MG : MyoGlobin

m_I : nuclear spin angular momentum quantum number

m_n : mass of the nucleus

MNR : Modulation-to-Noise Ratio

MS : Mass Spectrometry

m_S : electronic spin angular momentum quantum number

MTSSL : MethaneThioSulfonate Spin Label

MW : microwave

M_{zy} : transverse magnetisation

M_z : longitudinal magnetisation

μ_0 : magnetic permeability of vacuum

μ_B : Bohr magneton

NG : NeuroGlobin

NMR : Nuclear Magnetic Resonance

NN : Nucleus-Nucleus

NQ : Nuclear Quadrupolar

NZ : Nuclear Zeeman

OPO : Optical Parametric Oscillator

$\mathbf{P}$: nuclear quadrupolar coupling tensor

PCP : Peridinin Chlorophyll Protein

PDS : Pulsed Dipolar Spectroscopy

PE : Primary Echo

PELDOR : Pulsed ELectron DOuble Resonance

PFU : Pulse-Forming Unit

PP : Proto-Porphyrin IX

P_α, P_β : radical spin sub-level populations

P_-, P_0, P_+ : high-field triplet state spin sub-level populations

P_X, P_Y, P_Z : zero-field triplet state spin sub-level populations

Q : quality factor of the resonator

Φ_{fl} : fluorescence quantum yield

Φ_T : triplet quantum yield

R_0 : Förster radius

R6G : Rhodamine 6G

RB : Rose Bengal

ReLaserIMD : Refocused-echo Laser-Induced Magnetic Dipolar

ReLITTER : Refocused-echo Light-Induced Triplet-Triplet Electron Resonance

RIDME : Relaxation-Induced Modulation Enhancement

RMSD : Root-Mean-Square Deviation

$\hat{\mathbf{S}}$: total electronic spin operator

S : electronic spin quantum number

SDSL : Site-Directed Spin Labelling

SIFTER : SIngle-Frequency TEchnique for the Refocusing of electron-electron couplings

SNR : Signal-to-Noise Ratio

SOC : Spin-Orbit Coupling

SSC : Spin-Spin Coupling

$\hat{S}_x, \hat{S}_y, \hat{S}_z$: components of the total electronic spin operator

$\hat{\boldsymbol{\sigma}}$: spin density operator

$\mathbf{T}$: electron-nucleus dipolar coupling tensor

T : variable pulse delay time in an inversion-recovery experiment

TA : Transient Absorption spectroscopy

TB : Toluidine Blue-o

T_{mix} : duration of the mixing block in the RIDME pulse sequence

TOAC : 4-amino-1-oxyl-2,2,6,6-tetramethyl-piperidine-4-carboxylic acid

TPP : 5-(4-carboxyphenyl)-10,15,20-triphenylporphyrin

trESR : time-resolved Electron Spin Resonance

TWT : Travelling-Wave Tube

T_1 : longitudinal or spin-lattice relaxation time

T_2 : transverse or spin-spin relaxation time

T_m : phase-memory time

t_p : duration of a microwave pulse

T_-, T_0, T_+ : high-field triplet state spin sub-levels

T_X, T_Y, T_Z : zero-field triplet state spin sub-levels

$\hat{\mathbf{U}}$: propagator operator of the spin density

UV : Ultra-Violet

UV-Vis : Ultra-Violet-Visible

V : dipolar signal

Ω : offset between rotating-frame and microwave frequencies

ω_0 : Larmor frequency

ω_1 : amplitude of the microwave magnetic field in frequency units

ω_{dd} : orientation-independent part of the dipolar frequency

ω_{MW} : microwave frequency

XRD : X-Ray Diffraction

x_L, y_L, z_L : axes of the laboratory frame

x_R, y_R, z_R : axes of the rotating frame

YAG : Ytrium Aluminium Gallium

ZFS : Zero-Field Splitting

Chapter 1

Introduction

Measuring distances in biology at the molecular level is of great importance for understanding the structure and function of proteins, nucleic acids and other biological molecules and their complexes. Electron spin resonance (ESR) pulsed dipolar spectroscopy (PDS) offers advantages with respect to other methods as it is specific to the electronic spin transitions of paramagnetic centres and allows measurements in near-native conditions, comprising the in-cell environment.[1,2] PDS methods allow the measurement of the electron spin–spin dipolar interaction between paramagnetic centres, which are often stable radicals, and the elucidation of their relative distance and orientation, informing on the structure of the molecule. Recent developments have introduced transient triplet states, photogenerated by a laser pulse, as spin labels and probes, thereby establishing a new family of techniques: light-induced PDS (LiPDS).[3] This has increased the sensitivity and relevance of PDS structural studies.

The objective of this thesis is to advance the existing knowledge and methods in the novel field of LiPDS, with the aim of applying them to the structural investigation of complex biological macromolecular systems that contain endogenous or artificially-introduced photoexcitable chromophores.

This chapter presents the theoretical concepts necessary for the under-

standing and appreciation of this thesis, with a detailed introduction to ESR spectroscopy and PDS, followed by a review of the state of the art of the novel field of LiPDS.

1.1 Electronic spin and the spin Hamiltonian

Evidenced by the famous magnetic deflection experiment by Stern and Gerlach in the early 1920s,[4] the existence of a quantised magnetic moment of electrons led to the concept of spin. Spin is an intrinsic angular momentum ($\hat{\mathbf{S}}$) with eigenvalues $m_S = -S, -S+1, ..., S-1, S$. For electrons, the spin quantum number is $S = \frac{1}{2}$, leading to two possible eigenstates, with $m_S = \pm\frac{1}{2}$. The corresponding electronic spin magnetic moment is given by[5]

$$\hat{\boldsymbol{\mu}}_e = -g_e \frac{e\hbar}{2m_e}\hat{\mathbf{S}} = -g_e\beta_e\hat{\mathbf{S}} \tag{1.1}$$

where β_e is the electronic Bohr magneton, e is the elementary charge, m_e is the mass of the electron and $g_e = 2.0023$ is the free electron g-factor. The g-factor accounts for the deviations in the behaviour of a quantum object from the behaviour of a classical charged particle.

Analogously, the nuclear spin angular momentum is $\hat{\mathbf{I}}$, with eigenvalues $m_I = -I, -I+1, ..., I-1, I$ and a corresponding nuclear spin magnetic moment given by

$$\hat{\boldsymbol{\mu}}_n = g_n \frac{e\hbar}{2m_n}\hat{\mathbf{I}} = g_n\beta_n\hat{\mathbf{I}} \tag{1.2}$$

In the presence of an external magnetic field ($\mathbf{B}_0$, with $B_0 \equiv |\mathbf{B}_0|$), the electron spin magnetic moment experiences a torque, which leads to a precession motion of this magnetic magnetic moment around $\mathbf{B}_0$ (Larmor precession). The angular frequency for this precession (Larmor frequency, ω_0) is given by[5]

$$\omega_0 = \frac{-g_e\beta_e}{\hbar}B_0 = \gamma_e B_0 \tag{1.3}$$

where $B_0 = |\mathbf{B}_0|$ and γ_e is the gyromagnetic ratio of the electron.

The interactions experienced by the spins in a system can be expressed using rank-two tensors and are compiled in the spin Hamiltonian. For a system of one electron and m nuclei under an applied magnetic field $\mathbf{B}_0 \parallel z$, these interactions are the electronic Zeeman (EZ), zero-field splitting (ZFS), hyperfine (HF), nuclear Zeeman (NZ), nuclear quadrupolar (NQ), and nucleus-nucleus (NN) interactions; and the spin Hamiltonian is[6]

$$\begin{aligned}\hat{H}_0 =& \hat{H}_{EZ} + \hat{H}_{ZFS} + \hat{H}_{HF} + \hat{H}_{NZ} + \hat{H}_{NQ} + \hat{H}_{NN} \\ =& \frac{\beta_e}{\hbar}\mathbf{B}_0\mathbf{g}\hat{\mathbf{S}} + \hat{\mathbf{S}}\mathbf{D}\hat{\mathbf{S}} + \sum_{k=1}^{m}\hat{\mathbf{S}}\mathbf{A}_k\hat{\mathbf{I}}_k - \beta_n\sum_{k=1}^{m}\frac{g_{n,k}}{\hbar}\mathbf{B}_0\hat{\mathbf{I}}_k \\ &+ \sum_{I_k>\frac{1}{2}}\hat{\mathbf{I}}_k\mathbf{P}_k\hat{\mathbf{I}}_k + \sum_{i\neq k}\hat{\mathbf{I}}_i\mathbf{d}^{(i,k)}\hat{\mathbf{I}}_k\end{aligned} \tag{1.4}$$

where $\mathbf{g}$, $\mathbf{D}$, $\mathbf{A}$, $\mathbf{P}$ and $\mathbf{d}$ are the corresponding interaction tensors. The following sections deal with the spin interactions relevant for this thesis, namely electronic Zeeman, hyperfine and zero-field splitting.

1.1.1 Zeeman interaction

The electronic Zeeman interaction is the interaction of the electronic spin with an external magnetic field and is governed by the real-valued and symmetric g-tensor ($\mathbf{g}$).[7] When diagonalised in its principal axis system, the principal values g_{xx}, g_{yy} and g_{zz} of this tensor reflect the anisotropy of the Zeeman interaction. If $g_{xx} \neq g_{yy} \neq g_{zz}$ the tensor is orthorhombic, if $g_\perp \equiv g_{xx} = g_{yy} \neq g_{zz} \equiv g_\parallel$ it is axial, and if $g \equiv g_{xx} = g_{yy} = g_{zz}$ the tensor is cubic and the interaction is fully described by a scalar g-value. Only in high-viscosity solutions or solid samples can the anisotropies of the g-tensor be resolved by ESR, while in low-viscosity liquids these interactions are averaged by fast molecular motions to give an isotropic effective g-value $g_{iso} = \frac{1}{3}(g_{xx} + g_{yy} + g_{zz})$. For the cases of cubic g-tensor or fast molecular

motion, and strong $\mathbf{B}_0$ applied along the z direction, the electronic Zeeman Hamiltonian, in units of angular frequency, simplifies to

$$\hat{H}_{EZ} = \frac{\beta_e}{\hbar} B_0 g \hat{S}_z \tag{1.5}$$

and the energies of the two eigenstates are given by

$$E = \frac{\beta_e}{\hbar} B_0 g m_S, \qquad m_S = \pm\frac{\hbar}{2} \tag{1.6}$$

in units of angular frequency. The energy difference between these two electronic spin states is

$$\Delta E = \frac{\beta_e}{\hbar} g B_0 \tag{1.7}$$

and corresponds to photon frequencies in the GHz range, while the Zeeman energy splitting between $I = \frac{1}{2}$ nuclear spin levels is

$$\Delta E = \frac{\beta_n}{\hbar} g_n B_0 \tag{1.8}$$

and resonates with photon frequencies in the MHz range. This large difference between the resonance frequencies of the two Zeeman interactions leads to the differences between ESR and nuclear magnetic resonance (NMR) instrumentation.

1.1.2 Hyperfine interaction

The hyperfine interaction is the interaction between the electron spin and nuclear spins. The corresponding hyperfine tensor $\mathbf{A}$ is real-valued and symmetric, and consists of two parts: an isotropic Fermi-contact contribution due to the finite electron spin at the nucleus described by the isotropic hyperfine coupling constant a_{iso}, and an anisotropic electron-nucleus dipolar interaction described by the tensor $\mathbf{T}$.[8]

$$\hat{H}_{HF} = a_{iso} \hat{\mathbf{S}} \hat{\mathbf{I}} + \hat{\mathbf{S}} \mathbf{T} \hat{\mathbf{I}} \tag{1.9}$$

The isotropic hyperfine coupling constant is defined as

$$a_{iso} = \frac{2}{3}\frac{\mu_0}{\hbar} g_e \beta_e g_n \beta_n |\psi_0(0)|^2 \tag{1.10}$$

where $|\psi_0(0)|^2$ accounts for the probability of the electronic ground-state wavefunction at the nucleus. The elements of the anisotropic electron-nucleus dipolar hyperfine tensor are given by

$$T_{ij} = \frac{\mu_0}{4\pi\hbar} g_e \beta_e g_n \beta_n \left\langle \psi_0 \left| \frac{3r_i r_j - \delta_{ij} r^2}{r^5} \right| \psi_0 \right\rangle \tag{1.11}$$

where $\mathbf{r}$ is the distance vector between electron and nucleus, and δ_{ij} is the Kronecker delta function.

The hyperfine interaction of one electron spin with m identical nuclear spins splits the electronic spin levels into $2mI + 1$ sub-levels.

1.1.3 Zero-field splitting interaction

The zero-field splitting (ZFS) interaction is the dipolar interaction between electronic spins in systems with $S > \frac{1}{2}$. As its name indicates, this interaction removes the $(2S + 1)$-fold degeneracy of the different m_S sub-levels in the absence of an applied magnetic field. In the principal axes system of the symmetric and traceless ZFS tensor $\mathbf{D}$, X, Y, Z, the ZFS Hamiltonian can be written in terms of just two ZFS parameters, $D = \frac{3}{2}D_z$ and $E = \frac{1}{2}(D_X - D_Y)$, where the principal values of $\mathbf{D}$ follow the convention $|D_Y| \leq |D_X| < |D_Z|$.[9] The ZFS Hamiltonian is then given by

$$\hat{H}_{ZFS} = D\left[\hat{S}_z^2 - \frac{1}{3}S(S+1)\mathbf{1}\right] + E(\hat{S}_x^2 - \hat{S}_y^2) \tag{1.12}$$

Spin triplets

For the case of a spin triplet ($S = 1$), the eigenstates of the ZFS Hamiltonian at zero field, the zero-field basis, are $\{|T_X\rangle, |T_Y\rangle, |T_Z\rangle\}$, with energies given

by[10]

$$E_X = \frac{1}{3}D - E, E_Y = \frac{1}{3}D + E, E_Z = -\frac{2}{3}D \tag{1.13}$$

Their relative ordering depends on the signs and magnitudes of D and E.

If a magnetic field is applied along the Z principal axis of the ZFS tensor ($\mathbf{B}_0 \parallel Z$) such that the corresponding electronic Zeeman interaction exceeds the the ZFS interaction, then the total spin Hamiltonian is more conveniently expressed in the eigenstates of $\hat{S}_z$, the so-called high-field basis $\{|T_+\rangle, |T_0\rangle, |T_-\rangle\} \equiv \{|S, m_S\rangle\} = \{|1, +1\rangle, |1, 0\rangle, |1, -1\rangle\}$. This basis is related to the zero-field basis as follows

$$|T_X\rangle = \frac{1}{\sqrt{2}}(|T_+\rangle - |T_-\rangle), |T_Y\rangle = \frac{i}{\sqrt{2}}(|T_+\rangle + |T_-\rangle), |T_Z\rangle = |T_0\rangle \tag{1.14}$$

and the energies of the high-field states are given by

$$\begin{aligned} E_+ &= \frac{1}{3}D + \sqrt{E^2 + (g\beta_e B_0)^2} \\ E_0 &= -\frac{2}{3}D \\ E_- &= \frac{1}{3}D - \sqrt{E^2 + (g\beta_e B_0)^2} \end{aligned} \tag{1.15}$$

This yields two allowed transitions for a given $\mathbf{B}_0$, according to the $|\Delta m_S| = 1$ selection rule: $|T_-\rangle \leftrightarrow |T_0\rangle$ and $|T_0\rangle \leftrightarrow |T_+\rangle$. For $\mathbf{B}_0 \parallel Z$, these transitions are labelled Z^- and Z^+, respectively. Fig. 1.1 shows these transitions for $\mathbf{B}_0$ along the three principal axes of the ZFS tensor, leading to the six turning points observed in the ESR spectrum. The continuous spectrum is the result of adding together the individual spectra of an ensemble of molecules with isotropically distributed orientations (powder averaging), such as that of an isotropic frozen solution. The ZFS parameters D and E can be determined from the distance between these turning points.

The intensity and sign of each turning point is given by the populations of the high-field states, which for $\mathbf{B}_0 \parallel Z$ are related to the populations of

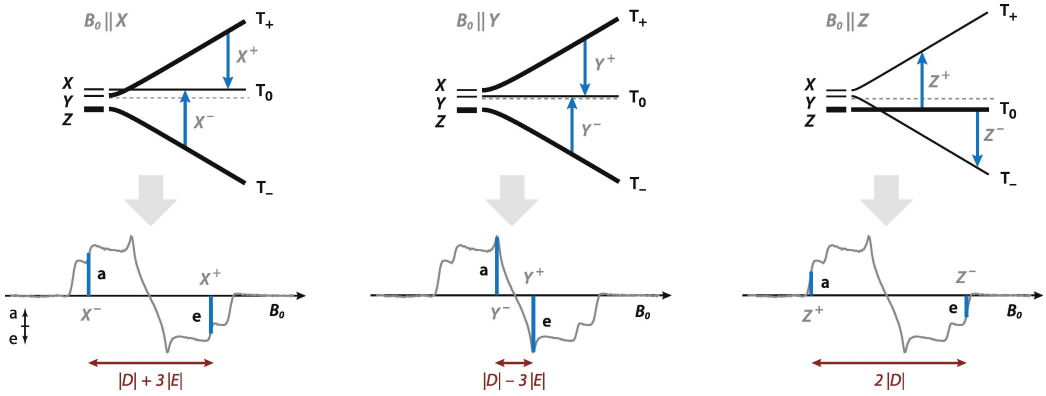


Figure 1.1: Electronic spin energy level diagrams as a function of an external magnetic field with the field vector, $\mathbf{B}_0$, aligned with the ZFS axes X, Y and Z, respectively, for a triplet with $D > 0$, $E < 0$ and $|D| > 3|E|$. Whenever the energy of the microwave radiation matches the energy gap between $|T_0\rangle$ and either $|T_-\rangle$ or $|T_+\rangle$, a transition can be observed. The transitions can be either emissive (e) or enhanced absorptive (a) depending on the relative populations of the high-field sublevels involved, indicated by the thickness of the level bars. In a powder spectrum, the transitions corresponding to the canonical field orientations are characterised by turning points, indicated with vertical lines on the spectrum and labelled $X^{\pm}$, $Y^{\pm}$ and $Z^{\pm}$. *Reprinted (adapted) with permission from Richert, S., Tait, C. E. and Timmel, C. R. (2017). Delocalisation of photoexcited triplet states probed by transient EPR and hyperfine spectroscopy. Journal of Magnetic Resonance, 280, 103–116. doi:10.1016/j.jmr.2017.01.005. Copyright 2017 Elsevier.*[10]

the zero-field states as follows[10]

$$P_0 = P_Z, \quad P_{\pm} = \frac{1}{2}(P_X + P_Y) \tag{1.16}$$

The presence of both enhanced absorptive (positive) and emissive (negative) features is a result of the mechanisms by which the triplet is formed, leading to significant deviations of the spin state populations from the expected values for a Boltzmann distribution at that temperature.[11] Such an ESR spectrum is referred to as being spin polarised.

Two different interactions generally contribute to the ZFS: a first-order contribution arising from the spin-spin dipolar coupling (SSC) and a second-order contribution arising from the spin-orbit coupling (SOC). For triplet states of organic molecules, the SSC is the dominant contribution and the

SOC contribution can be safely neglected. The SSC between the two unpaired electrons of the triplet state can be described using the point-dipole approximation, by which the spin density of each electron is considered to be localised on a finite number of atoms. The dipolar interaction between the two unpaired electrons spins under this approximation results from the atom-atom pairwise interaction averaged over all atoms bearing electronic spin density, and the ZFS parameters can be expressed as[10]

$$\begin{aligned} D &= \frac{3\mu_0 g_1 g_2 \beta_e^2}{16\pi\hbar} \left\langle \frac{r^2 - 3z^2}{r^5} \right\rangle \\ E &= \frac{3\mu_0 g_1 g_2 \beta_e^2}{16\pi\hbar} \left\langle \frac{x^2 - y^2}{r^5} \right\rangle \end{aligned} \tag{1.17}$$

where g_1 and g_2 are the g-values for the two electrons and $\mathbf{r} = (x, y, z)$ is the distance vector connecting them, with $r \equiv |\mathbf{r}|$. From equation 1.17 we can see that D is a measure of the elongation of the electronic spin density of the triplet state along the Z axis, with oblate distributions having $D > 0$, while E measures its ellipticity in the $X - Y$ plane, with $E > 0$ indicating elongation along the X axis.

1.1.4 Electron-electron dipolar interaction

For systems with $S > \frac{1}{2}$ where the interaction between electron spins is weak, the ZFS description is not convenient and it is better to consider a total spin Hamiltonian consisting of the spin Hamiltonians of the individual electrons interacting *via* through-space dipolar coupling ($\hat{H}_{dd}$) and through-bonds exchange coupling ($\hat{H}_{ex}$) Hamiltonians. For a system with two electron spins (S_1 and S_2), the total spin Hamiltonian is[6]

$$\hat{H}(S_1, S_2) = \hat{H}(S_1) + \hat{H}(S_2) + \hat{H}_{dd} + \hat{H}_{ex} \tag{1.18}$$

For the molecules studied in this thesis, the exchange coupling term can always be safely neglected and the weak interaction between electron spins

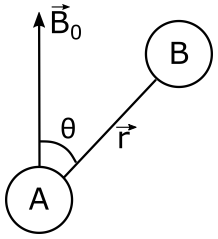


Figure 1.2: Schematic two-electron spin system, where the two spins A, B are linked by a distance vector $\mathbf{r}$ of length r at an angle θ with the applied magnetic field $\mathbf{B}_0$.

is purely dipolar.

The dipolar contribution to the two-electron spin Hamiltonian is

$$\hat{H}_{dd} = \frac{\mu_0}{4\pi\hbar}\frac{g_1 g_2 \beta_e^2}{r^3}\left[\hat{\mathbf{S}}_1\hat{\mathbf{S}}_2 - \frac{3}{r^2}(\hat{\mathbf{S}}_1\mathbf{r})(\hat{\mathbf{S}}_2\mathbf{r})\right] \tag{1.19}$$

If the electronic Zeeman interaction is much larger than the dipolar interaction and the difference in resonance frequency between the two spins is larger than the dipolar frequency (ω_{dd}), then this Hamiltonian simplifies to

$$\hat{H}_{dd} = \frac{\mu_0}{4\pi\hbar}\frac{g_1 g_2 \beta_e^2}{r^3}(1 - 3\cos^2\theta)\hat{S}_{1z}\hat{S}_{2z} = \omega_{dd}(1 - 3\cos^2\theta)\hat{S}_{1z}\hat{S}_{2z} \tag{1.20}$$

where θ is the angle between the applied field and the vector connecting the two electron spins,$\mathbf{r}$ (Figure 1.2). This electron-electron dipolar interaction is the basis of Pulsed Dipolar Spectroscopy (PDS) and will be treated in more detail in Section 1.4.

1.2 Electron spin resonance (ESR) spectroscopy

ESR spectroscopy is a magnetic resonance technique used for the study of systems with unpaired electron spins (*i.e.* $S \neq 0$), allowing for the determina-

tion of the different terms of the spin Hamiltonian. Exploiting the electronic Zeeman interaction, microwave (MW) radiation is used to drive transitions between the different m_S spin sub-levels of the system of study by interaction of the magnetic component of the radiation ($\mathbf{B}_1$) with the electronic magnetic moment, under a static applied magnetic field ($\mathbf{B}_0$). The most commonly employed MW frequency bands are X-band (∼9.5 GHz), Q-band (∼34 GHz) and W-band (∼95 GHz), which for a free electron are resonant with Zeeman energy splittings corresponding to applied magnetic fields of 0.34, 1.12 and 3.4 T, respectively. Using higher frequencies and fields improves both the spectral resolution of field-dependent interactions and the sensitivity, which is determined by the population differences between the energy levels involved in the probed transitions. Nevertheless, in a similar way to NMR, the small population differences involved in ESR require the use of resonant cavities to reach reasonable sensitivities, which are still much lower than in optical spectroscopy.

MW radiation in ESR can be applied either continuously at low intensity, in continuous-wave ESR (cwESR), or in sequences of short (nanosecond length) intense pulses, in pulsed ESR. The following sections introduce the basic principles and instrumentations for these two different modes of implementation of ESR spectroscopy.

1.2.1 Continuous-wave ESR

In cwESR, the sample is continuously irradiated with MW of a fixed frequency and amplitude while B_0 is swept. For fields at which the energy difference between two spin sub-levels becomes resonant with the MW radiation, absorption is observed.

A typical setup for cwESR is shown in Fig. 1.3.[12] The main components are a MW source, an electromagnet to generate the tunable B_0, a resonant cavity used to amplify the input and output ESR signal and a detection system. For the most commonly used frequencies (X- and Q-band), MW

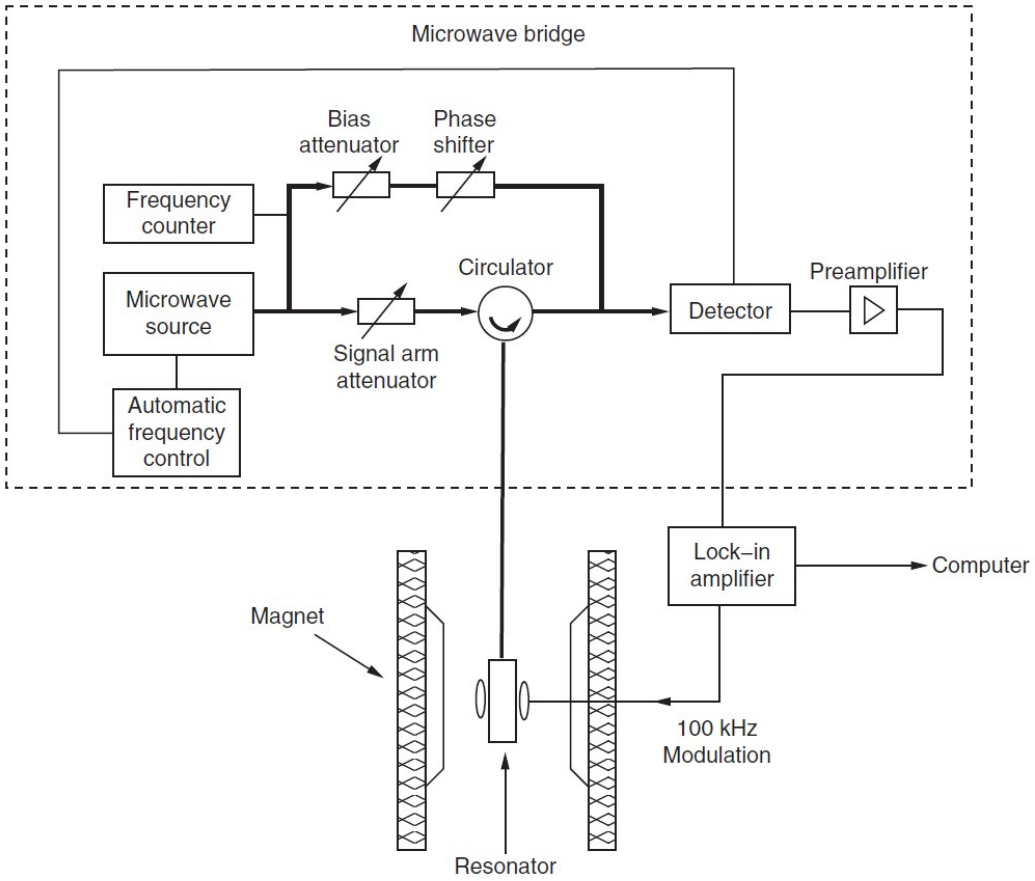


Figure 1.3: Schematic diagram of a cwESR spectrometer. For a detailed description, see text. *Reproduced with permission from A. van der Est, in EPR Spectroscopy - Fundamamentals and Methods, ed. D. Goldfarb and S. Stoll, John Wiley and Sons, Inc., Chichester, 1st edn., 2018, ch. 1, pp. 3–16. doi:10.1002/9780470034590.emrstm1508. Copyright 2018 John Wiley & Sons.*[12]

radiation is transmitted to and from the cavity using waveguides. After the MW source, an isolator reduces MW fluctuations and prevents reflected radiation from reaching the source. MWs are attenuated before reaching the circulator, which directs radiation from the source into the cavity, and sends the reflected MWs coming from the cavity towards the detector.

The MW radiation generates a standing wave inside the cavity, which is designed to have maximum B_1 and minimum electric field amplitudes at the centre, where the sample sits, in order to minimise MW energy losses by dielectric heating. The usual spectrometer geometry is such that $\mathbf{B}_1 \perp \mathbf{B}_0$,

in the so-called perpendicular mode ESR. By matching the impedance of the cavity to that of the MW line, the quality factor (Q) of the cavity is maximised in a tuning procedure involving the fine adjustment of the MW source frequency and the coupling of the MW line into the cavity using a coupling element (iris). When the maximum Q is achieved (critical coupling), the MW power reflected back from the cavity is minimised. When the resonance condition is met ($\Delta E = h\nu$), B_1 induces a transition between spin energy levels by absorption of MW photons, which causes a change in the impedance of the cavity (impedance mismatch) leading to an increase of the reflected MW power. This change constitutes the ESR signal.

The detector is usually a diode, which needs to be biased to its linear response regime. This is achieved by diverting part of the MW radiation from the source to by-pass the circulator through a reference arm, whose power is adjusted with an attenuator. The MW phase difference between the two arms is corrected by a phase shifter, in order to obtain a purely absorptive ESR signal.

To reduce the noise of the measurement, phase-sensitive detection is employed. A small oscillating magnetic field B_{mod} is applied in the same direction of B_0 at frequencies of typically 100 KHz using an additional pair of coils (modulation coils) outside the cavity, and the ESR signal oscillating at that frequency is filtered from the noise using a lock-in amplifier. As a consequence of this field modulation, the acquired spectrum shows the first derivative of the ESR signal. Therefore, care must be taken to make sure that B_{mod} is sufficiently smaller than the ESR linewidth in order not to distort the shape of the spectrum.

Linewidth and lineshape of ESR spectra

The linewidth and lineshape of ESR spectra depend on the mechanisms of line broadening, which can be homogeneous or inhomogeneous.[6]

Homogeneous line broadening occurs when all spins in the sample expe-

rience the same net magnetic field resulting as a combination of the applied and local field due to the nearby dipoles, yielding the same transition probability as a function of B_0. Homogeneous broadening leads to Lorentzian lineshapes. Fluctuating local magnetic fields due to neighbouring nuclear and electron spin flips are a cause of homogeneous broadening.

Inhomogeneous line broadening occurs when groups of spins in the sample (spin packets) are subjected to slightly different magnetic fields, leading to slightly different B_0 values for the resonance condition of the different spin packets. As a result, the ESR absorption line is a superposition of the individual lines of all the spin packets, each having a Lorentzian profile, yielding a Gaussian envelope. An inhomogeneous B_0, unresolved hyperfine interactions or the presence of spin Hamiltonian strain (the small variation of the Hamiltonian parameters due to the inhomogeneous nature of the sample) are causes of inhomogeneous broadening.

In most real samples, however, ESR lines are neither purely Lorentzian nor Gaussian but a convolution of the two profiles (Voigtian lineshape). Rather than the usual Full Width at Half Maximum (FWHM) measurement of linewidth, which is difficult to obtain in derivative spectra, the peak-to-peak linewidth (ΔB_{pp}) is used instead in cwESR.

Time-resolved ESR (trESR)

The increase in sensitivity due to field modulation in cwESR comes at the expenses of time resolution, as the acquisition of a spectrum requires a continuous field sweep. In systems with inherently large population differences between the probed spin sub-levels, such as photogenerated triplet states or radical pairs, the enhanced sensitivity arising from the strong spin polarisation enables direct detection of the ESR signal, without the need for field modulation and phase-sensitive detection. In those cases, the sign of the ESR signal directly reflects the polarisation of the resonant transition, with positive signals corresponding to absorptive transitions and negative signals

corresponding to emissive transitions. This transient or time-resolved mode of cwESR (trESR) allows for the study of short-lived paramagnetic species with nanosecond time resolution.[10]

Following a short light pulse, usually provided by a pulsed laser, that generates the paramagnetic species and that serves as zero time for the data acquisition, the ESR signal is monitored as a function of time at a fixed B_0. After repeating the acquisition at the same B_0 multiple times to yield a transient with the desired signal-to-noise ratio (SNR), the field is increased and the next transient is recorded. The iteration of this process results in a two-dimensional dataset, consisting in ESR signal data as a function of B_0 and time. Each time slice of the dataset corresponds to a field-swept cwESR spectrum recorded at that time after the light pulse.

Experimentally, a conventional cwESR setup can be upgraded to perform transient measurements, by the addition of a pulsed laser source and an oscilloscope.[13] MW bridges with high time resolution suitable for trESR are nowadays commercially available. The pulsed light source is often a laser, such as a dye laser, and excimer laser or a Nd:YAG laser. The latter is a common choice, offering a fundamental wavelength of 1064 nm which can be doubled or tripled to 532 and 355 nm for visible and ultra-violet (UV) excitation, respectively. If other wavelengths are required, the laser source can be used to pump an optical parametric oscillator (OPO), providing a tunable output in the visible range of the spectrum and sometimes extensible into the UV and infra-red (IR). This light can be delivered to the sample either *via* direct beam path through an optical window in the ESR cavity, or through a light-guide directly inserted into the sample tube (see Figures 5.1 and 5.2 in Appendix I). Care must be taken to minimise the jitter of the laser power and zero-time trigger in order to reduce the power and time noises. In addition, the repetition frequency for successive transient acquisitions, which is normally fixed by the laser source, must be low enough to allow for the system to fully return to the ground state before the next light pulse.

The cw nature of trESR makes this technique less dependent on spin

relaxation effects than pulsed methods, as will be discussed in Section 1.2.2, allowing for the detection of fast-relaxing species that would otherwise be impossible by pulsed ESR. Spin relaxation will be discussed in more detail in Section 1.3.

1.2.2 Pulsed ESR

In pulsed ESR, the sample is exposed to sequences of intense MW pulses of nanosecond duration. This requires some modifications and additions to the ESR setup presented in Section 1.2.1.[14] The MW radiation coming from the source passes through a pulse-forming unit (PFU), which has different channels with individual attenuators and phase shifters, allowing for the amplitude, length and phase of each rectangular pulse to be adjusted. Shaped pulses can be generated with an arbitrary waveform generator (AWG).[15] The resulting pulses are amplified by a high-power travelling-wave tube (TWT) amplifier before being sent to the cavity.

A fundamental problem resulting from the high-energy MW radiation used in pulsed ESR is that detection cannot be carried out during MW irradiation, and not even shortly after the end of the last pulse, while high-energy MWs are still ringing inside the cavity. During this period of time, the sensitive diode detector needs to be protected from the high-energy MWs by a gated limiter or switch (usually referred as defence pulse or protection gate). Only after the ringing radiation has decayed to safe levels can the MWs coming from the resonator be allowed to reach the detector. Consequently, pulsed ESR has a dead time that depends on the MW frequency and the Q-factor of the cavity. In order to minimise this dead time, the Q-factor is reduced by over-coupling the cavity. However, the lowering of the Q-factor also reduces the sensitivity of the measurements, so a trade-off between dead time and sensitivity must be reached for each particular sample.

Another consequence of the use of an over-coupled cavity is the increase in cavity bandwidth with respect to the critically-coupled case. The cavity

bandwidth is defined as the frequency difference between the two frequency points where the MW power in the cavity is attenuated by a factor of 2 (3 dB) relative to the centre of resonance, and it limits the excitation profile of the MW pulses. The excitation profile of a pulse in the frequency domain is approximately given by the Fourier transform of its pulse shape in the time domain. For rectangular pulses, this gives a sinc function ($\sin(x)/x$), with an excitation bandwidth inversely proportional to the pulse duration.

The ESR signal is detected by frequency downconversion using a frequency mixer. The MW signal coming from the sample is mixed with the radiation from the reference arm and the final difference frequency signal is amplified before reaching the detector. Quadrature detection is normally employed, involving the detection of both components of the magnetisation in the plane perpendicular to $\mathbf{B}_0$, often referred as the real and imaginary parts of the signal. Using the phase shifter in the reference arm, the phase of the signal is normally adjusted to minimise the imaginary component.

The vector model of pulsed ESR

The effect of simple MW pulse sequences on the ensemble magnetic moment of the sample (magnetisation, $\mathbf{M}$) can be described in an approximated semi-classical way by representing individual spin packets by their magnetisation vector. As introduced in Section 1.1, under a static external magnetic field $\mathbf{B}_0$, which we will assume to be parallel to the z axis of the laboratory frame (z_L), electron spin magnetic moments will precess with Larmor frequency ω_0 around z_L. Assuming a population of the two m_S sub-levels according to a Boltzmann distribution, there will be a small excess of spins with μ_z parallel (as opposed to anti-parallel) to $\mathbf{B}_0$, and there will be no correlations between the spin magnetic moment components in the transverse plane (x_L-y_L), yielding a net magnetisation of the sample $\mathbf{M} \parallel \mathbf{B}_0$, with longitudinal magnetisation $M_z = |\mathbf{M}|$.

The linearly polarised MWs used in pulsed ESR experiments can be

treated as the superposition of two counter-rotating circularly polarised electromagnetic waves of the same angular frequency $\pm\omega_{MW}$. Assuming the magnetic field component of the linearly polarised MWs to be parallel to x_L, the circularly polarised components ($\mathbf{B}_1^{\pm}$) rotate in the x_L-y_L plane (Fig. 1.4).

The problem is simplified by defining a non-inertial reference frame, the rotating frame, with z-axis collinear with the laboratory frame ($z_R \parallel z_L$) and which rotates around z_L with angular frequency ω_{MW} anticlockwise (Fig. 1.4, red).[14] In this frame, the magnetic field of one of the circularly polarised MW components ($\mathbf{B}_1^+ \equiv \mathbf{B}_1$) is stationary on x_R while the other component ($\mathbf{B}_1^-$) rotates in the x_R-y_R plane with angular frequency $-2\omega_{MW}$ and has no net effect on $\mathbf{M}$. For spin packets satisfying the resonance condition, $\omega_0 = \omega_{MW}$ and their spins appear stationary in the rotating frame in the absence of a MW field, meaning that $\mathbf{B}_0$ vanishes for these spins. The evolution of on-resonance spins during a MW pulse in the rotating frame is a precession around $\mathbf{B}_1$, which corresponds to a nutation motion in the laboratory frame. However, for off-resonance spin packets, with $\omega_0 \neq \omega_{MW}$, $\mathbf{B}_0$ does not disappear completely and the precession during a MW pulse occurs around the resulting effective magnetic field, leading to a small spread of the spin packets and a corresponding decrease in the net magnetisation of the sample after the pulse.

The duration of the MW pulse (t_p) and the amplitude of $\mathbf{B}_1$ in angular frequency units (ω_1) determine the angle of rotation of $\mathbf{M}$, called the flip angle of the pulse ($\beta = \omega_1 t_p$). All pulses used in this thesis have β values of $\frac{\pi}{2}$ or π. For simplicity, these pulses will be designated by their β and their $\mathbf{B}_1$ direction (e.g. a π pulse with $\mathbf{B}_1 \parallel x_R$ will be denoted $(\pi)_x$).

We can now use this intuitive vector model in the rotating frame to describe the two-pulse spin echo or Hahn echo experiment (Fig. 1.5). Following the application of an initial $(\frac{\pi}{2})_x$ pulse, which transforms the longitudinal magnetisation of the sample into transverse magnetisation, $\mathbf{M}$ has rotated onto $-y_R$. Once the MW pulse finishes and $\mathbf{B}_1$ is removed, the electronic

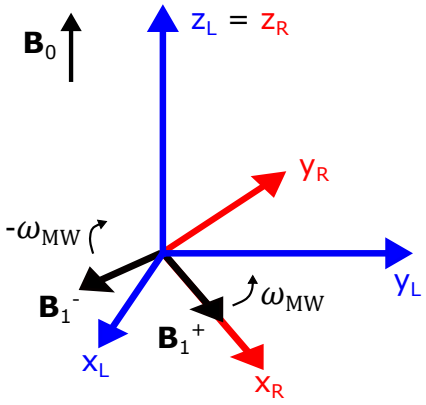


Figure 1.4: Laboratory (L, blue) and rotating (R, red) reference frames for the description of pulsed ESR. The rotating frame rotates around z_L with angular frequency ω_{MW} anticlockwise. The magnetic field vectors for the two counter-rotating circularly polarised MW components at angular frequencies $\pm\omega_{MW}$ in the laboratory frame are shown in black ($\mathbf{B}_1^{\pm}$).

spin magnetic moments in the sample resume their Larmor precession around $\mathbf{B}_0$. Spin packets satisfying the resonance condition (black) will remain static on $-y_R$, while off-resonance packets with $\omega_0 > \omega_{MW}$ (blue) or $\omega_0 < \omega_{MW}$ (red) will rotate anticlockwise or clockwise, respectively, in the x_R-y_R plane, leading to a spreading of the spin packets and a corresponding decrease of net magnetisation. The spreading can be reverted by the application of a $(\pi)_x$ pulse a time τ after the first pulse, which rotates the spins around x_R. In the absence of incoherent processes, all spin packets will converge back on y_R a time τ after the application of the second MW pulse, to recover the initial $|\mathbf{M}|$. This recovery of the transverse magnetisation of the sample is detected and constitutes the spin echo, which can be integrated to yield an echo intensity signal comparable to the signal in cwESR.

Density-operator description of pulsed ESR

The vector model of pulsed ESR is useful to describe simple experiments, but the explanation of complex pulse sequences requires the rigorous quantum mechanical approach provided by the density operator formalism.

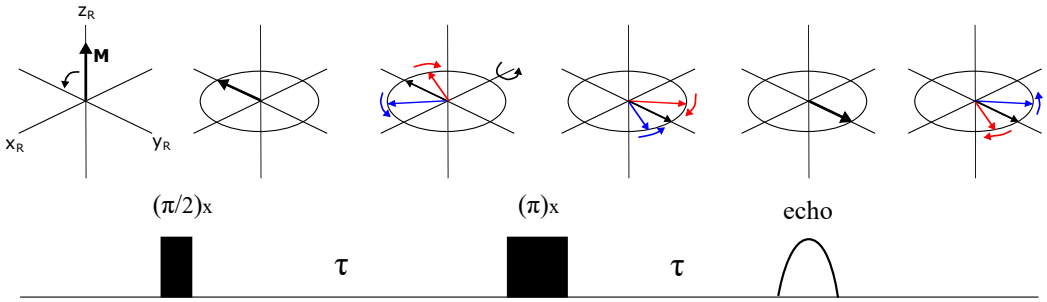


Figure 1.5: Vector model description of a two-pulse or Hahn-echo experiment in the rotating frame. Black arrows represent on-resonance spin packets. Coloured arrows represent off-resonance spin packets with Larmor frequencies $\omega_0 > \omega_{MW}$ (blue) and $\omega_0 < \omega_{MW}$ (red).

The quantum mechanical state of an ensemble of spins can be described by a density operator $\hat{\boldsymbol{\sigma}}$.[6] For the simplest case of an ensemble of isolated electron spins ($S = \frac{1}{2}$, $|\alpha\rangle \equiv |m_S = +\frac{1}{2}\rangle$, $|\beta\rangle \equiv |m_S = -\frac{1}{2}\rangle$), where each individual spin wavefunction has the form $|\psi\rangle = c_\alpha|\alpha\rangle + c_\beta|\beta\rangle$, the matrix representation of the density operator is given by

$$\hat{\boldsymbol{\sigma}} = \begin{bmatrix} \overline{|c_\alpha|^2} & \overline{c_\alpha c_\beta^*} \\ \overline{c_\alpha^* c_\beta} & \overline{|c_\beta|^2} \end{bmatrix} \tag{1.21}$$

where the over-line stands for ensemble average and the asterisk indicates complex conjugate.

The diagonal elements of the density matrix correspond to the populations of the different spin states. Their difference is called polarisation and is related to the classical concept of longitudinal magnetisation. The relation of spin polarisation with ESR sensitivity has already been discussed in Section 1.1.3. The off-diagonal elements represent phase-coherent superpositions of states, called coherences, and are related to the concept of transverse magnetisation.

In the absence of relaxation and other non-coherent processes, the time evolution of the density operator under a Hamiltonian $\hat{H}$ is described by the

Liouville-von Neumann equation[6]

$$\frac{d\hat{\boldsymbol{\sigma}}}{dt} = -i[\hat{H}, \hat{\boldsymbol{\sigma}}] \tag{1.22}$$

where $[\hat{H}, \hat{\boldsymbol{\sigma}}] = \hat{H}\hat{\boldsymbol{\sigma}} - \hat{\boldsymbol{\sigma}}\hat{H}$ is the commutator. If $\hat{H}$ is time-independent, the solution to Equation 1.22 for an evolution time t is given by

$$\hat{\boldsymbol{\sigma}}(t) = \exp(-i\hat{H}t)\hat{\boldsymbol{\sigma}}(0)\exp(i\hat{H}t) = \hat{\mathbf{U}}_{\hat{H}}(t)\hat{\boldsymbol{\sigma}}(0)\hat{\mathbf{U}}^{\dagger}_{\hat{H}}(t) \tag{1.23}$$

where $\hat{\boldsymbol{\sigma}}(0)$ is the density operator at $t = 0$ and $\hat{\mathbf{U}}_{\hat{H}}$ is the propagator of $\hat{\boldsymbol{\sigma}}$ under the Hamiltonian $\hat{H}$, a unitary operator ($\hat{\mathbf{U}}^{-1}_{\hat{H}} = \hat{\mathbf{U}}^{\dagger}_{\hat{H}}$) corresponding to a rotation in Hilbert space.

Pulsed ESR experiments can be considered as a succession of spin evolution periods under different time-independent Hamiltonians. Therefore, the expression of the density operator at the time of the final spin echo of the experiment can be obtained by successive application of the different propagators corresponding to the periods of nutation under MW field and of free precession under $\mathbf{B}_0$ in the given pulse sequence ($\hat{\mathbf{U}}_{total} = \hat{\mathbf{U}}_n \cdots \hat{\mathbf{U}}_2\hat{\mathbf{U}}_1$). The expectation value of the transverse magnetisation at that time, which corresponds to the observable measured in quadrature detection, can be calculated as follows

$$V(t) = \langle \hat{S}_x + i\hat{S}_y \rangle = trace\{(\hat{S}_x + i\hat{S}_y)\hat{\boldsymbol{\sigma}}(t)\} \tag{1.24}$$

1.3 Relaxation

Relaxation is the return of the magnetisation of the sample to its equilibrium value after a perturbation, and arises from the interactions between the spin system and its environment, which cause fluctuations in the local magnetic field experienced by the spins of the system. Relaxation determines

spectral linewidths in cwESR and limits the maximum time length of pulse sequences and the maximum repetition rate of pulsed ESR experiments. Depending on their mechanism, two main types of relaxation are distinguished.[6] Spin-lattice or longitudinal relaxation is the return of the longitudinal magnetisation M_z to its equilibrium value $M_{z,equil.}$, and it is characterised by the relaxation time T_1:

$$M_z(t) = M_{z,equil.}\left[1 - \exp\left(-\frac{t}{T_1}\right)\right] \tag{1.25}$$

assuming $M_z(0) = 0$. Spin-spin or transverse relaxation is the decay to zero of the magnetisation in the transverse plane M_{xy} by the loss of coherence in the precessing motion of the spins, and it is characterised by the relaxation time T_2.

$$M_{xy}(t) = M_{xy}(0)\exp\left(-\frac{t}{T_2}\right) \tag{1.26}$$

The mechanisms leading to these two types of relaxation are briefly discussed in the following sections.

1.3.1 Spin-lattice or longitudinal relaxation

In spin-lattice relaxation the magnetic quantum number m_S and thus the energy of the spin system change, involving an exchange of energy between the system and the lattice that establishes thermal equilibrium. The mechanisms of spin-lattice relaxation are different in solids and in liquids.

In liquid samples, molecular tumbling is the main mechanism contributing to relaxation both by spin rotation and by modulation of the anisotropic interactions, such as Zeeman, hyperfine and dipolar. Internal thermally-activated molecular motions, such as methyl or amino group rotation, also contribute to relaxation. These processes are most effective when the rotational or tumbling frequency matches the Larmor frequency and are therefore temperature dependent. Collisions with other paramagnetic species, such as molecules of the same type or dissolved oxygen, also lead to relaxation, in a

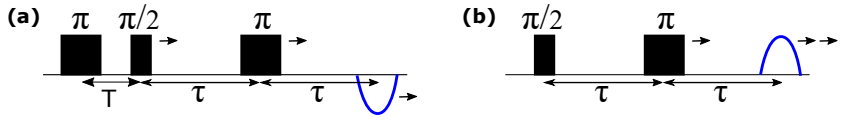


Figure 1.6: Pulse sequences for the characterisation of electron spin relaxation. (a) Inversion-recovery sequence for the characterisation of spin-lattice relaxation, where the delay T is increased stepwise. (b) Variable-delay Hahn-echo sequence for the characterisation of spin-spin relaxation, where τ is increased stepwise.

concentration-dependent manner.

In solid samples, spin-lattice relaxation is driven by thermal motion and the system exchanges energy with the lattice in form of phonons. Three main processes of spin-lattice phonon exchange can be distinguished, direct, Raman and Orbach processes, with different temperature and magnetic field dependence.[16] The direct process occurs when the unpaired electron spin flip energy exactly matches a lattice phonon energy, leading to a direct transfer of energy. In the two-phonon Raman process, the energy transferred from the spin system to the lattice is the difference between the absorption energy to a virtual excited phonon state and the emission energy from this virtual state to a high-energy phonon state. The Orbach process is also a two-phonon process, but in this case the excited state that mediates the energy exchange is a real state.

The corresponding T_1 is often measured with an inversion-recovery experiment (Fig. 1.6 (a)), where an initial π pulse to invert the direction of $\mathbf{M}$ to be antiparallel with $\mathbf{B}_0$ is followed after a variable delay T by a Hahn echo sequence, which forms a spin echo. Spin-lattice relaxation during the period T leads to a recovery of the original longitudinal magnetisation. By increasing T stepwise, an echo intensity recovery trace is obtained, with the maximum negative intensity for $T \to 0$ and saturating to a maximum positive intensity for $T \to \infty$.

1.3.2 Spin-spin or transverse relaxation

The relaxation mechanisms described in the previous section also contribute to the loss of transverse magnetisation, but the main mechanism governing spin-spin relaxation is the energy-conserving spin flip-flop, by which two lattice spins coupled to the spin system change spin state simultaneously.[16] These spins can be electronic or nuclear. Although nuclear spin flip is a much slower process than electronic spin flip, the very large number of nuclei that are coupled to the spin system in usual samples makes nuclear spin flip-flops a major contributor to spin-spin relaxation. Protons are particularly effective for this process and spin-spin relaxation can be slowed down by deuterating the sample.

If $1/T_2'$ is the spin flip-flop rate, then the transverse relaxation time T_2 is given by[16]

$$\frac{1}{T_2} = \frac{1}{T_2'} + \frac{1}{2T_1} \tag{1.27}$$

This implies that $T_2 \leq 2T_1$.

Experimentally, however, the spin phase-memory time (T_m) is normally used instead of T_2, as it includes T_2 and it accounts for any other processes causing loss of electron spin coherence.[6] It is measured with a variable-delay Hahn-echo pulse sequence (Fig. 1.6 (b)), where the spin-spin relaxation occurring during the two τ periods leads to a loss of spin echo intensity, eventually decaying to zero for $\tau \to \infty$.

Magnetisation diffusion processes, which change the resonance frequency of the electron spin and thus move magnetisation between different regions of the ESR spectrum, can move spins out of the detection window and therefore appear as relaxation, contributing to T_m.[6] In pulsed ESR experiments where only a part of the spectrum is excited, the relaxation of non-excited spins is a cause of this effect and is known as spectral diffusion. Similarly, the change in the local magnetic field experienced by an excited spin due to the excitation of a dipolarly-coupled spin also contributes to T_m and is know as instantaneous diffusion.

1.4 Pulsed dipolar spectroscopy (PDS)

The work presented in this thesis is concerned with the study of weakly-interacting electronic spins and the quantification of their through-space dipolar coupling. The strength of this interaction is of interest as it is related to the magnitude of the distance vector connecting the two spins (dipolar vector) and its orientation relative to $\mathbf{B}_0$ (Fig. 1.7 (a)). PDS is the set of pulsed ESR techniques aimed at the measurement of the electron-electron dipolar interaction. This section introduces the principles of PDS and its practicalities through the example of the double electron-electron resonance (DEER) technique,[17] which is the most widely-used PDS technique and the basis of the novel methods developed in this work.

1.4.1 The dipolar spectrum

Figure 1.7 (a) shows the ideal spin system studied in PDS: an isolated electron spin pair A-B interacting dipolarly, separated by a dipolar vector $\mathbf{r}$ of magnitude r and forming an angle θ with $\mathbf{B}_0$. Their Zeeman frequencies at the applied field are ω_A and ω_B, respectively. For simplicity, let us choose $S_A = S_B = \frac{1}{2}$, so that the pure states of the spin system are $\{|\alpha_A\alpha_B\rangle, |\alpha_A\beta_B\rangle, |\beta_A\alpha_B\rangle, |\beta_A\beta_B\rangle\}$. The spin-allowed (single-quantum) transitions in this system are shown in Fig. 1.7 (b), together with their corresponding resonance frequencies.[1] Assuming the validity of the high-field (Zeeman interaction $\gg$ dipolar interaction) and the weak-coupling ($|\omega_A - \omega_B| > \omega_{dd}$) approximations, then the dipolar interaction Hamiltonian is given by equation 1.20. Taking into account the angular dependence of the dipolar interaction and the probability of encountering an orientation with angle θ ($\propto \sin\theta$), the dipolar spectrum for an ensemble of identical spin systems A-B with uniform angular distribution is a Pake pattern (Fig. 1.7 (c)). This spec-

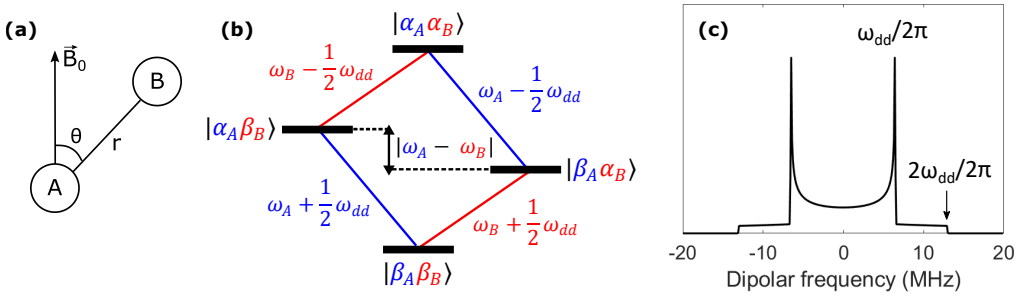


Figure 1.7: (a) Schematic two-electron spin system, where the two spins A, B are linked by a distance vector $\mathbf{r}$ of length r at an angle θ with the applied magnetic field $\mathbf{B}_0$. (b) Energy level scheme for the system shown in panel a. (c) Simulated dipolar spectrum (Pake pattern) with $r = 2$ nm. The frequencies corresponding to the main features of the spectrum are indicated.

trum has singularities at frequency values of $\nu_\perp = \pm\omega_{dd}/2\pi$, and outer edges at $\nu_\parallel = \pm\omega_{dd}/\pi$. The distance between the two spins can be determined from the position of the singularities as follows:

$$r = \left(g_A g_B \beta_e^2 \frac{\mu_0}{4\pi\hbar\omega_{dd}} \right)^{1/3} \tag{1.28}$$

The dipolar interaction splits the ESR line corresponding to the resonance of each of the spins (ω_A and ω_B) in two, with a size of the splitting in frequency units equal to ω_{dd}.

The double-frequency technique DEER, in its 4-pulse version (Fig. 1.8 (b)), is by far the most widely-used method for the determination of ω_{dd} and it is the subject of the following sections. Other PDS techniques based on single-frequency pulse sequences, namely the '2+1' experiment, single-frequency techniques for refocusing electron-electron couplings (SIFTER) and double-quantum coherence (DQC), have also been developed for this purpose.[18]

1.4.2 Double electron-electron resonance (DEER)

The DEER technique, also known as pulsed electron double resonance (PELDOR), is based on the use of two different MW frequencies to selectively excite spins A and B.[1,19] Choosing A to be the 'observer' or 'detection' spin, whose spin echo intensity is monitored, a π pulse is applied resonant with 'pump' spin B. This pump pulse excites both B-spin transitions marked in red in Fig. 1.7 (b), causing the inversion of spin B and the corresponding change in the local magnetic field experienced by spin A. As a result, the resonant frequencies of transitions $|\beta_A\alpha_B\rangle \leftrightarrow |\beta_A\beta_B\rangle$ and $|\alpha_A\alpha_B\rangle \leftrightarrow |\alpha_A\beta_B\rangle$ change by $+\omega_{dd}$ and $-\omega_{dd}$, respectively (Fig. 1.7 (b)), leading to an oscillation of the echo intensity of the coupled spin A with the time delay of the pump pulse t, of the form $\cos(\omega_{dd}t)$. The repetition of the experiment with different time positions of the pump pulse yields an oscillating echo intensity time trace from which ω_{dd} can be extracted.

A real ESR sample contains an ensemble of non-identical spin systems A-B, where ω_A and ω_B are given by frequency distributions due to the different magnetic environments of the spins. The widths of these resonance frequency distributions may exceed the bandwidths of the detection and pump pulses used in the PDS experiment, leading to partial excitation of the spins. Only detected A spins coupled to B spins that have been inverted by the pump pulse contribute to the modulated part of the echo intensity. The overall echo intensity depends on the inversion efficiency of the pump pulse as follows:[1,20]

$$\frac{F(t)}{F(0)} = 1 - \Delta[1 - \cos(\omega_{dd}t)] \tag{1.29}$$

where Δ is the dipolar modulation depth and corresponds to the inversion efficiency of the pump pulse. For the ideal case where each partner B spin of a detected A spin is inverted by the pump pulse, $\Delta = 1$.

$F(t)$ is often called the 'form factor' and accounts for the electron-electron dipolar interactions within the same nano-object. The modulated contribu-

tion to $F(t)$ is the reduced form factor ($f(t)$), given by

$$f(t) = \frac{F(t) - (1 - \Delta)}{\Delta} \tag{1.30}$$

However, spin systems in a real sample are not isolated and dipolar interactions between different spin systems lead to a decaying background contribution ($B(t)$) to the signal, called the 'background factor'. The total echo intensity is given by the product of these two contributions[1,20]

$$V(t) = F(t)B(t) \tag{1.31}$$

The background factor is often described by a stretched exponential function of the form

$$B(t) = \exp(-kt^{d/3}) \tag{1.32}$$

where k is proportional to the concentration of spins excited by the pump pulse and d is the dimensionality of the background. For a homogeneous distribution of spin systems in three-dimensional space, $d = 3$. If the distribution of spin systems is restricted in space, such as in membrane-bound systems, then $d \approx 2$. A value of $d > 3$ is an indication of distortions of the homogeneous distribution by excluded volumes at short distances or significant longitudinal B spin relaxation occurring within the duration of the PDS experiment. The background contribution can be reduced by working at relatively low spin concentrations (~ 100 μM). If this contribution cannot be modelled appropriately, an experimental background function acquired in absence of B spins is necessary.

The DEER pulse sequence: 3-pulse *vs* 4-pulse DEER

The DEER sequence in its 3-pulse version was first introduced by Milov *et al.*[21] A detection Hahn-echo MW sequence in resonance with spins A completely refocuses the dipolar coupling in A-B spin pairs in absence of relaxation (Fig. 1.8 (a)). The application of a π pump pulse resonant with

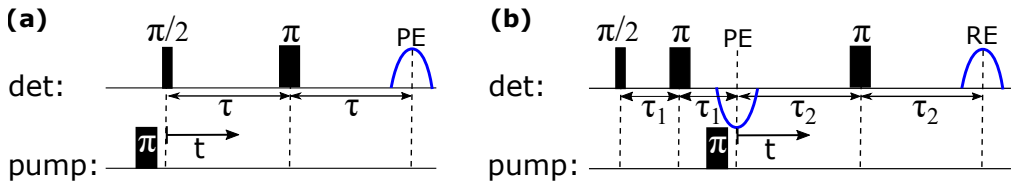


Figure 1.8: Pulse sequences for (a) 3-pulse and (b) 4-pulse DEER.

spins B at a variable time $0 \leq t \leq \tau$ after the $\frac{\pi}{2}$ pulse reintroduces the dipolar coupling and results in a modulation of the echo intensity. The main limitation of the 3-pulse DEER sequence comes from the fact that detection and pump pulse overlap around $t = 0$ causes distortions in the initial part of the DEER trace, giving rise to a dead time during which a dipolar signal cannot be obtained. The impossibility of capturing the initial part of the dipolar modulation introduces uncertainties in the determination of the zero time, which is essential for an accurate analysis. The dead time and inaccurate zero time lead to problems in the determination of the inter-spin distance distribution, especially for inter-spin distances shorter than 3 nm.

To address these problems and provide a dead time-free dipolar trace, a 4-pulse version of the DEER sequence was introduced, taking advantage of the two spin echoes formed by a 3-pulse refocused-echo sequence (Fig. 1.8 (b)).[17] The primary echo resulting from the first two detection pulses ($\frac{\pi}{2} - \tau_1 - \pi - \tau_1 - echo$) is used to define the zero time as it is crossed by the pump pulse, while detection is performed on the refocused echo formed after the third detection pulse ($\frac{\pi}{2} - \tau_1 - \pi - (\tau_1 + \tau_2) - \pi - \tau_2 - echo$). The overlap of the pump pulse and the primary echo does not cause any artefact and a full dipolar trace can be acquired moving the pump pulse between this primary echo and the refocusing detection pulse ($0 \leq t \leq \tau_2$), with $\tau_1 < \tau_2$. This yields a symmetric echo intensity feature which allows for an accurate determination of the zero time of the dipolar trace.

Despite its advantages, the longer refocused-echo sequence makes 4-pulse DEER less suited for the study of spin systems with very long spin-spin

distances and/or very short T_m, as the magnetisation loss due to transverse spin relaxation occurring between the first MW pulse and the final echo may yield prohibitively low SNR values. Especially in the case of very long distances, where the effects of the dead time and zero-time uncertainty on the obtained distance distribution may be very small, 3-pulse DEER may be a better choice. Alternatively, a long 3-pulse and a short 4-pulse DEER trace measured using the same parameters can be 'stitched' together, where the distorted initial part of the 3-pulse trace is replaced by the corresponding part of the 4-pulse trace, to yield a long and artefact-free dipolar trace with good SNR and accurate zero time.[22]

DEER relies on the selective excitation of A- and B-spins by the detection and pump pulses, respectively. A high degree of excitation selectivity is achievable even when A and B are identical spin centres.[23] Due to the magnetic anisotropies in the spin Hamiltonian and the potentially different orientation of the two spin centres, the ESR lines of the individual spins A and B in a particular spin system will be distinct and therefore selectively addressable. Provided that the width of the full ESR spectrum is larger than the excitation bandwidth of the MW pulses, detection and pump can be positioned on distinct regions of the spectrum with a large-enough detection-pump frequency offset so that overlap between the main excitation bands of the two MW pulses can be avoided. In the common case of two nitroxide radicals at Q-band, g-anisotropy can be exploited by applying the pump pulse to the spectral maximum (g_{xy} region) and the detection pulse to the g_z region, making it possible to selectively excite the two centres owing to their different orientations (Fig. 1.9).[24] In the case of rectangular pulses, however, for which the excitation frequency profile is given by a sinc function, the overlap of the > 0 order maxima of the pump with the central maximum of the detection (and *vice-versa*) may occur. This could be avoided by the use of adequately shaped pulses.[25]

The overlap of the detection and pump pulse excitation profiles can lead to the occurrence of nuclear modulations in the dipolar trace, which could

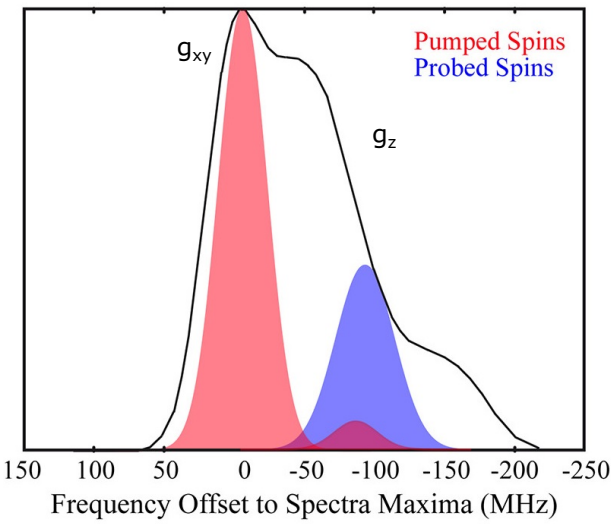


Figure 1.9: Frequency-domain Q-band spectrum of a nitroxide radical (black) plotted with the excitation profiles of 16 ns rectangular pump (red) and detection (blue) pulses. The pump-detection offset is 100MHz. *Reprinted (adapted) with permission from Schiemann, O., Heubach, C. A., Abdullin, D., Ackermann, K., Azarkh, M., Bagryanskaya, E. G., ... Jeschke, G. (2021). Benchmark test and guidelines for DEER/PELDOR experiments on nitroxide-labeled biomolecules. Journal of the American Chemical Society, 143(43), 17875–17890. doi:10.1021/jacs.1c07371. Copyright, 2021 American Chemical Society.*[24]

r_{max}	Distance (nm)
r_{shape}	3
r_{width}	4
r_{mean}	5
r_{detect}	6

Table 1.1: Maximum distances for which different characteristics of the electron spin-spin distance distribution can be reliably determined (shape, width, mean and detect) from a 2 μs DEER trace.

be misinterpreted as an electron-electron dipolar interaction, and therefore should be avoided.[1] If unavoidable, this modulation effect, known as electron spin echo envelope modulation (ESEEM), can be reduced by averaging over different τ values in a process called τ-averaging, where τ is incremented in steps of $d\tau$ to cover a full period of nuclear modulation. For proton and deuterium modulations at X-band, an 8-step τ-averaging cycle with $d\tau = 8$ ns and $d\tau = 56$ ns, respectively, is commonly used. At Q-band, 8 steps with $d\tau = 16$ ns are efficient for averaging deuterium modulations.

The upper limit of the distance range accessible with DEER (r_{max}) is set by the T_m of the observer A spins, as distance determination is only reliable if the recorded dipolar trace is long enough to characterise the distance. The dipolar trace length necessary to determine different characteristics of the distance distribution is given by[6]

$$t_{max} = 2\mu s \left(\frac{r_{exp}}{r_{max}} \right)^3 \tag{1.33}$$

where r_{exp} is the centre of the expected distance distribution. For a dipolar trace of 2 μs, the maximum distances for which different characteristics of the distance distribution can be reliably determined (shape, width, mean and detect) are given in Table 1.1. The 'detect' case means that the length of the dipolar trace only allows to conclude that an inter-spin distance has been detected, but no information can be reliably obtained about the distance distribution.

If spin-spin relaxation is too fast to allow for the measurement of a dipolar trace of length t_{max}, deuteration of the solvent and even the molecule of interest are strategies to lengthen T_m. In addition, the use of low temperatures ($\sim$ 50 K for nitroxide radicals and $\leq$ 10 K for transition and rear-earth metal ions) also contributes to slowing spin relaxation. However, a trade-off must be reached between T_m and T_1, as excessive lengthening of T_1 at very low temperatures limits the rate at which the pulsed ESR experiment can be repeated and therefore increases the accumulation time necessary to reach a given SNR. The lower distance limit (r_{min}) is given by the requirement to excite the two lines that are split by ω_{dd} in the A-spin spectrum by the detection pulses and in the B-spin spectrum by the pump pulse.

1.4.3 Orientational effects

In cases where there is resolved anisotropy in the ESR spectrum of at least one of the spin centres and the excitation bandwidth of the pulses is narrow compared to the spectral width, excitation of only a subset of pump and/or detection spin centre orientations relative to $\mathbf{B}_0$ by the MW pulses may occur, and this is referred to as orientation selection.[1,26] In rigid spin systems, where there is a correlation between the orientation of the spin centres and the orientation of the dipolar vector $\mathbf{r}$ linking them, orientation selection translates into the selection of $\mathbf{r}$ orientations relative to $\mathbf{B}_0$, that is, the selection of a subset of θ values. Given the dependence of the dipolar interaction on the angle θ (equation 1.20), the obtained Pake pattern is incomplete. These orientational effects in dipolar traces are evidenced by a change in the modulation depth and oscillatory frequency of the traces with the changing position of the MW pulses in the ESR spectrum. These effects can be used to extract additional structural information about the spin system of study as discussed in more detail in Section 1.4.5.[26,27]

Despite the scope for additional structural information, orientational effects complicate the acquisition and analysis of dipolar data, and may be

undesirable if only the spin-spin distance distribution is of interest. Several experimental strategies exist for the suppression of orientation selection in PDS.[1] If there is flexibility in the choice of spin centres, centres with isotropic spin Hamiltonians can be used for this purpose. Gd(III) complexes and triarylmethyl (trityl) radicals display isotropic ESR spectra up to Q-band frequencies. Alternatively, the averaging of anisotropic interactions can be provided by the conformational flexibility of a spin centre attached to the spin system (spin label) through a flexible linker.[28] The popular nitroxide-based 1-oxyl-2,2,5,5-tetramethylpyrroline-3-methyl methanethiosulfonate, known as methanethiosulfonate spin label (MTSSL), has been shown to often suppress orientation selection. If the g-tensor is the main source of anisotropy, performing the experiments at low magnetic fields can suppress or at least reduce orientational effects, sensitivity permitting. At the data analysis stage, orientational effects can be suppressed by averaging a set of dipolar traces spanning the full ESR spectrum, as explained in Section 1.4.5.

1.4.4 Multi-spin effects

The dipolar signal in spin systems with multiple (> 2) dipolarly-coupled spin centres becomes much more complicated due to the possible inversion of more than one pump spin, leading to multi-spin effects. In a system of one detection spin A coupled to N pump spins B, excitation of more than one B-spin per A-spin by the pump pulse can lead to additional contributions to the modulation depth and dipolar frequency. If the B-spins are identical and the coupling between B-spins can be neglected, then the form factor is given by the following product of 2-spin contributions:[29]

$$\frac{F(t)}{F(0)} = \prod_{i=1}^{N}[1 - \delta_i(1 - \cos(\omega_{dd,i}t))] \tag{1.34}$$

If the inversion efficiency of the pump pulse is the same for all B-spins ($\delta \equiv \delta_i \; \forall i$), then the form factor contains terms that depend on the different

dipolar frequencies ($\omega_{dd,i}$) plus terms with products of cosines of different dipolar frequencies, which can be rewritten as the cosines of linear combinations of these frequencies. When these combination frequencies appear in the dipolar trace, they can be mistaken for true dipolar frequencies and thus lead to artefacts ('ghost' distances) in the distance distribution. In addition, the modulation depth of the trace depends on the number of coupled spins as[30]

$$\Delta = 1 - (1 - \delta)^N \tag{1.35}$$

This equation can be used to account for the effect of multiple spins on the modulation if N is known and δ is determined by calibration with model compounds with a known number of coupled spins, as it depends on the spectrometer settings and measurement conditions. However, this method is subjected to multiple sources of error and it has only been shown to work accurately for $N \leq 4$.[30]

Some strategies for the avoidance of multi-spin effects have been reported. For systems with a very small number of dipolarly-coupled electron spins, careful combination of different types of paramagnetic centres can yield non-overlapping (orthogonal) ESR spectra, allowing for selective excitation of each individual spin centre by the detection and pump pulses and therefore yielding pairwise distance distributions free of multi-spin artefacts. This approach has been successfully used in 3-spin systems combining nitroxide/trityl/Cu(II),[31] nitroxide/Gd(III)/Mn(II)[32] and nitroxide/Ni/Cu(II).[33] However, this flexibility in the choice of spin centres is a rare luxury. For systems with identical spin centres, the use of low pump pulse powers (i.e. small pump flip angles) has been shown to minimise multi-spin effects, at the expense of the modulation depth. Attempts have been made to develop methods for the analysis of dipolar traces containing multi-spin effects, involving the measurement of traces at several pump powers and the determination of the 2-spin contribution from the power dependence of the form factor using theoretical or empirical expressions.[29,34] These methods have only been shown to work well in relatively rigid spin systems with a small number of

coupled identical spin centres.

1.4.5 Analysis of PDS traces

When used for macromolecular structure determination, two main approaches exist for the interpretation of PDS data: to deduce the three-dimensional structure of the nano-object from several inter-spin distance constraints (model-free approach), or to simulate the DEER traces based on a model structure and to refine this model by comparison with the experiment (model-based approach).[1] The analysis methods differ significantly depending on the approach chosen and on whether orientational effects are present (orientation-dependent) or absent (orientation-independent) in the dipolar traces.

Orientation-independent analysis

The least biased orientation-independent model-free method for extracting a distance distribution $P(r)$ from a reduced form factor $f(t)$ obtained after background correction and modulation depth normalisation of an experimental PDS trace (Fig. 1.10 (a, b)) is Tikhonov regularisation.[1,35] The physical model for this ill-posed problem can be formulated as a matrix equation

$$\mathbf{f} = \mathbf{KP} \tag{1.36}$$

where $\mathbf{f}$ is the reduced form factor as a vector of n data points, $\mathbf{P}$ is the distance distribution as a vector of m points and $\mathbf{K}$ is the $n \times m$ kernel matrix with elements given by

$$K_{ij} = \int_0^1 \cos[(1 - 3\cos^2\theta)\omega_{dd}t]d(\cos\theta) \tag{1.37}$$

The ill-posedness of the problem comes from the instability of solutions $\mathbf{P}$ to small changes in $\mathbf{f}$. A small contribution to $\mathbf{f}$ that does not fit the model, such as noise, will lead to a large error in $\mathbf{P}$. Direct inversion of equation

1.36 to obtain $\mathbf{P}$ is therefore not possible.

The solution can be stabilised by requiring $P_j \geq 0 \; \forall j$. Additional stabilisation can be achieved by imposing that $P(r)$ is a smoothly varying function. This constraint is reasonable in the context of molecular structural studies, as $P(r)$ arises from the population of a continuum of conformations by the molecular ensemble in the sample. Smoothness can be quantified with the square norm of the derivative of $P(r)$. Tikhonov regularisation considers the smoothness of the solution against the goodness of the fit to the experimental data provided by this solution, and yields the vector $\mathbf{P}$ that minimises the weighted sum (G) of the square deviation between the data and the model and the square norm of the derivative of the solution

$$G(\alpha) = \|\mathbf{f} - \mathbf{KP}\|^2 + \alpha\|\hat{\mathbf{L}}\mathbf{P}\|^2 = \rho + \alpha\eta \tag{1.38}$$

where $\hat{\mathbf{L}}$ is a discrete differential operator matrix. The optimal value for the regularisation parameter α needs to be determined for each dataset. This can be done by plotting $\log(\eta)$ at minimum $G(\alpha)$ *vs* $\log(\rho)$ at minimum $G(\alpha)$, for a range of values of α. This plot is normally L-shaped (L-curve) and the value of α corresponding to the best compromise between smoothness and goodness of fit occurs at the corner of the L (Fig. 1.10 (d), inset). This method is implemented in freely-available software such as the Matlab-based *DeerAnalysis*[35] and it has been used for the orientation-independent analysis of the PDS data presented in this thesis. The relative intensities of the different peaks in a distance distribution are in principle indicative of the relative populations of the different structures giving rise to the different spin-spin distances in the sample. However, short distances are often relatively amplified when the recorded dipolar trace is short.[36]

Tikhonov regularisation can become problematic when the distance distribution contains both narrow and broad peaks.[37] In those cases, a single value of α cannot be optimal for all the features in the distribution. For protein samples, the narrow peak normally corresponds to the folded and

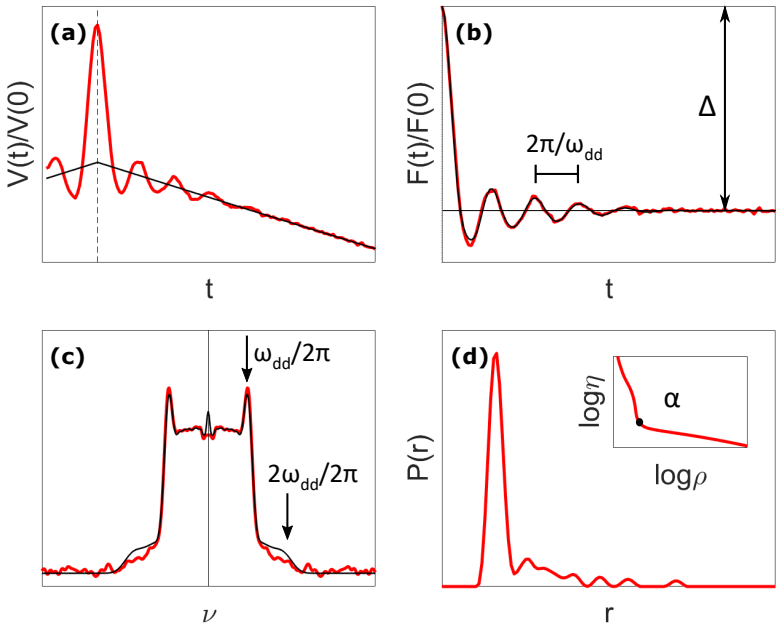


Figure 1.10: General example of orientation-independent analysis of a PDS dataset. (a) Q-band nitroxide-nitroxide 4-pulse DEER time trace as recorded (red), with the fitted homogeneous background (black). (b) Background-corrected time trace (red) with the modulation depth, Δ, and the dipolar frequency, ω_{dd}, indicated, and corresponding fit (black). (c) Fourier transform of the background-corrected time trace with the modulation depth normalised to 1 to remove the zero-frequency components, yielding a Pake pattern (red). The corresponding fit is also shown (black). (d) Distance distribution obtained by Tikhonov regularisation using *DeerAnalysis*.[35] Inset: L-curve showing the optimal regularisation parameter (α). *Reprinted (adapted) with permission from Bertran, A., Barbon, A., Bowen, A. M., Di Valentin, M. in Advances in Biomolecular EPR, ed. R. D. Britt, Elsevier Inc., 1st edn., 2022, Methods in Enzymology vol. 666, ch. 7, pp. 171–231. doi:10.1016/bs.mie.2022.02.012. Copyright 2022 Elsevier.*[107]

solubilised molecule, while broad peaks arise from unfolded or aggregated material. Therefore, it is good practice to optimise α for the narrow peak and to avoid interpretation of the broad features. In addition, the errors in the distance distribution from Tikhonov regularisation are not a linear function of the noise and must be estimated by repeating the analysis for different noise levels and background corrections in a process known as 'validation'.

If some rough structural model for the system of study exists *a priori*, it can be advantageous to follow a model-based analysis approach and to use the experimental data to refine this model. This reduces the uncertainty coming from the resolution of the ill-posed problem presented in equation 1.36, and it has more flexibility for explicitly incorporating orientational or multi-spin effects.[1] The model-based approach has been used in this thesis for the orientation-dependent analysis of PDS data, and it will be explained in detail in the following section.

Orientation-dependent analysis

The analysis of PDS data containing orientational effects requires simulation of the expected PDS traces based on a pre-existing structural model followed by the comparison of these simulations to the experimental data in order to refine the model.

An algorithm for the simulation of orientationally selective DEER data (*OriDEERsim*) was reported for spin systems where g-tensor anisotropy is the source of orientation selection (Fig. 1.11).[38] This algorithm is based on the point-dipole approximation, by which the total dipolar interaction between two spin centres is calculated as the sum of pairwise interactions between the finite number of points of electron spin density from each of the spin centres. *OriDEERsim* requires as inputs the MW frequencies for the detection and pump pulses, the pulse lengths, the B_0 values for the different DEER traces to simulate, the spin Hamiltonian parameters for the spin system of study and a structural model of this system, including the

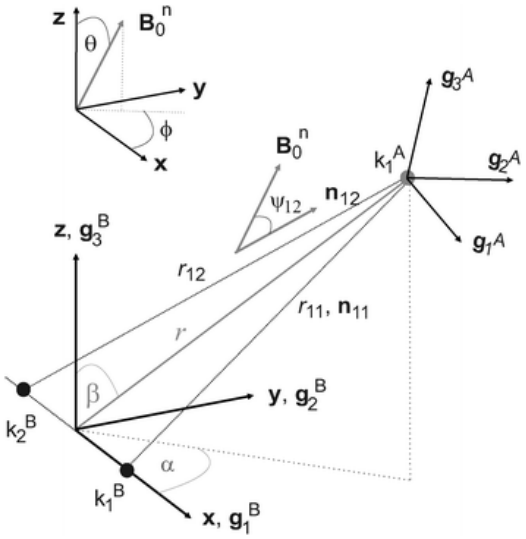


Figure 1.11: *OriDEERsim* geometric model for the orientation-dependent simulation of DEER traces between two weakly-coupled spin centres A, B with anisotropic g-tensors $\mathbf{g}^A$, $\mathbf{g}^B$. More detailed information is given in the text. *Reprinted (adapted) with permission from J. E. Lovett, A. M. Bowen, C. R. Timmel, M. W. Jones, J. R. Dilworth, D. Caprotti, S. G. Bell, L. L. Wong and J. Harmer, Phys. Chem. Chem. Phys., 2009, 11, 6840–6848. doi:10.1039/b913085n. Copyright, 2009 Royal Society of Chemistry.*[38]

positions of the atoms bearing electronic spin density and the corresponding values for the spin density, and the relative orientations of the g-tensors of the two spin centres given by three Euler angles (α, β and γ). A schematic depiction of a simplified spin system, with one atom bearing all the electronic spin density of the detection centre A and two atoms bearing the electronic spin density of pump centre B, is shown in Fig. 1.11. The reference frame for the calculation is taken to be the g-tensor frame of the detection spin centre ($\mathbf{g}^A$).

The *OriDEERsim* algorithm for the calculation of a DEER trace at a given B_0 involves the following steps:

1. Define the unit vectors $\{\mathbf{n}_{ij}\}$ and spin-spin distances $\{r_{ij}\}$ for all the pairwise dipolar interactions in the model of the spin system.

2. Generate a grid of n magnetic field orientations $\{\mathbf{B}_0^n(\theta, \phi)\}$, making

angles ψ_{ij}^n with respect to the pairwise dipolar vectors, and calculate the solid angle weights w^n.

3. Determine the subset of $\mathbf{g}^A$ orientations excited by the detection pulses at a given $\mathbf{B}_0^n$ (f_A^n), using the simulated ESR spectrum of centre A (I_A^n) and the calculated excitation profile of the detection pulses (P_{det}).

$$f_A^n = \int_0^\infty I_A^n(\omega) P_{det}(\omega) d\omega \tag{1.39}$$

4. Determine the $\mathbf{g}^B$ orientations corresponding to excited $\mathbf{g}^A$ orientations, using the structural model.

5. Determine the subset of these $\mathbf{g}^B$ orientations that is also excited by the pump pulse (c_{mod}^n), using the simulated ESR spectrum of centre B (I_B^n) and the calculated excitation profile of the pump pulse (P_{pump}).

$$c_{mod}^n = \int_0^\infty I_B^n(\omega) P_{pump}(\omega) d\omega \tag{1.40}$$

This fraction of flipped B-spins determines the contribution of orientation n to the modulation depth.

6. Calculate the strength of the dipolar interaction for each pair of excited A-B orientations by summing over all the A-B pairs of atoms bearing electronic spin density. The dipolar frequency for the n-th pairwise component is given by

$$\omega_{dd}^n = \frac{\mu_0}{4\pi\hbar} g_A^n g_B^n \beta_e^2 \sum_{i \neq j} \left[k_i^A k_j^B \frac{1 - 3\cos^2 \psi_{ij}^n}{r_{ij}^3} \right] \tag{1.41}$$

where k_i^A and k_j^B are the electronic spin densities on the atoms of centres A and B, respectively.

7. Construct the contribution of orientation n to the form factor as

$$F^n(t) = f_A^n [1 - c_{mod}^n (1 - \cos(\omega_{dd}^n t))] \tag{1.42}$$

8. Sum the form factor contributions over all orientations weighted by the corresponding solid angle weights.

$$F(t) = \sum_n w^n F^n(t) \tag{1.43}$$

Steps 7-8 can also be performed in frequency domain instead of time domain, and the time trace can be obtained by a final inverse Fourier transformation step.

If an ensemble of structural models is generated, for instance, by small geometry distortions from a given structure to emulate the flexibility of spin systems in real ESR samples, a library of orientation-dependent DEER traces for this model can be simulated using *OriDEERsim*. An iterative minimum-squares fitting procedure can be then followed to determine the linear combination of simulated traces that provide the best description of the experimental data.[39] The coefficients of this best-fitting linear combination of traces inform on the relative populations of the model structures in the sample and can be used to refine the initial model.

Such fitting procedure follows these simple steps:

1. Select, from all the traces of the library, the one that gives the minimum root-mean-square deviation (RMSD) from the experimental data and store it.

2. Find, from all the traces of the library, the one that, when added to the stored trace, gives the minimum RMSD from the experimental data.

3. Replace the stored trace by this new minimum-RMSD combination of traces.

4. Repeat 2-3 until a threshold RMSD or a maximum number of iterations is reached.

The frequency of occurrence of each simulated trace in the final minimum-RMSD combination, normalised to the total number of iterations performed, gives the relative weight of the corresponding structure contributing to the refined model.

The library-based iterative fitting procedure using traces simulated with the *OriDEERsim* algorithm[38] (or modified versions of it) has been used for the orientation-dependent analysis of PDS data in this thesis.

1.4.6 Biological applications of PDS

PDS techniques have been widely applied in the field of structural biology as the accessible length scale matches the size of biological assemblies.[23,40–42] Nitroxide-nitroxide DEER can access distances in the range between 1.5 to 12 nm, with extension to 16 nm if both the the biological system and the solvent are fully deuterated.[43] The ability of PDS to yield accurate distance distributions and, for rigid systems, information on the relative orientations of the spin centres, even in the case of very complex biological assemblies, makes this methodology advantageous and complementary to more conventional structure determination techniques such as X-ray diffraction (XRD), NMR or cryo-electron microscopy (cryo-EM). Despite its exquisite precision for molecular structure determination, XRD can only capture a single structure and does not give information on the distribution of molecular conformations known to exist and to play an important role in biological conditions. In addition, the requirement for high-quality crystals is often prohibitive for biological assemblies of high complexity containing unstructured regions. NMR provides shorter-range distance information and has an upper limit to the size of the system of study. In addition, it often yields very complex overlapping signals that are difficult to interpretate.

Much of biological PDS relies on the use of spin labels: paramagnetic

moieties that can be bound to the system of interest by means of reactive functional groups attached to the spin centre. In site-directed spin labelling (SDSL), the preferential reactivity of these functionalisations towards specific chemical motifs, such as a given amino acid side chain, is exploited to achieve selective labelling of particular positions on the macromolecular system. The most popular choice for protein studies is MTSSL, a thiol-reactive nitroxide radical very effective at labelling cysteine side chains.[8] If the protein of study does not have cysteines at the regions of interest, site-directed mutagenesis can be used to incorporate cysteines at known positions in the amino acid sequence, providing labelling points for SDSL.[44,45] Alternatively, if additional cysteines are present in other parts of the protein which are accessible to MTSSL, those can be replaced by non-thiol containing amino acids to avoid undesired labelling. Once labelled, the biological system of study is normally flash-frozen in the presence of a cryoprotectant to avoid structural distortions, yielding a glassy sample that can be studied by PDS.

With the transition of PDS to the study of systems under more biologically relevant conditions, new types of spin labels have been developed to address the issues of low sensitivity and poor stability of nitroxides, especially in the reductive cellular environment. Carbon-centred radicals, such as trityl radicals,[46] offer enhanced sensitivity thanks to their very narrow spectra, allowing for the use of shorter acquisition times, lower sample concentrations and higher temperatures. In terms of stability, complexes of transition metal (such as Cu(II),[27,47,48] Mn(II)[49,50] and Fe(II)[51–54]) and lanthanide (such as Gd(III)[55–57]) ions have been shown to be robust spin labels for PDS distance measurements inside cells.

More recently, a new type of spin label has come into play, the photogenerated triplet state of organic chromophores, offering enhanced ESR sensitivity and optical addressability.[3,58] This has led to a paradigm shift in PDS, starting the new field of light-induced pulsed dipolar spectroscopy (LiPDS).[3,59] In the next section, this novel spin label and the new PDS techniques derived from it are introduced in detail, followed by a review of the state of the art

of their application to the study of biological system.

1.5 Light-induced PDS (LiPDS)

This section has been adapted from the following book chapter:[60]

A. Bertran, A. Barbon, A. M. Bowen and M. Di Valentin, in *Advances in Biomolecular EPR*, ed. R. D. Britt, Elsevier Inc., 1st edn., 2022, Methods in Enzymology vol. 666, ch. 7, pp. 171–231.

In recent years, new adaptations of PDS using photogenerated triplet states as spin centres have been described, giving rise to the field of LiPDS. The use of light-activated spin centres in PDS experiments has several potential advantages, ranging from the ability to measure in both light and dark conditions, under which the spin centre is active or inactive, respectively, to the high sensitivity derived from the non-Boltzmann population of the triplet state sub-levels. Additionally, the large ZFS anisotropy of the triplet state spectrum can allow for the orientation between the spin centres to be resolved. Many biological molecules, such as photosynthetic proteins,[61,62] heme-proteins[62–64] and flavoproteins,[65] contain moieties that can act as light-activated spin centres.

1.5.1 The photogenerated triplet state

In photoexcited organic chromophores, the triplet state is populated mostly through inter-system crossing (ISC) from an excited singlet state. This process involves a change in spin angular momentum, which occurs *via* the de-phasing of one of the electronic spins of the singlet ($S \rightarrow T_0$) or the direct spin flip of one of the electronic spins ($T_0 \rightarrow T_+/T_-$), by the action of different magnetic torques on each of the spins.[66] Therefore, it is a process

forbidden by the spin selection rules. In order for ISC to occur, the change in electronic spin angular momentum must be coupled to another change in angular momentum of equal magnitude and opposite direction. In organic molecules this is often provided by the change in electronic orbital angular momentum through an orbital jump, where the magnetic moment due to the electron's orbital angular momentum interacts with the magnetic moment due to the electron's spin angular momentum, giving rise to a magnetic torque on the electronic spin. This change in orbital angular momentum is more likely to occur along certain directions of the molecular structure, leading to anisotropic ISC rates and therefore different populations of the triplet spin sublevels, giving rise to spin polarisation. The strength of this spin-orbit coupling (SOC) increases with the nuclear charge acting on the electron, leading to an enhancement of the ISC rate by the heavy-atom effect.

The quantum yield of triplet formation (Φ_T) is determined by the competition of ISC with other decay processes of the excited singlet state, namely, fluorescence and internal conversion to lower-energy singlet states. In turn, the triplet state can be depopulated via phosphoresce and reverse ISC back to the ground singlet state. These processes are exemplified in the Jablonski diagram of Figure 1.12 (a).

Triplet ESR spectra have already been discussed in Section 1.1.3 in terms of the ZFS interaction and non-Boltzmann population of the triplet spin sub-levels. These spectra are typically recorded at cryogenic temperatures in frozen solutions using trESR techniques.

In order to exploit the photogenerated triplet state as a paramagnetic probe in PDS experiments, it is important to consider the spin relaxation properties of the specific chromophore selected. Longitudinal relaxation in photoexcited triplets occurs simultaneously with the often much slower reverse ISC back to the singlet ground state. Therefore, the usual inversion-recovery experiment preceded by a laser pulse will yield a multi-exponential decay, with lifetimes corresponding to these two processes. Taking advantage

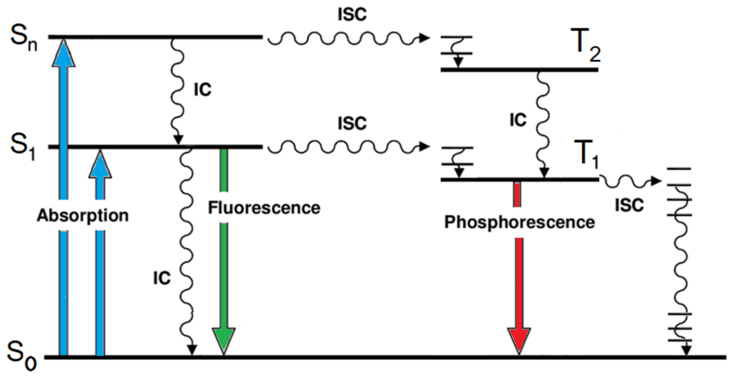


Figure 1.12: Jablonski diagram for the formation of a triplet state and its decay. *Reprinted (adapted) with permission from Bertran, A., Barbon, A., Bowen, A. M., Di Valentin, M. in Advances in Biomolecular EPR, ed. R. D. Britt, Elsevier Inc., 1st edn., 2022, Methods in Enzymology vol. 666, ch. 7, pp. 171–231. doi:10.1016/bs.mie.2022.02.012. Copyright 2022 Elsevier.*[107]

of the fact that the laser pulse already initialises the system and provides a well-defined zero time for the triplet echo intensity decay trace, the first MW inversion pulse of the inversion recovery experiment can be omitted and the signal can be monitored as a function of the DAF (see Fig. 1.13). Triplet transverse relaxation is only relevant for the experiments involving the formation of a triplet spin echo, where it determines the maximum time delay that can be used between a refocusing MW pulse and the echo formation, and it can be characterised with the usual phase-memory-time experiment preceded by a laser pulse (Fig. 1.13).

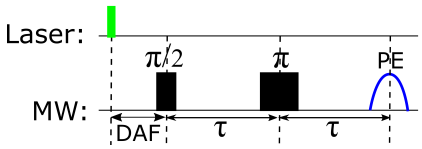


Figure 1.13: Light-induced Hahn-echo pulse sequence for the characterisation of photogenerated triplet states. For a longitudinal relaxation experiment, the DAF is increased stepwise. For a transverse relaxation or phase-memory experiment, τ is increased stepwise.

Triplet state chromophores for LiPDS

Porphyrins, 5-(4-carboxyphenyl)-10,15,20-triphenylporphyrin (TPP) in particular, have been the most recurrently used chromophores for LiPDS, especially in model peptides, thanks to their high Φ_T, strong spin polarisation, slow spin relaxation and decoherence, and good photostability.[58] They have strong absorption features in the visible region, corresponding to $S_0 \rightarrow S_1$ vibronic transitions (the so-called Q-bands), of which there are four in the free-base case. The complexation of a diamagnetic metal ion, such as Zn(II) or Mg(II), by the tetrapyrrolic ring of porphyrins leads to the collapse of the four Q-bands into two due to the increase from two-fold to four-fold symmetry of the chromophore. These are naturally-occurring chromophores, such as chlorophylls. For other endogenous porphyrin-based chromophores such as heme, substitution of the paramagnetic metal ion by Zn(II) or Mg(II) converts them into diamagnetic ground-state chromophores suitable for LiPDS. The presence of the metal further increases Φ_T via heavy atom-enhanced ISC, but it makes spin relaxation faster. The very favourable spectroscopic properties of both free-base and metallated porphyrins have made them the chromophores of choice for the majority LiPDS studies reported in the literature.

More recently, several xanthene- and thioxanthene-based dyes have been proposed for LiPDS,[67] and some of them have been successfully used in recently reported LiPDS studies.[68] These chromophores, namely Eosin Y (EO), Erythrosine B (EB), Rose Bengal (RB) and ATTO Thio12 (AT), are smaller than porphyrins and therefore more suitable for biolabelling, and some of them are already widely used as dyes in biological assays and can be purchased in suitable functionalised forms. These chromophores display very high extinction coefficients in the visible range, and high Φ_T owing to the heavy atom-enhanced ISC. However, the presence of heavy atoms significantly reduces their spin relaxation times, preventing their use for echo detection. Their smaller size and shorter spatial spin delocalisation lead to stronger dipolar interactions between the two unpaired electrons in the triplet

state, resulting in larger ZFS parameters compared to those of porphyrins.

Fullerenes, namely C_{60}, have also been successfully used for LiPDS in chemical model systems and proteins.[69–71] Their spectroscopic properties are excellent: $\Phi_T = 1$, narrow triplet ESR spectrum, slow spin relaxation and very good photostability. However, they are very bulky labels with bad biocompatibility, and they are not commercially available in functionalised forms suitable for biolabeling. Therefore, they are not a desirable choice for biological applications of LiPDS, unless the non-covalent binding of this chromophore to specific sites in proteins acting as supramolecular hosts is exploited, as already demonstrated.[69]

1.5.2 LiPDS techniques - State of the art

LiPDS techniques are designed to measure the dipolar interaction between a permanent spin centre and a photogenerated triplet state. They rely on a laser pulse to generate the triplet state, that can be used as detection or as pump spin centre. The first LiPDS technique reported was a modification of the DEER experiment, light-induced DEER (LiDEER), using a photogenerated triplet as the detection spin. Subsequently, several other techniques have been proposed, namely laser-induced magnetic dipole spectroscopy (LaserIMD) and its refocused-echo version (ReLaserIMD), and light-induced relaxation-induced dipolar modulation enhancement (LiRIDME). The pulse sequences for these techniques are shown in Fig. 1.14 and the methods are detailed in the following sections.

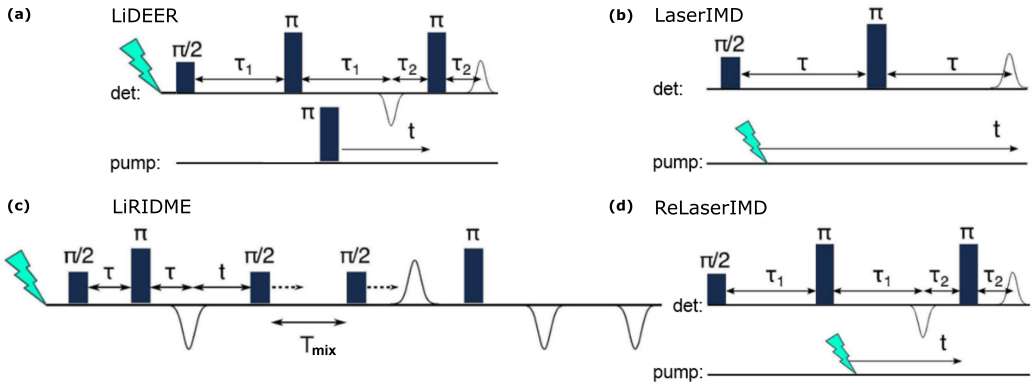


Figure 1.14: Pulse sequences for LiPDS techniques: (a) light-induced double electron–electron resonance (LiDEER), (b) laser-induced magnetic dipole spectroscopy (LaserIMD), (c) light-induced relaxation-induced dipolar modulation enhancement (LiRIDME) and (d) Refocused-echo LaserIMD (ReLaserIMD). *Reprinted (adapted) with permission from Bertran, A., Barbon, A., Bowen, A. M., Di Valentin, M. in Advances in Biomolecular EPR, ed. R. D. Britt, Elsevier Inc., 1st edn., 2022, Methods in Enzymology vol. 666, ch. 7, pp. 171–231. doi:10.1016/bs.mie.2022.02.012. Copyright 2022 Elsevier.*[107]

Light-induced double electron-electron resonance (LiDEER)

LiDEER is a modification of the 4-pulse DEER sequence, with an additional laser pulse preceding the microwave pulses, to photoexcite the chromophore and generate the triplet state.[58] It was initially tested on a molecular spectroscopic ruler consisting of a series of peptides with a nitroxide-containing 4-amino-1-oxyl-2,2,6,6-tetramethyl-piperidine-4-carboxylic acid (TOAC) residue and a TPP attached to the N-terminus, spanning porphyrin-nitroxide distances from 1.8 to 8.1 nm according to density functional theory (DFT) calculations (see Fig. 1.15).[72] The photogenerated porphyrin triplet state was used as the detection spin centre and a MW pump pulse was applied to the nitroxide radical as in conventional DEER. The refocused-echo MW detection sequence yielded a dead time-free trace with a clear zero time. These experiments were performed at X-band and the pump pulse was set to be resonant with the centre of the nitroxide spectrum. This feature comprises all orientations of the nitrogen $m_I = 0$ level, so orientation selection was

negligible.

In addition to porphyrin-based peptides, covalent dyads have also been used as model systems for LiDEER. The chromophore in this case was a C_{60} moiety and the stable paramagnetic probes were a spirocyclohexyl-substituted nitroxide (NIT) or a triarylmethyl radical (TAM) (Fig. 1.16 (a)).[69] LiDEER experiments were performed on these molecular dyads to validate the use of fullerenes as alternatives to porphyrin in the role of photoswitchable probes, with promising results (Fig. 1.16 (c, d)). The enhanced sensitivity owing to the small ZFS parameters of the C_{60} triplet and its longer T_m allowed measurements close to room temperature.

Using the photogenerated triplet for detection increases the sensitivity and the SNR of the recorded traces due to its strong spin polarisation. The length scale that can be measured in this experiment is primarily limited by the T_m of the triplet spins. The modulation depth of the collected data is determined by the inversion efficiency of the MW pump pulse and was improved by using a chirp pump pulse.[59] In theory, this could also be achieved by other adiabatic shaped pulses. These pulses can be generated using an AWG and can be designed to have a large bandwidth and a high inversion efficiency. With careful implementation, they can also be designed to compensate for the changing B_1 accessible at different frequencies due to the bandwidth of the resonator. However, care must be taken to ensure that these pulses are not too long, as spin evolution within the pulse length can lead to distortion of the experimental time trace. Several reviews on the application of shaped pulses to PDS have previously been published.[15,73]

Using the density-operator formalism, the following analytical expression for the form factor of the LiDEER experiment was derived[74]

$$F(t) = \frac{1}{\sqrt{2}}\Phi_T(P_- - P_0)\left[(P_\alpha + P_\beta)\cos((t-\tau_1)\omega_{dd}) + i(P_\alpha - P_\beta)\sin((t-\tau_1)\omega_{dd})\right] \tag{1.44}$$

where P_α and P_β are the populations of the $|\alpha\rangle$ and $|\beta\rangle$ states of the radical, respectively, as defined in Section 1.2.2, and P_0 and P_- are the populations

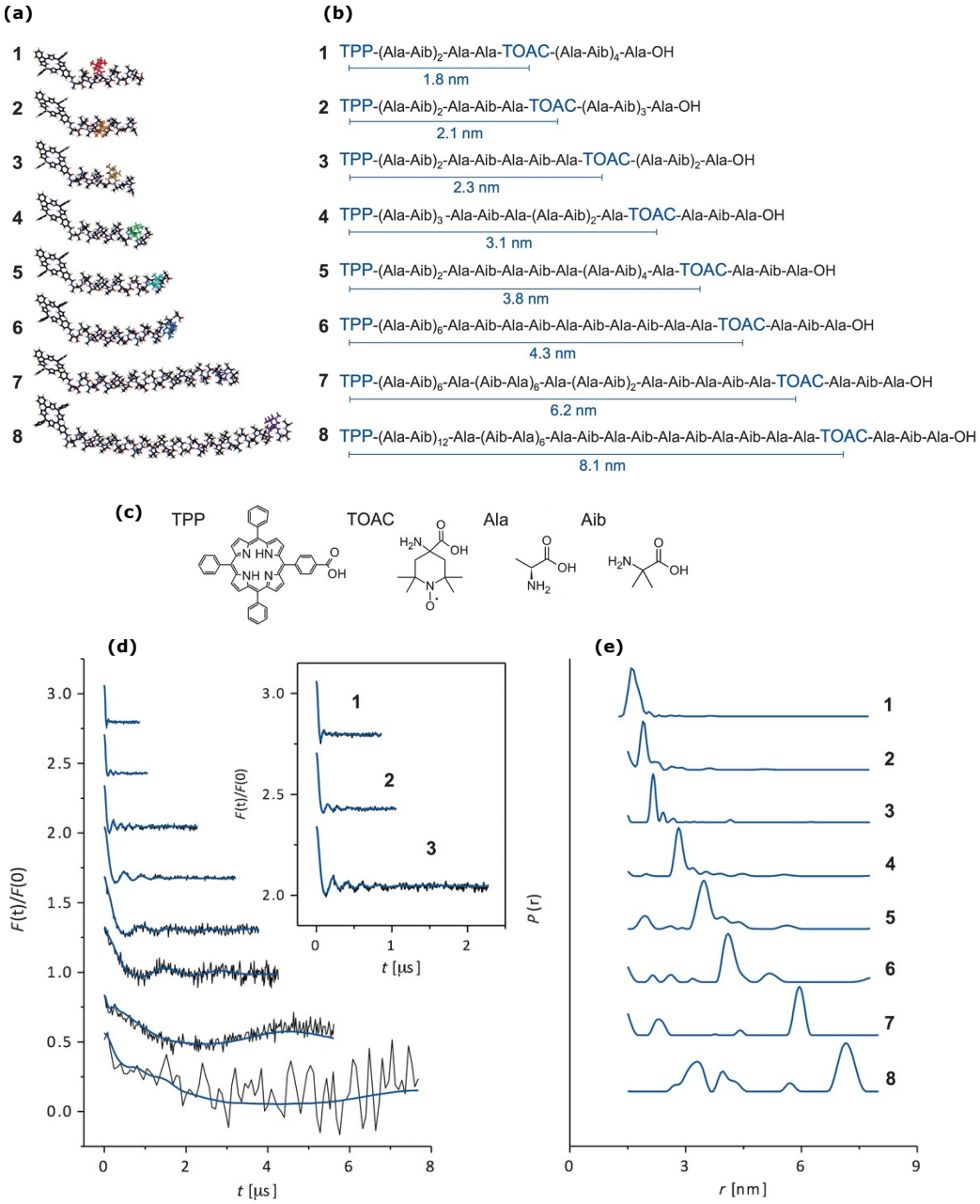


Figure 1.15: DFT-optimized structures (a) and sequences (b) of the porphyrin-nitroxide model systems, with the inter-spin distances indicated. (c) Building blocks for the model systems. (d) Background-corrected LiDEER traces for the systems. (e) Corresponding distance distributions. *Reprinted (adapted) with permission from Di Valentin, M., Albertini, M., Dal Farra, M. G., Zurlo, E., Orian, L., Polimeno, A. and Carbonera, D. (2016). Light-induced porphyrin-based spectroscopic ruler for nanometre distance measurements. Chemistry - A European Journal, 22(48), 17204–17214. doi:10.1002/chem.201603666. Copyright 2016 John Wiley & Sons.*[72]

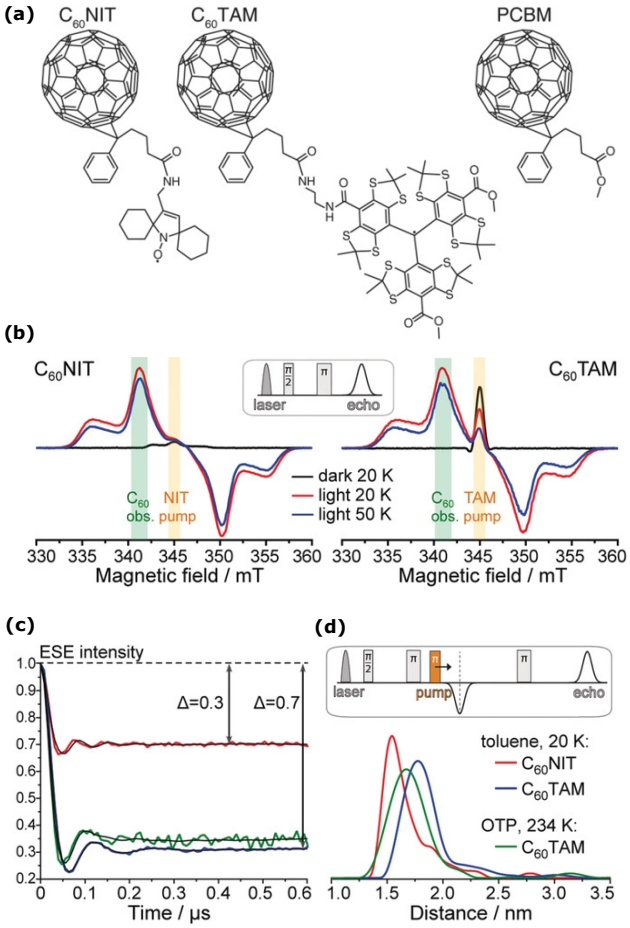


Figure 1.16: (a) Chemical structures of the fullerene-based covalent dyads. (b) X-band echo-detected field-swept spectra of the dyads in the dark (black), and after laser excitation at 20 K (red) and 50 K (blue). The detection (green) and pump (orange) positions for the LiDEER experiments are indicated. (c) Background-corrected and normalised LiDEER traces for C_{60}NIT in toluene at 20 K (red), C_{60}TAM in toluene at 20 K (blue) and C_{60}TAM in ortho-terphenyl at 234 K (green). Fits by Tikhonov regularisation are overlaid (black). (d) Corresponding distance distributions. The spin-echo and LiDEER pulse sequences are shown as insets. *Reprinted (adapted) with permission from Krumkacheva, O. A., Timofeev, I. O., Politanskaya, L. V., Polienko, Y. F., Tretyakov, E. V., Rogozhnikova, O. Y. and Fedin, M. V. (2019). Triplet fullerenes as prospective spin labels for nanoscale distance measurements by pulsed dipolar EPR spectroscopy. Angewandte Chemie, 131(38), 13405–13409. doi:10.1002/ange.201904152. Copyright 2019 John Wiley & Sons.*[69]

of the $|T_0\rangle$ and $|T_-\rangle$ states of the triplet, respectively, as defined in Section 1.1.3. The fact that $(P_\alpha + P_\beta) \gg (P_\alpha - P_\beta)$ in most cases allows to neglect the out-of-phase component. The derivation assumed the validity of the high-field approximation and the absence of any hyperfine interactions, g-tensor anisotropies and exchange coupling. A further assumption was that the MW detection pulses affect only the triplet spins whereas the MW pump pulse acts only on the radical spins, with the static spin Hamiltonian being neglected during the application of the pulses. The detection pulses were considered to be transition selective to account for orientation selection, driving transitions between the T_- and T_0 levels.

In this expression, the factor $P_\alpha + P_\beta$ corresponds to the modulation depth, which does not depend on the triplet state and has a maximum theoretical value of 1 corresponding to the excitation of all radical spins by the pump pulse. The triplet state polarisation contributes to the total signal intensity, which is also proportional to the triplet quantum yield. Therefore, LiDEER takes advantage of the enhanced sensitivity provided by the spin-polarised triplet state spectrum.

Laser-induced magnetic dipole spectroscopy (LaserIMD)

In LaserIMD, the permanent spin centre is used for detection and a variable-time laser pulse is used to photogenerate the triplet during the MW pulse sequence.[75] The formation of the triplet by the laser pulse can be thought as an optical pump, as it changes the spin state of the chromophore from $S = 0$ in the singlet state to $S = 1$ in the triplet state, leading to $|\Delta m_S| = 1$ if the triplet is formed in the $m_S = +1$ or $m_S = -1$ states. This event induces a change in the local magnetic field experienced by the detection spin analogous to the MW pump pulse in the DEER experiment, leading to the dipolar oscillation of the spin-echo intensity trace. If the triplet is formed in the $m_S = 0$ state, then $|\Delta m_S| = 0$, there is no change in the local magnetic field on the detection spin and no dipolar oscillation is observed.

The initial LaserIMD experiments were performed on the system labelled **3** in Fig. 1.15, the data recorded are shown in Fig. 1.17.[75] The detection sequence used in those experiments was a Hahn-echo sequence, which yields a trace that does not have a well-defined zero time. However, as the same dipolar oscillation is present at both the start and end of the trace, the zero time can be found by knowing the length of the pulses and delays in the pulse sequence and symmetrising the trace.[75] This has the advantage that both halves of the trace can be added up to increase the SNR.

The use of a Hahn-echo for detection follows the same principle as for 3-pulse DEER. However, unlike in 3-pulse DEER, where the start of the trace can be obscured by a dead-time artefact as a result of the TWT amplifier nonlinearity observed when two MW pulses cross, this is not the case in LaserIMD as the pump pulse is a light pulse. Hence, there is no dead time in this experiment and accurate determination of the zero time depends solely on the accuracy of the trace symmetrisation process. This relies on being able to record a complete trace to a good SNR and on how symmetric the trace is. Asymmetries in the trace are likely a result of different background contributions being present in each half of the trace (see Fig. 1.17 (a)). Care must be taken when applying the background correction to LaserIMD traces. Generation of the triplet state during the evolution time of the permanent spin induces not only a dipolar modulation of the echo intensity but also an increase in the number of paramagnetic centres in the sample, causing a change in the T_m of the permanent spin. This change causes the background form to deviate from the expected three-dimensional exponential for a homogeneous sample and to differ between the two halves of the trace, which may hamper the symmetrisation required to accurately determine the zero time.

An analytical expression for the form factor of the LaserIMD experiment was derived by the density-operator formalism[74]

$$F(t) = \frac{1}{2}(P_\alpha - P_\beta)\left[\Phi_T \cdot P_0 + \Phi_T(P_+ + P_-)\cos(t \cdot \omega_{dd})\right] \tag{1.45}$$

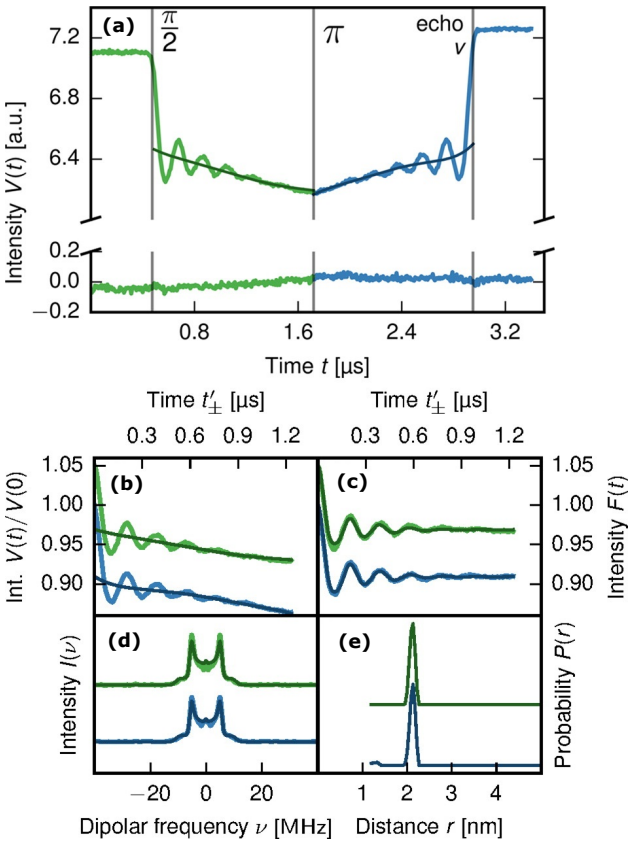


Figure 1.17: LaserIMD experiment with system **3** in Fig. 1.15, at Q-band, 10 K. Photoexcitation was carried out at 351 nm. (a) Raw data of the time domain signal with the background contribution determined experimentally. The top and bottom traces correspond to the real and imaginary parts of the quadrature signal, respectively. (b) Comparison of both branches (blue, right, and green, left) of the LaserIMD raw data. (c) Corresponding form factor after experimental background correction with a model-free fit obtained by Tikhonov regularisation. (d) Fourier-transformed dipolar spectra with fit. (e) Corresponding distance distribution with a mean distance of 2.12 nm and a width of 0.06 nm. *Reprinted (adapted) with permission from Hintze C., Bücker D., Domingo Köhler S., Jeschke G. and Drescher M. (2016), Laser-induced magnetic dipole spectroscopy. Journal of Physical Chemistry Letters, 7(12), 2204–2209, doi:10.1021/acs. jpclett.6b00765. Copyright 2016 American Chemical Society.*[75]

following a procedure similar to the one used for LiDEER, with the difference that now the triplet is formed during the pulse sequence, requiring a change of basis from the radical high-field eigenbasis to the direct product of the radical and triplet high-field eigenbases. In this case the modulation depth is given by the factor $\Phi_T(P_+ + P_-)$. Indeed, triplets formed in the $m_S = 0$ state by the laser pulse have an associated $|\Delta m_S| = 0$ and therefore do not contribute to the modulated part of the signal. In a sample with a uniform distribution of orientations and in absence of photoselection by the laser pump pulse, an orientational average over the surface of a sphere in the high-field limit yields $P_+ = P_0 = P_- = \frac{1}{3}$, making the maximum theoretically achievable modulation depth $\frac{2}{3}$ for an ideal $\Phi_T = 1$.[68] Importantly, this shows that the modulation depth of LaserIMD is insensitive to the relative populations of the triplet sub-levels under these conditions, but it only depends on Φ_T. The signal intensity and thus the sensitivity of the technique is determined by the polarisation of the radical, which is small at the magnetic fields and temperatures of PDS experiments. Therefore, unlike LiDEER, LaserIMD does not take advantage of the strong spin polarisation of the triplet state.

Refocused-echo LaserIMD (ReLaserIMD)

To improve the accuracy of zero time determination in LaserIMD, the Hahn-echo detection sequence can be replaced with a refocused-echo sequence, yielding the ReLaserIMD experiment.[64] ReLaserIMD is analogous to 4-pulse DEER, with a well-defined and symmetric zero time (see Fig. 1.10 (a)). As shown in Fig. 1.18, if the zero time is not accurately defined, this can lead to artefacts in the obtained distance distribution. This technique was first applied to the model peptide **3** in Fig. 1.15. Unlike 4-pulse DEER, where only the pump MW pulse is moving, in the implementation of ReLaserIMD (and LaserIMD) it is normally better to keep the laser pulse static in time and move the MW pulses relative to this light pulse, in order to minimise the jittering of the laser source. As the MW pulses can usually only be displaced in a positive direction, this leads to the laser pulse effectively moving back-

wards through the sequence. In this setup it can be easier to have $\tau_1 > \tau_2$, which is opposite to the standard 4-pulse DEER setup, to yield a trace where the zero time occurs at an early time. Alternatively, if $\tau_1 < \tau_2$ is used, this will yield a trace where the zero time occurs at a later time and the time axis will need to be inverted before analysis.

ReLaserIMD has the advantage over LaserIMD of providing a well-defined zero time. However, it can lead to lower SNR than LaserIMD as spin–spin relaxation is more effective during the longer sequence and part of the signal is lost with the application of each MW pulse due to pulse imperfections. Therefore, LaserIMD may be preferable in systems with a large separation between the spin centres, where small variations in the chosen position of the zero time lead to only very small changes in the distance distribution, and where a long trace is required to record sufficient dipolar oscillations. Conversely, ReLaserIMD is advantageous for the study of systems with small inter-spin separations, where only a short trace is required to capture the dipolar oscillation frequency and accurate determination of the zero time is vital for correct analysis.

Light-induced RIDME (LiRIDME)

LiRIDME is based on the RIDME sequence, with an additional laser pulse to populate the triplet state before the MW pulses.[64] It relies on using the longitudinal relaxation of one of the spin centres, changing its spin state during the mixing time T_{mix} (see Fig. 1.14 (c)). This technique was first demonstrated on a mutated human neuroglobin protein (ZnG19), where the heme group had been replaced by Zn(II) proto-porphyrin IX (ZnPP) and the only cysteine left had been labelled with MTSSL (see Fig. 1.19 (a)). In this case, as the chromophore is a metalled porphyrin, $T_1^{triplet} < T_1^{nitroxide}$ at the experiment temperature of 20 K and hence the nitroxide was chosen as the detection spin. As the triplet state has three spin sub-levels, relaxation is possible to cause $|\Delta m_S| = 2$ in addition to the desired $|\Delta m_S| = 1$, which leads to overtones, seen as a faster oscillation in the dipolar trace, particularly

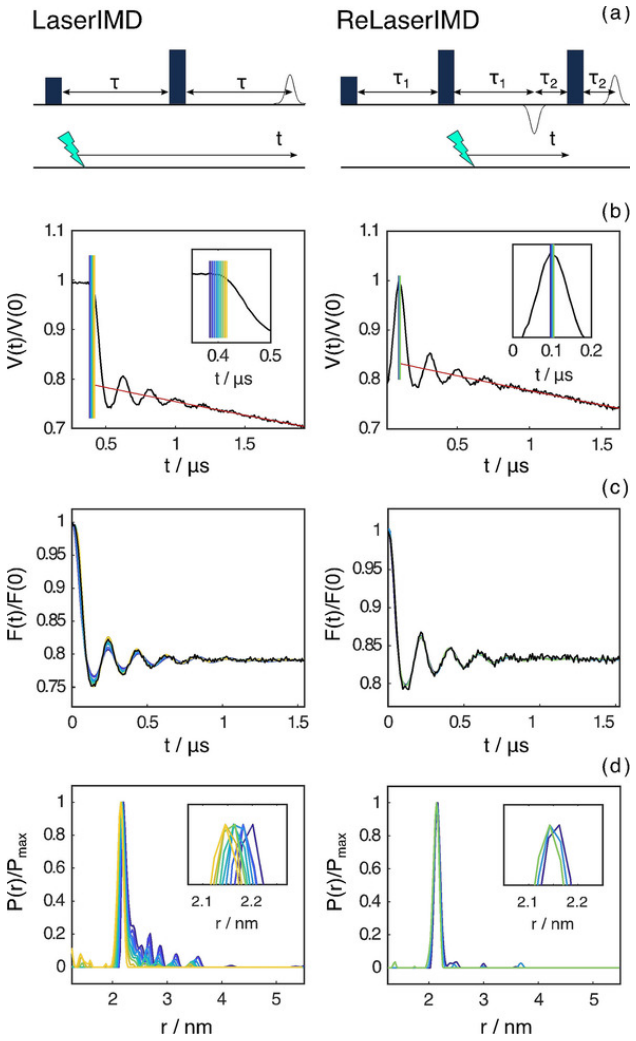


Figure 1.18: Influence of the zero time determination on the distance analysis in LaserIMD and ReLaserIMD measured on system **3** in Fig. 1.15. For both datasets: (a) pulse sequences, (b) raw dipolar time traces with the selected zero time positions used in the distance analysis, (c) form factors with the corresponding fits and (d) distance distributions obtained by Tikhonov regularisation. *Reproduced (adapted) with permission from Dal Farra, M. G., Ciuti, S., Gobbo, M., Carbonera, D. and Di Valentin, M. (2019). Triplet-state spin labels for highly sensitive pulsed dipolar spectroscopy. Molecular Physics, 117(19), 2673–2687. doi:10.1080/00268976. 2018.1503749. Copyright 2019 Wiley & Sons.*[64]

evident in the first oscillation period (see Fig. 1.19 (c)). In this example, a 50 % contribution from the overtone was observed, therefore it was important to take this into account in the analysis of the dipolar trace.

Choosing the right LiPDS technique

With several LiPDS techniques at the researcher's disposition, each having their strengths and weaknesses, the question comes of what method is best suited to answer a given research question. Multiple aspects must be taken into account when selecting which LiPDS technique to use. The most important aspect is the characteristics of the molecular system of study. If it already contains an endogenous chromophore that can be used for LiPDS, then the properties of its photo-activated triplet state will set the main experimental constraints. Triplets with very short T_m can only be used as the pump spin and the study will be limited to (Re)LaserIMD, while triplets with long T_m can also be used as detection spin and allow for both LiDEER and (Re)LaserIMD techniques. If the T_1 of the triplet is short, much shorter than the T_1 of the other spin label introduced in the molecule, then LiRIDME would be a suitable technique.

The range of distances to measure will determine the detection sequence to use. For the determination of short distances, a well-defined zero time in the dipolar trace is essential, and a refocused-echo detection sequence, such as those employed in 4-pulse LiDEER and ReLaserIMD, is necessary. For long distances, however, the long time traces necessary to correctly capture the dipolar frequency might lead to very low signal intensities if long 4-pulse sequences are used. The effects of the zero-time uncertainty on the determination of long distances are often small and the use of the Hahn-echo version of the LiDEER and LaserIMD techniques is acceptable. Alternatively, short refocused-echo traces can be combined with long Hahn-echo traces and "stitched" together as previously described for DEER,[22] simultaneously providing an accurate determination of the zero time and a higher signal intensity in the long trace.

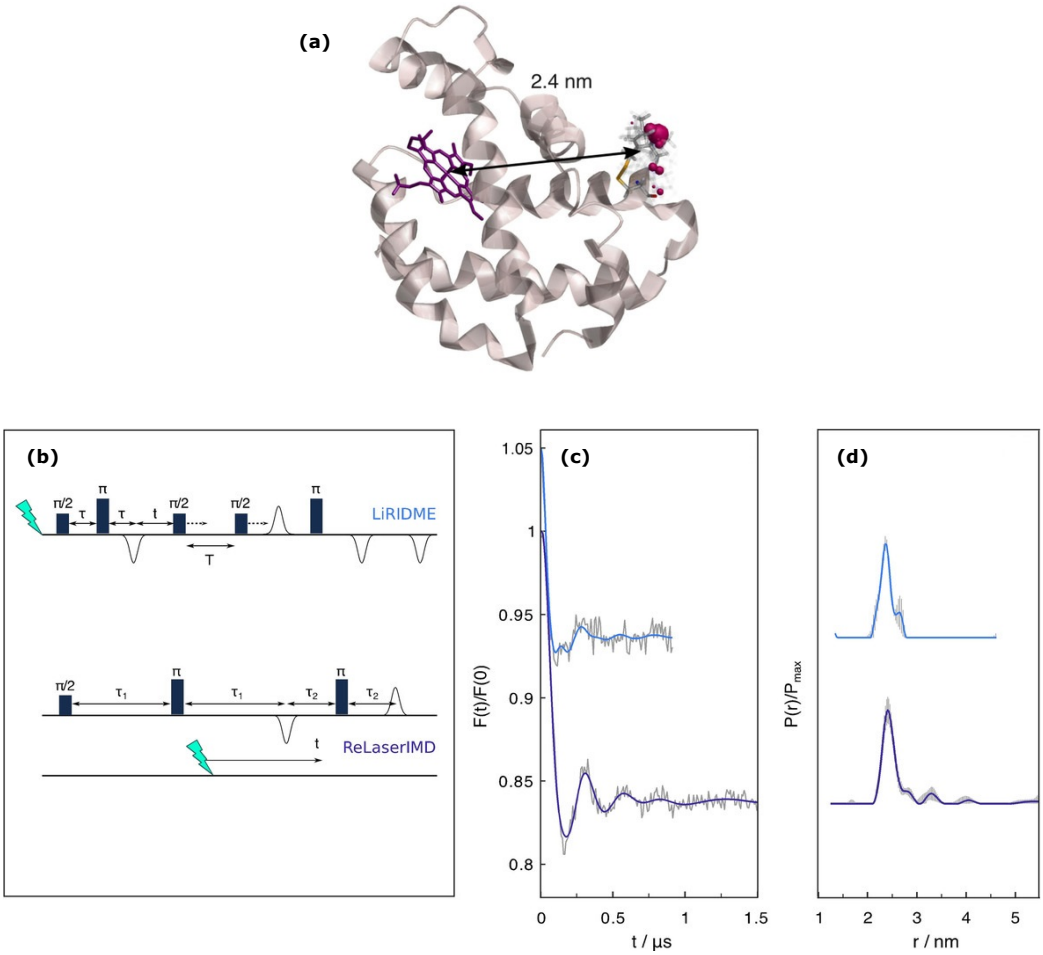


Figure 1.19: (a) Ribbon structure of ZnG19, a single-cysteine mutant of human neuroglobin, which is nitroxide-labeled and reconstituted with Zn(II) protoporphyrin IX (ZnPP). The predicted spin density distribution of the nitroxide is shown in magenta. (b) LiRIDME and ReLaserIMD pulse sequences. (c) Form factors (grey) and best fits to the LiRIDME (azure) and the ReLaserIMD (violet) data. (d) Corresponding distances distributions. The distance analyses have been performed with DeerAnalysis, for ReLaserIMD, and with OvertoneAnalysis for LiRIDME (with 50% contribution of the second harmonic overtone). The error bars have been obtained using the validation procedure, implemented in both software, varying the starting point for the background fitting between 300 and 500 ns and adding 50% of the original noise. *Reproduced (adapted) with permission from Dal Farra, M. G., Ciuti, S., Gobbo, M., Carbonera, D. and Di Valentin, M. (2019). Triplet-state spin labels for highly sensitive pulsed dipolar spectroscopy. Molecular Physics, 117(19), 2673–2687. doi:10.1080/00268976. 2018.1503749. Copyright 2019 Wiley & Sons.*[64]

Once the most suitable LiPDS technique for the study has been identified, adequate experimental parameters must be selected and optimised to obtain the best results. The choice of MW frequency is often limited by instrumentation, but if multiple frequencies are available, detection on permanent radicals should be done at high frequencies, such as Q-band. Signal intensity in these cases strongly benefits form the enhanced population difference between the two radical spin sub-levels provided by a larger Zeeman interaction. In addition, higher frequencies often provide higher orientational resolution. Detection on the photogenerated triplet, on the other hand, does not benefit from high MW frequencies, as the enhanced signal intensity arises from the non-Boltzmann population of the triplet spin sub-levels *via* ISC. Orientation resolution from triplets is frequency-insensitive too, because it relies on the ZFS, which is often much larger than the g-tensor anisotropy.

Temperature can have a large effect on spin relaxation and must be optimised for the detection spin centre. The temperature chosen must come from a trade-off between T_1 and T_m for the detection spin: T_1 must be shorter than the repetition rate of the experiment, which is determined by the repetition rate of the pulsed laser, and T_m must be sufficiently long to allow a pulse sequence that yields a dipolar trace of a suitable length to capture the dipolar frequencies. Some photogenerated triplet states require very low temperatures (e.g. 20 K) to show reasonable T_m values, while in the case of permanent radicals, such as nitroxides, higher temperatures may be beneficial for an optimal balance between T_1 and T_m (e.g. ca. 60 K for nitroxides at Q-band). The length of the pulse sequence must be kept as short as possible in order to maximise signal intensity, and it is limited by the length of trace necessary to capture the dipolar oscillations from the molecular system of study, which should match the inter-pulse delay for dipolar evolution (often τ for Hahn-echo detection and τ_2 for refocused-echo detection).

Both LiDEER and (Re)LaserIMD can potentially be applied to the same triplet–radical systems and complement each other. For the particular case of porphyrin–nitroxide systems, LiDEER is better suited for the measure-

ment of long inter-spin distances thanks to the longer T_m of the porphyrin triplet compared to that of the nitroxide.[64] With increasing MW frequency, the inversion efficiency of the pump pulse decreases as the spectral width of the nitroxide increases, leading to a degradation of the modulation depth in LiDEER. This can be compensated by using a broadband chirp pump pulse, that excites the whole bandwidth of the nitroxide spectrum (Fig. 1.20 (c, d)), red). However, as with DEER using shaped pump pulses, care must be taken to ensure that the length of the chirp pulse is sufficiently short as to not "wash out" the dipolar oscillation.[76] This can be explained by the fact that during the frequency sweep, spins with different resonance frequencies are inverted at different times resulting in an offset-dependent dispersion of the effective dipolar evolution times, since the zero time varies for spins at different spectral positions. LaserIMD techniques do not suffer from modulation depth reduction at higher MW frequencies because the depolarised laser pulse excites all orientations of the chromophore.[59] Despite not taking advantage of the triplet spin polarisation, sensitivity can be enhanced by using a critically-coupled resonator with a high Q-factor, which is not possible in double-frequency techniques such as LiDEER.

In LiDEER, the detection may be conducted either on the triplet or on the permanent paramagnetic species. When detecting on the triplet, pumping on the nitroxide with un-selective pulses that cover its full spectral width ensures that all triplet states are certainly affected by radical spin inversion, while taking advantage of the strong triplet spin polarisation. Alternatively, when detecting on the nitroxide, because of the limited photoexcitation capability, a fraction of the observed radicals will be bound to chromophores in the ground state, unaffected by the optical pumping. Consequently, a less sensitive detection of the modulation is expected in the later case.[73,77]

Another aspect to consider is the bandwidth of the ESR cavity. Bandwidth requirements are different for LiDEER compared to single-frequency techniques, as both frequencies need to be accommodated within the cavity bandwidth (typically up to 250 MHz for commercial cavities).[64] This implies

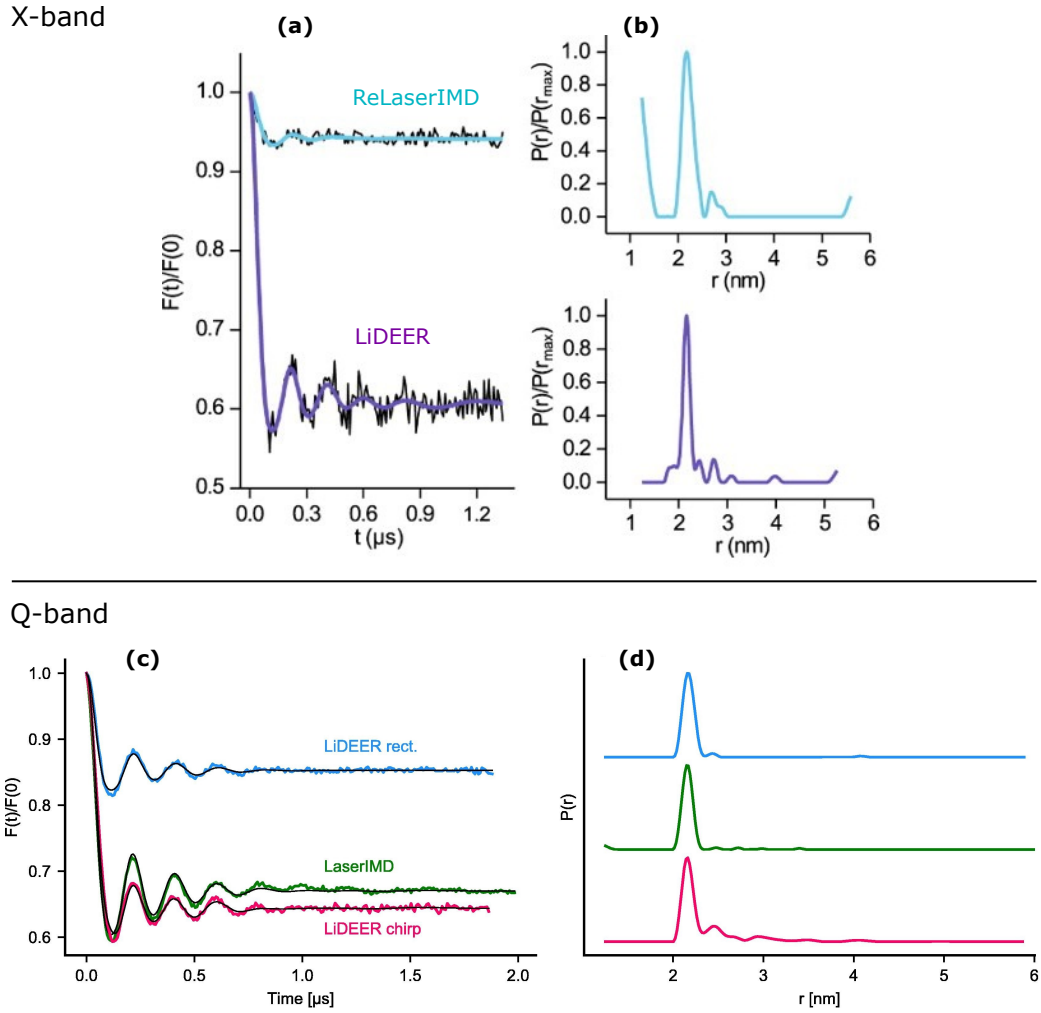


Figure 1.20: Comparison between LiDEER and ReLaserIMD at X-band (top) and Q-band (bottom) for peptide **3** in Fig. 1.15. Experimental form factors with fits (a and c) and corresponding distance distributions obtained by Tikhonov regularisation (b and d). The red dataset was acquired with a chirp pump pulse. *Panels (a and b) reprinted (adapted) with permission from Dal Farra, M. G., Ciuti, S., Gobbo, M., Carbonera, D. and Di Valentin, M. (2019). Triplet-state spin labels for highly sensitive pulsed dipolar spectroscopy. Molecular Physics, 117(19), 2673–2687. doi:10.1080/00268976.2018.1503749. Copyright 2019 Taylor & Francis Ltd., https://www.tandfonline.com.*[3] *Panels (c and d) reprinted (adapted) with permission from Bieber, A., Bücker, D. and Drescher, M. (2018). Light-induced dipolar spectroscopy—A quantitative comparison between LiDEER and LaserIMD. Journal of Magnetic Resonance, 296, 29–35. doi:10.1016/j.jmr.2018.08.006. Copyright 2018 Elsevier.*[59]

that a strongly over-coupled cavity must be used for LiDEER experiments. For single-frequency techniques, a less overcoupled cavity can be used, especially at Q-band, where even near-critically coupled conditions can be used.[59] This has beneficial effects on the echo intensity, as shorter pulses can be used to excite a larger fraction of the spin ensemble, improving sensitivity.

1.5.3 Biological applications of LiPDS - State of the art

LiPDS applications to proteins are currently restricted to distance measurements between a nitroxide radical, introduced by SDSL, and the photoexcitable centre.[64,68–70,75,78] When present, a photoactive prosthetic group can be used as endogenous probe, while for proteins that lack the intrinsic photoexcitable centre, SDSL procedures have been developed to introduce the triplet state probe.[68] Alternatively, the non-covalent binding of the chromophore to specific sites in proteins acting as supramolecular hosts has also been exploited.[69,70]

Hemeproteins, together with photosynthetic proteins and flavoproteins, contain photoactive cofactors and represent three important classes of proteins involved in fundamental biological processes. Tentatively, the hemeprotein cytochrome C, spin labeled with MTSSL at the free cysteine position, was investigated in order to demonstrate that LaserIMD could be employed for distance measurements between the endogenous prosthetic group and a nitroxide label.[75] However, no triplet state was observed by ESR, as expected for a low-spin ferric heme. The modulations appearing in the corresponding LaserIMD trace can probably be ascribed to higher spin states populated by photoexcitation. Unambiguous results on the feasibility of this LiPDS experiment for protein study were instead obtained with human neuroglobin. A mutant of this hemeprotein, containing a single cysteine, was expressed to avoid multiple labeling with MTSSL and was reconstituted with ZnPP to introduce the photoswitchable triplet state probe in the heme pocket.[64]

Analysis of the corresponding ReLaserIMD and LiRIDME traces provided accurate distance distributions, in perfect agreement with high-resolution X-ray structural data (see Fig. 1.19).

Not only porphyrin derivatives but other photoactive cofactors have been considered as endogenous probes. A LiPDS investigation of the photosynthetic light-harvesting peridinin chlorophyll protein (PCP) from *Amphidinium cartarae* was based on a triplet state carotenoid probe (a peridinin molecule) populated by triplet–triplet energy transfer from a neighbouring chlorophyll pigment (Fig. 1.21 (a, b)).[78] In general, the Φ_T for carotenoid molecules is negligible and a photosensitiser is required in order to use this chromophore as a photoswitchable probe. In the specific case of PCP, LiDEER was used with the precise aim of identifying the specific pair of chromophores involved in the photoprotection mechanism based on triplet–triplet energy transfer. By labelling the two free cysteines of the protein with MTSSL, distances between the triplet-bearing carotenoid and the two nitroxide radicals were determined. Comparing the experimental results to simulated LiDEER traces with all the possible positions of the peridinin triplet state, derived from the X-ray structure, the triplet-bearing carotenoid was identified (Fig. 1.21 (c-f)).

Porphyrin and C_{60} molecules are recognized by specific proteins, such as lysozyme and human serum albumin (HSA), which can act as supramolecular hosts for these chromophores. Exploiting this property, LiDEER measurements were performed on these systems to provide direct information on the location of the binding sites (Fig. 1.22).[69,70] SDSL of HSA with a nitroxide radical derivative (NIT) ensured the dipolar coupling between the guest chromophore triplet state and the radical species inserted on a specific cysteine site (Fig. 1.22 9a, b)).[70] Besides C_{60}, two distinct porphyrins with different properties were used: amphiphilic meso-tetrakis (4-hydroxyphenyl)-porphyrin (TMPyP4) and water-soluble cationic mesotetrakis(N-methyl-4-pyridyl)porphyrin (mTHPP), which are potential photosensitisers for photodynamic therapy (Fig. 1.22 (c, d)). While significant modulation depths

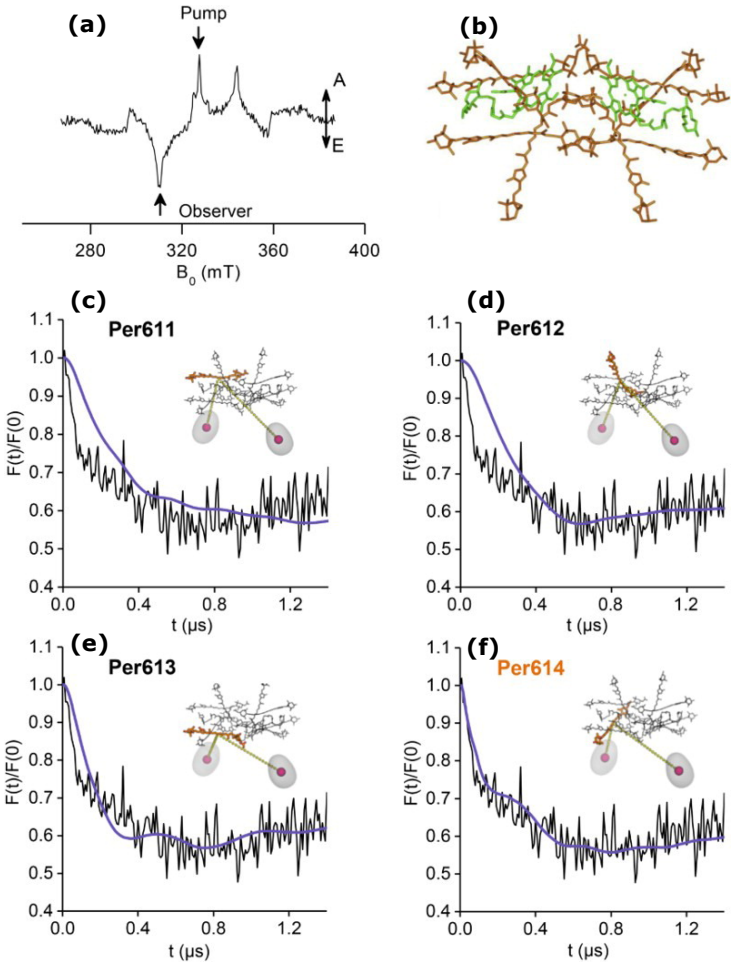


Figure 1.21: (a) X-band echo-detected field-swept spectrum recorded after photoexcitation for spin-labelled refolded peridinin chlorophyll protein (PCP). The arrows indicate the positions of the pump (nitroxide) and the detection spin (peridinin triplet state). (b) Structure of the pigments associated with the monomeric basic unit of the PCP complex from *Amphidinium cartarae*. (c–f) Comparison of background-corrected experimental and calculated LiDEER time traces for the triplet state localised on each of the four peridinin molecules. Peridinin 614 is highlighted as it corresponds to the peridinin involved in triplet-triplet energy transfer. *Reprinted (adapted) with permission from Dal Farra, M. G., Ciuti, S., Gobbo, M., Carbonera, D. and Di Valentin, M. (2019). Triplet-state spin labels for highly sensitive pulsed dipolar spectroscopy. Molecular Physics, 117(19), 2673–2687. doi:10.1080/00268976.2018.1503749. Copyright 2019 Taylor & Francis Ltd., https://www.tandfonline.com.*[3]

were obtained, especially for the supramolecular complex with C_{60}, providing clear evidence of the complex formation, the absence of defined oscillations in the LiDEER traces and the consequent broad distance distributions obtained were indicative of a lack of specificity in chromophore binding.

An important requisite to broaden the scope of triplet spin labels for biological applications is the availability of labelling procedures that allow the extension of LiPDS to classes of proteins lacking an intrinsic photoactive centre. A successful procedure was recently demonstrated using RB, EO and AT as photoswitchable triplet label candidates (Fig. 1.23 (a-c)).[68] These chromophores bear heavy atom substituents that promote ISC to the triplet state through increased SOC. For orthogonal labelling, the conventional maleimide–cysteine conjugation chemistry was combined with the copper-catalyzed azido–alkyne cycloaddition (CuCAAC) reaction between azide-functionalised chromophores and an alkyne-bearing non-canonical amino acid. LaserIMD experiments were performed on the protein oxidoreductase thioredoxin, which is a well-established model system in site-directed spin labeling owing to its rigid three-dimensional structure, the availability of X-ray structural data and the possibility to remove the native cysteines by site-directed mutagenesis without perturbing its structural integrity (Fig. 1.23 (d-i)). Although the results cannot compare to the narrow inter-spin distance distributions obtained for biomolecules with an intrinsic rigidly anchored chromophore, the achieved distance distribution widths were satisfactory and the inter-spin distances between the labelling sites were in agreement with the value derived from the X-ray structure.

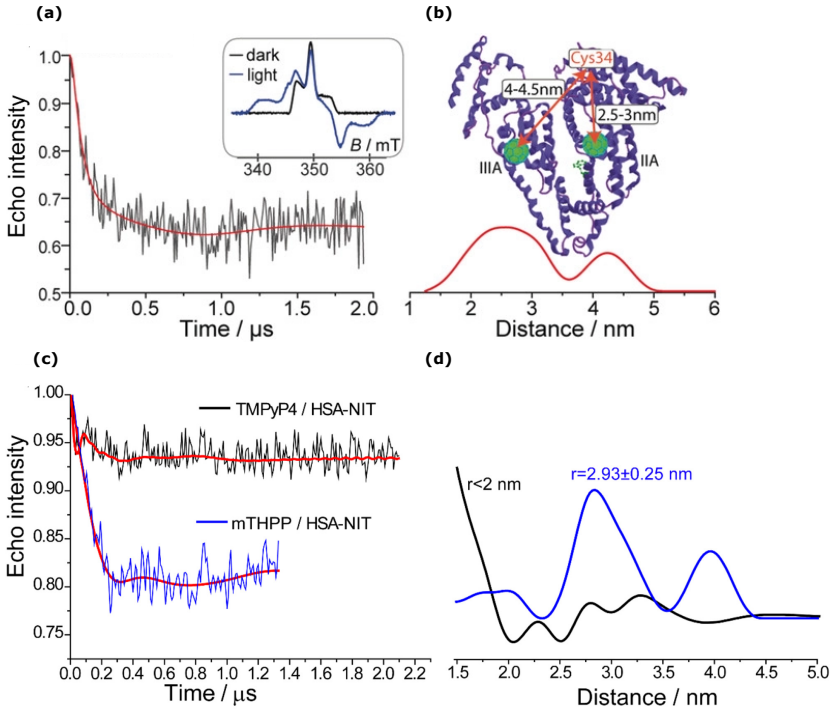


Figure 1.22: (a) Background-corrected and normalized X-band LiDEER trace for the HSA–NIT: PCBM complex at 50 K (black), and fit by Tikhonov regularisation (red). Inset: echo-detected field-swept ESR spectra at 50 K in the dark (black) and after laser excitation (blue). (b) Corresponding distance distribution obtained by Tikhonov regularisation. Inset: favourable binding sites of C_{60} (green) in HSA. (c) Background-corrected and normalised X-band LiDEER traces for TMPyP4/HSA-NIT (black) and mTHPP/HSA-NIT (blue) complexes at 10 K, with fits by Tikhonov regularisation (red). (d) Corresponding distance distributions. *Panels (A and B) reprinted (adapted) with permission from Krumkacheva, O. A., Timofeev, I. O., Politanskaya, L. V., Polienko, Y. F., Tretyakov, E. V., Rogozhnikova, O. Y. and Fedin, M. V. (2019). Triplet fullerenes as prospective spin labels for nanoscale distance measurements by pulsed dipolar EPR spectroscopy. Angewandte Chemie, 131(38), 13405–13409. doi:10.1002/ange.201904152. Copyright 2019 John Wiley & Sons.*[69] *Panels (C and D) reprinted (adapted) with permission from Sannikova, N. E., Timofeev, I. O., Chubarov, A. S., Lebedeva, N. S., Semeikin, A. S., Kirilyuk, I. A. and Krumkacheva, O. A. (2020). Application of EPR to porphyrin-protein agents for photodynamic therapy. Journal of Photochemistry & Photobiology, B: Biology, 211, 112008. doi:10.1016/j.jphotobiol.2020.112008. Copyright 2020 Elsevier.*[70]

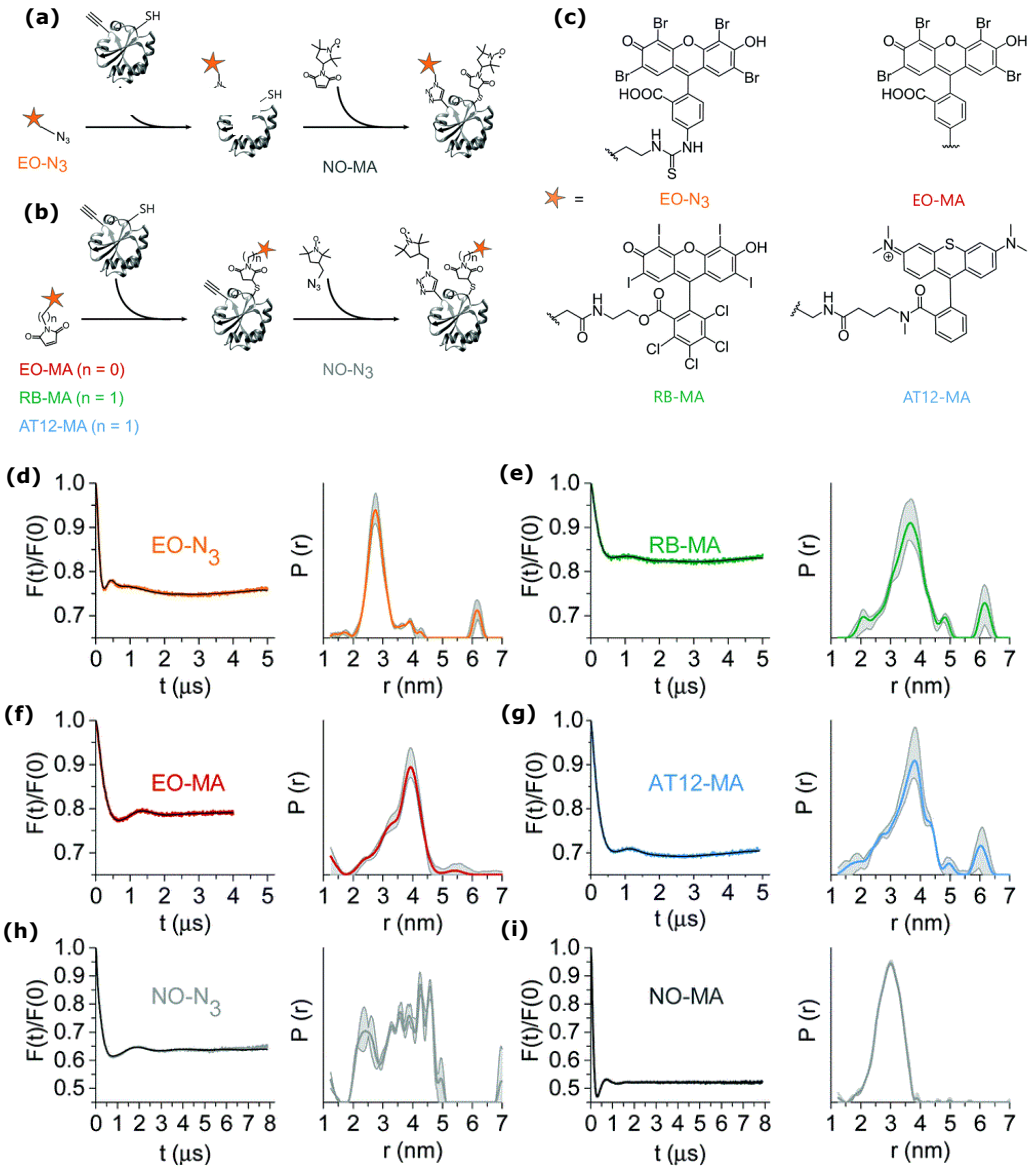


Figure 1.23: Orthogonal labelling of TRX at the ncAA pPrF (residue 14) and at the cysteine (residue 74). (a) EO-N_3 is attached via CuCAAC, followed by nitroxide labelling with NO-MA via cysteine–maleimide coupling. (b) EO-MA, RB-MA and AT-MA are attached via cysteine–maleimide coupling, followed by nitroxide labelling with EO-N_3 via CuCAAC.(c) Chemical structure of the chromophores. (d–g) Background-corrected and normalised LaserIMD traces (coloured) and fits (black) to obtain the corresponding distance distributions (right). (h and i) Bis-nitroxide control samples. *Reprinted (adapted) with permission from Williams, L., Tischlik, S., Scherer, A., Fischer, J. W. A. and Drescher, M. (2020). Site-directed attachment of photoexcitable spin labels for light-induced pulsed dipolar spectroscopy. Chemical Communications, 56, 14669–14672. doi:10.1039/d0cc03101a. Copyright 2020 Royal Society of Chemistry.*[68]

1.6 The structure of this thesis

This first chapter has presented the concepts in spin physics necessary for the understanding and appreciation of this thesis, with a detailed introduction to ESR spectroscopy and PDS, followed by a review of the state of the art in the novel field of LiPDS. The remaining chapters of this thesis present the results and conclusions of my effort to advance the promising methodology of LiPDS and to bring it closer to application in structural biology.

Chapter 2 investigates the orientational effects in previously reported LiPDS techniques and how to exploit them in order to extract additional information on the structure and the conformation of the molecules of study. Using a model peptide bis-labelled with porphyrin and nitroxide, the ReLaserIMD and LiDEER techniques are combined to fully characterise the relative orientation of the two spin centres. A new two-dimensional LiPDS technique (frequency-correlated ReLaserIMD) is introduced to capture the complete orientational dependence of the dipolar interaction with a single experiment. Finally, these novel methodologies are applied to molecules containing other non-porphyrin triplet chromophores, erythrosin B and I_2BODIPY, which had never been reported for PDS before.

Chapter 3 goes a step further to tackle the challenge of measuring the dipolar interaction between two photogenerated triplet states, therefore removing the need for having any permanent spin centre in order to perform PDS. A new LiPDS technique is developed for this purpose, light-induced triplet-triplet electron resonance (LITTER) spectroscopy, which combines the concepts of both LiDEER and LaserIMD to use photogenerated triplet states for both detection and pump. Proof-of-concept experiments on a bis-porphyrin-labelled model peptide are initially presented, followed by an in-depth conformational study performed on a spectroscopic molecular ruler exploiting the orientational effects in this new technique. LITTER is also compared to conventional DEER spectroscopy. To demonstrate the applicability of this novel technique to real structure determination problems,

studies of a dimeric heme protein and a supramolecular porphyrin tetramer are presented. Finally, factors limiting the performance of the technique are identified and discussed.

Chapter 4 is devoted to the improvement of the LITTER technique by addressing the limiting factors identified previously, focusing on the lack of selectivity in triplet state formation arising from the one-colour nature of the experiment. With this aim, a range of new chromophores are spectroscopically screened as potential triplet labels for a two-colour version of LITTER. The best candidates are incorporated into model peptides and proof-of-concept two-colour experiments are carried out to demonstrate the improved performance.

The closing **Chapter 5** presents the general conclusions of this work and suggests the future directions that LiPDS method development should follow in order to become a widespread spectroscopic technique complementary to conventional PDS and other molecular structure determination methods in biological sciences.

Chapter 2

Orientational effects in LiPDS

This chapter investigates the orientational effects in previously reported LiPDS techniques and how to exploit them in order to extract additional information on the structure and the conformation of the molecules of study. Using a model peptide bis-labelled with porphyrin and nitroxide, the ReLaserIMD and LiDEER techniques are combined to fully characterise the relative orientation of the two spin centres. A new two-dimensional LiPDS technique, frequency-correlated (FC) ReLaserIMD, is introduced to capture the complete orientational dependence of the dipolar interaction with a single experiment. Finally, these novel methodologies are applied to molecules containing other non-porphyrin triplet chromophores, erythrosin B and I_2BODIPY, which had never been reported for PDS before.

2.1 Orientationally selective porphyrin-nitroxide LiPDS

This section has been adapted from the following publication:[79]

A. M. Bowen, A. Bertran, K. B. Henbest, M. Gobbo, C. R. Timmel and M. Di Valentin, *J. Phys. Chem. Lett.*, 2021, **12**, 3819–3826.

The molecules used for this study were supplied by Prof. Marina Gobbo (University of Padova, Italy).

Despite the versatility of spin labels, the search for alternative probes, such as endogenous paramagnetic centres that eliminate the need to incorporate a non-native group in the macromolecule, is an active area of research.[40,80–83] Furthermore, in contrast to spin labels attached at surface accessible sites, native groups are rigidly held within proteins. As a consequence, distance and orientation distributions are narrower, enabling a more accurate analysis of these parameters. In particular, orientational analysis of PDS traces can be used to orientate interacting proteins or protein subunits with respect to one another.[84] Traditionally, the research of native paramagnetic probes has been mainly focused on metal-based centres such as Cu(II),[85,86] low-spin and high-spin Fe(III),[52–54] iron sulphur clusters,[84,87,88] and manganese clusters.[89] The sensitivity of PDS experiments on metal centres can suffer from the small fraction of spins within the excitation bandwidth of a typical rectangular MW pulse. However, at the same time the orientation selection can provide valuable structural information.

The photogenerated triplet states of organic chromophores have been proposed as a probe for PDS (see Section 1.5).[3] Many biological molecules, such as photosynthetic proteins,[78,90] hemeproteins,[63,74] and flavoproteins,[65] contain moieties that can act as photoswitchable spin centres. They are closed shell in their ground state but form electron spin-active triplet states after

photoexcitation at appropriate wavelengths. In addition to being photogenerated, these probes are formed in a spin-polarised state and thus their ESR signals are stronger compared to those of Boltzmann-populated paramagnetic centres (see Section 1.5.1).[91,92]

In this section, the first example of a two-dimensional (2D) light-induced frequency-correlated PDS experiment (FC ReLaserIMD) is demonstrated. Shaped MW pulses were used to excite the full nitroxide spectrum allowing the complete orientation dependence of the experiment to be determined in a single pulse sequence. To verify these results, one-dimensional (1D) orientationally selective ReLaserIMD experiments are also presented. These two techniques utilise the anisotropy of the nitroxide spectrum at Q-band. Finally, orientationally selective LiDEER experiments, which exploit both the anisotropy of the triplet state and the nitroxide spectra, are used to complete the orientational analysis. The orientationally selective data sets, recorded with the three different techniques, are compared and synergistically modelled using orientation-dependent simulations to prove the potential of LiPDS techniques in providing accurate information on the relative orientation of the spin-active moieties.

2.1.1 Characterisation of the model system

A geometrically well-defined model compound, the bis-labelled peptide **3** introduced in Section 1.5.2 (Figure 2.1), was chosen for these proof-of-concept experiments, as a narrow distance distribution between the paramagnetic centres, connected by a rigid α-helical linker, was demonstrated in previous LiPDS investigations.[58,72] A DFT energy-minimised structure of **3** is shown in Figure 2.2, where the calculation has been performed in the ground doublet state of the molecule. The calculated electron spin density distribution in the nitroxide radical is shown. The electron spin density distribution calculated on an isolated TPP-Ala molecule optimised in the triplet state is shown on the porphyrin chromophore. No significant structural changes were observed

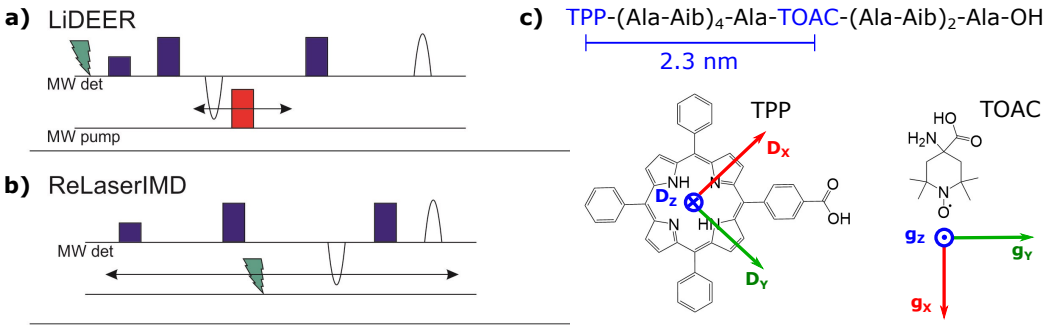


Figure 2.1: (a) LiDEER and (b) ReLaserIMD pulse sequences. (c) Amino acid sequence of molecule **3**. Key: TPP (5(4'-carboxyphenyl)-10,15,20-triphenylporphyrin), Ala (L-alanine), Aib (α-aminoisobutyric acid), and TOAC (2,2,6,6-tetramethylpiperidine-1-oxyl-4-amino-4-carboxylic acid). The distance between the centre of the porphyrin and the midpoint of the N-O bond in TOAC as predicted by DFT is indicated. The chemical structures of TPP and TOAC are included, showing their respective ZFS-tensor frame[93,94] (TPP triplet, left) and g-tensor frame[95] (nitroxide radical in TOAC, right). *Reprinted (adapted) with permission from Bowen, A. M., Bertran, A., Henbest, K. B., Gobbo, M., Timmel, C. R. and Di Valentin, M. Orientation-Selective and Frequency-Correlated Light-Induced Pulsed Dipolar Spectroscopy. J. Phys. Chem. Lett., 2021, 12(15), 3819–3826. doi:10.1021/acs.jpclett.1c00595. Copyright 2021 American Chemical Society.*[79]

between the energy-minimised structures of the chromophore in the ground and triplet states.

The field-swept electron spin-echo spectrum of the bis-labelled peptide (Fig. 2.3 (b)) shows the narrow central absorption signal due to the TOAC spin label and the broad contribution due to the TPP triplet state with an *eaeaea* spin polarisation pattern (e = emission, a = enhanced absorption). No magnetophotoselection is observed on the triplet spectrum. The spin relaxation properties of the TPP triplet are in agreement with reported values for similar molecules under the same conditions (Figure 2.3 (c, e)),[58,72] and the T_m of the nitroxide is not affected by photoexcitation (Figure 2.3 (d)).

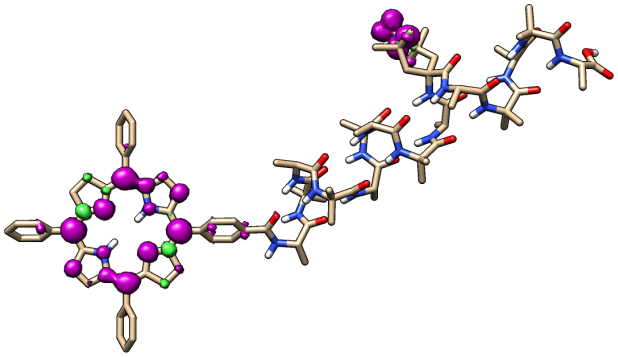


Figure 2.2: Electronic spin density in the DFT energy-minimised **3** (*Gaussian*,[96] PBE1PBE, 6-31(g)), where the TPP moiety has been photoexcited to form the first triplet state. Spin density calculated using the functional B3LYP and the basis set SV(P). *Reprinted (adapted) with permission from Bowen, A. M., Bertran, A., Henbest, K. B., Gobbo, M., Timmel, C. R. and Di Valentin, M. Orientation-Selective and Frequency-Correlated Light-Induced Pulsed Dipolar Spectroscopy. J. Phys. Chem. Lett., 2021, 12(15), 3819–3826. doi:10.1021/acs.jpclett.1c00595. Copyright 2021 American Chemical Society.*[79]

2.1.2 Orientationally selective ReLaserIMD

Orientationally selective ReLaserIMD data were obtained by measuring a series of dipolar evolution time traces at different field positions covering the complete nitroxide spectrum of the model peptide (Figure 2.4 (a, b)). The form factors show significant orientation selection as the MW detection pulses are moved across the ESR spectrum, leading to pronounced differences in the dipolar frequency with field position. These differences indicate a strong correlation between the orientations of the dipolar vector and the nitroxide moiety. This was expected for **3**, where the TOAC moiety holds the nitroxide in a rigid position with respect to the peptide backbone and the stiff α-helix of the peptide limits the orientational flexibility of the dipolar vector with respect to it.

The ReLaserIMD technique is particularly useful in this work as it allows more accurate selection of the experimental zero time, compared to Hahn-echo LaserIMD.[74] This is vital to the interpretation of different frequency components within the PDS trace shape found in orientationally selective

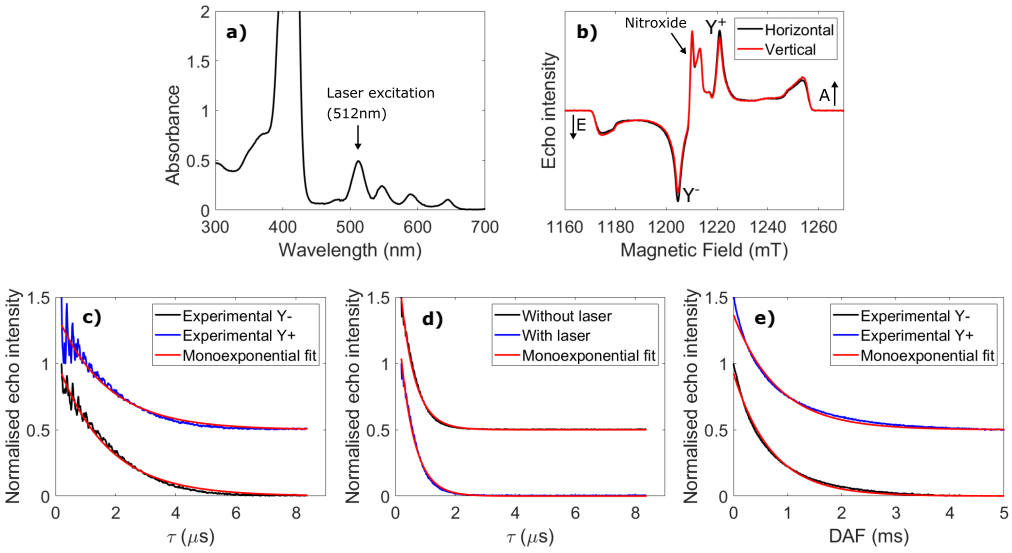


Figure 2.3: Spectroscopic characterisation of **3**. (a) Optical absorption spectrum of 100 μM **3** in a mixture of 98% d_4-methanol and 2% D_2O at room temperature. The laser excitation wavelength used for the ESR experiments, corresponding to the most intense maximum of the Q-band region, is indicated. (b) Echo-detected field-swept spectra after photoexcitation at 512 nm with polarised light parallel (black) and perpendicular (red) to $\mathbf{B}_0$. (c) Phase-memory experiments (black and blue) and corresponding monoexponential fits (red) measured on Y^- and Y^+ with T_m values of (1.65 ± 0.03) μs and (1.68 ± 0.04) μs, respectively. (d) Phase-memory experiments (black and blue) and corresponding monoexponential fits (red) measured on the nitroxide maximum without and with laser excitation, with T_2 values of (0.48 ± 0.05) μs and (0.48 ± 0.04) μs, respectively. (e) DAF experiment (black and blue) and corresponding monoexponential fits (red) measured on Y^- and Y^+ with lifetimes of (0.700 ± 0.005) ms and (0.820 ± 0.003) ms, respectively. *Reprinted (adapted) with permission from Bowen, A. M., Bertran, A., Henbest, K. B., Gobbo, M., Timmel, C. R. and Di Valentin, M. Orientation-Selective and Frequency-Correlated Light-Induced Pulsed Dipolar Spectroscopy. J. Phys. Chem. Lett., 2021, 12(15), 3819–3826. doi:10.1021/acs.jpclett.1c00595. Copyright 2021 American Chemical Society.*[79]

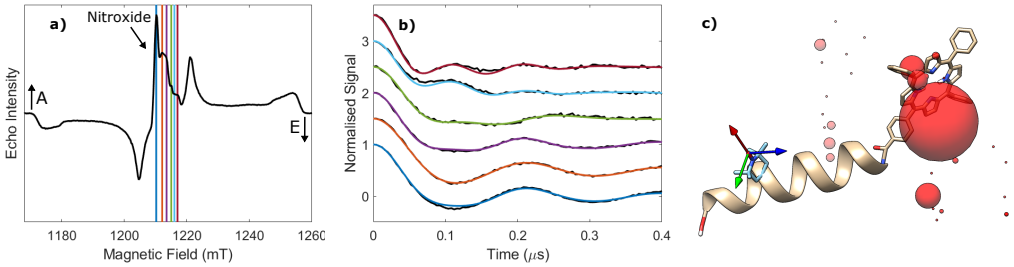


Figure 2.4: (a) Echo-detected field-swept spectrum of **3** measured using parameters optimised for the nitroxide radical. The experimental field values used for ReLaserIMD are indicated as vertical lines. (b) Measured ReLaserIMD traces (black) shown with the orientation-dependent fits (colours correspond to field positions in panel a). The modulation depth has been normalised to 1 for ease of analysis. See Figure 5.4 in Appendix II for RMSD plot. (c) DFT-optimised structure of **3** showing the different positions of the porphyrin centre determined by the fitting procedure as coloured spheres, relative to the nitroxide g-tensor frame (arrows: red = g_x, green = g_y, blue = g_z). The diameters of the spheres are proportional to the number of times each porphyrin position contributes to the complete fit shown in panel b. *Reprinted from Bowen, A. M., Bertran, A., Henbest, K. B., Gobbo, M., Timmel, C. R. and Di Valentin, M. Orientation-Selective and Frequency-Correlated Light-Induced Pulsed Dipolar Spectroscopy. J. Phys. Chem. Lett., 2021, 12(15), 3819–3826. doi:10.1021/acs.jpclett.1c00595. Copyright 2021 American Chemical Society.*[79]

data sets. The ReLaserIMD traces recorded at different field positions all yielded similar modulation depths. This likely indicates either that the laser power used was sufficient to saturate the transition and excite both Q_x and Q_y of TPP, or that photo-tautomerism of the pyrrolic protons exchanges the Q_x and Q_y by a pseudo-rotation, making the directions of the transition dipole moment indistinguishable in the porphyrin plane.[94] Furthermore, no magneto-photoselection effects were observed under the conditions of these experiments as minimal differences were seen in both field sweep spectra or ReLaserIMD traces recorded with the laser polarisation parallel and perpendicular to $\mathbf{B}_0$ (see Figure 2.3 (b)). Because the optical transition dipolar moments align with the ZFS-frame axes of the triplet state, as the Q_x and Q_y are interchangeable, the correlation between the g-tensor of the nitroxide and the ZFS-frame is lost. For this reason, while the information on the orientation of the dipolar vector relative to the g-tensor frame of the nitroxide can be extracted precisely, no information on the mutual orientation of the two paramagnetic centres is available from this experiment.

Orientationally dependent simulations were performed using the *OriDEER-sim* algorithm described in Section 1.4.5,[38] adapted to include the ZFS of the triplet and considering an infinite pump pulse bandwidth. The results were fitted to the experimental data using the iterative least-squares fitting process described in Section 1.4.5.[97] As it is not possible to resolve the orientation of the ZFS-tensor from these experiments, in the ReLaserIMD simulations the TPP moiety was modelled as a single point of spin density located at the centre of the porphyrin. In the fitting process, the modulation depth of the experimental traces was normalised to 1 for consistency with the calculated traces, which were simulated assuming 100% pumping efficiency of the laser pulse. Modulation depth values in LiPDS experiments with a laser pump pulse are often unreliable due to unpredictable changes in lase power, photobleaching, optical degradation of the solvent glass or condensation on the windows of the cryostat. The results of this analysis agree well with the DFT calculations. The rigidity of the system is demonstrated by the presence of a

single dominant conformer, which corresponds to an energy minimum where the backbone carboxylate group is axial to the piperidinyl ring of TOAC as depicted in Figure 2.4 (c). The simulations indicated that a small amount of a second chair conformation, with the backbone carboxylate group equatorial to the ring may also be present in a lower proportion (Figure 2.5). These conclusions are perfectly in line with XRD studies of an analogous peptide where the porphyrin moiety was not covalently bound.[98]

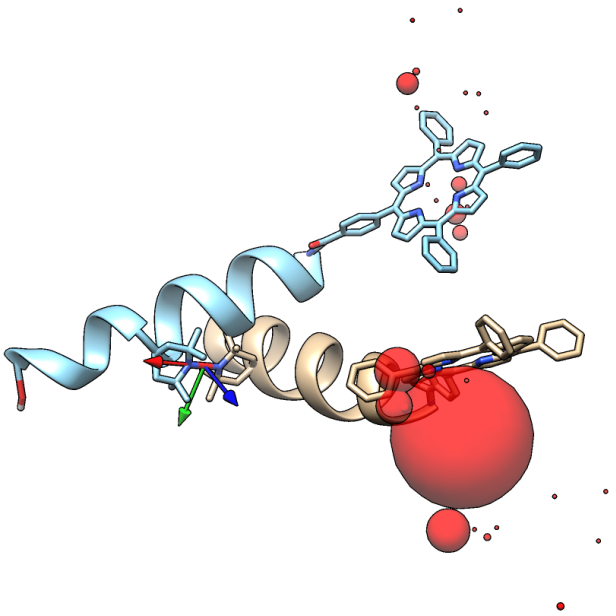


Figure 2.5: Different conformers of **3**. The taupe structure was determined by DFT optimisation (*Gaussian*, PBE1PBE, 6-31g(d)). The blue structure has the TOAC in a chair conformation.[99] The red spheres represent the different positions of the porphyrin centre determined by the fits shown in Figure 2.4 (b), relative to the nitroxide g-tensor frame (arrows: red = g_x, green = g_y, blue = g_z). *Reprinted (adapted) with permission from Bowen, A. M., Bertran, A., Henbest, K. B., Gobbo, M., Timmel, C. R. and Di Valentin, M. Orientation-Selective and Frequency-Correlated Light-Induced Pulsed Dipolar Spectroscopy. J. Phys. Chem. Lett., 2021, 12(15), 3819–3826. doi:10.1021/acs.jpclett.1c00595. Copyright 2021 American Chemical Society.*[79]

2.1.3 Frequency-correlated ReLaserIMD

For single-frequency PDS techniques, such as RIDME[100] and SIFTER,[101] it has been shown that it is possible to use shaped MW pulses to extract the complete orientation dependence of the dipolar spectrum in a single 2D frequency-correlated (FC) experiment.[102–104] The same principle can be applied to single-frequency LiPDS techniques.

In order to obtain the full orientation information from PDS data, FC ReLaserIMD was developed. The ReLaserIMD sequence was modified to use hyperbolic shaped pulses, which allow the bandwidth of the pulse to be extended compared to rectangular pulses and make complete excitation of the nitroxide spectrum at Q-band possible. The echo intensity traces were collected for each time step of the laser pulse, and after background correction along the time dimension, the absolute value of the Fourier transform was calculated. Results of this experiment conducted on molecule **3** are presented in Figure 2.6 (a). Simulations of the 2D FC ReLaserIMD, carried out using the conformer orientations found from fitting the individually measured 1D ReLaserIMD traces, reproduced the experimentally measured orientational features of the FC ReLaserIMD experiment (Figure 2.6 (b)). Good agreement was also seen between the experimental orientationally selective 1D ReLaserIMD form factors with their Fourier transforms and the corresponding slices of the 2D FC data set in the same spectral regions (Figure 2.6 (c, d)). In this way, we prove that the orientation correlation between the dipolar vector and the nitroxide g-frame can be accessed in a single experiment, whereas 1D techniques require a combination of multiple experiments. The orientation distribution fitting is the same for both data sets.

Looking at the results from a different perspective, orientational effects is informative, but it significantly complicates experiments and data analysis if only the distance distribution is of interest. The presence of orientation selection in the 1D ReLaserIMD experiments means that analysis of a single trace with *DeerAnalysis*,[35] which uses an orientation-independent kernel function,

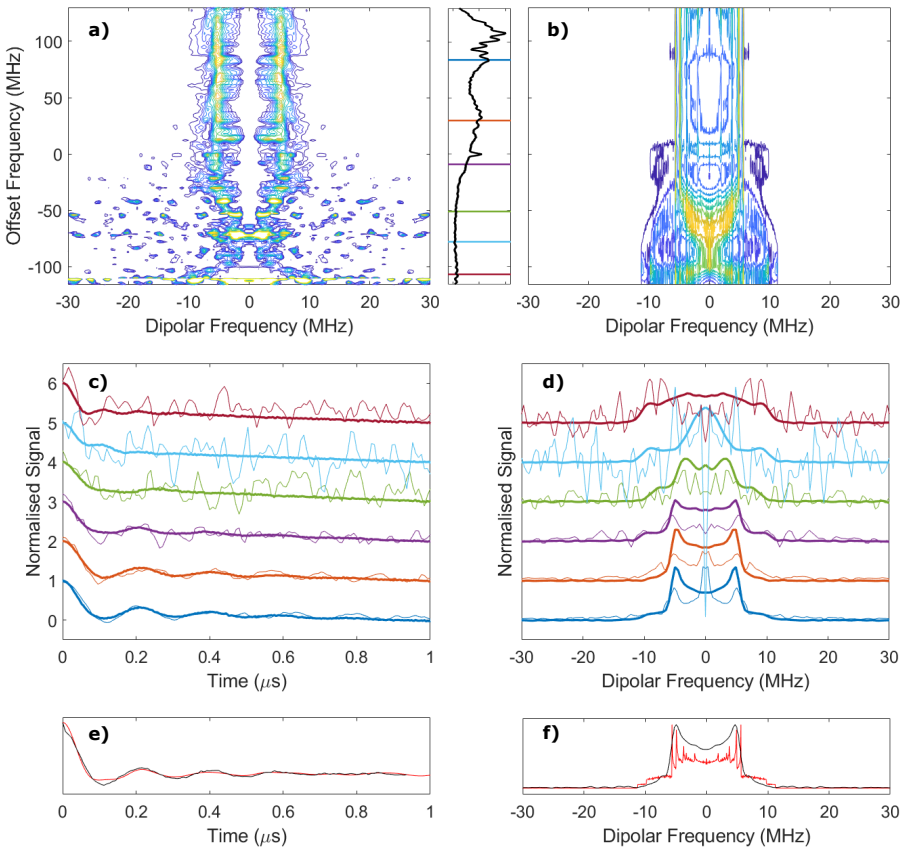


Figure 2.6: (a) Complete normalised experimental FC ReLaserIMD spectrum of **3** and (b) corresponding simulation with the panel between panels a and b displaying the Fourier transform of the FC ReLaserIMD echo recorded at the zero time of the experiment, with the experimental frequency values used for the ReLaserIMD indicated as horizontal lines. (c) Time-domain slices of the FC ReLaserIMD (thin lines) plotted with the 1D ReLaserIMD traces recorded at equivalent fields (thick lines). (d) Frequency-domain slices of the FC ReLaserIMD (thin lines) plotted with the 1D ReLaserIMD results recorded at equivalent fields (thick lines). The colours in panels c and d correspond to the frequency and field positions indicated in Figure 2a and the panel between panels a and b. (e) Sum over the offset frequency dimension of the FC ReLaserIMD experimental data (black) and simulation (red). (f) Fourier transform of panel e. *Reprinted (adapted) with permission from Bowen, A. M., Bertran, A., Henbest, K. B., Gobbo, M., Timmel, C. R. and Di Valentin, M. Orientation-Selective and Frequency-Correlated Light-Induced Pulsed Dipolar Spectroscopy. J. Phys. Chem. Lett., 2021, 12(15), 3819–3826. doi:10.1021/acs.jpclett.1c00595. Copyright 2021 American Chemical Society.*[79]

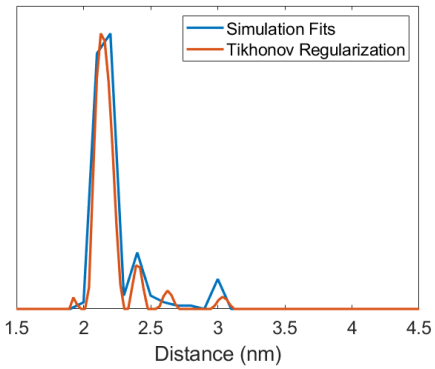


Figure 2.7: Inter-spin distance distributions from the simulation fits of the FC ReLaserIMD frequency slices shown in Figure 2.6 c and from Tikhonov regularisation of the summed trace shown in Figure 2.6 e. *Reprinted from Bowen, A. M., Bertran, A., Henbest, K. B., Gobbo, M., Timmel, C. R. and Di Valentin, M. Orientation-Selective and Frequency-Correlated Light-Induced Pulsed Dipolar Spectroscopy. J. Phys. Chem. Lett., 2021, 12(15), 3819–3826. doi:10.1021/acs.jpclett.1c00595. Copyright 2021 American Chemical Society.*[79]

may yield inaccurate distance distributions. When the orientation selection is solely due to the nitroxide moiety, it may be possible to remove this selectivity by measuring and combining several ReLaserIMD or LiDEER traces at different fields and/or detection-pump offsets.[104] However, the number and weighting of such traces required is not easily determined, and in the case of LiDEER the bandwidth of the resonator will restrict the experimental offsets that can be used between pump and detection frequencies (see following section), preventing the complete sampling of all orientation information. By comparison, orientation-averaged dipolar spectra can be easily obtained from the 2D experiment by summing over the offset frequency domain to yield the complete Pake pattern (Figure 2.6 (e, f)). The distance distribution obtained from analysis of this averaged trace by Tikhonov regularisation is presented in Figure 2.7.

2.1.4 Orientationally selective LiDEER

Although the orientationally selective ReLaserIMD experiments allowed the relative spatial position of the centre of the TPP moiety with respect to the TOAC nitroxide g-tensor frame to be determined, the technique did not provide information on the relative orientations of the two paramagnetic moieties, as there was no orientation dependence in the light excitation of the porphyrin. LiDEER traces encode additional information on the geometrical arrangement of the two spin labels, as orientation selection not only arises from the detection pulses but also from the MW pump pulse. The relative orientation of the nitroxide g-tensor frame and the porphyrin triplet ZFS-tensor frame can be derived. Combining this with the information on the tensor orientations in the individual moieties, which is well known in the case of the nitroxide radicals and porphyrin triplets,[93–95] the relative orientation of the two paramagnetic centres can be ultimately derived together with the relative spatial position, as determined from 1D and 2D FC ReLaserIMD.

To this end, LiDEER experiments using a refocused-echo detection scheme were performed with variable offsets between pump and detection frequencies and variable fields as reported in Figure 2.8. In all DEER experiments the maximum frequency offset between pump and detection pulses is limited by the bandwidth of the resonator. For this reason, it was necessary to record three sets of LiDEER experiments to sample the orientation selection of both the nitroxide and the triplet state. Initially, a set of five experiments, in which the detection frequency and field were fixed to the maximum positive peak in the triplet spectrum and the pump position varied across the nitroxide spectrum, were conducted (Figure 2.8 (a, d)). A second set of two experiments, in which the detection frequency and field were fixed to the maximum negative peak in the triplet spectrum and the pump position varied across the nitroxide spectrum, were completed (Figure 2.8 (b, e)).

Pumping at the position corresponding to the blue line in Figure 2.8 (a, b) and detecting either at the minimum or at the maximum of the triplet

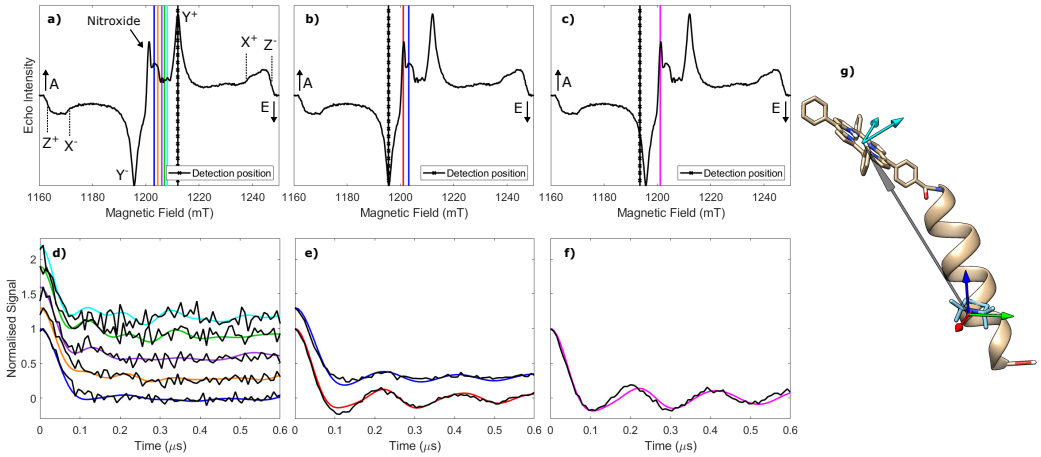


Figure 2.8: (a-c) Echo-detected field-swept spectra of **3** showing the detection (black crossed vertical lines) and pump (coloured vertical lines) positions used for LiDEER. (d-f) Experimental (black) and simulated (coloured) LiDEER traces. The colours of the simulated traces correspond to the pump positions shown in panels a-c. See Figure 5.5 in Appendix II for RMSD plot. (g) DFT-optimised structure of molecule **3** showing the Z-axes of the ZFS-tensors of the porphyrin centres (cyan arrows) most contributing to the best fitting set of simulated LiDEER traces, relative to the nitroxide g-tensor frame (arrows: red = g_x, green = g_y, blue = g_z) and the dipolar vector (gray arrow). *Reprinted (adapted) with permission from Bowen, A. M., Bertran, A., Henbest, K. B., Gobbo, M., Timmel, C. R. and Di Valentin, M. Orientation-Selective and Frequency-Correlated Light-Induced Pulsed Dipolar Spectroscopy. J. Phys. Chem. Lett., 2021, 12(15), 3819–3826. doi:10.1021/acs.jpclett.1c00595. Copyright 2021 American Chemical Society.*[79]

spectrum, corresponding to the Y canonical orientation of the ZFS-tensor, yielded traces with similar shape within the noise level (blue traces Figure 2.8 (d, e)). This was as expected, because the two maxima of the triplet spectra derive from resonance of the same molecular orientation.

The large width of the triplet spectrum made it impossible within the resonator bandwidth to sample all orientations of the triplet with respect to $\mathbf{B}_0$ while pumping the nitroxide spin. Although a complete set of experiments was precluded, a final trace was recorded where the detection frequency was set to select a field position of the triplet spectrum sampling orientations intermediate between those corresponding to the X and Y canonical orientations (Figure 2.8 (c, f)). The pump frequency was chosen to be resonant

with the maximum of the nitroxide spectrum. Comparing this to the trace recorded with the detection pulses resonant with the Y transition, while using the same pump pulse position, showed a difference in oscillation frequency between the traces. This indicates some orientation selection from the detection pulses, limited by the small difference between the detection positions.

Using the dominant orientation of the dipolar vector with respect to the g-tensor of the nitroxide determined from the ReLaserIMD experiments, LiDEER traces corresponding to a sample of all possible relative orientations of the nitroxide g-tensor frame and the porphyrin ZFS-tensor frame were calculated. In order to simultaneously analyse the complete set of orientation-dependent LiDEER traces and to account for the changing efficiency in the pump pulse when it is positioned at different frequencies within the resonator bandwidth, the modulation depth was normalised to 1 for both the simulated and experimental LiDEER form factors. The normalised experimental form factors were fitted to the calculated library of traces using an iterative process, where the number of iterations matched the number of contributions of the dominant conformer to the fit obtained for the ReLaserIMD data sets (Figure 2.4). The ZFS Z-axes of the two dominant conformers, obtained from this fitting process, are presented in Figure 2.8 (g). The corresponding orientations of the ZFS-tensor in the molecular frame show good agreement with the energy-minimised DFT structure and lie within the expected flexibility of molecule **3**. This fit might be improved by allowing flexibility in both the position and orientation of the two centres due to the conformational distribution expected. However, this increases the parameter space, and therefore, the uniqueness of the fit is likely reduced.

2.1.5 Conclusions

In conclusion, this work has demonstrated that orientational effects can be observed in both ReLaserIMD and LiDEER. A comprehensive analysis of

the results has been carried out, exploiting the complementary information provided by the two techniques, to localise and orientate the nitroxide centre with respect to the TPP moiety, yielding atomic-level geometric structural information. These results were validated using DFT calculations. The combination of the two techniques enabled the parameter space required for simulation to be reduced, simplifying the simulation process while enabling the relative positions and orientation of the centres to be accurately determined. Additionally, this work has presented the first example of 2D FC ReLaserIMD with a nitroxide observer sequence based on hyperbolic pulses, achieving, for the first time, complete excitation of a nitroxide spectrum at Q-band on a commercially-available ESR spectrometer. This technique lead to an improved frequency resolution and a larger span of frequency offsets compared to orientationally selective ReLaserIMD experiments in a reduced experimental measurement time. Alternatively, summation of the experimental results of FC ReLaserIMD over the offset frequency domain yielded an orientation-averaged dipolar trace enabling orientation-independent analysis.

Rigidly embedded endogenous spin centres, such as native cofactors which are either present in a paramagnetic state or can be photoexcited to form a suitable triplet state, are of significant interest for the measurement of PDS traces in unmodified protein systems. There is particular interest in the use of these centres in near-native environments where conventional spin labels, such as nitroxides, may degrade.[105] While the rigidity of the binding site within the protein structure may result in narrow distance distributions enabling more accurate reporting of protein structural changes, the likely orientation selection of PDS experiments on such systems necessitates careful analysis. Consequently, the combined approaches presented here for the PDS experiments measured between a photogenerated and a permanent paramagnetic centres will likely prove useful in the analysis of endogenous PDS studies. These methods offer the ability either to obtain geometric information on the structure of macromolecules, beyond the distance distribution, or to re-

duce the complexity of the measurements such that orientation-independent analysis of the dipolar trace can be confidently performed.

2.2 Orientationally selective LiPDS with non-porphyrin chromophores

This section has been adapted from the following publication:[106]

A. Bertran, L. Morbiato, S. Aquilia, L. Gabbatore, M. De Zotti, C. R. Timmel, M. Di Valentin and A. M. Bowen, *Molecules*, 2022, **27**, 7526.

The erythrosin B-containing system was supplied Prof. Marta de Zotti (University of Padova, Italy). The I_2BODIPY chromophore was supplied by Prof. Jianzhang Zhao (Dalian University of Technology, China). The I_2BODIPY-containing system was supplied Prof. Marina Gobbo (University of Padova, Italy).

The search for new photoswitchable spin labels for LiPDS, which could be attached to proteins that lack intrinsic photoexcitable groups, is an active area of research and a priority for the development of the field. In addition to having the right spectroscopic properties, good candidate labels for structural biology studies must be small, biocompatible, and commercially available in functionalised forms suitable for biolabelling.[107] Halogenated derivatives of fluorescein, such as eosin Y (EO) and rose Bengal (RB), and thioxanthene-based chromophores such as ATTO Thio12 (AT), were proposed as photoswitchable triplet labels based on spectroscopic characterisation and DFT calculations[67] and were subsequently used in LaserIMD studies of the protein oxidoreductase thioredoxin in conjunction with nitroxide labels.[68] Orthogonal labelling strategies were exploited, combining the conventional maleimide-cysteine conjugation chemistry with the copper-catalysed

azide-alkyne cycloaddition (CuCAAC) between azide-functionalised labels and alkyne-bearing non-canonical amino acids. Promising results were obtained at Q-band and liquid helium temperatures. However, these studies did not take into consideration the orientational effects arising from the anisotropy of the nitroxide ESR spectrum at Q-band.

This section reports the first utilisation of erythrosin B (EB) and 4,4-difluoro-diiodo-1,3,5,7,8-pentamethyl-4-bora-3a,4a-diaza-s-indacene (I_2BODIPY) as photoswitchable triplet spin labels for LiPDS. By performing multiple Re-LaserIMD experiments resonant with different parts of the nitroxide spectrum, the orientational effects arising from the anisotropy of the nitroxide spectrum at Q-band are exploited to extract information both on the inter-spin distance and on the conformation of a model peptide in frozen solution. In addition, the feasibility of these experiments above liquid nitrogen temperatures is shown for the first time, removing the need for expensive liquid helium or cryogen-free cryostats in LiPDS.

Attaching the chromophore: the colourless spirolactam problem

The initial work on LiPDS of model peptide systems used TPP labels attached to the N-terminus of the peptides via an amide bond with a carboxyl derivatisation of one of the phenyl rings.[58] If suitable for the system of study, this direct labelling strategy is very desirable because it only introduces a single-carbon linker between the biomolecule and the chromophore, minimising the distance distribution broadening and uncertainty due to label flexibility. However, this strategy is problematic for xanthene and thioxanthene dyes, as secondary amide formation with the ortho-carboxyl group enables an intramolecular ring closing reaction to yield a spirolactam form (Figure 2.9 (a)). The electronic conjugation over the chromophore is disrupted in the closed form, leading to the disappearance of the absorption bands in the visible region and therefore preventing visible photoexcitation. For rhodamine and thiorhodamine chromophore derivatives, the spirolactam formation process is pH dependent and can be reverted to the coloured open

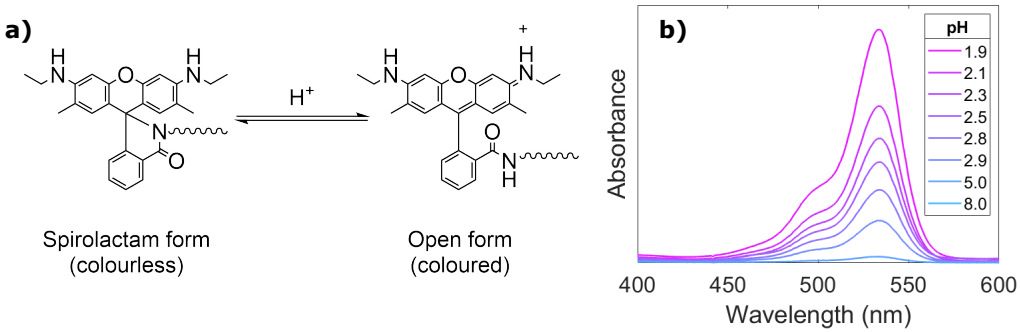


Figure 2.9: (a) Spirolactam formation equilibrium for rhodamine 6G (R6G) attached to the N-terminus of a peptide via direct amide bond. (b) Corresponding spectrometric pH titration for the peptide R6G–(Ala–Aib)$_7$–Ala in ethanol. *Reprinted (adapted) with permission from Bertran, A., Barbon, A., Bowen, A. M., Di Valentin, M. in Advances in Biomolecular EPR, ed. R. D. Britt, Elsevier Inc., 1st edn., 2022, Methods in Enzymology vol. 666, ch. 7, pp. 171–231. doi:10.1016/bs.mie.2022.02.012. Copyright 2022 Elsevier.*[107]

form by acidification (Figure 2.9 (b)). This approach was not successful for fluorescein derivatives such as EO, EB and RB.

Further modification of these xanthene and thioxanthene chromophores is necessary for their practical use in biological LiPDS. Williams *et al.*[68] recently reported biolabelling strategies for EO, RB and AT which do not involve forming a secondary amide on the ortho-carboxyl group (see Section 1.5.3). Additional modifications of the carboxyphenyl ring were used to introduce azide or maleimide moieties to EO, for CuAAC and cysteine–maleimide coupling, respectively. Alternatively, modification of the *ortho*-carboxy group to form esters or tertiary amides allowed successful introduction of maleimide moieties in RB and AT without compromising the electronic conjugation in the chromophore. However, these strategies involved the use of more expensive *para*-substituted derivatives of the chromophores as starting materials or introduced longer 5-atom linkers with additional unwanted conformational flexibility.

In this work, an alternative strategy to attach EB to the N-terminus of a peptide was devised, involving the use of a sarcosine (Sar) linker in or-

der to avoid the formation of the colourless spirolactam. This approach is advantageous to previously reported strategies, as it uses the more affordable non-derivatised form of EB and only introduces a 3-atom linker between the chromophore and the labelled molecule. Such an approach could also be extended to other carboxylate-containing dyes know to form colourless spirolactams, including EO and RB. In the case of I_2BODIPY, the chromophore was directly attached to the N-terminus of the peptide via amide bonding with the in-built *para*-carboxy group, which cannot form the spirolactam.

2.2.1 Characterisation of the model systems

The bis-labelled peptides **1** and **2** (Figure 2.10) were chosen as model compounds for this study because of the rigid α-helical structure expected from their alternating Leu-Aib and Ala-Aib sequences. *In-vacuo* DFT optimisations support the α-helical structure of the peptide backbones and predicts distances of 1.9 and 1.8 nm between the two labels for **1** and **2**, respectively.

The characterisation of the spin relaxation properties of the nitroxide radical in **2** is shown in Figure 2.11. Similar results were obtained for **1**. UV-Vis and ESR spectra of the photoswitchable triplet labels in **1** and **2** are shown in Figure 2.12. The two chromophores have similar UV-Vis spectra, with absorption maxima at 548 and 535 nm, respectively, and their triplet trESR spectra show the characteristic *eeeaaa* pattern of ISC-populated triplets. The smaller value of the ZFS $|D|$ parameter obtained from the I_2BODIPY triplet spectrum indicates a smaller delocalisation of the electronic spin density along the long axis of the chromophore (D_Z), while its larger $|E|$ value suggests a more planar spin density distribution than in the EB triplet. These observations are supported by DFT spin density calculations (Figure 2.13).

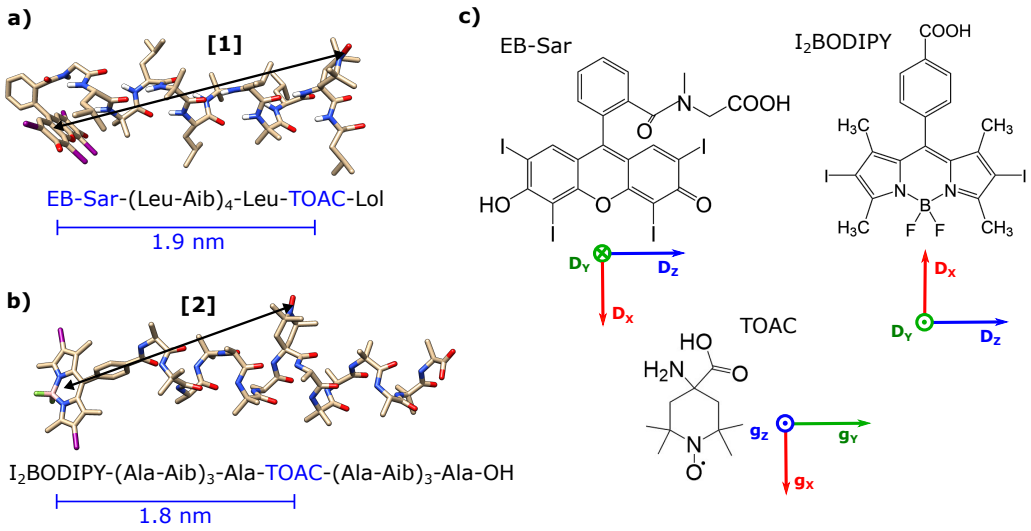


Figure 2.10: (a) Ground-state DFT-optimised structures and amino acid sequences of molecules **1** (a) and **2** (b), indicating the inter-spin distance predicted by DFT (*Gaussian*,[96] PBE1PBE, 6-31(g)). (c) Chemical structures of the spin labels, with the principal axes of their most anisotropic magnetic tensors (ZFS-tensor for EB and I_2BODIPY, g-tensor for TOAC) indicated (red = x, green = y, blue = z), as calculated by DFT (*Orca*;[108] BP86; Def2-SVP for H, C, N, O, B and F; Def2-TZVP for I; RI approximation with auxiliary basis set def2/J). Key: Sar (sarcosine), Leu (L-leucine), Aib (α-aminoisobutyric acid), TOAC (2,2,6,6-tetramethylpiperidine-1-oxyl-4-amino-4-carboxylic acid), and Lol (L-leucinol). *Reprinted (adapted) with permission from Bertran, A., Morbiato, L., Aquilia, S., Gabbatore, L., De Zotti, M., Timmel, C. R., Di Valentin, M. and Bowen, A. M. Erythrosin B as a New Photoswitchable Spin Label for Light-Induced Pulsed EPR Dipolar Spectroscopy. Molecules, 2022, 27(21), 7526. doi:10.3390/molecules27217526. Copyright 2022 MDPI.*[106]

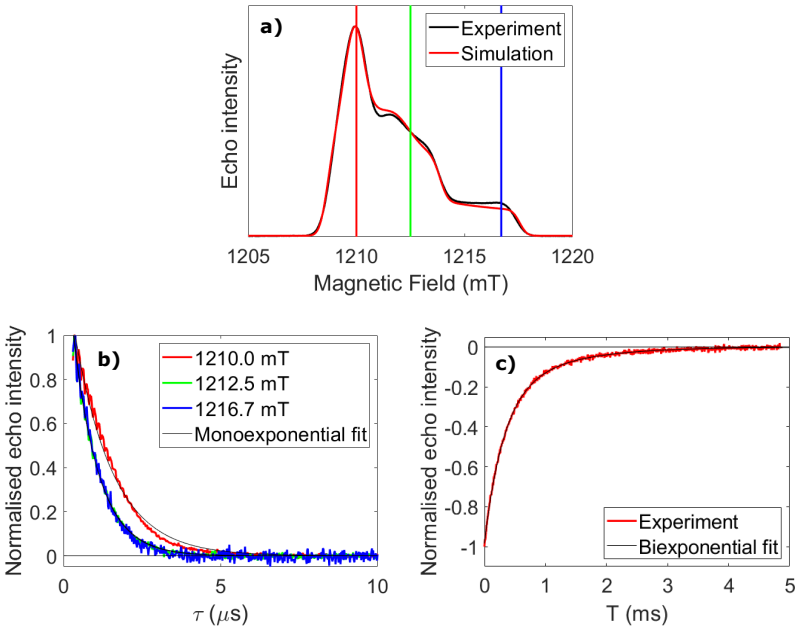


Figure 2.11: Q-band pulsed ESR characterisation of **2** in the dark. (a) Electron spin-echo field-swept spectrum (black, measured; red, simulation using *EasySpin*[109] *pepper* function), with the field positions used for phase-memory time experiments indicated as vertical lines. (b) Electron spin phase-memory time experiments at the field positions indicated in (a) (coloured lines) and monoexponential fits (black lines) yielding T_m values of (1.22 ± 0.02) μs, (0.818 ± 0.009) μs and (0.80 ± 0.01) μs, from left to right. (c) Inversion-recovery experiment performed at the signal maximum (red) and biexponential fit (black) with lifetimes of (0.315 ± 0.008) μs and (1.03 ± 0.04) μs. The same relaxation behaviour was observed for **1**.

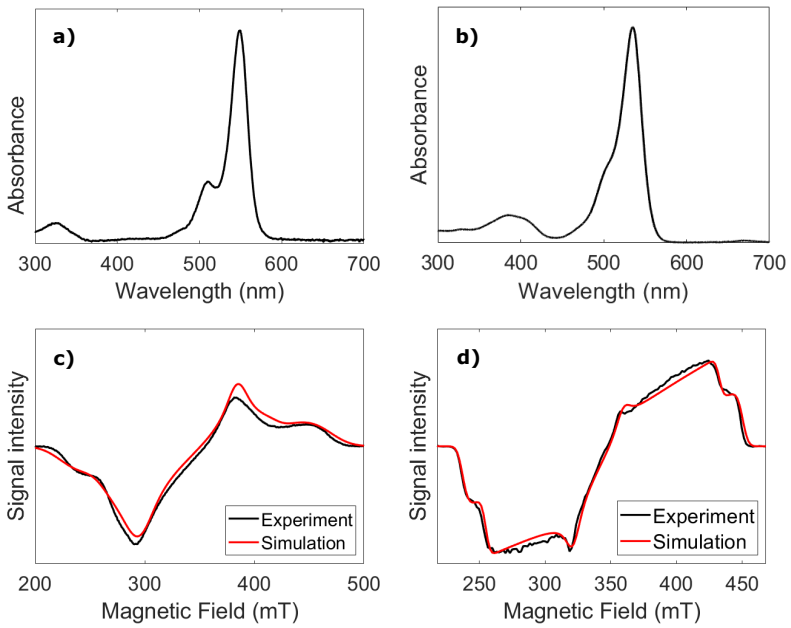


Figure 2.12: Room-temperature optical absorption spectra of **1** (a) and **2** (b) in ethanol. X-band trESR spectra of **1** (c) and **2** (d) measured after photoexcitation at 532 nm, 20 K (black) and simulations (red) using *EasySpin*[109] *pepper* function, with the following triplet state spin Hamiltonian parameters. **1**: D = -3486 MHz, E = 328 MHz, D-strain = 990 MHz, E-strain = 0 MHz, Gaussian linewidth = 3 mT, p_x = 0.6, p_y = 0.4, p_z = 0.0. **2**: D = -2995 MHz, E = 648 MHz, H-strain = [167, 230, 217] MHz, linewidth = [0.00, 1.48] mT, p_x = 0.00, p_y = 0.11 and p_z = 0.89. H-strain accounts for the anisotropic residual linewidth due to unresolved splittings, as the FWHM of a Gaussian broadening along each of the three dimensions. *Pannels (a, c) reprinted (adapted) with permission from Bertran, A., Morbiato, L., Aquilia, S., Gabbatore, L., De Zotti, M., Timmel, C. R., Di Valentin, M. and Bowen, A. M. Erythrosin B as a New Photoswitchable Spin Label for Light-Induced Pulsed EPR Dipolar Spectroscopy. Molecules, 2022, 27(21), 7526. doi:10.3390/molecules27217526. Copyright 2022 MDPI.*[106]

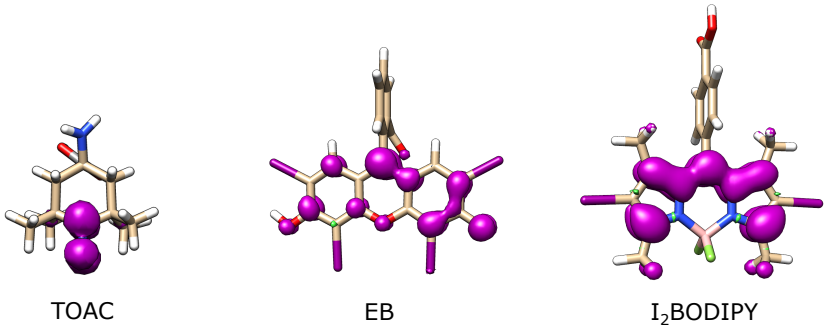


Figure 2.13: Calculated electronic spin densities for the spin labels (nitroxide radical, left; EB triplet, centre; I_BODIPY triplet, right) using *Orca*[108] (functional BP86, basis Def2-TZVP). *Reprinted (adapted) with permission from Bertran, A., Morbiato, L., Aquilia, S., Gabbatore, L., De Zotti, M., Timmel, C. R., Di Valentin, M. and Bowen, A. M. Erythrosin B as a New Photoswitchable Spin Label for Light-Induced Pulsed EPR Dipolar Spectroscopy. Molecules, 2022, 27(21), 7526. doi:10.3390/molecules27217526. Copyright 2022 MDPI.*[106]

2.2.2 Orientationally selective ReLaserIMD

The ReLaserIMD technique was applied at different field positions spanning the full width of the nitroxide ESR spectrum at Q-band to obtain orientation-resolved sets of dipolar traces for molecules **1** and **2** (Figures 2.14 (a) and 2.15 (a), respectively). The orientation selection of the MW detection pulses is evident from the appearance of a faster dipolar frequency component in the oscillating traces as the external magnetic field is increased (Figures 2.14 (b) and 2.15 (b), coloured lines).

Model-based orientation-dependent analysis

Orientation-dependent simulations were carried out following the protocol used in Section 2.1.2. Initial fits using molecular models generated around the DFT-optimised geometries of **1** and **2** were performed considering the photogenerated triplet spin density to be concentrated at the centre of the chromophores. This is a reasonable approximation as the light used for these experiments was not polarised and, consequently, there was no photoselection for different orientations of the chromophore with respect to $\mathbf{B}_0$. Modulation

depths were normalised to 1 for ease of analysis.

The results of these initial fits were used to refine the structural models and second fits were carried out including the delocalised triplet spin densities calculated by DFT (Figure 2.2). The relative orientation between the g-frame of the nitroxide radical and the ZFS-frame of the chromophore triplet were varied with three Euler angles. The results of these fits (Figures 2.14 (b) and 2.15 (b), black lines) are in excellent agreement with the experimental data and the corresponding spin–spin distance distributions have their main feature centred at 1.8 and 1.7 nm, respectively (Figures 2.14 (d) and 2.15 (d)), as predicted by DFT.

The conformational distributions of the molecules derived from the orientational analysis are plotted as spheres positioned at the centre of the chromophores with respect to the nitroxide g-frame, where the diameter of each sphere is proportional to the population of that particular conformation (Figures 2.14 (c) and 2.15 (c)). For **1**, these results suggest the EB chromophore folds back onto the peptide backbone as predicted by DFT. However, the direction of this fold is different from the DFT structure with the minimum calculated energy (Figure 2.14 (c), beige structure). The flexibility in the Sar linker and at the N-terminus of the α-helix means that other DFT-optimised structures with similar but slightly higher energies can be converged, leading to other local energy minima. Specifically, rotation around the C–N bond of the Sar linker yields a structure where the EB chromophore is closer to the results of the orientational analysis (Figure 2.14 (c), green structure). The fit results also show reasonable agreement of the Z-axis of the EB ZFS-frame (concurrent with the long axis of the EB moiety) with the green structure (Figure 2.16). This provides further evidence that this structure may be the dominant conformation in frozen solution. In addition, it should be considered that all DFT calculations in this work were performed *in vacuo*. Consequently, the presence of solvent could stabilise alternative conformations of the peptide that involve further rotation around the Sar C–N bond and/or change the hydrogen bonding network at

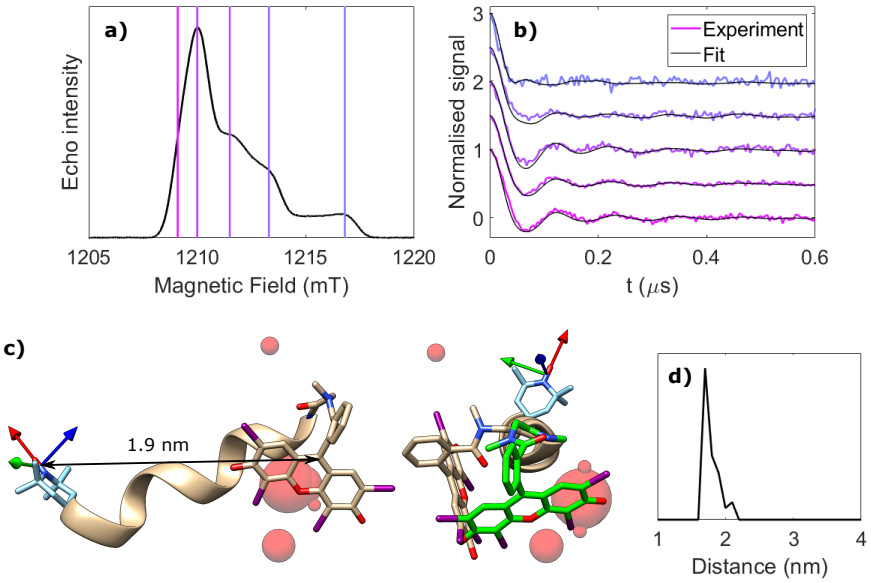


Figure 2.14: Orientationally selective ReLaserIMD on **1**. (a) Echo-detected field-swept spectrum in the dark, showing the field positions where ReLaserIMD traces were acquired. (b) Background-corrected and modulation depth-normalised ReLaserIMD traces (coloured lines) and corresponding model-based orientation-dependent fits (black lines). Modulation depths before normalisation were ~ 7 % for all traces. See Figure 5.6 in Appendix II for RMSD plot. (c) DFT-optimised structure of **1** (side and projection views) showing the different positions of the EB centre determined by the fitting procedure as red spheres, relative to the nitroxide g-tensor frame (arrows: red = g_x, green = g_y, blue = g_z). The diameter of the spheres is proportional to the number of times a single EB position contributes to the complete fit shown in panel b. The green structure on the right of the panel corresponds to another local energy minimum conformation identified by DFT. (d) Spin-spin distance distribution obtained from the orientation-dependent analysis. *Reprinted (adapted) with permission from Bertran, A., Morbiato, L., Aquilia, S., Gabbatore, L., De Zotti, M., Timmel, C. R., Di Valentin, M. and Bowen, A. M. Erythrosin B as a New Photoswitchable Spin Label for Light-Induced Pulsed EPR Dipolar Spectroscopy. Molecules, 2022, 27(21), 7526. doi:10.3390/molecules27217526. Copyright 2022 MDPI.*[106]

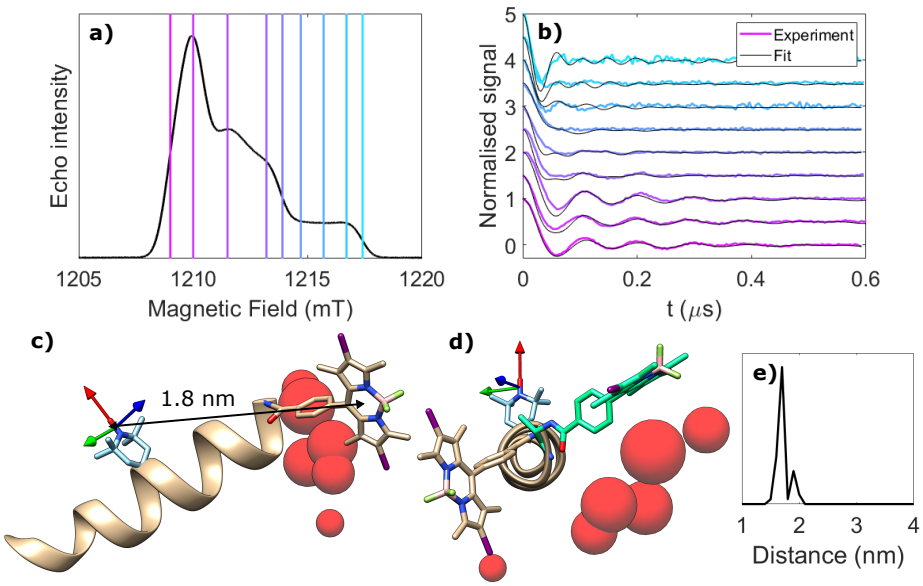


Figure 2.15: Orientationally selective ReLaserIMD on **2**. (a) Electron spin-echo field-swept spectrum in the dark, showing the magnetic field values where ReLaserIMD traces were acquired. (b) Background-corrected and modulation depth-normalised ReLaserIMD traces (coloured lines) and orientation-dependent model-based fits (black lines). Modulation depths before normalisation were between 3 and 6 %. See Figure 5.7 in Appendix II for RMSD plot. (c) DFT-optimised structure of **2** showing the different positions of the I_2BODIPY centre determined by the fitting procedure as red spheres, relative to the nitroxide g-tensor frame (arrows: red = g_x, green = g_y, blue = g_z). The diameter of the spheres is proportional to the number of times a single I_2BODIPY position contributes to the fit shown in panel b. (d) Projection view of panel c, including a second local energy minimum conformation identified by DFT (green). (e) Spin–spin distance distribution obtained from the orientation-dependent analysis.

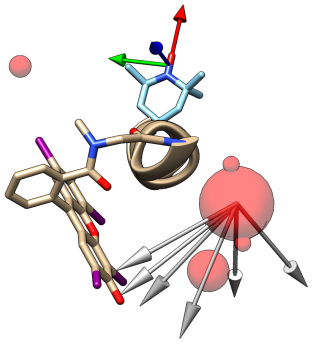


Figure 2.16: Orientations of the ZFS-tensor Z-axis of the EB triplet (parallel to the long axis of the chromophore) for the dipolar vector most contributing to the best fit in Figure 2.14. *Reprinted (adapted) with permission from Bertran, A., Morbiato, L., Aquilia, S., Gabbatore, L., De Zotti, M., Timmel, C. R., Di Valentin, M. and Bowen, A. M. Erythrosin B as a New Photoswitchable Spin Label for Light-Induced Pulsed EPR Dipolar Spectroscopy. Molecules, 2022, 27(21), 7526. doi:10.3390/molecules27217526. Copyright 2022 MDPI.*[106]

the N-terminus. For **2**, the results of the orientational analysis including the triplet spin density delocalisation are close to the DFT minimum-energy structure and they also suggest some degree of rotational flexibility around the N-terminus of the peptide. Indeed, higher local energy minimum conformations were identified by DFT through rotation of the C–C bond of the first Ala residue (Figure 2.15 (d), green structure).

Model-free orientation-dependent analysis

A model-free analysis of the same ReLaserIMD datasets, involving a more time-consuming exploration of the full conformational space, yielded very similar results, with only a slightly wider conformational spread due to the unrestricted nature of this approach (Figures 2.17 and 2.18). Due to the higher computational cost of this method, the triplet spin density was considered to be concentrated at the centre of the chromophores. These results validate the model-based analysis and confirm that the use of the minimum-energy DFT structure as a guide to the conformational space in which the model is constructed does not skew the conformational information obtained.

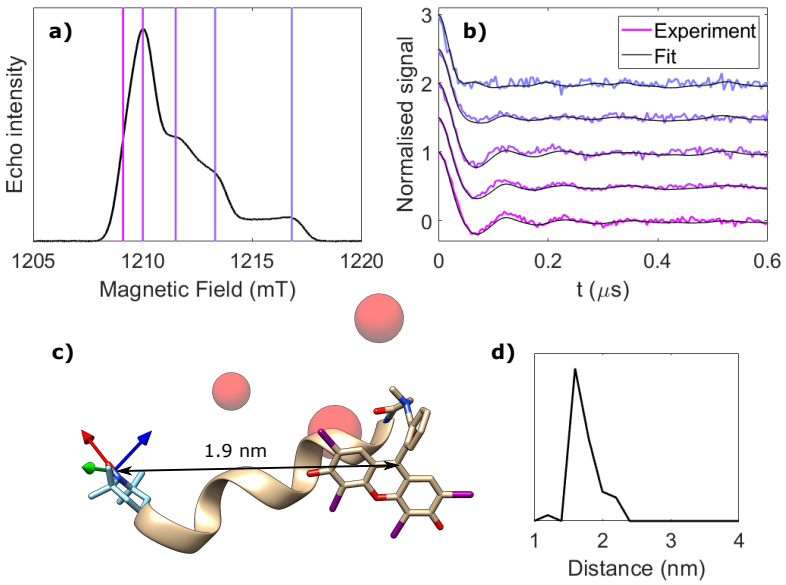


Figure 2.17: Results of the model-free orientation-dependent analysis of the ReLaserIMD data on **1**, with the triplet spin density in the centre of the EB moiety. (a) Echo-detected field-swept spectrum in the dark, showing the field positions where ReLaserIMD traces were acquired. (b) Background-corrected and modulation depth-normalised ReLaserIMD traces (thick lines) and corresponding orientation-dependent fits (thin lines). See Figure 5.8 in Appendix II for RMSD plot. (c) DFT-optimised structure of **1** showing the different positions of the EB centre determined by the fitting procedure as red spheres, relative to the nitroxide g-tensor frame (arrows: red = g_x, green = g_y, blue = g_z). The diameter of the spheres is proportional to the number of times a single EB position contributes to the complete fit shown in panel b. (d) Spin–spin distance distribution obtained from the orientation-dependent analysis. *Reprinted (adapted) with permission from Bertran, A., Morbiato, L., Aquilia, S., Gabbatore, L., De Zotti, M., Timmel, C. R., Di Valentin, M. and Bowen, A. M. Erythrosin B as a New Photoswitchable Spin Label for Light-Induced Pulsed EPR Dipolar Spectroscopy. Molecules, 2022, 27(21), 7526. doi:10.3390/molecules27217526. Copyright 2022 MDPI.*[106]

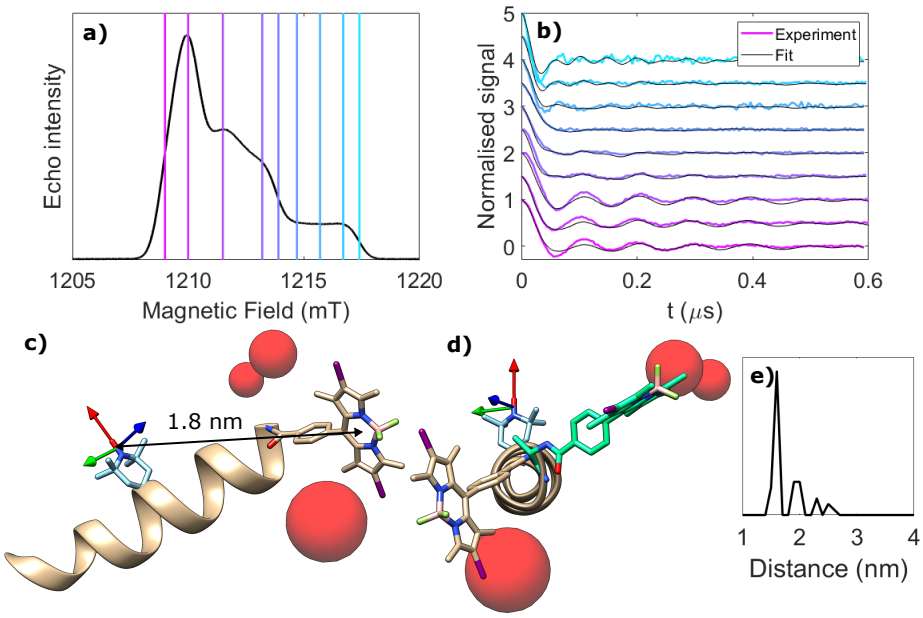


Figure 2.18: Results of the model-free orientation-dependent analysis of the ReLaserIMD data on **2**, with the triplet spin density in the centre of the I_2BODIPY moiety. (a) Electron spin-echo field-swept spectrum in the dark, showing the magnetic field values where ReLaserIMD traces were acquired. (b) Background-corrected and modulation depth-normalised ReLaserIMD traces (coloured lines) and orientation-dependent model-free fits (black lines). See Figure 5.9 in Appendix II for RMSD plot. (c) DFT-optimised structure of **2** showing the different positions of the I_2BODIPY centre determined by the fitting procedure as red spheres, relative to the nitroxide g-tensor frame (arrows: red = g_x, green = g_y, blue = g_z). The diameter of the spheres is proportional to the number of times a single I_2BODIPY position contributes to the fit shown in panel b. (d) Projection view of panel c, including a second local energy minimum conformation identified by DFT (green). (e) Spin–spin distance distribution obtained from the orientation-dependent analysis.

Orientation-independent analysis

If only the spin–spin distance distribution is of interest, the dipolar traces measured across the nitroxide spectrum can be added together to average and thus remove the orientational effects, resulting in an orientation-independent form factor that can be analysed by Tikhonov regularisation using standard software such as *DeerAnalysis*.[110] This approach is exemplified in Figure 2.19

for molecule **1**. For this system, the resulting distance distribution agrees well with that obtained from the orientation-dependent analysis and with the DFT prediction (Figure 2.14 (b)), and the small deviations are likely a result of incomplete orientational averaging caused by the discreet nature of the traces measured.

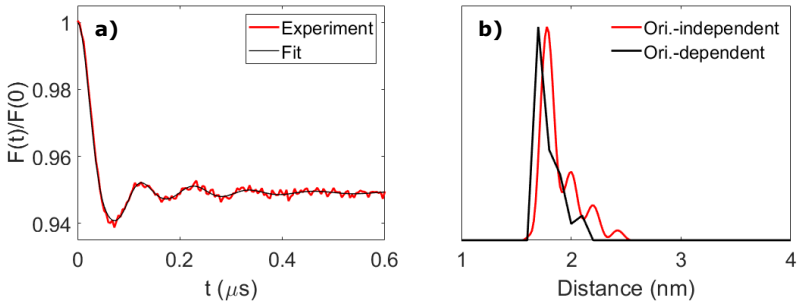


Figure 2.19: Orientational averaging of ReLaserIMD on **1**. (a) Averaged form factor (red) and fit by Tikhonov regularisation using *DeerAnalysis* (black). (b) Corresponding distance distribution (red) and distribution obtained from the orientation-dependent analysis (black, Figure 2.14 (d)). *Reprinted (adapted) with permission from Bertran, A., Morbiato, L., Aquilia, S., Gabbatore, L., De Zotti, M., Timmel, C. R., Di Valentin, M. and Bowen, A. M. Erythrosin B as a New Photoswitchable Spin Label for Light-Induced Pulsed EPR Dipolar Spectroscopy. Molecules, 2022, 27(21), 7526. doi:10.3390/molecules27217526. Copyright 2022 MDPI.*[106]

Comparison to an orientation-independent analysis of each individual dipolar trace by Tikhonov regularisation shows that the traces acquired around the nitroxide spectral maximum are not subjected to strong orientational effects in the studied molecule and yielded very similar distance distributions (Figure 2.20). It is therefore possible, for this particular molecule, to measure a single dipolar trace at the spectral maximum and to analyse it without taking orientational effects into consideration. However, this is not a general result, and it might not be true for other bis-labelled molecules, as the orientational effects on the dipolar traces depend on the relative orientation between the nitroxide g-frame and the dipolar vector. If this relative orientation is not known a priori, orientation-dependent analysis or orientational averaging, involving the measurement of several dipolar traces at different

parts of the spectrum of the detection spin centre, are the recommended approaches.

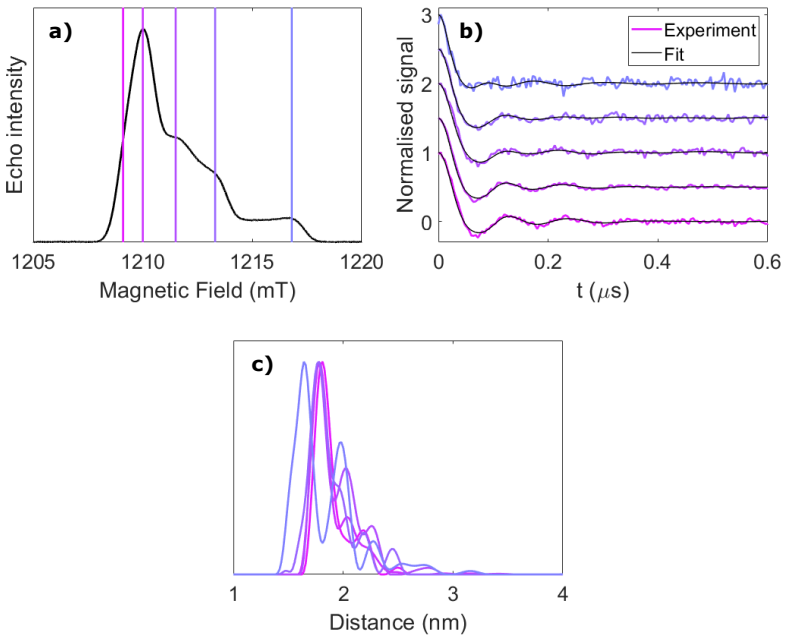


Figure 2.20: Orientation-independent analysis of individual ReLaserIMD traces for **1**. (a) Echo-detected field-swept spectrum in the dark, showing the field positions where ReLaserIMD traces were acquired. (b) Background-corrected and modulation depth-normalised ReLaserIMD traces (thick lines) and orientation-independent fits by Tikhonov regularisation using *DeerAnalysis* (black), using a regularisation parameter $\alpha = 12.6$. (c) Corresponding distance distributions. *Reprinted (adapted) with permission from Bertran, A., Morbiato, L., Aquilia, S., Gabbatore, L., De Zotti, M., Timmel, C. R., Di Valentin, M. and Bowen, A. M. Erythrosin B as a New Photoswitchable Spin Label for Light-Induced Pulsed EPR Dipolar Spectroscopy. Molecules, 2022, 27(21), 7526. doi:10.3390/molecules27217526. Copyright 2022 MDPI.*[106]

2.2.3 High-temperature LiPDS

LiPDS experiments have always been reported at temperatures close to liquid helium (c.a. 10-20 K), as these are optimal for the spin-spin relaxation properties of photogenerated triplet states. However, the requirement of expensive liquid helium or cryogen-free cryostates restrict the wider applicability of

these techniques and can be prohibitive for some researchers and institutions. In single-frequency LiPDS experiments such as (Re)LaserIMD, where echo detection is performed on the nitroxide spins, the T_m of the photogenerated triplet is irrelevant and measurements should be feasible at higher temperatures provided that T_1 remains long enough. To demonstrate this idea, the previous ReLaserIMD measurements on **1** were repeated at temperatures up to 100 K (Figure 2.21), demonstrating that LiPDS experiments can be carried out in the same conditions as conventional nitroxide–nitroxide PDS. This constitutes a big step towards the widespread use of LiPDS in structural biology.

The modulation-to-noise ratio (MNR) of the traces averaged for the same number of scans, calculated as the modulation depth relative to the noise level at the end of the trace, is significantly reduced at 100 K; however, the values for the data measured at 60 and 80 K are very similar: 70 and 73, respectively (Figure 2.21 (d)). This can be rationalised as the T_m times of the nitroxide measured at 60 and 80 K are very similar, whereas that measured at 100 K is approximately 3 times shorter (Figure 2.21 (b) and Table 2.1). Comparison of the data measured at 60 and 80 K shows that fewer oscillations are resolved in the trace recorded at 80 K compared to that recorded at 60 K (Figure 2.21 (c, d)). One possible explanation for this could be an increase in the longitudinal spin relaxation and thermalisation of the non-Boltzmann sub-level populations of the EB triplet at higher temperatures such that the spin state of EB generated by the laser pulse changes during the precession of the nitroxide spin, causing additional fluctuations in the nitroxide electron spin-echo intensity. It was not possible to observe a spin echo from the EB triplet at any of the temperatures studied (60-120 K), consequently it was not possible to measure a DAF experiment to determine the relaxation of the EB triplet at those temperatures and investigate this hypothesis. An alternative explanation is that, as the temperature increases, molecular motions also increase, and these motions may broaden the distribution of the dipolar frequencies observed at higher temperatures, leading to faster damping of

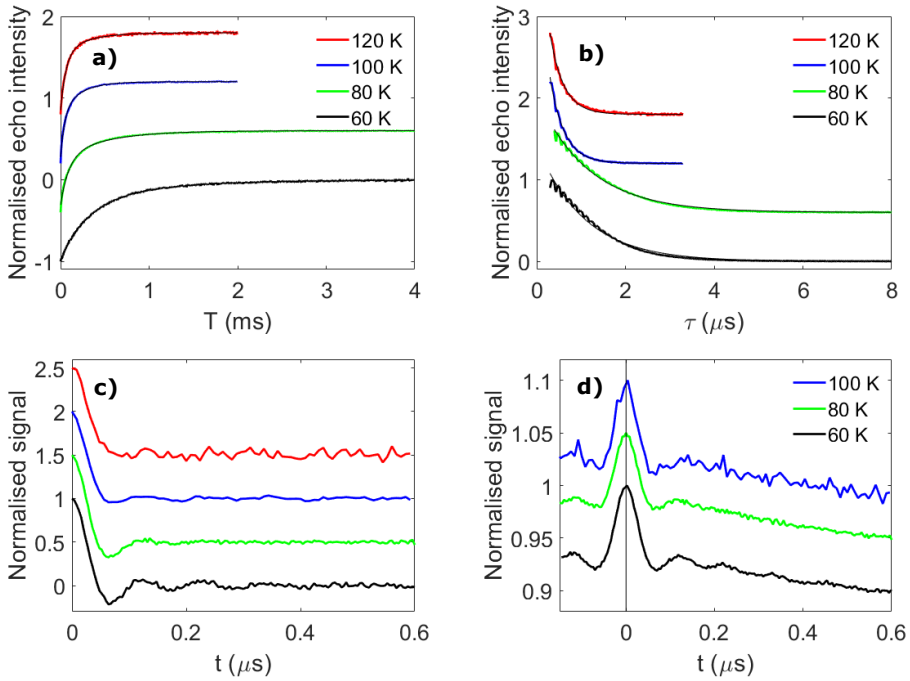


Figure 2.21: Characterisation of the relaxation of the nitroxide spectral maximum of **1** in the dark at different temperatures: 60 K (black), 80 K (green), 100 K (blue) and 120 K (red). (a) Inversion-recovery experiments (thick lines) with biexponential fits (thin lines). (b) Phase-memory time experiments (thick lines) with monoexponential fits (thin lines). The lifetimes determined from the fits are reported in Table 2.1. (c) Background-corrected and modulation-depth normalised ReLaserIMD traces acquired at the nitroxide signal maximum. The traces have been averaged for the following number of scans: 1875, 2520, 6960 and 29350, respectively. A time step of 8 ns was used to acquire the traces at 100 K and 120 K in order to reduce the acquisition time, while a 4 ns step size was used at 60 and 80 K. Modulation depths were $\sim$ 7 % before normalisation in all cases. (d) Raw ReLaserIMD traces acquired at the nitroxide signal maximum, at different temperatures: 60 K (black), 80 K (green), and 100 K (blue). The traces were measured for the same number of scans (750). The MNR values are 70, 73, and 23, respectively. The trace measured at 120 K has not been included due to its poor SNR at 750 scans. *Reprinted (adapted) with permission from Bertran, A., Morbiato, L., Aquilia, S., Gabbatore, L., De Zotti, M., Timmel, C. R., Di Valentin, M. and Bowen, A. M. Erythrosin B as a New Photoswitchable Spin Label for Light-Induced Pulsed EPR Dipolar Spectroscopy. Molecules, 2022, 27(21), 7526. doi:10.3390/molecules27217526. Copyright 2022 MDPI.*[106]

Temperature [K]	Inversion-recovery lifetimes [ms]	T_m [μs]
60	0.315 ± 0.008; 1.03 ± 0.04	1.07 ± 0.01
80	0.094 ± 0.003; 0.51 ± 0.01	1.15 ± 0.01
100	0.046 ± 0.002; 0.24 ± 0.01	0.323 ± 0.003
120	0.061 ± 0.003; 0.29 ± 0.02	0.309 ± 0.006

Table 2.1: Lifetimes extracted from the fits in Figure 2.21.

the oscillations.[111,112]

2.2.4 Conclusions

The variety of choice in photoswitchable spin labels and the affordability of the experiments are critical for the expansion of LiPDS to become a widespread and complementary methodology to conventional PDS. This work takes an important step in this direction by introducing new photoswitchable spin labels and by removing the need for expensive cryogenics in these experiments.

This section reports the use of EB and I_2BODIPY as photoswitchable triplet spin labels for LiPDS. Their strong light absorption in the green and their high triplet quantum yield allow for low-demanding photoexcitation using the second harmonic of a simple Nd:YAG laser. In addition, their small size, biocompatibility, and commercial availability in functionalised forms for biolabeling make them ideal candidates for biological applications.

Employing the ReLaserIMD technique to measure the dipolar interaction between the triplet and a permanent nitroxide radical in rigid model peptides, the orientational effects in the dipolar traces were exploited to obtain information on both the distance and relative orientation between the two spin-bearing moieties. The agreement between different data analysis approaches and DFT calculations demonstrates the robustness of this methodology. This showed the importance of capturing the orientational effects underlying these experiments, which can then be correctly averaged to perform an orientation-independent analysis free of orientational artefacts if

only the distance distribution is of interest.

The library-based iterative fitting procedure used in this thesis to obtain the spin-spin distance distribution from orientation-dependent LiPDS datasets has been previously shown to work well for systems with a well-defined geometry in frozen solution.[97] However, in the hypothetical scenario of a sample with two significantly different structures of the molecule of study, an unrestricted fit to the entire conformational space could be biased towards an artificial intermediate structure whose dipolar traces resemble the experimental dataset (if the data can indeed be generated around a single structure). The fitting algorithm in this case would not recognise that the experimental data results from the combination of traces from two different structures. However, it is unlikely that a single structure could reproduce well a set of orientation-dependent dipolar traces arising from two different structures.

In addition, this work demonstrates the feasibility of these experiments above liquid nitrogen temperatures, removing the need for expensive liquid helium or cryogen-free cryostats, which often restricts the accessibility of LiPDS to institutions and researchers with reduced funding.

2.3 Methods

See Appendix I for general instrumentation.

Sample preparation

Molecules **2** and **3** were supplied by Prof. Marina Gobbo (University of Padova, Italy). Molecule **1** was supplied by Prof. Marta de Zotti (University of Padova, Italy). ESR samples of **1** were prepared to 100 μM in 98% deuterated methanol (99 % atom, Merck), 2% D_2O (99 % atom, Merck). Samples of **1** and **2** were prepared to 50 μM in deuterated ethanol (99 %

atom, Merck). All samples were degassed by several freeze-pump-thaw cycles and flash-frozen in liquid nitrogen before being inserted into the ESR spectrometer.

The solvents used for these studies were chosen for their solubility and spectroscopic properties. They easily dissolved the molecules of interest to concentrations of several hundreds of μM. They are know to form good optical glasses when flash frozen at cryogenic temperatures, which is essential to achieve a good illumination of the sample volume. After flash-freezing and prior to insertion into the spectrometer, samples were visually inspected for any cracks in the solvent glass. If necessary, the flash-freezing process was repeated until a good optical glass was achieved.

ESR spectroscopy

Rectangular MW pulses with equal amplitude and double the length for the π pulse were used for all experiments except from FC ReLaserIMD, where shaped pulses generated by an AWG were used. In the later case, the pulses used were hyperbolic with a sech/tanh frequency function and a WURST amplitude function calculated to have bandwidths of ca. 300 MHz, B_1 strengths of 10 MHz, measured from the TII resonator, and lengths of 800 ns (π) and 1600 ns ($\frac{\pi}{2}$), calculated according to previous work.[73] Using π pulses with double the chirp rate of the $\frac{\pi}{2}$ pulses allows all frequency components of the primary echo to be refocused at the same time. This gives a constant zero time of all components relative to the laser pulse. Application of the second π pulse causes the zero times of the different frequency components to vary with the time at which each component is inverted by the second π pulse; however, this is predictable and the zero times can easily be corrected to occur at the same time.

Laser excitation was performed at 512 nm for molecule **3** and 532 nm for molecules **1** and **2**, at 2 mJ per pulse in all cases.

DFT calculations

Initial geometries for molecules **1**, **2** and **3** were built based on previous DFT calculations[72] and XRD studies,[98] using *UCSF Chimera*.[113] Geometry optimisations and spin density calculations were performed *in vacuo* using *Gaussian 16* (revision A.03).[96] Ground-state geometry optimisations were carried out in the doublet spin state using the PBE1PBE functional and the 6-31g(d) basis set. The halogen atoms of the chromophores were replaced by hydrogens to speed up the calculation. The electronic spin densities on the nitroxide radical were obtained by single-point calculation using the BP86 functional and the Def2-SVP basis set. The geometries of the chromophores were subsequently optimised in the triplet state to obtain the electronic spin densities, taken as atomic Mulliken spin densities, and the magnetic tensor orientations. These calculations were performed in *Gaussian* (B3LYP, Def2-SVP) for TPP, and in *Orca*[108] (release version 4.2.0) (BP86, Def2-SVP for H, C, N and O; Def2-TZVP for I) for EB and I_2BODIPY. The resolution of identity (RI) approximation, with the auxiliary basis set def2/J, was used in the latter cases.

Orientation-dependent analysis

For molecule **3**, the *OriDEERsim* algorithm[38] was modified to incorporate the ZFS-tensor of the triplet and it was used to simulate both the orientation-selective LiDEER and ReLaserIMD experiments. In the case of the ReLaser-IMD experiments, the bandwidth of the pump pulse was set to be infinite, reflecting the fact that the light pulse used in these experiments was non-selective. A library of pre-simulated ReLaserIMD traces was fitted to the experimental data following the protocol described in Section 1.4.5.[97] 200 least-squares fitting iterations were performed. The best-fitting relative position of the two centres from the ReLaserIMD simulation was used as a starting point for the LiDEER simulation, which allowed the orientation of the ZFS-tensor on the porphyrin to be determined. The number of least

squares fitting iterations matched the number of contributions of the dominant conformer to the fit obtained for the ReLaserIMD data sets. The following spin Hamiltonian parameters were used to generate the TPP triplet spectrum for the simulations: D = 41.4 mT, E = -8.4 mT, H-strain = 3.8 mT, g = 2.0059, Gaussian linewidth = 0.7 mT and triplet state sub-level populations $p_x = 0.32$, $p_y = 0.46$ and $p_z = 0.23$. The nitroxide was simulated using the following parameters: g = [2.0101, 2.0071, 2.0034], A_N = [0.4573, 0.7019, 3.6418] mT, H-strain = [0.5636, 0.4955, 0.7120] mT.

In the case of molecule **1**, for the model-based fit, an initial model consisting of a cone of 1200 dipolar vectors around the DFT-optimised geometry was generated ($\Delta\theta = \Delta\phi = 30°$, $\Delta r = 0.2$ nm) and the corresponding dipolar traces at the 5 different field positions were simulated considering the spin density of the EB triplet to be concentrated at a single point in space in the centre of the chromophore. The 20 dipolar vectors found to give the largest contributions to this first fit were then selected to generate a second model, where the spin delocalisation of the triplet and orientation of the EB moiety with respect to the nitroxide were considered. The orientation of the EB moiety with respect to the nitroxide was varied by $\Delta\alpha = \Delta\beta = \Delta\gamma = 45°$, where α, β and γ are the Euler angles defining the orientation of the ZFS-tensor frame of the EB triplet with respect to the g-tensor frame of the nitroxide radical. The electron spin delocalisation in the EB triplet state was included as calculated by DFT. For the model-free fit, one quarter of a spherical shell of $\Delta r = 0.5$ nm around $r = 1.9$ nm, containing 5115 dipolar vectors, was used to simulate the library of dipolar traces, again considering the spin density of the EB triplet to be concentrated at the centre of the chromophore. A total of 50 least-squares fitting iterations was sufficient to reach convergence of the RMSD from the experimental data in all the cases.

For molecule **2**, the model-based fit used an initial model consisting of a cone of 1000 dipolar vectors around the DFT-optimised geometry ($\Delta\theta = \Delta\phi = 30°$, $\Delta r = 0.2$ nm), where the orientation of the chromophore was varied with $\Delta\alpha = \Delta\beta = \Delta\gamma = 20°$). The corresponding dipolar traces at

the 9 different field positions were simulated taking into account the spin density delocalisation in the I_2BODIPY triplet as calculated by DFT. A second library of dipolar traces was calculated from a finer set of 1000 dipolar vectors around the best fitting structure of the first model ($\Delta\theta = \Delta\phi = 15°$, $\Delta r = 0.2$ nm, $\Delta\alpha = \Delta\beta = \Delta\gamma = 10°$), and it was used to fit the experimental data again. For the model-free fit, a set of 10000 dipolar vectors over one quarter of a spherical shell of $r = 1.8$ nm with $\Delta r = \pm 1$ nm were employed to simulate the library of dipolar traces used for the fit to the experimental data, and all the electron spin density of the I_2BODIPY triplet was considered to be concentrated at the centre of the chromophore, whose orientation was kept constant. A total of 50 least-squares fitting iterations was sufficient to reach convergence of the RMSD from the experimental data in all cases.

The spin Hamiltonian parameters used for the simulation of the triplet and nitroxide spectra of molecules **1** and **2** are reported in Figures 2.11 and 2.12.

Chapter 3

Light-induced triplet-triplet electron resonance (LITTER) spectroscopy

Light-induced pulsed dipolar spectroscopy (LiPDS) techniques reported so far are limited to the measurement of the dipolar interaction between a permanent paramagnetic centre and a transient triplet state, and cannot access dipolar interactions between two photogenerated spin centres. Detection of dipolar interactions between two light-activated paramagnetic centres would afford the possibility of measuring distances in macromolecules, containing suitable chromophores, which are ESR silent, and thus undetectable, in their ground states.

This chapter goes a step further in LiPDS methodology to tackle the challenge of measuring the dipolar interaction between two photogenerated triplet states, therefore removing the need for having any permanent spin centre in order to perform PDS. A new LiPDS technique is developed for this purpose, light-induced triplet-triplet electron resonance (LITTER) spectroscopy, which combines the concepts of both LiDEER and LaserIMD to use photogenerated triplet states for both detection and pump. Proof-of-concept

experiments on a bis-porphyrin-labelled model peptide are initially presented, followed by an in-depth conformational study performed on a spectroscopic molecular ruler exploiting the orientational effects in this new technique. LITTER is also compared to conventional DEER spectroscopy. To demonstrate the applicability of this novel technique to real structure determination problems, studies of a dimeric heme protein and a supramolecular porphyrin tetramer are presented. Finally, an analytical description of the pulsed experiment is provided and the factors limiting the performance of the technique are identified and discussed.

3.1 Development of the technique

This section has been adapted from the following publication:[114]

A. Bertran, K. B. Henbest, M. De Zotti, M. Gobbo, C. R. Timmel, M. Di Valentin and A. M. Bowen, *J. Phys. Chem. Lett.*, 2021, **12**, 80–85.

The molecules used for this study were supplied by Prof. Marta de Zotti and Prof. Marina Gobbo (University of Padova, Italy).

This section presents a new LiPDS technique, LITTER, which enables the measurement of the dipolar interaction between two photogenerated triplet states and the determination of the distance distribution between the two triplet-bearing moieties. This technique removes the restriction of having to use a permanent paramagnetic centre in LiDEER, (Re)LaserIMD, and LiRIDME. LITTER combines the advantages of both LiDEER and LaserIMD: the detection of a spin-polarised triplet state formed by an initial laser pulse, the use of the short Hahn-echo detection sequence, and the unlimited pump bandwidth afforded by using a second variable time laser pulse to form the second triplet (Figure 3.1 (a)). The second laser pulse switches

on the dipolar interaction and gives rise to a time-dependent modulation of the primary echo intensity (Figure 3.1 (b)). Experimentally, this is realised by coupling two pulsed lasers to the ESR cavity: laser 1, delivered *via* direct beam path through the optical window of the cavity and used to form the first triplet for detection, and laser 2, delivered *via* an optical fibre directly inserted in the sample tube from the top and used to form the second triplet for pumping (Figure 3.1 (c)). The two laser sources are synchronised with the ESR spectrometer using an external pulse delay generator. The experimental setup is described in more detail in Appendix I.

3.1.1 Characterisation of the model system

The novel LITTER experiment was tested on a bis-porphyrin model peptide (**1**, Figures 3.3 and 3.5). DFT optimisations identified a most stable *bent* conformation of **1** and a less stable *extended* conformation, interconverted through bond rotation of the N-terminal amino acid of the peptide backbone (Figure 3.2). The photoexcitation of both porphyrin moieties in the molecule was performed at 512 nm, corresponding to the most intense absorption maximum of the TPP Q-band (Figure 3.4 (a)). Illumination on the Soret band (around 410 nm), although potentially more efficient, would excite the $S_0 \rightarrow S_2$ transition, increasing the risk of photodegradation. The ESR spectrum and spin relaxation properties of the porphyrin photogenerated triplet state in **1** are in good agreement with reported values for other porphyrin-containing peptides in similar conditions (Figure 3.4 (b-d)).[58,72]

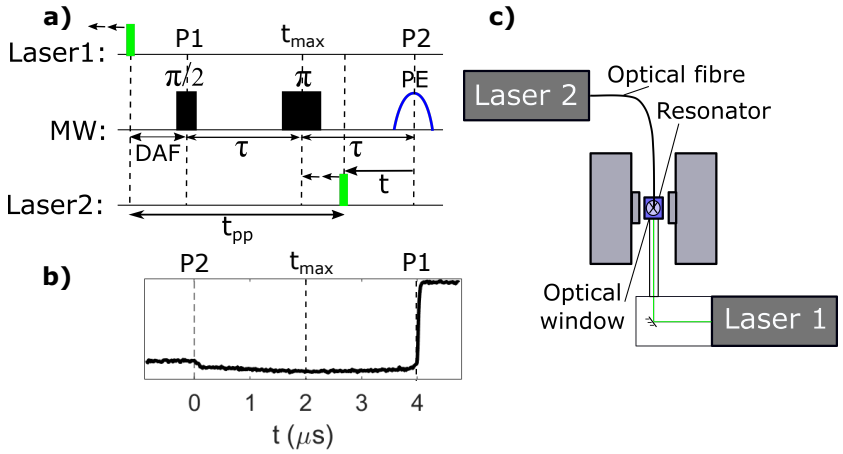


Figure 3.1: The LITTER experiment. (a) Pulse sequence and (b) spin-echo intensity time trace (in arbitrary units) for the bis-porphyrin model system TPP–Ala–$[(\alpha\,\mathrm{Me})\mathrm{Val}]_4$–NH–$C_6H_{10}$–NH–TPP [**1**] (see Figure 3.5 for the molecular structure). At $t = 0$ (P2), laser 2 crosses the primary echo (PE). When $t > 0$, a drop in the echo intensity occurs due to the change in the local magnetic field on the detection triplet caused by the formation of the second triplet during the free evolution time. At $t = 2$ μs (t_{max}, maximum free evolution time), laser 2 crosses the π pulse, which corresponds to the minimum in the time trace. Finally, at $t = 4$ μs (P1), laser 2 crosses the $\frac{\pi}{2}$ pulse, so when $t > 4$ μs, the triplet spins formed by both lasers are fully refocused at the PE, leading to an increase in signal intensity and the disappearance of modulation. The time delay between the two laser flashes (t_{pp}) is kept constant throughout the experiment, while the delay after flash (DAF) is increased stepwise. (c) Schematic diagram of the experimental setup. The experiment is achieved by synchronising two laser sources with the pulse ESR spectrometer via delay pulse generators. *Reprinted (adapted) with permission from Bertran, A., Henbest, K. B., De Zotti, M., Gobbo, M., Timmel, C. R., Di Valentin, M. and Bowen, A. M. Light-Induced Triplet-Triplet Electron Resonance spectroscopy. J. Phys. Chem. Lett., 2021, 12(1), 80–85. doi:10.1021/acs.jpclett.0c02884. Copyright 2021 American Chemical Society.*[114]

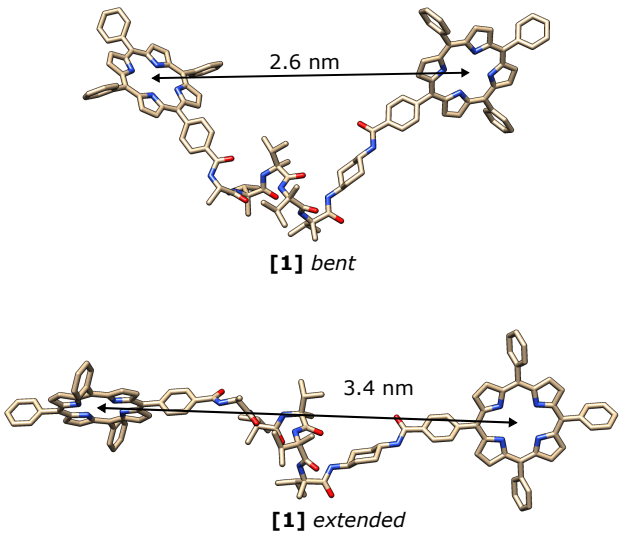


Figure 3.2: Ground state optimised geometries of the two local energy minima of [**1**], calculated using *Gaussian*[96] (PBE1PBE, 6-31g(d)). (top) **1** *bent* conformer (most stable), and (bottom) **1** *extended* conformer, with centre-to-centre inter-porphyrin distances of 2.6 nm and 3.4 nm, respectively. The calculated energy difference between the two geometries is 0.84 kJ/mol. *Reprinted (adapted) with permission from Bertran, A., Henbest, K. B., De Zotti, M., Gobbo, M., Timmel, C. R., Di Valentin, M. and Bowen, A. M. Light-Induced Triplet-Triplet Electron Resonance spectroscopy. J. Phys. Chem. Lett., 2021, 12(1), 80–85. doi:10.1021/acs.jpclett.0c02884. Copyright 2021 American Chemical Society.*[114]

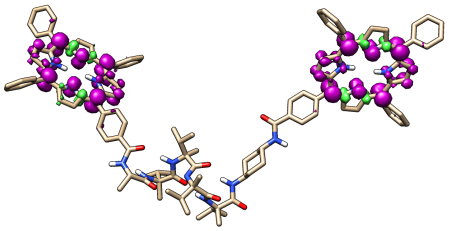


Figure 3.3: Electronic spin density in the DFT-optimised **1** *bent* conformer, where both TPP moieties are in the first triplet state, calculated using *Gaussian*[96] (B3LYP, Def2-SVP). *Reprinted (adapted) with permission from Bertran, A., Henbest, K. B., De Zotti, M., Gobbo, M., Timmel, C. R., Di Valentin, M. and Bowen, A. M. Light-Induced Triplet-Triplet Electron Resonance spectroscopy. J. Phys. Chem. Lett., 2021, 12(1), 80–85. doi:10.1021/acs.jpclett.0c02884. Copyright 2021 American Chemical Society.*[114]

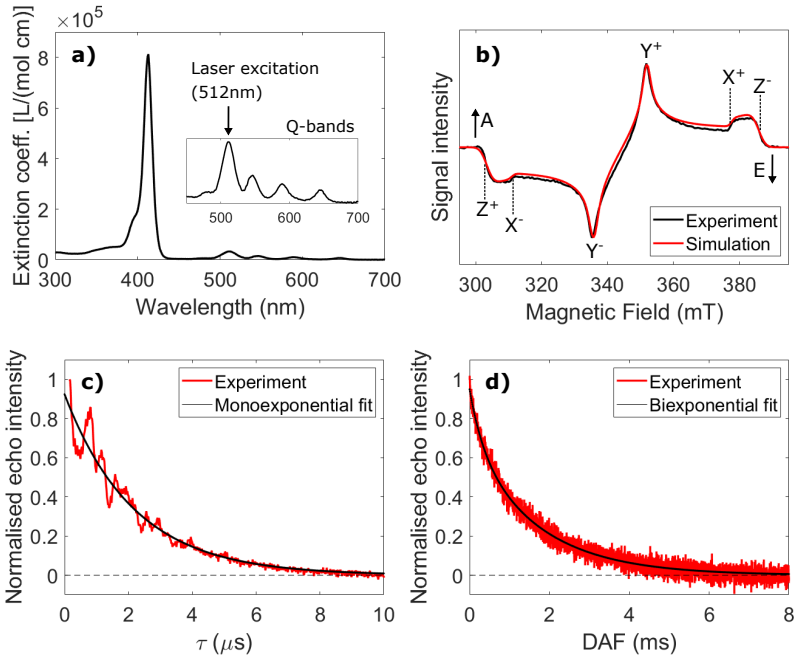


Figure 3.4: Spectroscopic characterisation of **1**. (a) Room-temperature optical absorption spectrum in a mixture of 98 % d_4-methanol and 2 % D_2O. (inset) Zoom in the porphyrin Q-bands, indicating the laser excitation wavelength used for the LITTER experiment, corresponding to the most intense maximum of the Q-band region. (b) trESR spectrum measured at 20 K after laser flash (black) and simulation (red) using *EasySpin pepper* function[109] with the following spin Hamiltonian parameters: D = 41.4 mT, E = -8.4 mT, D-strain = 3.8 mT, E-strain = 0.0 mT, g = 2.006, Gaussian linewidth = 0.7 mT, p_x = 0.32, p_y = 0.46 and p_z = 0.23. The turning points, corresponding to the canonical orientations of the anisotropic ZFS tensor, are labelled (Z^+, X^-, Y^-, Y^+, X^+ and Z^-, from left to right) and the absorptive (A) and emissive (E) parts of the spectrum are indicated. (c) Phase-memory experiment measured at 20 K (red) and corresponding monoexponential fit (black) with a T_m value of (2.15 ± 0.05) μs. (d) DAF experiment measured at 20 K (red) and corresponding biexponential fit (black) with lifetimes of (0.34 ± 0.04) ms and (1.68 ± 0.03) ms for the two exponentials. *Reprinted (adapted) with permission from Bertran, A., Henbest, K. B., De Zotti, M., Gobbo, M., Timmel, C. R., Di Valentin, M. and Bowen, A. M. Light-Induced Triplet-Triplet Electron Resonance spectroscopy. J. Phys. Chem. Lett., 2021, 12(1), 80–85. doi:10.1021/acs.jpclett.0c02884. Copyright 2021 American Chemical Society.*[114]

3.1.2 Proof-of-concept experiments

The LITTER trace recorded for bis-porphyrin **1** was compared to a LITTER trace recorded using the same experimental settings but with the single-porphyrin peptide **2** as a control (Figure 3.5, black). The trace of system **2** did not show a modulation and displayed only a slow decay. This background decay results from the combination of longitudinal relaxation from the nascent non-Boltzmann population, decay of the triplet state, and intermolecular dipolar interactions. The absence of modulation in **2** proves that the effect observed in **1** is due to the intramolecular dipolar interaction between the two photogenerated triplet states.

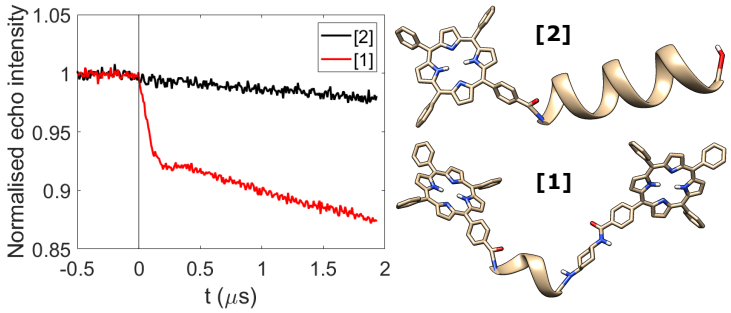


Figure 3.5: LITTER traces (left) for the bis-porphyrin peptide model system TPP–Ala–$[(\alpha\,\mathrm{Me})\mathrm{Val}]_4$–NH–$C_6H_{10}$–NH–TPP **1** (red) and the single-porphyrin peptide TPP–$(\mathrm{Ala–Aib})_6$–Ala–OH **2** used as control (black). Amino acid key: Ala (L-alanine), (αMe)Val (L-α-methyl valine), and Aib (α-aminoisobutyric acid). The external magnetic field was set to the emissive maximum of the photogenerated triplet spectrum, and only the first half of the LITTER trace was recorded. Lowest-energy geometries (right) of molecules **1** and **2** optimised by DFT, with an expected distance between the centres of the two porphyrins in **1** of 2.6 nm. *Reprinted (adapted) with permission from Bertran, A., Henbest, K. B., De Zotti, M., Gobbo, M., Timmel, C. R., Di Valentin, M. and Bowen, A. M. Light-Induced Triplet-Triplet Electron Resonance spectroscopy. J. Phys. Chem. Lett., 2021, 12(1), 80–85. doi:10.1021/acs.jpclett.0c02884. Copyright 2021 American Chemical Society.*[114]

The ZFS-tensor for a TPP triplet is significantly anisotropic and the limited excitation bandwidth of the MW detection pulses can lead to orientation selection, as discussed in Chapter 2. LITTER traces (Figure 3.6 (b))

acquired on the turning points of the photogenerated triplet state spectrum corresponding to the Y^- and Z^- canonical orientations of the ZFS-tensor (Figure 3.6 (a)) demonstrate significant orientational effects. An orientation-independent analysis by Tikhonov regularisation yielded apparent distance distributions (Figure 3.6 (d)). These distributions show some agreement with the DFT-optimised structures of **1** *bent* and **1** *extended* conformers, with centre-to-centre interporphyrin distances of 2.6 and 3.4 nm, respectively (Figure 3.2). To determine if either of these models is consistent with both Y^- and Z^- LITTER data sets, it was necessary to perform orientation-dependent simulations considering the ZFS anisotropy in combination with orientation selection of the detection MW pulses.

Orientation-dependent LITTER simulations were carried out using a modified form of the *OriDEERsim* algorithm described in Section 1.4.5. The simulation with the model **1** *bent* conformation yielded good fits to both Y^- and Z^- LITTER data sets (Figure 3.7 (b)), with the positions of the pump spin centres contributing to the simulated form factors reasonably distributed around the geometry of minimum energy (Figure 3.7 (a)). The relative orientation of the pump spin centre with respect to the dipolar vector was found to have a negligible effect on the results of the simulation, as expected from the effectively infinite spin excitation bandwidth of the laser pump pulse and the lack of polarisation in laser 2. The resulting spin-spin distance distribution was in good agreement with that obtained from the orientation-independent analysis of the Y^- dataset (Figure 3.7 (c)), showing that the longer spin-spin distances obtained from Z^- were indeed an orientational artefact.

The results of the analogous simulation with the model **1** *extended* conformation did not fit the experimental LITTER data sets (Figure 3.8), which indicated that this conformer was not the dominant conformer in frozen d_6-ethanol solution. This conclusion was reaffirmed by the results of a third simulation considering both **1** *bent* and **1** *extended* models simultaneously, which yielded positions of the pump spin centre clustered around the **1** *bent* conformation (Figure 3.9).

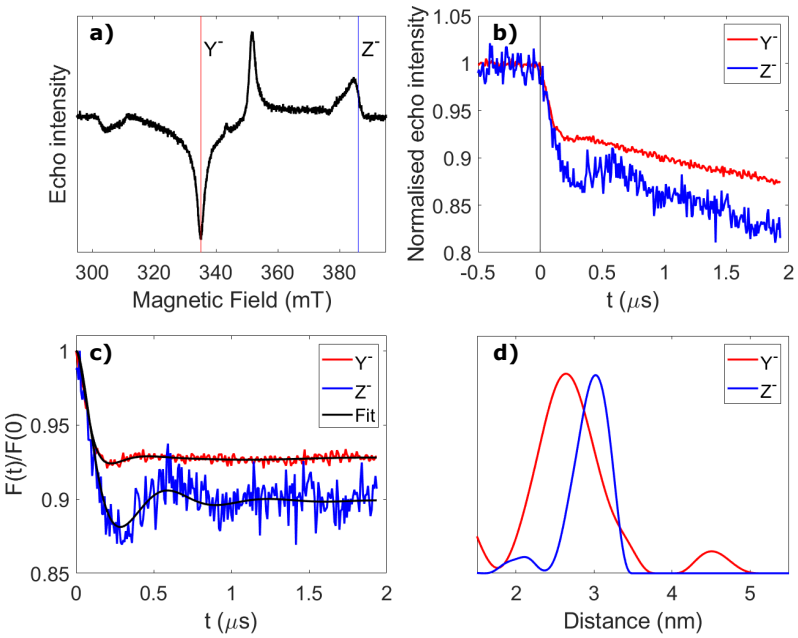


Figure 3.6: LITTER results for molecule **1** measured on Y^- and Z^-. (a) Echo-detected field-swept spectrum after photoexcitation at 512 nm, showing the Y^- (red) and Z^- (blue) turning points. (b) Raw LITTER traces. (c) Form factors with the corresponding fits obtained with by Tikhonov regularisation using *DeerAnalysis*,[110] showing modulation depths of 8% and 13%. (d) Resulting spin-spin distance distributions, with maxima at 2.7 nm (red) and 3.0 nm (blue). *Reprinted (adapted) with permission from Bertran, A., Henbest, K. B., De Zotti, M., Gobbo, M., Timmel, C. R., Di Valentin, M. and Bowen, A. M. Light-Induced Triplet-Triplet Electron Resonance spectroscopy. J. Phys. Chem. Lett., 2021, 12(1), 80–85. doi:10.1021/acs.jpclett.0c02884. Copyright 2021 American Chemical Society.*[114]

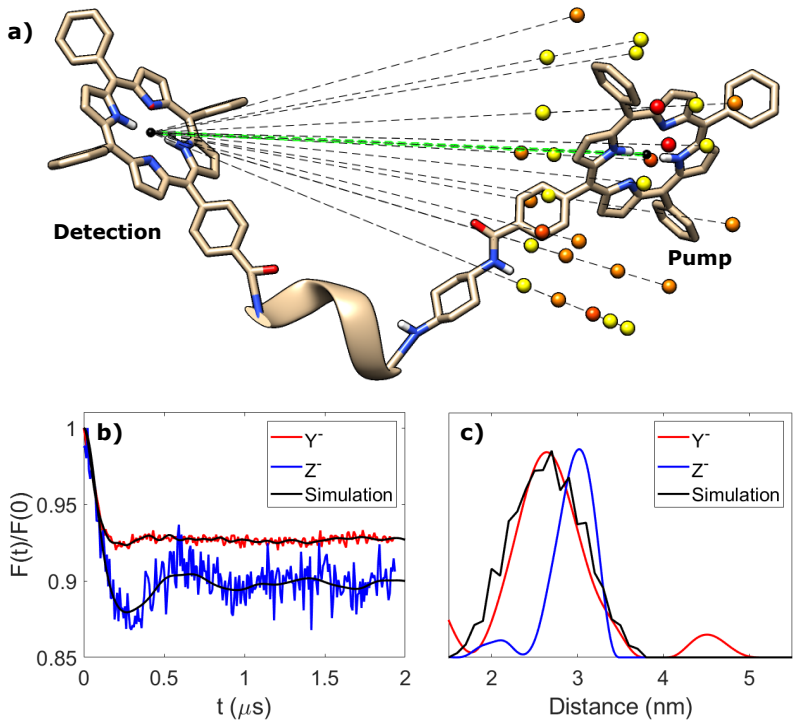


Figure 3.7: Orientation-dependent LITTER simulation for the **1** *bent* conformer. (a) DFT-optimised geometry with the different positions of the pump spin centre contributing to the simulated form factor shown as spheres representing the centres of the corresponding porphyrins. The relative weight of each pump position in the simulated form factor is represented by the colour of the sphere (yellow, 1; orange, 2; dark orange, 3; red, 4). The dipolar vector between the centres of the two porphyrins of the DFT-optimised geometry is highlighted in green. (b) Form factors obtained experimentally (red and blue) and from orientation-dependent simulation fits (black). (c) Spin-spin distance distributions obtained using *DeerAnalysis* (red and blue) and from orientation-dependent simulations (black). *Reprinted (adapted) with permission from Bertran, A., Henbest, K. B., De Zotti, M., Gobbo, M., Timmel, C. R., Di Valentin, M. and Bowen, A. M. Light-Induced Triplet-Triplet Electron Resonance spectroscopy. J. Phys. Chem. Lett., 2021, 12(1), 80–85. doi:10.1021/acs.jpclett.0c02884. Copyright 2021 American Chemical Society.*[114]

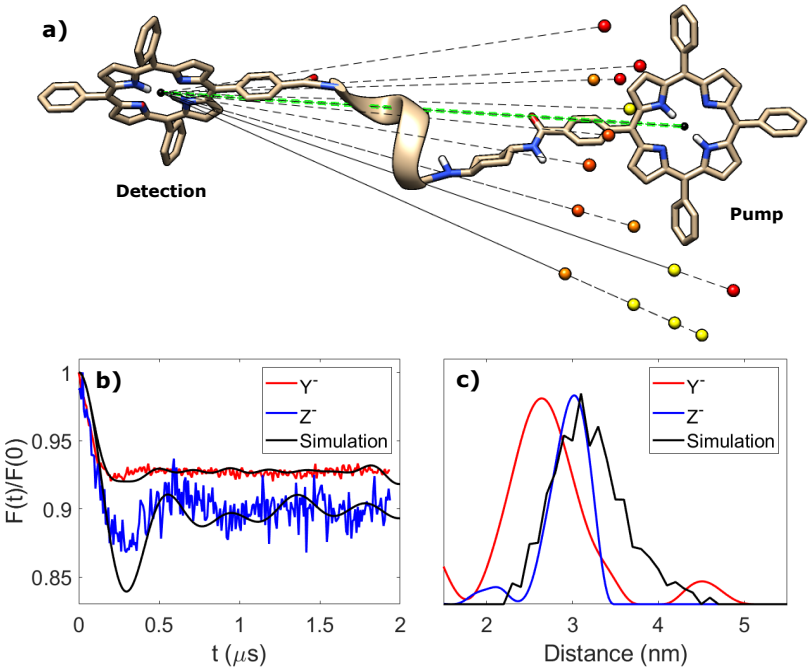


Figure 3.8: Orientation-dependent LITTER simulation for **1** *extended* conformer. (a) DFT-optimised geometry with the different positions of the pump spin centre contributing to the simulated form factor shown as spheres representing the centres of the corresponding porphyrins. The relative weight of each pump position in the simulated form factor is represented by the colour of the sphere (yellow = 1, orange = 2, dark orange = 3 and red = 4). The dipolar vector between the centres of the two porphyrins of the DFT-optimised geometry is highlighted in green. (b) Form factors obtained experimentally (red and blue) and from orientation-dependent simulation fits (black). (c) Spin-spin distance distributions obtained using *DeerAnalysis*[110] (red and blue) and from orientation-dependent simulations (black). *Reprinted (adapted) with permission from Bertran, A., Henbest, K. B., De Zotti, M., Gobbo, M., Timmel, C. R., Di Valentin, M. and Bowen, A. M. Light-Induced Triplet-Triplet Electron Resonance spectroscopy. J. Phys. Chem. Lett., 2021, 12(1), 80–85. doi:10.1021/acs.jpclett.0c02884. Copyright 2021 American Chemical Society.*[114]

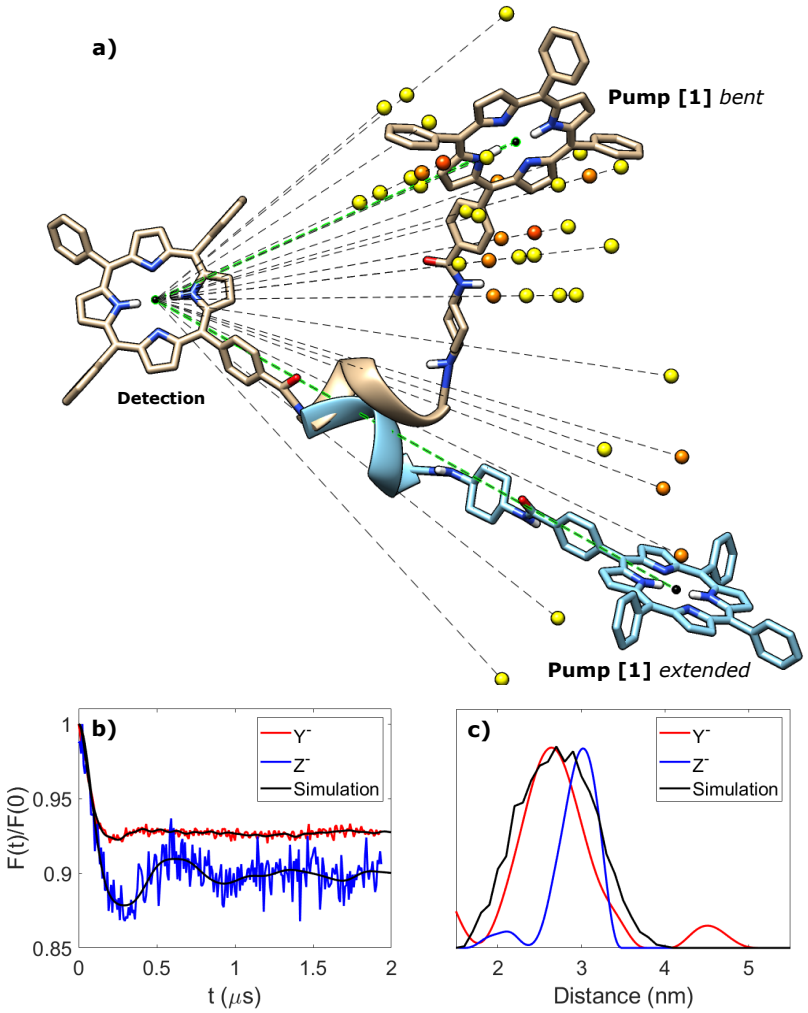


Figure 3.9: Orientation dependent LITTER simulation considering both **1** *bent* and **1** *extended* conformers simultaneously. (a) DFT-optimised geometries of **1** bent (brown) and **1** extended (blue), with the different positions of the pump spin centre contributing to the simulated form factor shown as spheres representing the centres of the corresponding porphyrins. The relative weight of each pump position in the simulated form factor is represented by the colour of the sphere (yellow = 1, orange = 2 and dark orange = 3). The dipolar vector between the centres of the two porphyrins of the DFT-optimised geometries is highlighted in green. (b) Form factors obtained experimentally (red and blue) and from orientation-dependent simulations (black). (c) Spin-spin distance distributions obtained using *DeerAnalysis*[110] (red and blue) and from orientation-dependent simulations (black). *Reprinted (adapted) with permission from Bertran, A., Henbest, K. B., De Zotti, M., Gobbo, M., Timmel, C. R., Di Valentin, M. and Bowen, A. M. Light-Induced Triplet-Triplet Electron Resonance spectroscopy. J. Phys. Chem. Lett., 2021, 12(1), 80–85. doi:10.1021/acs.jpclett.0c02884. Copyright 2021 American Chemical Society.*[114]

The prevalence of the more stable **1** *bent* conformer in frozen solution is consistent with the energetics of *bent-extended* interconversion obtained by DFT (Figure 3.10, dihedral A (blue)), with an energy barrier (10.7 kJ/mol) much larger than the thermal energy at room temperature (2.5 kJ/mol). Major rotations of the porphyrin moieties with respect to the rest of the molecule are expected to be energetically unfavourable (Figure 3.10, dihedrals B (green) and C (red)), suggesting that the distribution of pump spin centre positions may originate mainly from the flexibility of the peptide spacer. This also suggests that the synthesis of **1** did not produce other significantly different conformers of the molecule, such as those with the axially-substituted 1,4-diaminocyclohexane linker or with non-α-helical peptide backbones, expected to be less energetically stable.

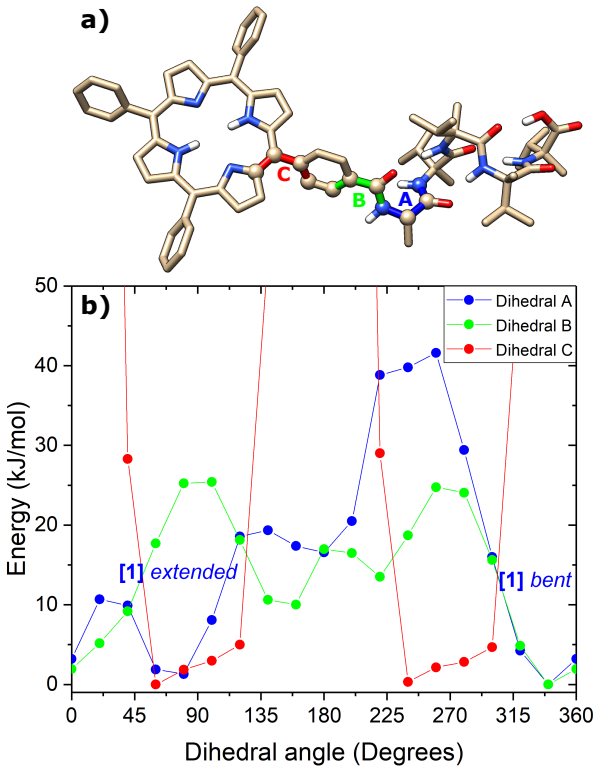


Figure 3.10: Energetics of bond rotation in **1**. (a) Structure of **1** *bent* conformer, where the second porphyrin has been omitted for clarity. The bonds defining the three dihedral angles studied are indicated as 'A' (blue, rotation around the $C_{\alpha}-C_{amide}$ bond of the Ala, corresponding to the conversion between the bent and extended conformers), 'B' (green, rotation around the $C_{phenyl}-C_{amide}$ bond) and 'C' (red, rotation around the $C_{porphyrin}-C_{phenyl}$ bond). (b) Energy profiles of the rotation around the aforementioned bonds, calculated using *Gaussian*[96] (PBE1PBE, 6-31g(d)). The two energy minima in the profile for dihedral A (blue) corresponding to the **1** *bent* and **1** *extended* conformers are indicated, with an energy barrier of interconversion of 11 kJ/mol. The absolute minimum of each energy profile has been assigned an energy of 0 kJ/mol. *Reprinted (adapted) with permission from Bertran, A., Henbest, K. B., De Zotti, M., Gobbo, M., Timmel, C. R., Di Valentin, M. and Bowen, A. M. Light-Induced Triplet-Triplet Electron Resonance spectroscopy. J. Phys. Chem. Lett., 2021, 12(1), 80–85. doi:10.1021/acs.jpclett.0c02884. Copyright 2021 American Chemical Society.*[114]

3.1.3 Optimisation of experimental conditions

The effects of laser pulse energy on signal intensity and modulation depth were studied (Figure 3.11). Higher laser 1 energies improved signal intensity (Figure 3.11 (a)), in consistence with the formation of more triplet spins before the Hahn-echo sequence, but the signal was nearly saturated at 2 mJ. However, they did not cause any effective change in modulation depth (Figure 3.11 (b)) as expected, therefore yielding better modulation-to-noise ratio (MNR) values at higher energies, calculated as the modulation depth relative to the noise level at the end of the trace. Higher laser 2 energies clearly improved modulation depth (Figure 3.11 (d)), as expected from more triplet spins being formed during the Hahn-echo sequence, but had a negative effect on signal intensity (Figure 3.11 (c)). Two different factors seem to be contributing to the observed decrease in signal intensity at high laser 2 energies. First, the shorter T_m due to the formation of more triplets by laser 2 (Figure 3.12). Second, the incomplete decay of the photogenerated triplets back to the ground state due to the TPP triplet lifetime at cryogenic temperatures being comparable to the shot-to-shot repetition time (50 ms) used in the LITTER experiment, which becomes more important when larger numbers of triplet states are formed by larger laser energies. That would also be consistent with the non-linearity in the laser 1 energy dependence of the signal intensity (Figure 3.11 (a)). The sample was aerated in an attempt to increase signal intensity by reducing triplet lifetime. The signal was indeed slightly increased for very short τ values, but the improvement was lost for the $\tau \sim 2$ μs of the LITTER experiment, due to the reduction of T_m caused by the presence of paramagnetic oxygen.

The importance of a good overlap volume between the two laser beams for modulation depth was studied by changing the sample position and concentration (Figure 3.13). In the optimised setup, the 5 mm-high sample is centred in the resonator and laser 1 is focused in a ~ 1 mm spot on the centre of the sample (Figure 3.14). The sample above the volume excited by laser 1 absorbs light from laser 2 but does not contribute to the signal, reducing the

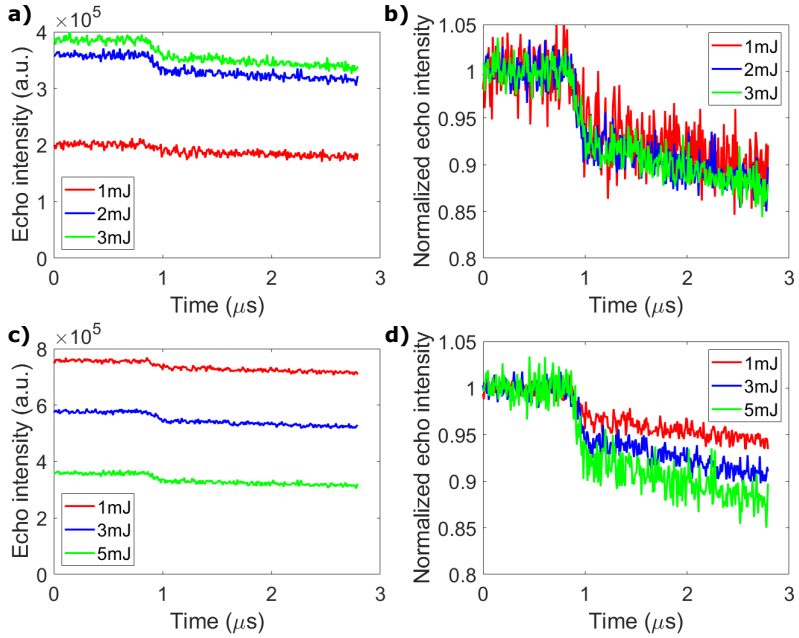


Figure 3.11: Laser energy studies. (a, b) LITTER traces on **1** measured on Y^- with a laser 2 energy of 5 mJ per pulse and laser 1 energies of 1 mJ (red), 2 mJ (blue) and 3 mJ (green) per pulse. (c, d) LITTER traces measured with a laser 1 energy of 2 mJ per pulse and laser 2 energies of 1 mJ (red), 3 mJ (blue) and 5 mJ (green) per pulse. The data in (b) and (d) has been normalised to the start of the traces. The lower SNR compared to the traces presented in Figures 3.5 and 3.6 is due to the shorter averaging times used for the optimisation studies. *Reprinted (adapted) with permission from Bertran, A., Henbest, K. B., De Zotti, M., Gobbo, M., Timmel, C. R., Di Valentin, M. and Bowen, A. M. Light-Induced Triplet-Triplet Electron Resonance spectroscopy. J. Phys. Chem. Lett., 2021, 12(1), 80–85. doi:10.1021/acs.jpclett.0c02884. Copyright 2021 American Chemical Society.*[114]

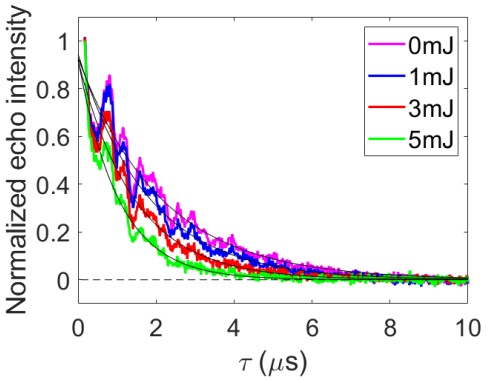


Figure 3.12: Phase-memory experiments on **1** at different laser 2 energies per flash: 0 mJ (magenta), 1 mJ (blue), 3 mJ (red) and 5 mJ (green), with the corresponding monoexponential fits. The energy of laser 1 was fixed to 3 mJ per pulse. Data has been normalised to the start of the traces. *Reprinted (adapted) with permission from Bertran, A., Henbest, K. B., De Zotti, M., Gobbo, M., Timmel, C. R., Di Valentin, M. and Bowen, A. M. Light-Induced Triplet-Triplet Electron Resonance spectroscopy. J. Phys. Chem. Lett., 2021, 12(1), 80–85. doi:10.1021/acs.jpclett.0c02884. Copyright 2021 American Chemical Society.*[114]

number of laser 2 photons that reach the overlap volume (therefore it will be called 'dead volume'). By pushing the sample tube further down into the resonator, the dead volume is reduced, leading to an increase in the number of laser 2 photons that reach the overlap volume and a corresponding increase in modulation depth (Figure 3.13 (b)), similar to the effect of increasing the energy of laser 2 (Figure 3.11 (d)). The decrease in signal intensity could be explained by a fraction of the laser 1 photons missing the sample, above the top.

Doubling the concentration of **1** from 40 μM to 80 μM in the optimised setup also doubled signal intensity because of twice as many molecules being photoexcited by laser 1 (Figure 3.13 (c)). However, this also intensified the attenuation of laser 2 due to the absorption of photons by the dead volume, leading to a significant decrease in modulation depth.

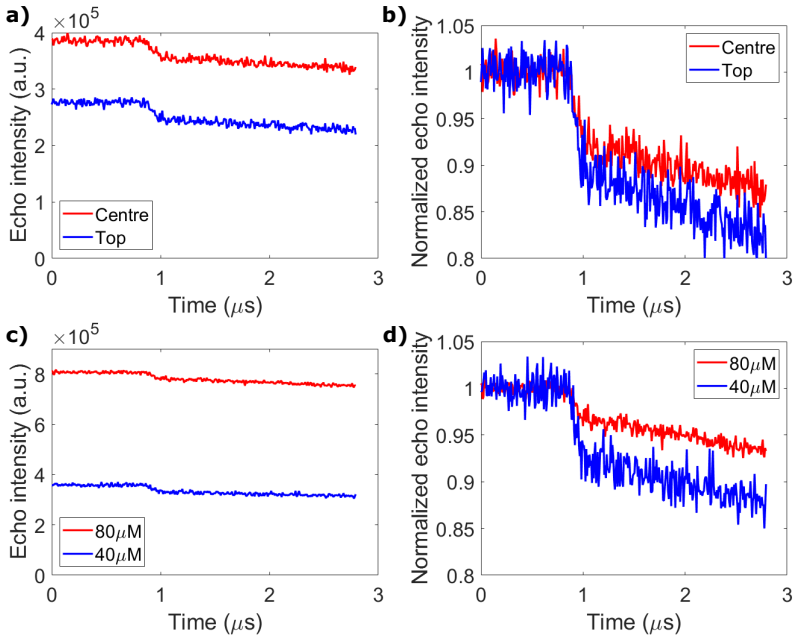


Figure 3.13: Sample position and concentration studies with **1**. (a, b) LITTER traces measured with the sample at two different positions, with laser 1 hitting the centre (red) and the top (blue) of the sample. Laser energies per pulse were 3 mJ (laser 1) and 5 mJ (laser 2). (c, d) LITTER traces for two different concentrations of molecule **1**: 80 μM (red) and 40 μM (blue). Laser energies per pulse were 2 mJ (laser 1) and 5 mJ (laser 2). The data in (b) and (d) has been normalised to the start of the traces. *Reprinted (adapted) with permission from Bertran, A., Henbest, K. B., De Zotti, M., Gobbo, M., Timmel, C. R., Di Valentin, M. and Bowen, A. M. Light-Induced Triplet-Triplet Electron Resonance spectroscopy. J. Phys. Chem. Lett., 2021, 12(1), 80–85. doi:10.1021/acs.jpclett.0c02884. Copyright 2021 American Chemical Society.*[114]

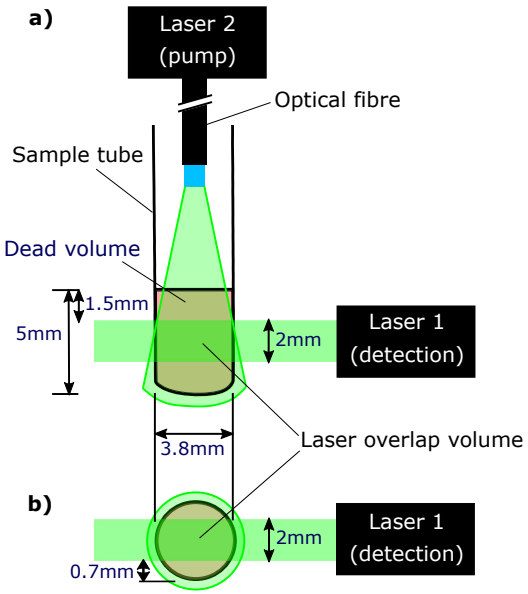


Figure 3.14: Geometry of the LITTER laser setup at the sample. (a) Side view and (b) top view. *Reprinted (adapted) with permission from Bertran, A., Barbon, A., Bowen, A. M., Di Valentin, M. in Advances in Biomolecular EPR, ed. R. D. Britt, Elsevier Inc., 1st edn., 2022, Methods in Enzymology vol. 666, ch. 7, pp. 171–231. doi:10.1016/bs.mie.2022.02.012. Copyright 2022 Elsevier.*[107]

3.1.4 Conclusions

This section has demonstrated that LITTER allows the measurement of the dipolar interaction between the photogenerated triplet states of two free-base porphyrin moieties separated by a short peptide spacer. The dipolar traces obtained showed strong orientation effects due to the large anisotropy in the ZFS-tensor of the photogenerated porphyrin triplet state, yielding different apparent distance distributions upon analysis by Tikhonov regularisation. Using orientation-dependent simulations complemented with DFT calculations, it has been possible to successfully describe these orientation effects and to obtain the real spin-spin distance distribution and information about the dominant conformation of the bis-porphyrin molecule in a frozen solution. The large anisotropy of the triplet state ZFS-tensor and the resulting strong orientation dependence of the LITTER experiment have the

potential to distinguish between small differences in the orientation of two chromophores in rigid systems. Although orientation dependence can also be observed in PDS of metal-containing systems,[27,38,40,47,115] photogenerated triplet states have proven to be superior for detection owing to their strong spin polarisation and more favourable relaxation properties.[72] Additionally, the single-frequency nature of LITTER removes the restriction of resonator bandwidth, which often prevents the complete exploitation of the orientation dependence in stable bis-radical systems. Finally, the origin of the orientation dependence is the ZFS, removing the need to use high field, which is often required for greater orientation resolution in spin-half paramagnetic centres.

LITTER removes the restriction, recurrent in all of the LiPDS techniques reported so far, of having to use one stable paramagnetic centre to perform distance measurements. By accessing the dipolar interaction between two photogenerated triplet states, LITTER has the potential to enable distance distributions and relative orientations to be obtained for unmodified macromolecular systems containing endogenous photoexcitable moieties, such as light-harvesting proteins, heme proteins and flavoproteins, or systems modified with several photoexcitable triplet spin labels. This technique could also be used in combination with Förster resonance energy transfer (FRET) spectroscopy if suitable photoexcitable moieties are chosen, exploiting the complementary features of the two techniques. It must be noted, however, that FRET requires chromophores with high fluorescence quantum yield and therefore low triplet quantum yield, while high triplet quantum yields and correspondingly low fluorescence yields are necessary for LITTER. Consequently, the combination of these two spectroscopic techniques using the same chromophores would require reaching a compromise allowing for the observation of reasonable fluorescence and triplet signals.

In a manner similar to that for FRET, which has found significant applications in cells,[116] the novel LITTER technique is a strong candidate for measuring structural information between chromophores in the cellular en-

vironment, using triplet states that can be photogenerated within cells.[117] Removing the need to have a permanent paramagnetic centre, such as nitroxide spin labels, which are known to be unstable and rapidly degraded inside cells,[118,119] is a key point for the success of in-cell structural studies and also mitigates the need to use more complex spin labels such as trityl radicals or gadolinium complexes.[120–122] Furthermore, the combination of LITTER with microscopy techniques might facilitate the observation of structural changes for a system in different parts of a cell, for instance, by using microscopy to pinpoint the location of the chromophores within the cell before using LITTER to probe structural parameters. Consequently, LITTER is an exciting new technique with the potential to cause a step change in the application of PDS to biological systems.

3.2 Conformational information from orientationally selective LITTER

This section has been adapted from the following publication:

A. Bertran, M. De Zotti, C. R. Timmel, M. Di Valentin and A. M. Bowen, *Chem. Eur. J.*, *under review.*

The molecules used for this study were supplied by Prof. Marta de Zotti (University of Padova, Italy).

In the proof-of-concept LITTER experiments presented in the previous section, two dipolar traces, acquired on the turning points of the photogenerated triplet state spectrum corresponding to the Y^- and Z^- canonical orientations of the ZFS-tensor, demonstrated significant orientational effects, and were analysed using orientation-dependent simulations to yield conformational information in good agreement with DFT predictions. However,

obtaining the complete orientational dependence of the dipolar interaction would require acquiring multiple LITTER traces spanning the full ESR spectrum of the porphyrin triplet state. In addition, in order to understand the general performance and limitations of LITTER, a molecular spectroscopic ruler study and a comparison to a well-established PDS technique, would need to be carried out.

In this section, an extensive orientational LITTER study of a series of bis-porphyrin synthetic model peptide systems with different porphyrin-porphyrin relative orientations and distances ranging between 2.1 and 3.6 nm is presented (Figure 3.15 (b, c)). Multiple orientationally selective traces were acquired at different parts of the porphyrin triplet ESR spectrum to capture with detail the information on the relative orientation of the ZFS tensor and the dipolar vector. The orientation-dependent analysis of these traces yields information on the conformation of the molecules in frozen solution which is in good agreement with the minimum energy geometries predicted by DFT. In addition, a direct comparison between LITTER and DEER is performed by introducing Cu(II) in the two porphyrins of one of the synthetic model peptides. Finally, an alternative treatment of the orientationally selective data is shown which consists in the averaging of the orientational effects in the dipolar traces to carry out a computationally faster orientation-independent analysis. The results of this analysis are compared to those obtained from the full orientation-dependent treatment.

3.2.1 Spectroscopic ruler study

This series of bis-labelled peptides **1**-**4** was designed so as to allow for a systematic variation of the distances and relative orientations between the two porphyrin moieties, thus providing a spectroscopic ruler (Figure 3.15 (b)). Molecule **3** here corresponds to the model system **1** used for the proof-of-concept experiments presented in Section 3.1. The [(α-Me)Val]n peptide backbone favours a rigid α-helical conformation, especially in polar solvents

such as ethanol, used in this study.[123] *In-vacuo* DFT optimisations support the α-helical conformation of the backbones of **2**, **3** and **4** and yield porphyrin-porphyrin centre-to-centre distances of 2.4, 2.6 and 3.6 nm (Figure 3.15 (c)). The peptide backbone of **1** is too short to form a full α-helical loop and is therefore expected to be more flexible, with a predicted porphyrin-porphyrin distance of 2.1 nm according to DFT optimisation.

LITTER for all four peptides was carried out at different positions across the ESR spectrum of the photogenerated TPP triplet state at X-band (Figure 3.16 (i)), in order to obtain orientation-resolved sets of dipolar traces (Figure 3.16 (ii)). The strong orientational effects, originating from the orientation selection of the narrow-bandwidth MW pulses in comparison to the large ZFS of the photogenerated TPP triplet state, are clear from the deep dipolar oscillations around Z^- compared to the very shallow oscillations around Y^-. It was not possible to acquire LITTER traces at X^- due to the negligible ESR intensity at this turning point. In addition, the significant difference in dipolar frequencies between molecules **2** and **3**, despite having very similar porphyrin-porphyrin distances, is another manifestation of the strong dependence of the dipolar interaction on the relative orientation of the dipolar vector and the ZFS-tensor of the detection spin centre in these experiments.

Orientation-dependent simulations were carried out as described in Section 3.1, using an orientation-dependent pre-simulated library of dipolar traces[38] to fit the experimental LITTER datasets in an iterative least-squares global fitting procedure[97] until convergence of the RMSD was achieved (Figure 3.16 (ii) black, see Figure 5.10 in Appendix II for RMSD plots). The molecular models used in the simulations were generated around the DFT-optimised geometries of the molecules and the electronic spin density delocalisation in the photogenerated TPP triplet state was included as calculated by DFT (Figure 3.3). The resulting distance distributions were generated from the conformations contributing to the best fit, as the weighted sum of pairwise distances between atoms bearing electronic spin density.

This orientation-dependent analysis yielded good fits to the experimental

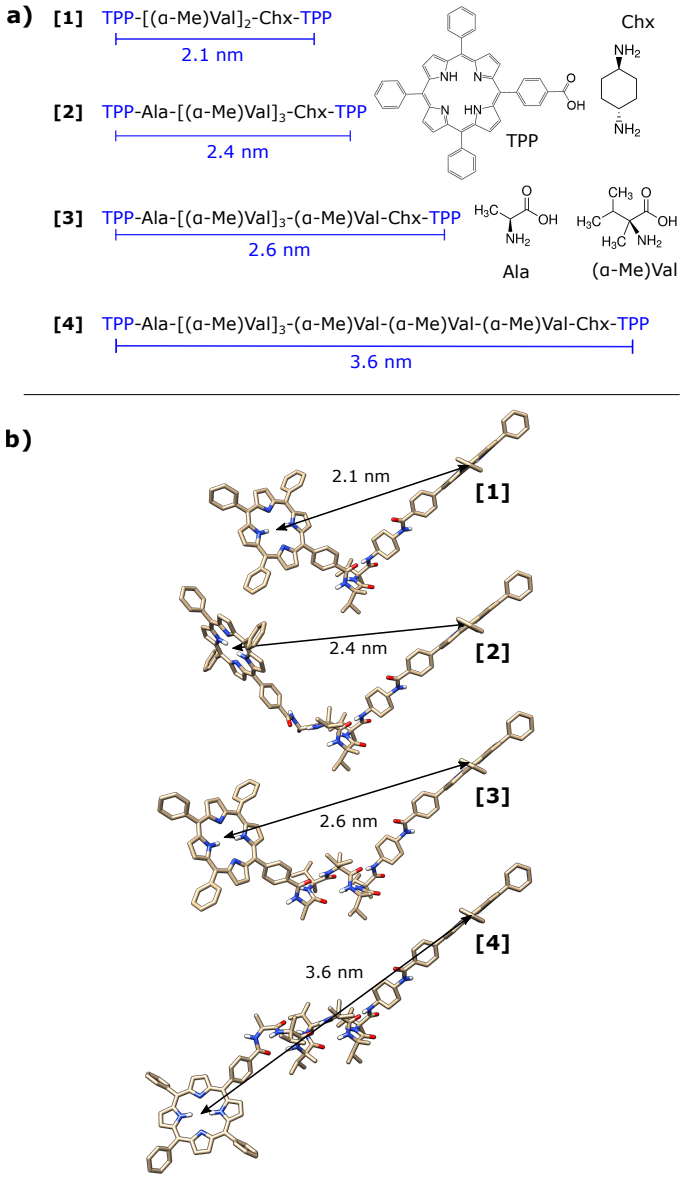


Figure 3.15: (a) Amino acid sequences for the bis-porphyrin synthetic model peptides used in this study, with the porphyrin-porphyrin distances predicted by DFT. The chemical structures of the different building blocks are shown on the right. Amino acid key: Ala (L-alanine), (αMe)Val (L-α-methyl valine) and Chx (*trans*-1,4-diaminocyclohexane). (b) *In-vacuo* DFT-optimised geometries of the molecules.

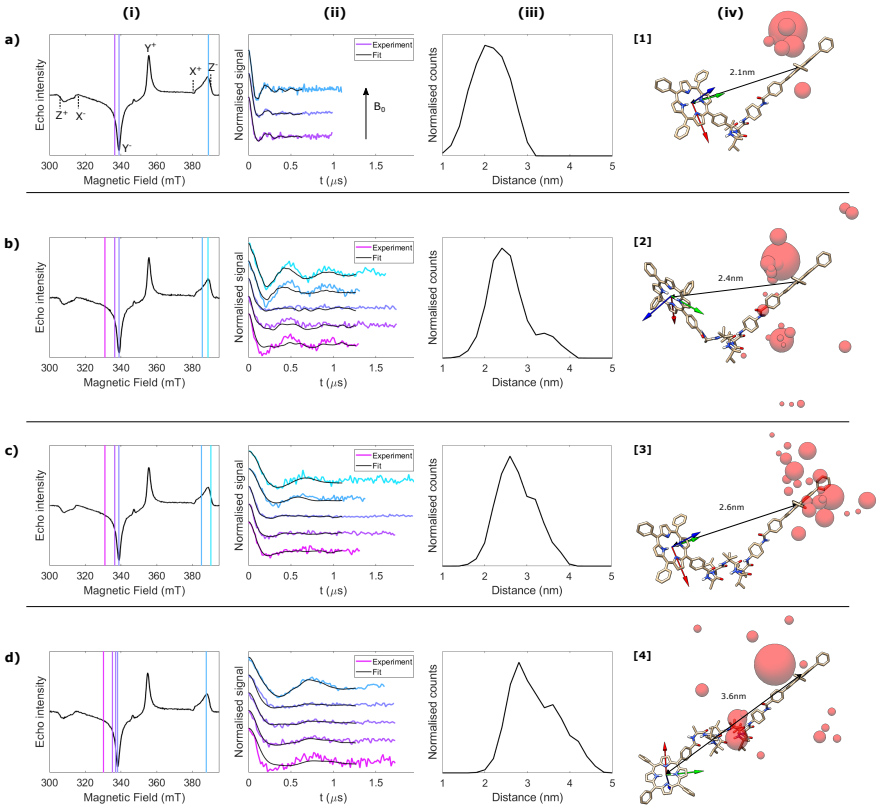


Figure 3.16: Orientational LITTER study of molecules (a) **1**, (b) **2**, (c) **3** and (d) **4** at X-band, 20 K. By columns: (i) Echo-detected field-swept ESR spectra of the molecules recorded after 512 nm laser excitation. The field positions used for LITTER are indicated with vertical lines. (ii) Background-corrected and modulation depth-normalised LITTER traces acquired at the different field positions (colour) and corresponding orientation-dependent fits (black). Modulation depths were $\sim 10\%$ before normalisation in all cases. (iii) Spin-spin distance distributions obtained from the orientation-dependent analysis. (iv) DFT-optimised geometries showing the different positions of the TPP centre most contributing to the fits as red spheres, relative to the ZFS-tensor frame of the other TPP triplet (arrows: red $= D_x$, green $= D_y$, blue $= D_z$). The diameter of the spheres is proportional to the number of times a single conformation contributes to the complete fit shown in panels (ii).

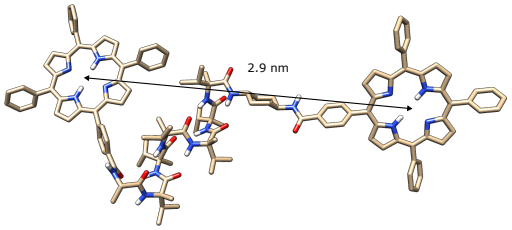


Figure 3.17: Higher local energy minimum conformation of **4** (+7 kJ/mol) identified by *in-vacuo* DFT (*Gaussian*, PBE1PBE, 6-31(g)) through the unwinding of the first amino acid of the α-helix at the N-terminus, leading to a shorter porphyrin–porphyrin distance of 2.9 nm.

LITTER datasets for all four molecules studied, successfully capturing the orientational effects in the dipolar traces (Figure 3.16 (ii)). The corresponding spin-spin distance distributions have their maxima in agreement with the DFT predictions for molecules **1**, **2** and **3** (Figure 3.16 (iii)), with a small population of a longer distance ($>$ 3.5 nm) identified in molecules **2** and **3**, probably corresponding to a more extended higher-energy conformation of these molecules in frozen solution. The spread of TPP positions is expected from the fact that these molecules are not completely rigid in solution and therefore slightly different conformations will be trapped in the frozen state upon flash-freezing of the sample in liquid nitrogen.

For molecule **4**, in addition to the long distance ($\sim$3.6 nm) corresponding to the extended conformation predicted by DFT, a more intense distance feature centred around 2.5 nm was obtained from the orientation-dependent analysis. Other stable molecular conformations, with porphyrin-porphyrin distances below 3 nm, were identified by *in-vacuo* DFT through bond rotations of the first amino acid of the peptide backbone, suggesting that the short distance feature in the distance distribution could be explained by unwinding of the α-helix (Figure 3.17).

In general, the larger width of the obtained distance distributions compared to the DFT-derived histograms reflects the conformational flexibility of the molecules in solution.[123] In the case of molecule **4**, the wider spread

of TPP positions suggests a larger degree of conformational flexibility, consistent with the longer peptide backbone in this molecule. While previous studies of these systems used IR spectroscopy to monitor the formation of the stable helical structure by measuring the signal associated with intramolecular N−H hydrogen bonding,[123] this technique does not report on conformational changes associated with torsional motion of the bonds at the end of the helix, where the TPP moieties are linked to the peptide, the rotation of which can cause relatively large changes in the porphyrin-porphyrin distance measured by the LITTER experiment.

3.2.2 Comparison to Cu-Cu DEER

Orientationally selective 4-pulse DEER between Cu(II) centres was used to benchmark LITTER against a more conventional PDS technique. For that, Cu(II) was introduced in both porphyrins of **3** to give Cu_2-**3**. The spectroscopic characterisation of Cu_2-**3** is shown in Figure 3.18. The increase from 2-fold to 4-fold symmetry in the porphyrin due to the loss of the two pyrrolic protons upon Cu(II) complexation leads to the four $S_0 \rightarrow S_1$ visible transitions becoming degenerated in pairs, yielding only two Q-bands in the absorption spectrum (Figure 3.18 (a)). This indicates complete metalation of the sample. The echo-detected ESR spectrum shows the characteristic shape for Cu(II)-porphyrin, with strongly axial g-tensor and resolved $A_{^{65}Cu}$ and $A_{^{14}N}$ couplings (Figure 3.18 (b)).[38] The measured spin relaxation behaviour is in agreement with the literature (Figure 3.18 (c, d)).[38,124]

Orientation-resolved DEER traces were acquired at different positions in the high-intensity region of the CuTPP ESR spectrum, dominated by the in-plane components of the axial g-tensor (Figure 3.19 (a)). Orientation selection in this case originates from the large spectral width of CuTPP, due to its large g-tensor anisotropy, compared to the narrow bandwidth of the MW pulses used in DEER. To improve the ESR signal intensity by increas-

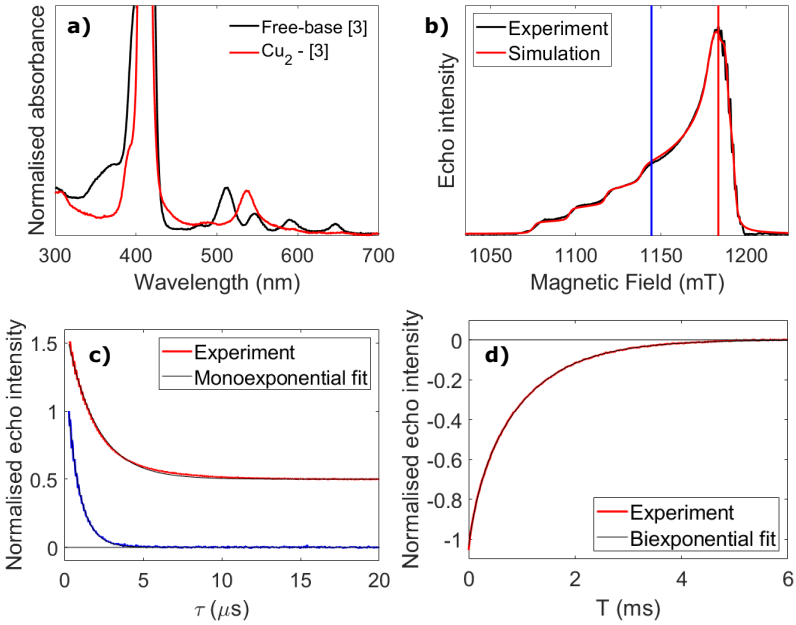


Figure 3.18: (a) Room-temperature optical absorption spectrum of **3** before (black) and after (red) Cu(II) complexation, in d_6-ethanol. Absorbances have been normalised to the absolute maximum (Soret band). (b) Echo-detected field-swept ESR spectrum at 15 K(black) and simulation (red) using *EasySpin pepper* function,[109] with spin Hamiltonian parameters: g = [2.041, 2.051, 2.191], A^{65}_{Cu} = [72, 89, 639] MHz and linewidth = [2, 2] mT. The field positions used for the spin relaxation experiments at 15 K are indicated with vertical lines. (c) Phase-memory time experiments at the lowest (blue) and highest (red) field positions used for DEER, and corresponding monoexponential fits (black) with T_m values of (0.78±0.01) μs and (1.89±0.02) μs, respectively. (d) Inversion-recovery experiment at the spectral maximum (red) and corresponding biexponential fit (black) with lifetimes of (0.19 ± 0.01) ms and (1.02 ± 0.05) ms.

ing the spin polarisation of this Boltzmann-populated spin-half centre, the measurements were performed at Q-band. Despite that, the low ESR signal intensities due to short T_m (0.78 μs) and the small modulation depths prevented the acquisition of DEER traces in the low-field region of the CuTPP ESR spectrum, where the stronger orientational effects are expected. Therefore, the dataset presented here does not capture the complete orientational dependence of the dipolar interaction and only shows very weak orientational effects (Figure 3.19 (b)). This dataset was acquired over 5 days, as was the corresponding LITTER dataset on **3**, showing that the weak spin polarisation of the CuTPP centre limits the DEER orientational information that can be obtained in a given period of time compared to LITTER with strong spin-polarised photogenerated TPP triplet states.

Orientation-dependent DEER simulations were carried out using the *OriDEERsim* algorithm,[38] with the same molecular model used for LITTER on **3**, and the same iterative least-squares global fitting procedure was followed.[97] The electronic spin densities and magnetic tensor orientations used for these simulations are shown in Figure 3.20. The resulting distance distribution has its maximum at 2.6 nm, as predicted by DFT and determined by LITTER, and its width is likely because of the experimental data not capturing the relative orientation between g_z and the dipolar vector (Figure 3.19 (c)). This translates into a wider conformational spread, with very few conformations standing out from the rest in the fitting procedure (Figure 3.19 (d)). In particular, one of the conformations most contributing to the fit, shown in the bottom right corner of Figure 3.19 (d), is far from the DFT prediction because of having a very different orientation of the dipolar vector relative to the g-frame of the detection CuTPP (indicated in the figure), despite the spin-spin distance being close to the value predicted by DFT. This is again likely to be due to the limited orientational information contained in the experimental dataset, which does not constrain the conformation of the fitting model strongly. In fact, the experimental DEER dataset on Cu_2-**3** can be simulated reasonably well using the molecular model resulting from

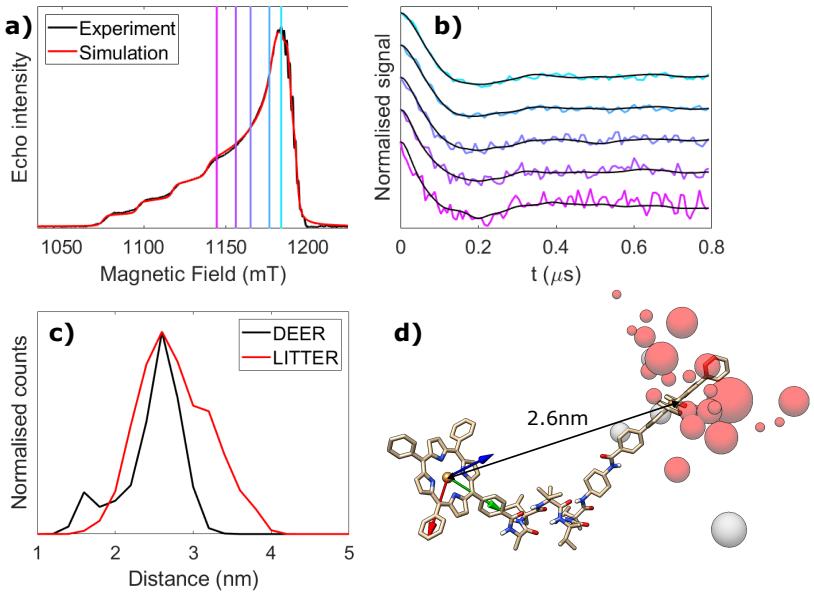


Figure 3.19: Orientational DEER study of Cu_2-**3** at Q-band, 15 K. (a) Echo-detected field-swept ESR spectrum, where the field positions used fo DEER are indicated with vertical lines. (b) Background-corrected and modulation depth-normalised DEER traces acquired at the different field positions (colour) and corresponding orientation-dependent fits (black). Modulation depths were $\sim$ 2-3% before normalisation in all cases. (c) Spin-spin distance distributions obtained from the orientation-dependent analysis of the DEER on Cu_2-**3** (black) and LITTER on **3**(red). (d) DFT-optimised geometry showing the different positions of the CuTPP centre most contributing to the fit as gray spheres, relative to the g-tensor frame of the other CuTPP (arrows: red = g_x, green = g_y, blue = g_z). The diameter of the spheres is proportional to the number of times a single conformation contributes to the complete fit shown in panel (b). The spheres from Figure 3.16 c iii are shown in red for comparison.

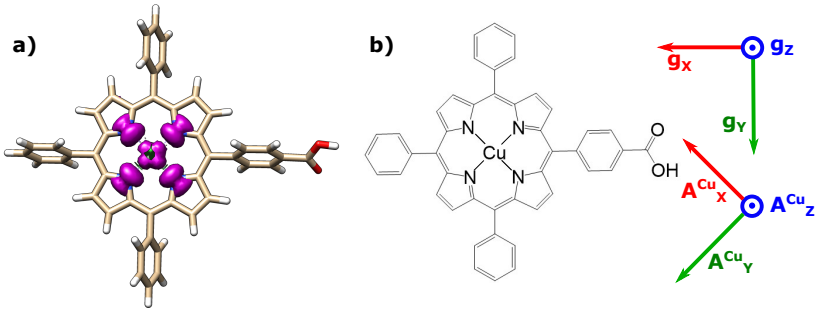


Figure 3.20: (a) Electronic spin density in the ground state of CuTPP calculated using *Gaussian*[96] (B3LYP, Def2SVP, and DefTZVP for Cu). (b) Magnetic tensor principal axes for the ground state doublet of CuTPP (**g** and $\mathbf{A}^{65}\mathbf{Cu}$), calculated using *Orca*[108] (B3LYP, EPR-II, and DefTZVP for Cu).

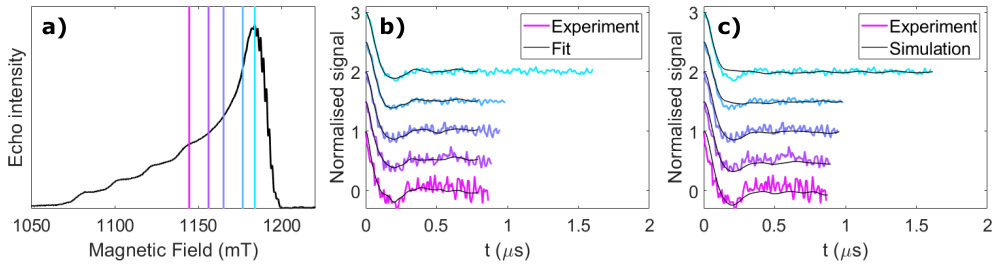


Figure 3.21: Comparison between (b) the results of the orientation-dependent fit to the DEER dataset with Cu_2-**3** shown in Figure 3.19, and (c) the simulation of the Cu–Cu DEER traces using the molecular model resulting from the orientation-dependent analysis of the LITTER dataset with **3** shown in Figure 3.16 c.

the orientation-dependent analysis of the LITTER dataset with **3** shown in Figure 3.16 (c iv), demonstrating that the two techniques applied to the same molecule yield results compatible with the same molecular structure (Figure 3.21).

The higher dipolar signal intensities thanks to the non-Boltzmann population of the triplet state sub-levels, longer T_m of the TPP triplet and larger modulation depths of LITTER compared to Cu-Cu DEER facilitate the obtention of dipolar datasets capturing a more complete orientational dependence of the dipolar interaction, and therefore allow for the determination of more accurate conformational information of the molecule of study. In the particular case of molecules with long spin-spin distances, that require the

measurement of long dipolar traces for an accurate analysis, the longer T_m of the photogenerated TPP triplet state compared to CuTPP, even when the temperature is lowered from 20 to 15 K for the latter, makes LITTER even more advantageous over Cu-Cu DEER. In addition, for distances down to 2 nm it has been previously shown that the wider electronic spin density delocalisation in the photogenerated TPP triplet with respect to CuTPP has no negative effect on the obtained spin-spin distance distribution in porphyrin-nitroxide LiDEER.[72] This has been attributed to the symmetric electronic spin density distribution in the TPP triplet state. The same reasoning can be applied to the LITTER experiment and here we have successfully measured the porphyrin-porphyrin separation centred at 2.1 nm for molecule **1**. The upper limit of the distance measurement in PDS is defined by the length of time trace that can be collected, which is limited by the T_m of the detection spin centre. It is therefore expected that the LITTER technique measured on systems where the detection spin species is a TPP triplet will have a longer maximum distance than corresponding DEER using a CuTPP species for detection, as $T_m^{TPPtriplet} > T_m^{CuTPP}$. The upper distance limit for the LITTER experiment using a photogenerated TPP triplet for detection will likely be slightly shorter than that measured for the LiDEER TPP triplet-nitroxide systems,[72] as the modulation depth for the LITTER experiment is smaller than that of LiDEER, and the corresponding MNR is therefore lower.

3.2.3 Orientation-independent analysis

To show the importance of taking orientational effects into account in LITTER measurements, each individual dipolar trace has been analysed via Tikhonov regularisation using *DeerAnalysis*,[110] which uses an orientation-independent kernel function. The results for molecule **3** are presented in Figure 3.22 (a, b) as an example; the analysis for molecules **1**, **2** and **4** can be found in Appendix II, Figures 5.12, 5.13 and 5.14. Significant differences in the shape and position of the distance distribution features can be observed, indicating that the dipolar traces are not representative of the

complete distribution when considered individually. For the traces recorded around the Z^- region of the TPP triplet ESR spectrum, a distance distribution with a longer average distance is obtained compared to those recorded around Y^- (Figure 3.22 (b)). All of the individual distance distributions lie within the distribution calculated from the fitting procedure considering the orientational effects, and they have narrower widths. This shows that even if the orientational information contained in the dipolar traces is not of interest for the study, measuring a single LITTER trace at a given field position and analysing it with an orientation-independent method could lead to an erroneous distance distribution, not reflective of the true spin-spin distances, resulting from artefacts due to the orientational dependence of the dipolar interaction.

As optical excitation with non-polarised light is orientation independent, for cases where only the spin-spin distance distribution, and not the orientational distribution, is of interest, an approximate idea of the distance distribution can be obtained by acquiring multiple LITTER traces at different field positions across the triplet spectrum and averaging them, following a similar methodology previously applied to DEER experiments using a non-selective pump pulse.[128] In the case of free-base TPP, isomerisation of the porphyrin ring nitrogen protonation sites interchanges the x- and y-axes of the ZFS-tensor. This means that reasonable orientation averaging can be achieved by measuring and taking the average, weighted by the spectral intensities at the corresponding field positions, of traces recorded only across the Z^- and Y^- transitions, where the signal is most intense, to suppress the orientational effects. The distance distribution resulting from Tikhonov regularisation analysis of this averaged trace can yield more accurate information on the position of the most probable spin-spin distance than any of the individual trace. However, detailed interpretation of the shape of this distribution should be avoided as it may still contain small orientational artefacts, the extent of which will depend on the system and the number of traces recorded. The true validity of such an averaging treatment relies heavily on

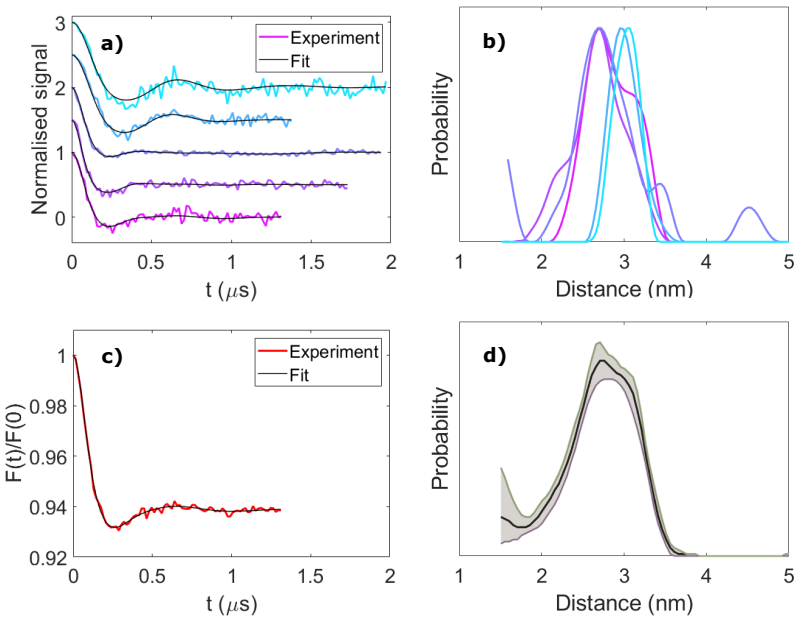


Figure 3.22: Orientation-independent analysis of LITTER with **3**. (a) Background-corrected and modulation depth-normalised LITTER traces shown in Figure 3.16 (c ii) (colour) and individual orientation-independent fits by Tikhonov regularisation using *DeerAnalysis*[110] (black). (b) Spin-spin distance distributions obtained from the analysis shown in panel a. (c) Averaged LITTER trace (red) and corresponding orientation-independent fit by Tikhonov regularisation (black). (d) Spin-spin distance distribution obtained from the analysis shown in panel c, showing the 95% confidence intervals estimated using the Comparative DEER Analyser (CDA) tool in *DeerAnalysis2022*.[125–127]

sufficient traces being recorded across different orientations of the ZFS-tensor within the triplet spectrum, to capture all orientations of the dipolar vector with respect to the external magnetic field. For example, only measuring around the Z^- and Y^- turning points cannot be generalised to all types of chromophores.

The results of this averaging treatment are shown in Figure 3.22 (c, d) for molecule **3** and in Appendix II,(Figures 5.12, 5.13 and 5.14) for molecules **1**, **2** and **4**. For these systems and the number of traces recorded, the distance distributions from the averaged traces are in good agreement with those obtained from the orientation-dependent analysis. Interestingly, for molecule **4**, the shorter distance found in the complete orientation-dependent LITTER analysis survives the orientational averaging process (Figure 5.14), providing further evidence that it is not due to an orientational artefact but rather due to the presence of a second conformation of this molecule in the sample.

This treatment has shown, by comparison to DFT predictions and orientation-dependent analysis, that orientational averaging of LITTER traces capturing the orientational dependence of the dipolar interaction is a valid analysis procedure for these systems to obtain reliable spin-spin distance distributions free of orientational artefacts, and that it can be used when orientational information is not required, removing the need for the lengthy orientational simulations and iterative fits associated with an orientation-dependent analysis. This has also demonstrated that a true spin-spin distance distribution free of orientational artefacts cannot be extracted directly from the orientation-independent analysis of a single LITTER trace, and that the acquisition of multiple dipolar traces at different field positions is necessary even when the orientational information is not of interest, in order to be able to correctly average out the orientational effects.

3.2.4 Conclusions

This section has reported a systematic orientational LITTER study of a spectroscopic ruler of bis-porphyrin synthetic model peptides spanning porphyrin-porphyrin distances from 2.1 to 3.6 nm and different relative orientations. Using orientation-dependent simulations and fits, information on the conformational distribution of the molecules in frozen solution has been obtained, in good agreement with DFT predictions, demonstrating that porphyrin-porphyrin distances as short as 2 nm can be accurately determined with this technique. By direct comparison to conventional Cu-Cu DEER spectroscopy, it has been shown that LITTER is advantageous in allowing data to be recorded in a shorter amount of time and at a higher temperature thanks to the strong spin polarisation and longer T_m of the photogenerated porphyrin triplet state compared to CuTPP.[72] In addition, being a single-frequency technique, LITTER removes the restriction of resonator bandwidth in DEER, and its orientational resolution does not require the use of high fields as it originates from the triplet ZFS, unlike for conventional spin-half centres. This highly anisotropic ZFS offers orientational resolution comparable or exceeding that of metal centres with large g-anisotropy, such as Cu(II) and Fe(III). Finally, an alternative treatment of the orientationally selective data has been presented, by averaging the orientational effects in the dipolar traces to carry out a computationally faster orientation-independent analysis. By comparison to DFT predictions and orientation-dependent analysis, it has been shown that this orientational averaging is a valid procedure to obtain reliable spin-spin distance distributions free of orientational artefacts, and that it can be used when orientational information is not required, removing the need for lengthy orientational simulations and iterative fits.

It must be pointed out that the spin-spin distance distributions resulting from the orientation-dependent analysis of the LITTER datasets have been provided without confidence intervals. Error estimation in the orientation-independent analysis of PDS traces can be routinely performed in *DeerAnalysis*[35] by means of a validation procedure where the analysis is repeated with

different background fits and adding different levels of noise to the data. More sophisticated approaches combine the confidence bounds from different analysis methods to provide a better estimate of the error in the distance distribution (Tihkonov regularisation and neural network analyses are combined in the Comparative DEER Analyzer (CDA)[125–127] tool). However, the validation procedure was not feasible for error estimation in the orientation-dependent analysis of LITTER traces presented in this thesis, due to the computational time required for the fitting of the simulated library of traces to the experimental dataset (from several hours to several days, depending on the number of traces and iterations). If the fitting is to be repeated with different background corrections and added noise of the experimental data, the algorithm would need to be computationally optimised to significantly reduce the duration of the calculation.

This study completes and complements the proof-of-concept LITTER work presented in Section 3.1 and sets the base knowledge for the use of this technique in structural investigations of complex biological macromolecules of interest. In the next section, preliminary work on the application of LITTER to homodimeric heme proteins, containing two identical porphyrin groups, will be presented. In that case, other spectroscopic techniques capable of measuring the distance between the two chromophores, such as FRET, require the chromophores to adopt different orientations relative to the polarisation of the light, and are therefore limited by the particular structure of the systems studied.[129] LITTER, on the other hand, is free of this limitation. It is envisioned that the structure of other unmodified macromolecular systems containing endogenous photoexcitable moieties, such as light-harvesting proteins and flavoproteins, and systems modified with several photoswitchable triplet labels, could be studied with LITTER. Removing the need for any nitroxide radicals, which are known to be unstable in the intracellular environment,[118,119] and using only photogenerated triplets, which can be generated within cells,[117] LITTER is better suited for in-cell structural studies and could be combined with optical microscopy techniques to correlate pro-

tein structural information to its location in the cell.

3.3 Application to a protein system: Zn(II) myoglobin dimer

This section has been adapted from the following publication:

A. Bertran, J. Sawyer, C. J. Rogers, D. J. Heyes, M. De Zotti, C. R. Timmel, M. Di Valentin, S. Hay and A. M. Bowen, *in preparation*.

The bis-porphyrin peptide used for this study was supplied by Prof. Marta de Zotti (Univerisy of Padova, Italy). Protein sample preparation, mass spectrometry experiments and rigid-body docking simulations were carried out by Jack Sawyer (University of Manchester, United Kingdom). RIDME data was acquired by Jack Sawyer and Ciarán Rogers (University of Manchester, United Kingdom).

In the previous section, a systematic orientational LITTER study of a spectroscopic ruler of bis-porphyrin synthetic model peptides was presented. The current section reports the the first example of the application of LITTER to the structural study of a protein system, Zn(II) myoglobin (ZnMG) dimer (Figure 3.23). Using two naturally-occurring photoswitchable spin centres as endogenous probes allowed to study the unmodified protein directly, without need for any labelling, which is unusual in conventional PDS and was not possible with previous LiPDS techniques. The main features in the distance distribution obtained from LITTER agree well with the crystallographic structure of MG dimer, and a shorter feature suggests the presence of some ZnMG trimer, supported by mass spectrometry (MS). Using a model peptide bis-labelled with ZnTPP, the large modulation depth of LITTER with ZnMG compared to previous experiments with free-base porphyrins is

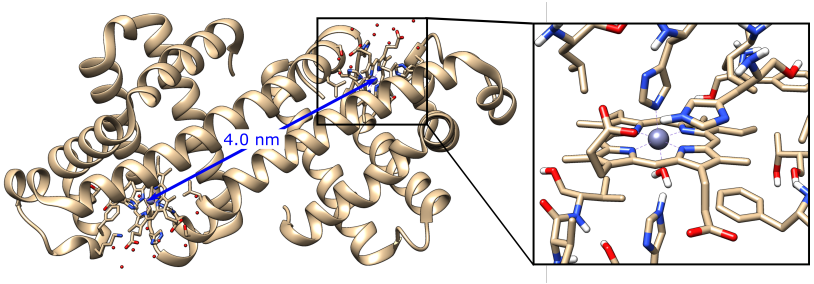


Figure 3.23: Structure of horse myoglobin dimer (from PDB 3VM9), with a metal-metal distance of 4.0 nm. The inset shows the Zn(II) protoporphyrin IX (ZnPP) replacing the native heme groups in the Zn(II)-myoglobin (ZnMG) dimer studied in this work.

shown to arise from the presence of Zn(II). Finally, distance measurements by RIDME are performed on the same protein containing Cu(II) instead of Zn(II), with results that validate the findings from LITTER.

3.3.1 LITTER on a ZnTPP-ZnTPP model peptide

All LITTER experiments presented so far have been performed using free-base TPP chromophores. To demonstrate the feasibility and understand the differences of using ZnTPP instead, Zn(II) was introduced in the bis-porphyrin model system **3** of Section 3.2, yielding Zn_2-**3**, and ZnTPP – ZnTPP LITTER was performed (Figure 3.24). LITTER traces show enhanced modulation depth of 20% for Zn_2-**3** (Figure 3.24 (c)), attributed to the higher triplet quantum yield (ϕ_T) of ZnTPP and to the photoexcitation of more chromophore orientations due to the collapse of the four porphyrin Q-bands into two upon metalation. Analysis by Tikhonov regularisation yields nearly identical distance distributions (Figure 3.24 (d)), consistent with the previous LITTER results on this molecule (Figure 3.16), showing that LITTER can also be successfully performed between two ZnTPP centres.

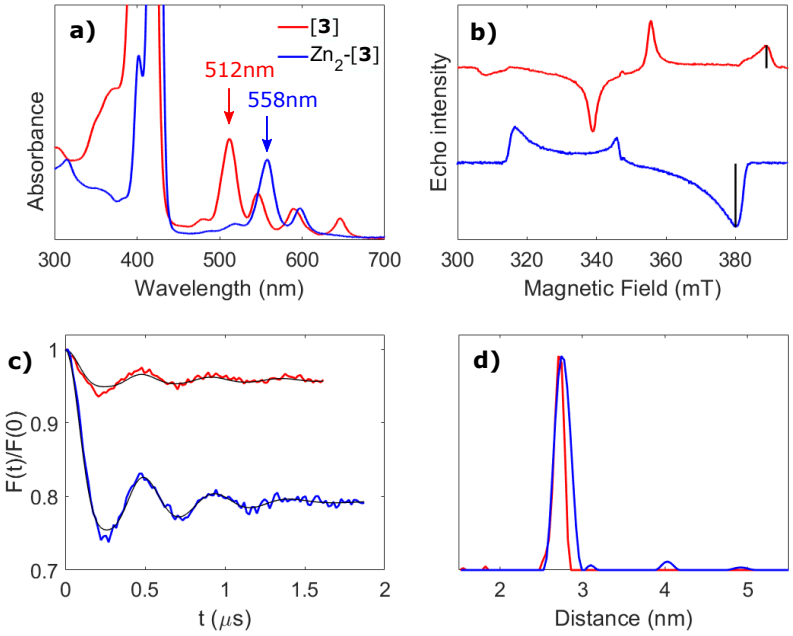


Figure 3.24: Spectroscopic results on molecules **3** (red) and Zn_2-**3** (blue). (a) Room-temperature optical absorption spectra showing the laser excitation wavelengths used for LITTER with each molecule (512 and 558 nm, respectively). (b) Echo-detected field-swept ESR spectra after laser excitation. The field positions used for LITTER are indicated with vertical lines. (c) Background-corrected and normalised LITTER time traces (colours) and fits by Tikhonov regularisation (black). Modulation depths: 5 % (red) and 20 % (blue). (d) Corresponding spin-spin distance distributions.

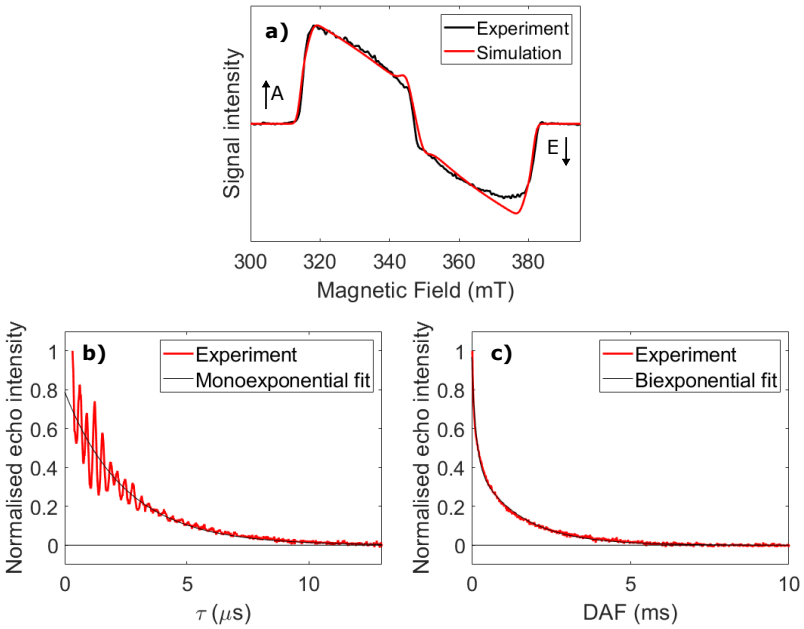


Figure 3.25: ESR characterisation of Zn_2-**3**. (a) trESR spectrum measured at 10 K (black) and simulation (red) with *EasySpin pepper* function[109] using the following spin Hamiltonian parameters: D = 935 MHz, E = -268 MHz, D-strain = 12 MHz, E-strain = 38 MHz, Gaussian linewidth = 2.0 mT, p_x = 0.10, p_y = 0.18, p_z = 0.71. The simulated spectrum is unchanged when inverting the sign of E and exchanging p_x and p_y simultaneously. (b) Phase-memory experiment at 10 K (red), with monoexponential fit (black) yielding a T_m value of 2.5 μs. (e) DAF experiment at 10 K (red), with monoexponential fit (black) yielding lifetimes of 0.13 and 1.4 ms.

3.3.2 LITTER on Zn-myoglobin dimer

MG dimer was studied after reconstitution of the apo form with Zn(II) protoporphyrin IX (ZnPP) (Figure 3.23). Dimer formation was promoted by lyophilisation. The photogenerated ZnPP triplet in ZnMG (Figure 3.26) shows faster transverse spin relaxation and slower longitudinal relaxation than the ZnTPP triplet in Zn_2-**3** (Figure 3.25). This could be attributed to the more delocalised spin density of ZnPP triplet (Figure 3.27) and to the more restricted mobility of ZnPP in the heme pocket, respectively.

The LITTER trace acquired for ZnMG dimer shows a modulation depth of 27 % and well-defined dipolar oscillations, with two clearly differentiated frequency components (Figure 3.28 (c)). Analysis by Tikhonov regularisation reveals that the slow frequency component corresponds to a spin-spin distance of 4.6 nm (Figure 3.28 (d)), close to the metal-metal distance extracted from the crystallographic structure (Figure 3.23). The fast frequency component corresponds to a spin-spin distance of 2.7 nm, suggesting the presence of a third ZnMG (or ZnPP) unit in the system studied. This fast dipolar oscillation was captured better with a refocused-echo version of the LITTER experiment (Figure 3.29), although analysis of the short ReLITTER trace by Tikhonov regularisation yields a poor fit to the experimental form factor due to the underlying slow oscillation.

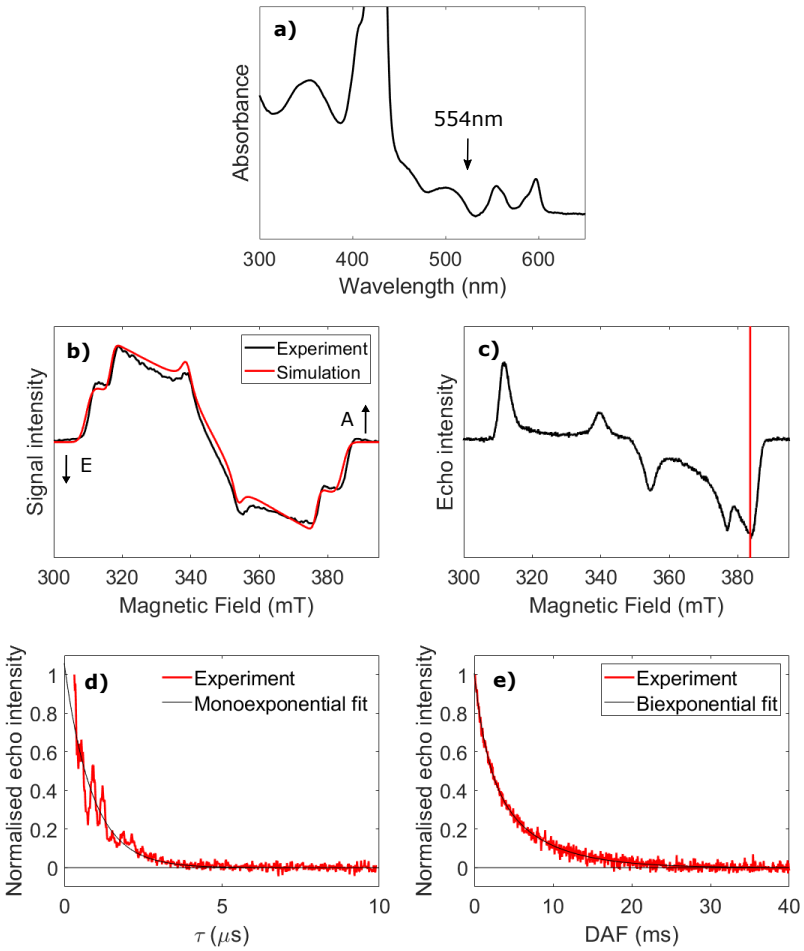


Figure 3.26: Spectroscopic characterisation of ZnMG dimer. (a) Room-temperature optical absorption spectrum showing the laser excitation wavelength used for LITTER (554 nm). (b) trESR spectrum measured at 10 K (black) and simulation (red) with *EasySpin pepper* function[109] using the following spin Hamiltonian parameters: D = 1051 MHz, E = -210 MHz, D-strain = 85 MHz, E-strain = 0 MHz, Gaussian linewidth = 1.5 mT, p_x = 0.10, p_y = 0.18, p_z = 0.72. The simulated spectrum is unchanged when inverting the sign of E and exchanging p_x and p_y simultaneously. (c) Echo-detected field-swept ESR spectrum after laser excitation. The field position used for the relaxation experiments is indicated with a vertical line. (d) Phase-memory-time experiment at 10 K (red), with monoexponential fit (black) yielding a T_m value of 0.81 μs. (e) Delay-after-flash experiment at 20 K (red), with monoexponential fit (black) yielding lifetimes of 1.7 and 6.4 ms. Longitudinal spin relaxation could not be characterised at 10 K, as the decay of the echo intensity with the DAF was significantly longer than the 50 ms shot repetition time imposed by the 20 Hz laser. A full decay curve could only be captured after rising the temperature to 20 K.

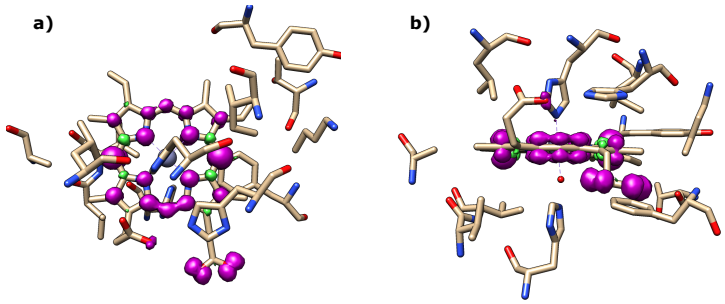


Figure 3.27: Calculated electronic spin density distribution in the photogenerated state of ZnPP in ZnMG. (a) Top and (b) side views.

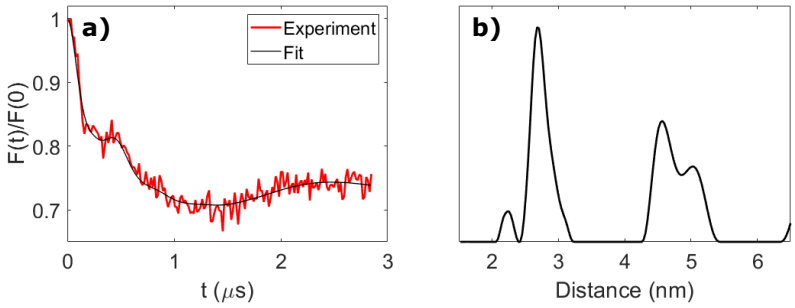


Figure 3.28: LITTER results on ZnMG dimer. (a) Background-corrected and normalised LITTER time trace (red), measured on the field position indicated in Figure 3.26 c, and fit by Tikhonov regularisation in *DeerAnalysis*[35] (black), with $\alpha = 10$. Modulation depth: 27%. (b) Corresponding spin-spin distance distribution.

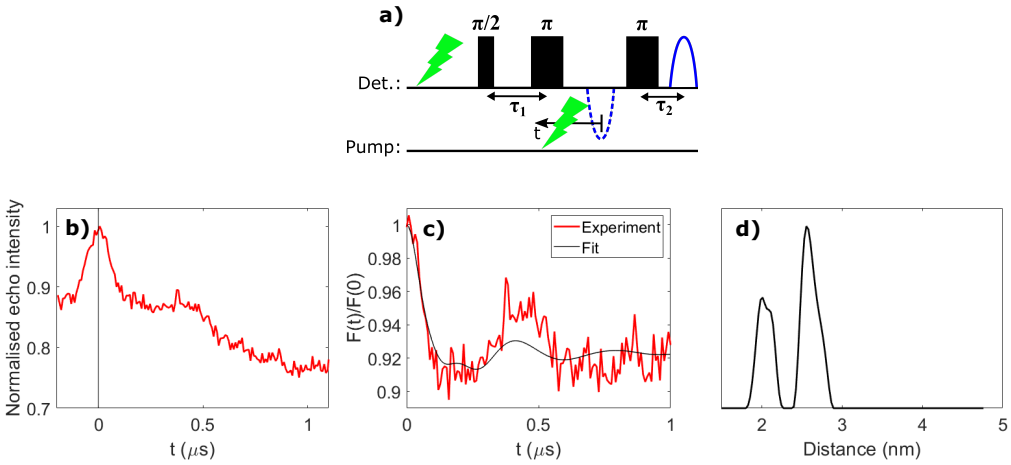


Figure 3.29: Refocused-echo LITTER (ReLITTER) on ZnMG dimer. (a) ReLITTER pulse sequence. (b) Normalised ReLITTER trace on ZnMG dimer acquired on the most intense emissive ESR feature. (c) Background-corrected and normalised trace (red) and fit by Tikhonov regularisation in *DeerAnalysis*[35] (black), with $\alpha = 10$. (d) Corresponding spin-spin distance distribution.

3.3.3 Complementary experiments and simulations

MS confirmed the presence of ZnMG trimer in addition to dimer and monomer, with no evidence of a third ZnPP unit attached to dimers, suggesting that the short distance could originate from a fraction of trimeric protein in the sample (Figure 3.30 (a)). Rigid-body docking calculations identified sterically favourable ZnMG trimer conformations with metal-metal distances of 2.7 and 4.4 nm to the third ZnMG unit (Figure 3.30 (b)), in addition to the crystallographic dimer value of 4.0 nm (Figure 3.23). These are consistent with the LITTER results, where the shortest distance corresponds to the fast dipolar frequency component and the longest distance could explain the longest distance feature in the distribution from LITTER (Figire 3.28 (d)).

In order to validate the findings from LITTER, distance measurements were performed using a standard PDS technique on a MG dimer sample reconstituted with Cu(II) proto-porphyrin IX (CuPP). DEER measurements were attempted, but the MNR achieved was insufficient due to instrumental problems in the Manchester ESR laboratories that reduced the B_1 at

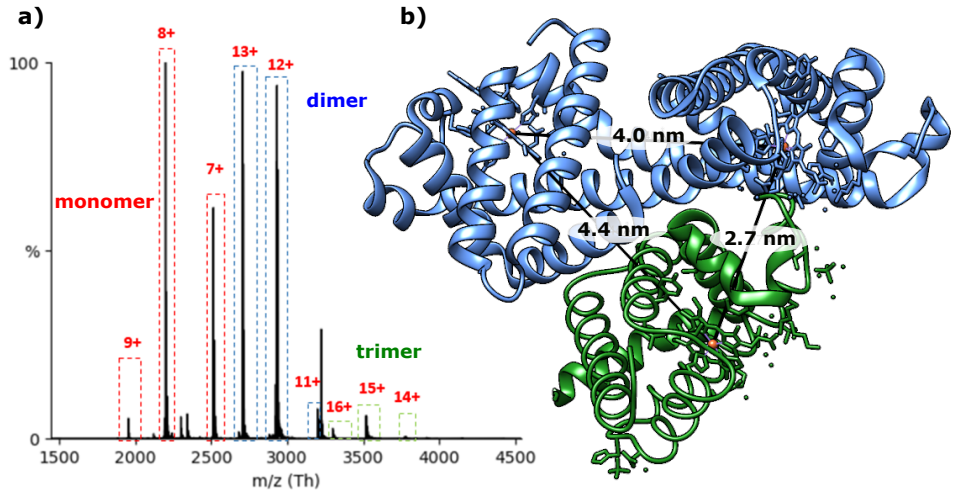


Figure 3.30: (a) MS of the ZnMG sample studied by LITTER. Peaks are associated to ZnMG monomer (red), dimer (blue) and trimer (green). (b) Sterically favourable ZnMG trimer conformation identified by rigid-body docking simulations of a third monomer unit (green) onto the crystallographic dimer structure (blue), with metal-metal distances of 2.7, 4.0 and 4.4 nm.

the sample, severely limiting the excitation bandwidth of the MW pulses. RIDME was used instead (Figure 3.32), taking advantage of the unlimited pump bandwidth provided by the longitudinal relaxation of pump spins (Figure 3.31 (c)) during the delay T_{mix}. The length of the acquired trace was limited by the short T_m of CuMG (Figure 3.31 (d)) and the long RIDME pulse sequence. Orientation-independent analysis of the RIDME trace by Tikhonov regularisation also yields a spin-spin distance of 2.7 nm (Figure 3.32 (d)), confirming that this short distance is not an artefact of the LITTER technique and supporting the presence of trimer.

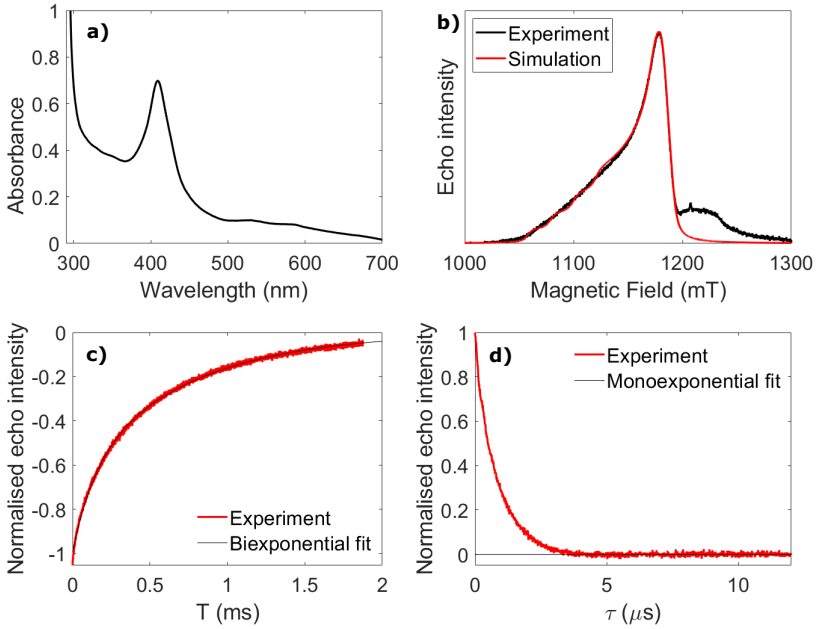


Figure 3.31: Spectroscopic characterisation of CuMG. (a) Room-temperature optical absorption spectrum in PBS. (b) Echo-detected field-swept ESR spectrum measured at 15 K (black) and simulation with *EasySpin pepper* function,[109] using the following spin Hamiltonian parameters: g = [2.038, 2.054, 2.220], A^{65}_{Cu} = [80, 80, 640] MHz and linewidth = [5, 4.8] mT. The broad signal above 1200 mT corresponds to a Mn impurity. (c) Inversion-recovery experiment (red) with biexponential fit (black) yielding lifetimes of 0.14 and 0.72 ms. (d) Phase-memory experiment (red) with monoexponential fit (black) yielding a T_m = 0.82 μs.

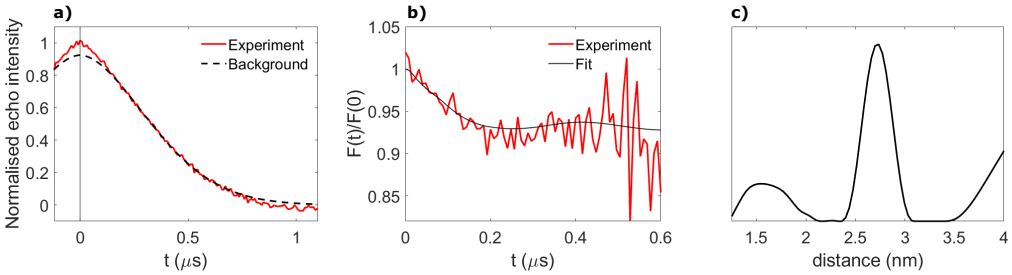


Figure 3.32: RIDME on CuMG dimer. (a) RIDME trace recorded at the spectral maximum (red) and fitted background (black). (b) Form factor (red) and fit by Tikhonov regularisation in *DeerAnalysis*[35] (black). (c) Corresponding spin-spin distance distribution.

3.3.4 Conclusions

This work demonstrates the applicability of LITTER to the structural study of proteins containing endogenous chromophores that can be photoexcited to form triplet states. With the paradigmatic heme protein myoglobin as a model system, reconstituted with Zn(II) protoporphyrin IX in the heme pocket, LITTER has been employed to study protein oligomerisation and the structure of the oligomers. Using naturally-occurring photoswitchable spin centres as endogenous probes allowed to study the unmodified protein directly, without need for any labelling, which is unusual in conventional PDS and was not possible with previous LiPDS techniques. The obtained results are in partial agreement with the reported crystallographic structure of myoglobin dimer and suggest the presence of some trimer, supported by mass spectrometry and rigid-body docking simulations. Finally, these results have been validated by RIDME distance measurements on the same protein, containing Cu(II) instead of Zn(II). These results show the potential of LITTER for the study of other unmodified macromolecular systems containing endogenous photoexcitable moieties, such as light-harvesting proteins and flavoproteins, or systems modified with several photoexcitable triplet spin labels.

The presence of different oligomers of the protein together with the fact that the main spin-spin distance obtained from LITTER was longer than the expected value from the crystallographic structure suggests that the state of the protein in the ESR sample was significantly different than in the original MG dimer publication,[130] which described the dimerisation procedure employed for the preparation of this sample. It is unclear whether the prior reconstitution with Zn(II) protoporphyrin IX to yield ZnMG could have negatively impacted the subsequent dimerisation. The study of another bisporphyrin protein system of well-known structure by LITTER would provide a clearer demonstration of its applicability to structural biology problems.

3.4 Application to multiporphyrin supramolecular nanostructures

This section has been adapted from the following publication:

A. Jozeliūnaitė, A. Neniškis, A. Bertran, A. M. Bowen, M. Di Valentin, S. Raišys, P. Baronas, K. Kazlauskas, L. Vilčiauskas and E. Orentas, *J. Am. Chem. Soc.*, 2023, , **145**, 455-464.

The molecules used for this study were supplied by Prof. Edvinas Orentas (Univerisy of Vilnius, Lithuania), who also prepared Figures 3.33, 3.34 and 3.35.

In addition to biological macromolecular systems that contain multiple chromophores or that can be labelled with several triplet-forming moieties, LITTER has great potential for the structural and conformational study of synthetic molecules or molecular assemblies where some of the building blocks are based on chromophores that can be photoexcited to form triplet states. An example of this application of LITTER is presented in this section, where the conformational changes undergone by a tetraporphyrin supramolecular cage upon complexation of a C_{60} molecule have been studied by synergistically combining LITTER and DEER spectroscopies (Figure 3.33).

3.4.1 Characterisation of the system

The system of study consists of monomers of TPP derivatised to contain a functionalisation with ureidopyrimidinone (UPy) and isocytosine (IC) units (TPP–UPy–IC–C_{10}, Figure 3.34). The rigid and chiral bicyclo[3.3.1]nonane between the UPy and IC units bears two 10-carbon alkyl chains (R) for solubility purposes. In non-protic solvent, the TPP–UPy–IC–C_{10} monomers assemble *via* alternating 4H- and 2H-bonds between neighbouring UPy and

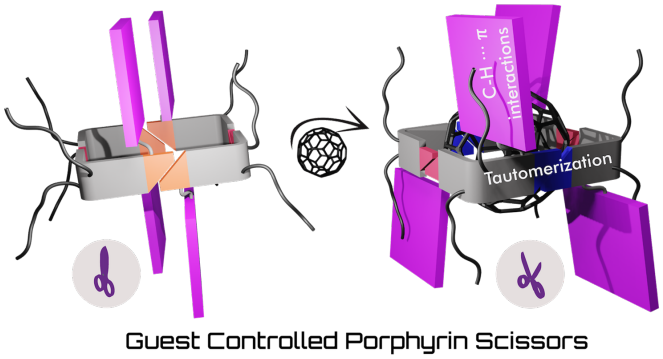


Figure 3.33: Schematic representation of the conformational change undergone by the tetraporphyrin cage upon C_{60} complexation. *Reprinted (adapted) from Jozeliūnaitė, A., Neniškis, A., Bertran, A., Bowen, A. M., Di Valentin, M., Raišys, S., Baronas, P., Kazlauskas, K., Vilčiauskas, L., Orentas, E. Fullerene Complexation in Hydrogen-Bonded Porphyrin Cavitands via Induced-Fit: Cooperative Action of Tautomerization and C–H···π Interactions. J. Am. Chem. Soc., 2023, 145(1), 455-464. doi:10.1021/jacs.2c10668. Copyright 2023 American Chemical Society.*[131]

IC units to form a tetrameric cavitand ($(TPP-UPy-IC-C_{10})_4$, Figure 3.35 (a)), which forms a strong complex with C_{60} ($C_{60}(TPP-UPy-IC-C_{10})_4$, Figure 3.35 (b)). NMR studies performed in the group of Prof. Orentas showed that the cavity adjusts to the guest via keto-enolic tautomerisation of the UPy unit, and suggested that the porphyrin substituents might move apart from each other as a result. Complementary computational studies identified that the rearrangement is accompanied by C–H$\cdots\pi$ interaction between the alkyl solubilising chains and the nearby porphyrin π-systems. The latter interaction was found to be crucial for the guest complexation event, providing the energetic compensation for the costly tautomerisation process.

LITTER was identified as the ideal tool to verify and quantify the relative movement of the porphyrin substituents upon C_{60} complexation. The visible absorption spectra of the system before (black) and after (red) C_{60} complexation are shown in Figure 3.36 (a), with a Q-band absorption maximum at 517 nm. Minimal changes occur to the visible spectrum upon C_{60}

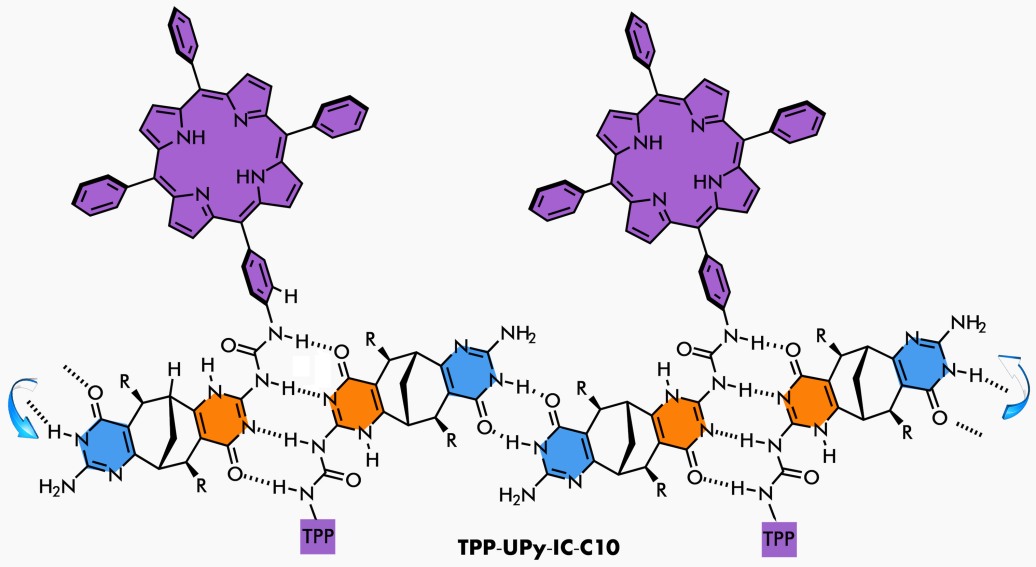


Figure 3.34: Schematic representation of the $(\mathrm{TPP-UPy-IC-C_{10}})_4$ tetramer and its H-bond interactions. *Reprinted (adapted) with permission from Jozeliūnaitė, A., Neniškis, A., Bertran, A., Bowen, A. M., Di Valentin, M., Raišys, S., Baronas, P., Kazlauskas, K., Vilčiauskas, L., Orentas, E. Fullerene Complexation in Hydrogen-Bonded Porphyrin Cavitands via Induced-Fit: Cooperative Action of Tautomerization and C–H$\cdots\pi$ Interactions. J. Am. Chem. Soc., 2023, 145(1), 455-464. doi:10.1021/jacs.2c10668. Copyright 2023 American Chemical Society.*[131]

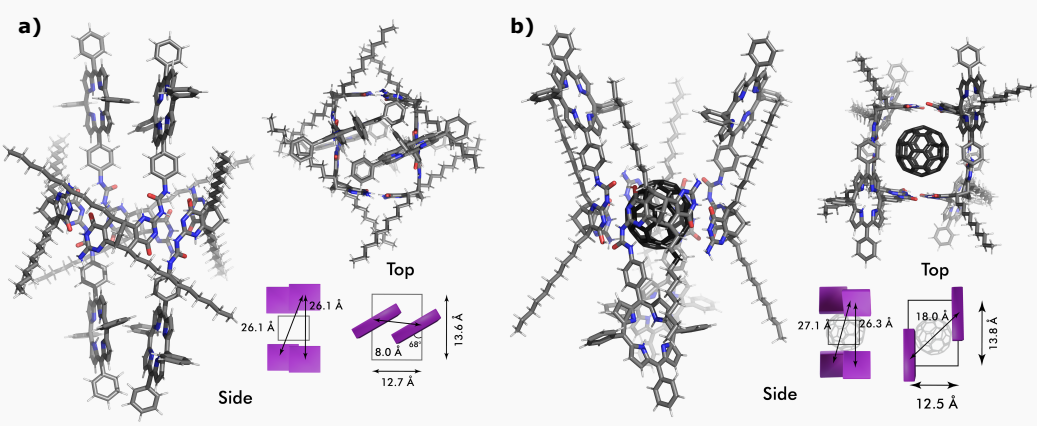


Figure 3.35: Side and top views of (a) (TPP–UPy–IC–C_{10})$_4$ and (b) C_{60}(TPP–UPy–IC–C_{10})$_4$ based on molecular models. (insets) Schematic representations showing the dimensions of the structures. *Reprinted (adapted) with permission from Jozeliūnaitė, A., Neniškis, A., Bertran, A., Bowen, A. M., Di Valentin, M., Raišys, S., Baronas, P., Kazlauskas, K., Vilčiauskas, L., Orentas, E. Fullerene Complexation in Hydrogen-Bonded Porphyrin Cavitands via Induced-Fit: Cooperative Action of Tautomerization and C–H$\cdots\pi$ Interactions. J. Am. Chem. Soc., 2023, 145(1), 455-464. doi:10.1021/jacs.2c10668. Copyright 2023 American Chemical Society.*[131]

complexation, due to the low extinction coefficient of C_{60}. The corresponding trESR spectra show the usual free-base porphyrin triplet shape, overlapping with the intense narrow line due to the C_{60} triplet (Figure 3.36 (b)). However, pulsed ESR characterisation after photoexcitation revealed substantial differences from the behaviour of weakly-coupled porphyrin triplets observed in the previous sections of this chapter. The pulsed ESR characterisation of the spin-spin relaxation in C_{60}(TPP–UPy–IC–C_{10})$_4$ after photoexcitation is shown in Figure 3.37. The shorter T_m of the porphyrin triplet compared to the bis-porphyrin peptides (Figure 3.4 (c)) is likely due to the presence of multiple triplets in close proximity (see predicted porphyrin-porphyrin distances in Figure 3.35 (b)). No electron spin-echo could be observed for TPP–UPy–IC–C_{10}, which suggests that the enhanced spin decoherence due to the proximity of multiple triplet states makes T_m shorter than the ringdown time of the ESR cavity used (< 200 ns). This supports the hypothesis of the porphyrin substituents being closer to each other in

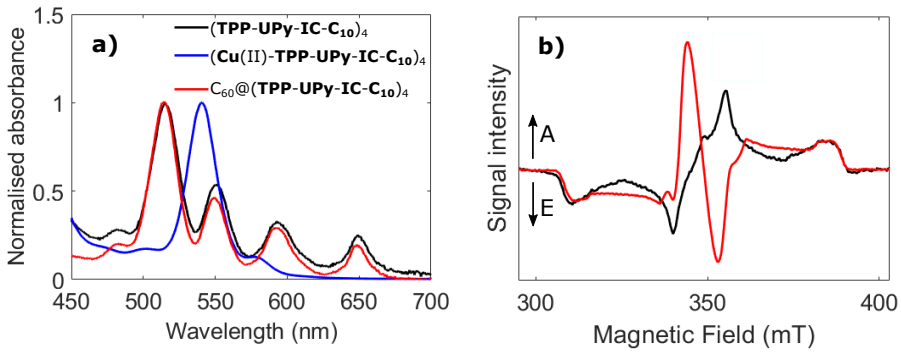


Figure 3.36: (a) Room-temperature optical absorption spectra of $(TPP-UPy-IC-C_{10})_4$ (black), $(Cu(II)TPP-UPy-IC-C_{10})_4$ (blue) and $C_{60}(TPP-UPy-IC-C_{10})_4$ (red). (b) trESR spectra of $(TPP-UPy-IC-C_{10})_4$ (black) and $C_{60}(TPP-UPy-IC-C_{10})_4$ (red) acquired after laser excitation at 517 nm, X-band, 20 K. Both spectra have been normalised to the intensity of the Z^- shoulder of the porphyrin triplet. *Reprinted (adapted) with permission from Jozeliūnaitė, A., Neniškis, A., Bertran, A., Bowen, A. M., Di Valentin, M., Raišys, S., Baronas, P., Kazlauskas, K., Vilčiauskas, L., Orentas, E. Fullerene Complexation in Hydrogen-Bonded Porphyrin Cavitands via Induced-Fit: Cooperative Action of Tautomerization and $C-H\cdots\pi$ Interactions. J. Am. Chem. Soc., 2023, 145(1), 455-464. doi:10.1021/jacs.2c10668. Copyright 2023 American Chemical Society.*[131]

the absence of C_{60} inside the cage. The inability to detect an electron spin-echo from $TPP-UPy-IC-C_{10}$ prevented its study by LITTER. For this reason, the porphyrins were metalated with Cu(II) and the resulting $(Cu(II)TPP-UPy-IC-C_{10})_4$ was studied by DEER.

3.4.2 PDS study

PDS measurements were conducted to quantitively probe the distances between the porphyrin substituents in the cages with and without C_{60}. In case of $C_{60}(TPP-UPy-IC-C_{10})_4$, LITTER was used to measure the dipolar interaction between the photogenerated triplet states of the free-base porphyrin chromophores (Figure 3.38 (a, b)). The orientation-averaged LITTER trace (Figure 3.39 (a)) and the corresponding distance distribution (Figure 3.39 (b)) show distances in the same range as predicted from the model of this

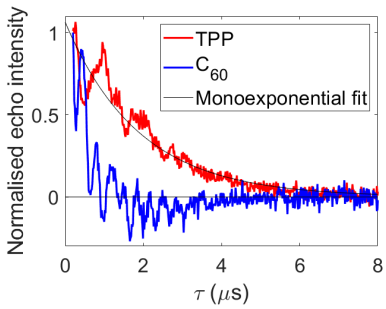


Figure 3.37: Phase-memory characterisation of C_{60}(TPP−UPy−IC−C_{10})$_4$ at 20 K. Time traces measured at the most intense porphyrin triplet emissive feature after photexcitation at 517 nm (red) and at the maximum of the C_{60} after photoexcitation at 537 nm. The monoexponential fit to the red curve yields a T_m value of (1.89 ± 0.07) μs. *Reprinted (adapted) with permission from Jozeliūnaitė, A., Neniškis, A., Bertran, A., Bowen, A. M., Di Valentin, M., Raišys, S., Baronas, P., Kazlauskas, K., Vilčiauskas, L., Orentas, E. Fullerene Complexation in Hydrogen-Bonded Porphyrin Cavitands via Induced-Fit: Cooperative Action of Tautomerization and C−H$\cdots\pi$ Interactions. J. Am. Chem. Soc., 2023, 145(1), 455-464. doi:10.1021/jacs.2c10668. Copyright 2023 American Chemical Society.*[131]

system (Figure 3.35 (b)). Excitation of this system at 517 nm induced the formation of triplet states on both the porphyrins and the C_{60} guest (Figure 3.36 (b)). It is therefore expected in the LITTER trace analysis to see both distances between two porphyrin moieties and between a porphyrin and the C_{60}. The expected distances from the model are plotted as grey and red bars, respectively (Figure 3.39 (b)). While the distance ranges observed experimentally are a good match to the expected model, deviations in the expected intensity across this distance range may be a result of different T_m values of the porphyrin triplet state used for detection in the presence and absence of other triplet state moieties, and a function of the trace length used (shorter distances are often relatively amplified when the recorded trace is short).[36] In this case, the length of trace recorded was limited by T_m.

In the case of (Cu(II)TPP−UPy−IC−C_{10})$_4$, standard 4-pulse DEER was used to measure the dipolar interaction between the Cu (II) ions coordinated into the porphyrins (Figure 3.38 (c, d)). The distance distribution resulting from the orientationally-averaged DEER trace (Figure 3.39 (c, d)) is in good

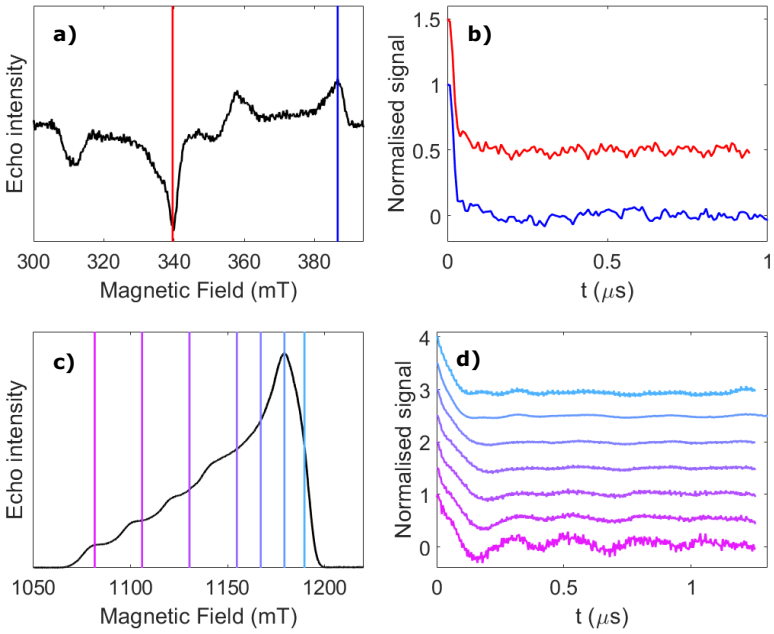


Figure 3.38: (a) Echo-detected field-swept ESR spectrum of C_{60}(TPP−UPy−IC−C_{10})$_4$ measured after laser excitation at 517 nm, X-band, 20 K, showing the field positions where LITTER traces were acquired (vertical lines). (b) Background-corrected and modulation depth-normalised LITTER traces acquired at the indicated field positions. (c) Echo-detected field-swept ESR spectrum of (Cu(II)TPP−UPy−IC−C_{10})$_4$ measured in the dark, Q-band, 15 K, showing the field positions where DEER traces were acquired (vertical lines). (d) Background-corrected and modulation depth-normalised DEER traces acquired at the indicated field positions. *Reprinted (adapted) with permission from Jozeliūnaitė, A., Neniškis, A., Bertran, A., Bowen, A. M., Di Valentin, M., Raišys, S., Baronas, P., Kazlauskas, K., Vilčiauskas, L., Orentas, E. Fullerene Complexation in Hydrogen-Bonded Porphyrin Cavitands via Induced-Fit: Cooperative Action of Tautomerization and C−H···π Interactions. J. Am. Chem. Soc., 2023, 145(1), 455-464. doi:10.1021/jacs.2c10668. Copyright 2023 American Chemical Society.*[131]

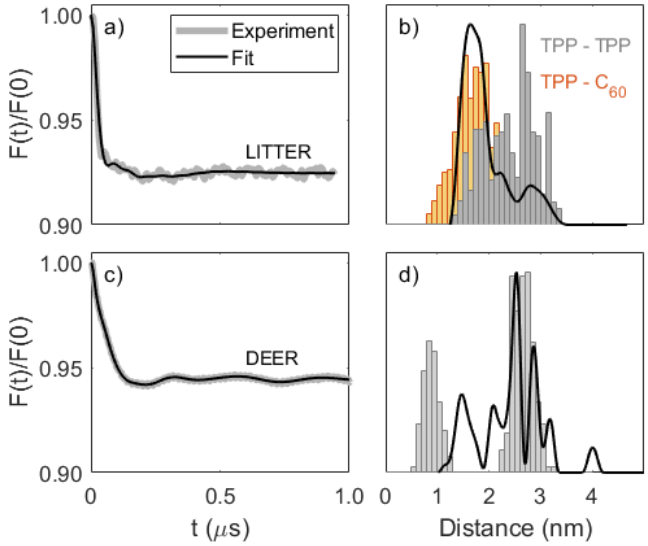


Figure 3.39: Orientation-independent analysis of averaged dipolar traces. Background-corrected averaged dipolar traces (grey) and Tikhonov regularisation fits (black) for LITTER measured on C_{60}(TPP–UPy–IC–C_{10})$_4$ (a) and DEER measured on (Cu(II)TPP–UPy–IC–C_{10})$_4$ (c). Corresponding spin-spin distance distributions (black lines) and expected distances from the molecular models (grey bars) for LITTER (b) and DEER (d). Individual distances in the histograms have been weighted by the electron spin densities on the involved atoms, as determined from DFT calculations. The contributions from TPP–TPP and TPP–C_{60} distances to each bar have been indicated separately in (b) in grey and red, respectively, weighted by the corresponding extinction coefficients and triplet quantum yields. Histograms and distance distributions are normalised to their absolute maximum. *Reprinted (adapted) with permission from Jozeliūnaitė, A., Neniškis, A., Bertran, A., Bowen, A. M., Di Valentin, M., Raišys, S., Baronas, P., Kazlauskas, K., Vilčiauskas, L., Orentas, E. Fullerene Complexation in Hydrogen-Bonded Porphyrin Cavitands via Induced-Fit: Cooperative Action of Tautomerization and C–H$\cdots\pi$ Interactions. J. Am. Chem. Soc., 2023, 145(1), 455-464. doi:10.1021/jacs.2c10668. Copyright 2023 American Chemical Society.*[131]

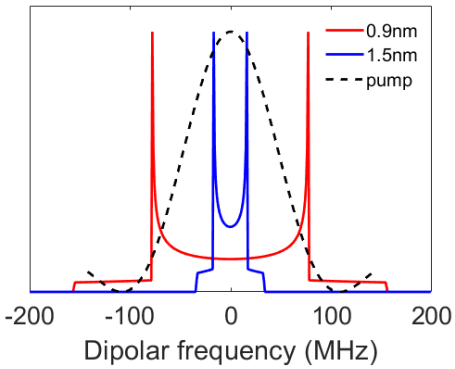


Figure 3.40: Simulated DEER dipolar spectra for spin-spin distances of 0.9 nm (red, corresponding to the left maximum of the histogram in Figure 3.39 (d)) and 1.5 nm (blue, corresponding to the left maximum of the DEER-derived distance distribution in Figure 3.39 (d)). The excitation profile of the 8 ns pump pulse used in the DEER experiment is shown as dashed line. *Reprinted (adapted) with permission from Jozeliūnaitė, A., Neniškis, A., Bertran, A., Bowen, A. M., Di Valentin, M., Raišys, S., Baronas, P., Kazlauskas, K., Vilčiauskas, L., Orentas, E. Fullerene Complexation in Hydrogen-Bonded Porphyrin Cavitands via Induced-Fit: Cooperative Action of Tautomerization and C–H···π Interactions. J. Am. Chem. Soc., 2023, 145(1), 455-464. doi:10.1021/jacs.2c10668. Copyright 2023 American Chemical Society.*[131]

agreement with that predicted from the model (grey bars) in the region above 2.0 nm. The model predicts an additional short distance centred at 0.8 nm and arising from the effective stacking of porphyrin moieties. DEER has a lower detection limit of ca. 1.5 nm due to two main reasons.[132] First, due to the fact that, in order to detect a dipolar spectrum, this spectrum must fit within the bandwidths of the pulses used (Figure 3.40). Second, because below 1.5 nm exchange interactions can cause deviations from the purely dipolar model used in analysis of DEER data. As such, it is likely that the experimentally determined distances between 1.0 and 2.0 nm are a result of partial detection of the Pake patterns of the distances < 1.0 nm predicted from the model. In this way, the obtained PDS results corroborate the expected models of the systems, where the porphyrin substituents move apart from each other in a scissor blade-like opening fashion upon C_{60} complexation.

3.4.3 Conclusions

This work has demonstrated the first example of a host-guest system based on a dynamic H-bonded receptor operating by the cooperative action of tautomerisation and C–H$\cdots\pi$ interactions. The tetramer assembled by sterically-induced homodimerisation of 2H- and 4H-bonding isocytosine and ureidopyrimidinone units, respectively, exhibits cavity plasticity towards the C_{60} guest via tautomerisation. This conformational change has been quantified here by a combination of LITTER and DEER experiments as a movement of the porphyrin rings by a distance of $\sim$1 nm apart upon C_{60} complexation, corroborating the NMR and computational studies. In addition, LITTER provided information on the porphyrin-fullerene distance.

The principle for controlling host-guest chemistry studied here could be implemented into future allosteric systems with photoresponsive side chains to enable light modulation of chemical receptors.

3.5 Analytical treatment of LITTER

This section presents an analytical treatment of the LITTER experiment. First, a description of the spin evolution during the LITTER pulse sequence is presented following the density-operator formalism. Later, an expression for the modulation depth of the LITTER dipolar traces as a function of triplet quantum yields and photoexcitation efficiencies is derived. This expression is used to explain some of the limitations of LITTER, and to hypothesize the superior performance of a two-colour experiment using non-identical chromophores.

3.5.1 Density-operator description

The following description is based on density-operator descriptions of LiDEER and LaserIMD previously reported.[3,78]

In the LITTER experiment, the laser pulses move backwards in time with respect to the MW pulses and the trace is acquired with laser 2 moving from the primary echo (PE) to the π pulse. For the simulation (Figure 3.41), laser 2 is considered to move forwards in time with respect to the MW pulses and the trace is obtained with laser 2 moving from the $\pi/2$ to the π pulse (i.e. in the other half of the trace). As the ideal dipolar trace is symmetric with respect to the π pulse, the two halves of the simulated trace are equivalent.

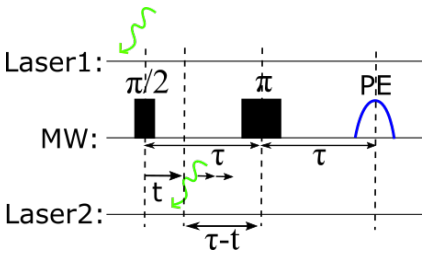


Figure 3.41: LITTER sequence as simulated. The MW pulse sequence is considered to be static and laser 2 is considered to move forwards in time.

Assumptions and approximations

The system of study is a general 2-chromophore system A–B, where A is the chromophore whose photogenerated triplet state is used for detection and B is the chromophore used as pump. The following description assumes that the triplet spin density is localised in a single point on each chromophore, and that there are no anisotropic Zeeman interactions, unresolved hyperfine couplings or exchange coupling. The high-field (Zeeman interaction $\gg$ dipolar interaction) and weak-coupling ($|\omega_A - \omega_B| > \omega_{dd}$) approximations are evoked, allowing for the rejection of the non-secular and pseudo-secular dipolar terms of the spin Hamiltonian, respectively. MW pulses are considered to be transition selective, only exciting the $|T_-\rangle \leftrightarrow |T_0\rangle$ transition of

the detection triplet state (T^A). As no MW pulses are acting on the pump triplet state (T^B), the Zeeman and ZFS spin Hamiltonian terms corresponding to this triplet are neglected. Finally, for simplicity, the approximation of selective photoexcitation of the chromophores is made, considering that laser 1 does not affect B chromophores and that laser 2 does not affect A chromophores. This last approximation is clearly not fulfilled for the version of LITTER presented in this chapter, using identical chromophores for detection and pump, and its effect on the modulation depth of the experiment will be discussed in the following section.

Evolution before laser 2

Before the formation of the pump triplet T^B by laser 2 there is only one paramagnetic centre, the detection triplet T^A formed by laser 1. Therefore, the spin evolution of the system is conveniently described in the high-field eigenbasis of T^A ($\{|T^A_+\rangle, |T^A_0\rangle, |T^A_-\rangle\}$, indicated with $'$). The initial density operator is that of the detection triplet

$$\hat{\boldsymbol{\sigma}}'_0 = \hat{\boldsymbol{\sigma}}'_A = \begin{bmatrix} p_{+,A} & 0 & 0 \\ 0 & p_{0,A} & 0 \\ 0 & 0 & p_{-,A} \end{bmatrix} \tag{3.1}$$

where $p_{+,A}, p_{0,A}, p_{-,A}$ are the populations of the triplet sub-levels of T^A. The propagator for the transition-selective $\frac{\pi}{2}$ MW detection pulse is

$$\hat{\mathbf{U}}_{\pi/2} = \exp(-i\frac{1}{\sqrt{2}}\hat{S}'_{x,A,-1\leftrightarrow 0}\frac{\pi}{2}) \tag{3.2}$$

where the transition-selective spin operator is given by

$$\hat{S}'_{x,A,-1\leftrightarrow 0} = \frac{1}{\sqrt{2}}\begin{bmatrix} 0 & 0 & 0 \\ 0 & 0 & 1 \\ 0 & 1 & 0 \end{bmatrix} \tag{3.3}$$

The free evolution before laser 2 is given by the spin Hamiltonian of T^A in the rotating frame

$$\hat{H}_{pre} = \Omega_A \hat{S}'_{z,A} + D(\hat{S}'^2_{z,A} - \frac{1}{3}\hat{S}'^2_A) \tag{3.4}$$

where $\Omega_A = |\omega_A - \omega_{MW}|$ is the offset between the Larmor frequency of T^A and the carrier frequency of the MW. The corresponding propagator for the time t between the $\pi/2$ pulse and laser 2 is

$$\hat{\mathbf{U}}_{t,pre} = \exp(-i\hat{H}_{pre}t) \tag{3.5}$$

The total propagator before laser 2 is

$$\hat{\mathbf{U}}_{pre} = \hat{\mathbf{U}}_{t,pre}\hat{\mathbf{U}}_{\pi/2} \tag{3.6}$$

and the density operator at the time of laser 2 is given by

$$\hat{\boldsymbol{\sigma}}'_{pre} = \hat{\mathbf{U}}_{pre}\hat{\boldsymbol{\sigma}}'_0\hat{\mathbf{U}}^\dagger_{pre} \tag{3.7}$$

Evolution after laser 2

After the formation of T^B by laser 2, the system needs to be described in the high-field eigenbasis of $T^A + T^B$: $\{|m_{s,A},\ m_{s,B}\rangle\} = \{|1,1\rangle, |0,1\rangle, |-1,1\rangle, |1,0\rangle, |0,0\rangle, |-1,0\rangle, |1,-1\rangle, |0,-1\rangle, |-1,-1\rangle\}$, indicated without primes. The density operator right after laser 2 is given by

$$\hat{\boldsymbol{\sigma}}_{post} = \hat{\boldsymbol{\sigma}}''_B \otimes \hat{\boldsymbol{\sigma}}'_{pre} \tag{3.8}$$

where the density operator of T^B is

$$\hat{\boldsymbol{\sigma}}''_B = \begin{bmatrix} p_{+,B} & 0 & 0 \\ 0 & p_{0,B} & 0 \\ 0 & 0 & p_{-,B} \end{bmatrix} \tag{3.9}$$

and $''$ indicates that it is defined in the high-field eigenbasis of T^B ($\{|T^B_+\rangle, |T^B_0\rangle, |T^B_-\rangle\}$). The propagator for the transition-selective π detection pulse is

$$\hat{\mathbf{U}}_\pi = \exp(-i\frac{1}{\sqrt{2}}\hat{S}_{x,-1\leftrightarrow 0}\cdot\pi) \tag{3.10}$$

where the transition-selective spin operator is given by

$$\hat{S}_{x,-1\leftrightarrow 0} = \frac{1}{\sqrt{2}}\begin{bmatrix} 0 & 0 & 0 & 0 & 0 & 0 & 0 & 0 & 0 \\ 0 & 0 & 1 & 0 & 0 & 0 & 0 & 0 & 0 \\ 0 & 1 & 0 & 0 & 0 & 0 & 0 & 0 & 0 \\ 0 & 0 & 0 & 0 & 0 & 0 & 0 & 0 & 0 \\ 0 & 0 & 0 & 0 & 0 & 1 & 0 & 0 & 0 \\ 0 & 0 & 0 & 0 & 1 & 0 & 0 & 0 & 0 \\ 0 & 0 & 0 & 0 & 0 & 0 & 0 & 0 & 0 \\ 0 & 0 & 0 & 0 & 0 & 0 & 0 & 0 & 1 \\ 0 & 0 & 0 & 0 & 0 & 0 & 0 & 1 & 0 \end{bmatrix} \tag{3.11}$$

The free evolution periods after laser 2 are given by the spin Hamiltonian of $T^A + T^B$

$$\hat{H}_{post} = \Omega_A\hat{S}_{z,A} + \omega_{dd}(1-3\cos^2\theta)\hat{S}_{z,A}\hat{S}_{z,B} + D(\hat{S}^2_{z,A} - \frac{1}{3}\hat{S}^2_A) \tag{3.12}$$

The corresponding propagators for the time periods t and $\tau - t$ (considering $\tau = t + (\tau - t)$) are

$$\hat{\mathbf{U}}_{t,post} = \exp(-i\hat{H}_{post}t) \tag{3.13}$$

$$\hat{\mathbf{U}}_{\tau-t,post} = \exp(-i\hat{H}_{post}(\tau - t)) \tag{3.14}$$

The total propagator after laser 2 is

$$\hat{\mathbf{U}}_{post} = \hat{\mathbf{U}}_{\tau-t,post}\hat{\mathbf{U}}_{t,post}\hat{\mathbf{U}}_\pi\hat{\mathbf{U}}_{\tau-t,post} \tag{3.15}$$

The LITTER form factor is obtained as

$$F(t) = trace\{(\hat{S}_y + i\hat{S}_x)\hat{\boldsymbol{\sigma}}_{echo}\} \tag{3.16}$$

with $0 \leq t \leq \tau$.

3.5.2 Modulation depth analysis

This section has been adapted from the following publication:

A. Bertran, C. Dalla Torre, J. Sawyer, L. Morbiato, D. Heyes, S. Hay, C. R. Timmel, M. Di Valentin, M. De Zotti and A. M. Bowen, *J. Am. Chem. Soc.*, *in preparation.*

The previous description of the LITTER experiment assumed complete photoexcitation selectivity of the chromophores by the two laser pulses, which does not occur in general, especially when both chromophores have identical absorption spectra as is the case of the systems studied in this chapter. To derive an analytical expression for the expected modulation depth of LITTER, the excitation efficiencies of each of the chromophores by each of the lasers and the triplet quantum yields of each chromophore need to be taken into account.

For the sake of generality of this derivation, the excitation efficiencies and triplet quantum yields of each chromophore are treated as different quantities. For a general 2-chromophore system A–B, where A is the chromophore whose photogenerated triplet state is used for detection and B is the chromophore used as pump, these quantities are designated as follows:

- Excitation efficiency of chromophore α by laser i: e_i^α, with $\alpha = A, B$ and $i = 1, 2$. *E.g.* $e_1^A = 1$ means that laser 1 excites all chromophores A in the sample.

- Triplet quantum yield of chromophore α: Φ_α, with $\alpha = A, B$.

The modulation depth of a PDS experiment is defined as

$$\Delta = \frac{S_M}{S_0} \tag{3.17}$$

where S_M is the modulated part of the electron spin-echo intensity and S_0 is the total echo intensity. To calculate these two quantities, the following assumptions are made:

1. The detection MW pulses are resonant with a part of the triplet ESR spectrum of A where triplet B has negligible intensity and therefore the detected echo is only due to triplets A.

2. The excitation efficiencies do not depend on the number of chromophores left in the singlet ground state and are therefore constant throughout the experiment.

3. All systems have two chromophores that can be photoexcited.

Only molecules where the pump triplet is formed in states $|T_+\rangle$ or $|T_-\rangle$, causing a $|\Delta m_S| = 1$, contribute to the modulated signal, while $|T_0\rangle$, with a $\Delta m_S = 0$, only contributes to the unmodulated echo intensity.[68] For the cases with no preferential molecular orientation and no photoselection, such as the experiments carried out in this work, the ensemble population of each triplet sub-level is independent of the chromophore and equal to $\frac{1}{3}$.

The modulated part of the signal in LITTER (S_M) arises from molecules where laser 1 forms the triplet of chromophore A, leaving chromophore B in the ground singlet state, and laser 2 subsequently forms the triplet of chromophore B in states $|T_+\rangle$ or $|T_-\rangle$. This modulated signal can be calculated as the product of the probabilities of these two events (see Figure 3.42):

$$S_M = P(T_1^A S_1^B) P(T_2^B, +/-) = e_1^A \Phi_A (1 - e_1^B \Phi_B) \frac{2}{3} e_2^B \Phi_B \tag{3.18}$$

where the factor $(1-e_1^B\Phi_B)$ accounts for the probability of laser 1 not forming a triplet on chromophore B. The total echo intensity is given by the probability of laser 1 forming the triplet of chromophore A, independently of the spin state of chromophore B:

$$S_0 = P(T_1^A) = e_1^A\Phi_A \tag{3.19}$$

The modulation depth of the LITTER experiment is therefore

$$\Delta = \frac{2}{3}e_2^B\Phi_B(1 - e_1^B\Phi_B) \tag{3.20}$$

As expected, Δ does not depend on the properties of chromophore A. The maximum theoretically achievable modulation depth is $\frac{2}{3}$ and it occurs when $e_1^B = 0$, $e_2^B = 1$ and $\Phi_B = 1$. It must be noted that the formation of triplets A by laser 2 is a possibility for chromophores A that have not been photoexcited by laser 1 or that have already returned to the ground state before laser 2. However, as this would occur after the first MW pulse, the spins from those triplets will not be refocused at the time of the echo. An intermolecular contribution to the background of the experiment, similar to the contribution from triplets B formed by laser 2 in nearby molecules, is expected for these events.

Given the experimental conditions used in the LITTER experiments reported, where laser 2 has been delivered directly to the sample via optical fibre and with high power, it is reasonable to assume $e_2^B = 1$. The dependence of the modulation depth on Φ_B under this assumption is plotted in Figure 3.43 for different values of e_1^B. For small values of e_1^B, the modulation depth increases with Φ_B. Conversely, for large values of e_1^B, the modulation depth reaches a maximum and decreases as $\Phi_B \to 1$.

Using equation 3.20 with the assumption $e_2^B = 1$ and the Φ_T values for TPP and ZnTPP (0.88 and 0.90, respectively),[133] the expected modulation depths for the TPP–TPP and ZnTPP–ZnTPP LITTER experiments reported in this chapter can be plotted as a function of their excitation ef-

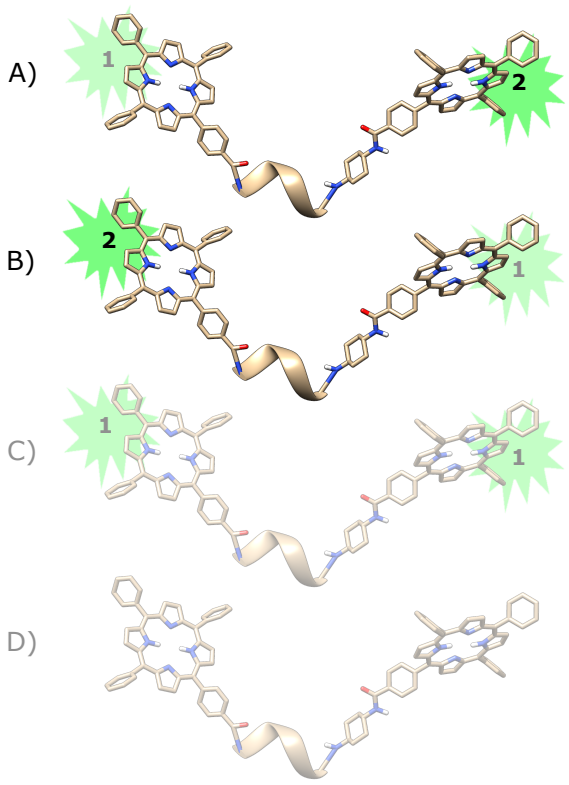


Figure 3.42: Different photoexcitation scenarios in one-colour LITTER, where the formation of a porphyrin triplet state is represented as a green star. Only cases A and B contribute to the dipolar modulation. C contributes to the un-modulated part of the echo intensity, reducing the modulation depth of the experiment.

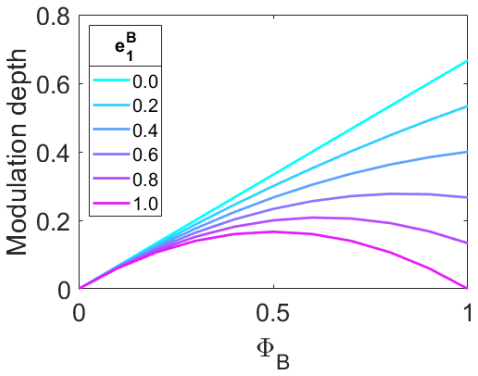


Figure 3.43: Expected modulation depth for LITTER as a function of the triplet quantum yield of the pump chromophore (Φ_B), for different values of the excitation efficiency of the pump chromophore by laser 1 (e_1^B) and a value of excitation efficiency of pump chromophore by laser 2 of $e_2^B = 1$. The maximum value for the modulation depth is limited to $\frac{2}{3}$ due to the pump triplets formed in the $|T_0\rangle$ not contributing to the change in local magnetic field of spins A.

ficiency by laser 1 ($e_1 \equiv e_1^A \equiv e_1^B$) (Figure 3.44). Because both A and B chromophores were identical and the wavelengths of both lasers were set to the absorption maximum of the chromophores in these experiments, the e_1 vaules are expected to be high and the resulting modulation depths are expected to be low, with the higher Φ_T of ZnTPP being advantageous in these circumstances.

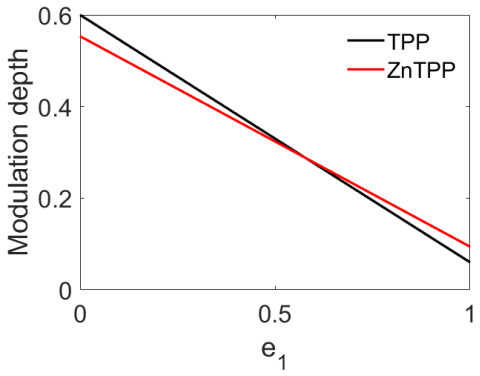


Figure 3.44: Expected modulation depths for TPP – TPP (black) and ZnTPP – ZnTPP (red) LITTER experiments, as a function of the excitation efficiency of the chromophores by laser 1 ($e_1 \equiv e_1^A \equiv e_1^B$) and a value of excitation efficiency of pump chromophore by laser 2 of $e_2^B = 1$. Triplet quantum yields ($\Phi \equiv \Phi_A \equiv \Phi_B$) for TPP and ZnTPP have been taken as 0.88 and 0.90, respectively.[133]

3.6 Limitations and advantages of the technique

The version of LITTER presented in this chapter uses only a single colour of light excitation. This imposes a limitation on the observable modulation depth by making the excitation efficiency of the second chromophore by laser 1 (e_1^B) close to 1 (see Section 3.5.2 and Figure 3.43). This is schematically depicted in Figure 3.42. In addition, the similar extinction coefficients of ^{1}TPP and ^{3}TPP in the visible region may allow additional photoexcitation of ^{3}TPP by the second laser flash,[134] leading to a partial loss of detection triplet spins.[135] These limitations could be overcome by a two-colour version of LITTER, replacing one of the porphyrins by a suitable optically-orthogonal photoexcitable moiety.[67] The development of two-colour LITTER and the search for suitable optically-orthogonal chromophores are the central matter of the next chapter.

Conversely, the ability to measure the dipolar interaction and thereby structural information between two identical chromophores is useful for sys-

tems in which orthogonal labelling is difficult, for example, homodimeric systems. In such systems, FRET between two chromophores of the same type is very complicated and only possible by observing fluorescence depolarisation.[129] In addition, this effect is observed only when the chromophores adopt different orientations relative to the polarization of the light. Such a limitation does not apply to LITTER.

3.7 Conclusions

This chapter has introduced a new light-induced PDS technique, light-induced triplet-triplet electron resonance (LITTER) spectroscopy, which enables the measurement of the dipolar interaction between two photogenerated triplet states and the determination of the distance distribution between the two triplet-bearing moieties. A spectroscopic ruler consisting in a series of bis-porphyrin synthetic model peptides has been used to study the range of applicability and the structural information attainable by the technique. The strong orientational effects in the LITTER traces of the model peptides, resulting from the large anisotropy in the ZFS-tensor of the photogenerated porphyrin triplet state, have been exploited *via* orientation-dependent analysis to obtain information on the distance and relative orientation of the two chromophores in the studied molecules. Alternative fast and simple analysis procedures have been presented for cases when only the distance information, and not the relative orientation, are of interest.

After the methodological development of this novel technique, LITTER has been applied in combination with other structure determination methods to the study of more complex supramolecular systems, such as the Zn(II)-substituted dimeric heme protein myoglobin and a tetra-porphyrin cage hosting C_{60}. In myoglobin dimer, LITTER yielded results in good agreement with crystallographic data and standard PDS techniques, showing its applicability and potential for the study of other unmodified macromolecular systems containing endogenous photoexcitable moieties, such as light-harvesting proteins and flavoproteins, or systems modified with several photoexcitable triplet spin labels. For the tetra-porphyrin molecular host, LITTER confirmed and quantified the conformational change caused by the complexation of the C_{60} guest molecule suggested by NMR and computational studies.

Finally, a density-operator description of the LITTER experiment has been provided, and analytical expressions for the dipolar modulation depth have been derived as a function of chromophore photoexcitation efficiencies

and triplet quantum yields. Several limitations of this new technique arising from the use of identical chromophores and one-colour photoexcitation have been identified, reducing the modulation depth of the dipolar traces and restricting its applicability to unmodified homodimeric systems or systems labelled with the same chromophore. These limitations could be overcome by a two-colour version of LITTER, replacing one of the porphyrins with a suitable optically-orthogonal photoexcitable moiety,[67] as it will be discussed in the next chapter.

LITTER removes the restriction, recurrent in all of the LiPDS techniques reported so far, of having to use one stable paramagnetic centre to perform distance measurements. In addition, being a single-frequency technique, LITTER also removes the limitation of resonator bandwidth in DEER, and its orientational resolution does not require the use of high fields as it originates from the triplet ZFS, unlike for conventional spin-half centres, making it advantageous for orientational studies.

LITTER could be used in combination with FRET spectroscopy if suitable photoexcitable moieties are chosen, exploiting the complementary features of the two techniques. In a manner similar to that for FRET, which has found significant applications in cells,[116] LITTER is a strong candidate for measuring structural information between chromophores in the cellular environment, using triplet states that can be photogenerated within cells.[117] Removing the need to have a permanent paramagnetic centre, such as nitroxide spin labels, which are known to be unstable and rapidly degraded inside cells,[118,119] is a key point for the success of in-cell structural studies and also mitigates the need to use more complex spin labels such as trityl radicals or Gd(III) complexes.[120–122] Furthermore, the combination of LITTER with microscopy techniques might facilitate the observation of structural changes for a system in different parts of a cell, for instance, by using microscopy locate the chromophores within the cell before using LITTER to probe structural parameters. Consequently, LITTER is an exciting new technique with the potential to cause a step change in the application of PDS to biological sys-

tems.

3.8 Methods

See Appendix I for general instrumentation.

Sample preparation

Bis-porphyrin peptides were supplied by Prof. Marta de Zotti (University of Padova, Italy). The single-porphyrin peptide was supplied by Prof. Marina Gobbo (University of Padova, Italy). Free-base and metalated samles of the tetra-porphyrin cage, with and without C_{60} were supplied by Prof. Edvinas Orentas (University of Vilnius, Lithuania). Protein samples were prepared by Jack Sawyer (University of Manchester, United Kingdom).

Cu(II) and Zn(II) were introduced into the bis-porphyrin peptides by stirring a solution of the peptide ($\sim$ 200-300 μM) in d_6-ethanol (99 % atom D, Sigma-Aldrich) at room temperature overnight in an excess of Cu(II) or Zn(II) acetate (98 %, Sigma-Aldrich). The complete metalation of the porphyrins was verified by UV-Vis absorption spectroscopy.

ZnMG and CuMG were prepared following previously reported procedures[136,137] and under red light. Lyophilised horse myoglobin (Sigma-Aldrich) was treated with 2-butanone (>99%, Sigma-Aldrich) under acidic conditions to remove the heme group from the pocket. The protein was reconstituted with ZnPP or CuPP (Inochem) in DMSO (Honeywell) overnight. Dimerisation was induced by addition of 5% ethanol followed by lyophilisation by freeze-drying. A final size-exclusion column step was carried out to separate the dimer fraction from the monomer and higher oligomers, which was buffer-exchanged into deuterated PBS (Sigma-Aldrich).

Samples for ESR were prepared in quartz tubes (3.9 mm for X-band, 1.6

mm for Q-band). Peptide samples were prepared in deuterated ethanol at $\sim$ 40 μM for light-induced experiments and at 100 μM for DEER. Samples of the tetra-porphyrin cages were prepared in 80 % 2-methyl tetrahydrofuran ($\geq$ 99 %, Sigma-Aldrich), 20 % deuterated toluene (99 % atom D, Sigma-Aldrich), at porphyrin concentrations of $80\mu M$ for light-induced experiments and 320 μM for DEER. Protein samples were prepared inside a N_2 glovebox under red light, in 66 % deuterated glycerol ($\geq$ 98 % atom D, Sigma-Aldrich), 33 % deuterated PBS, at MG concentrations of $\sim$ 70 μM. Except from protein samples, all other samples for light-induced ESR experiments were degassed by 3 freeze-pump-thaw cycles in a Schlenk line prior to flash freezing in liquid N_2.

ESR spectroscopy

Light-induced pulsed experiments were performed in a pulsed X-band spectrometer (ElexSys E680, Bruker) using an over-coupled dielectric resonator (EN 4118XMD5, Bruker) and an Oxford Instruments cryostat. The temperature was kept at 20 K for free-base porphyrins and at 10 K for Zn(II)-porphyrins, using liquid helium. Rectangular MW pulses of 16-32 ns for $\frac{\pi}{2} - \pi$ (6-12 ns for the tetra-porphyrin cage) were used. Laser 1 (OPOlette, Lambda Photometrics) was directed into the resonator through the optical window of the cryostat, while laser 2 (VersaScan OPO, GWU) was delivered via a 1 mm x 6 m optical fibre (FT1000-EMT, Thorlabs) directly inserted inside the sample tube. Laser energies were set to 2 and 3 mJ per flash, respectively, unless otherwise stated, with a time delay between the two laser pulses of 7 μs. A pulse delay generator was used to externally trigger both lasers and the spectrometer at a repetition rate of 20 Hz, and the MW pulses were moved forward in time with respect to the fixed laser pulses. All spectra were acquired with one shot per point.

Time-resolved ESR (trESR) was carried out in a critically-coupled resonator using laser 1 only, without field modulation or phase sensitive detection. The signal was averaged around the intensity maximum of the time

trace.

DEER experiments were performed in a pulsed Q-band spectrometer (ElexSys E580, Bruker) using an over-coupled dielectric resonator (EN 5107D2, Bruker) and an Oxford Instruments cryostat, at a temperature of 15 K. MW pulses of 16 ns for detection and 12 ns for pump were used for Cu_2-**3**, and 10 ns detection - 8 ns pump were used for the tetra-porphyrin cage. The pump frequency was set at -100 MHz from the detection frequency. A 16-step phase cycle and 8-step averaging cycles over τ_1 and τ_2 were used. The experiment was repeated at a rate of 500 Hz, with 20 shots per point.

RIDME experiments were performed in a pulsed Q-band spectrometer (ElexSys E580, Bruker) using an over-coupled resonator (ER 5106QT2, Bruker) and a helium-free cryostat (Cryogenics), at a temperature of 15 K. MW pulses of $32 - 64$ ns ($\frac{\pi}{2} - \pi$) were used, with $T_{mix} = 400$ μs.

Mass spectrometry

Mass spectra were acquired in a quadrupole orbitrap mass spectrometer (Q-Exactive). The sample was ionized by nano electron spray ionization using a Pt wire. All voltages in the source and instrument were kept low to avoid fragmentation. Tips were pulled in-house using a P-200 laser-based micropipette puller and filled with 10 μL of sample under red light.

DFT calculations

Initial geometries for the bis-porphyrin peptides were built based on previous spectroscopic and DFT studies[123,138] using *UCSF Chimera*.[113] Geometry optimisations and spin density calculations were performed *in vacuo* using *Gaussian 16* (revision A.03).[96] Ground-state geometry optimisations of the free-base molecules were carried out in the singlet spin state using the PBE1PBE functional and the 6-31g(d) basis set. The geometries of the chromophores were subsequently optimised in the triplet state for free-base and Zn(II)-porphyrin or in the doublet state for Cu(II)-porphyrin (B3LYP;

Def2-SVP for H, C, N and O; Def2-TZVP for Zn(II) and Cu(II)), to obtain the electronic spin densities, taken as atomic Mulliken spin densities. The triplet spin densities in ZnMG were calculated using the same method and the geometry of the Zn(II)-substituted heme group extracted from the crystal structure of horse myoglobin dimer (PDB 3VM9). The electronic spin density in the C_{60} triplet state was approximated to be equally distributed over the 60 atoms for the purposes of spin-spin histogram generation.

Magnetic tensor orientations (ZFS for photogenerated triplets, **g** and $\mathbf{A}_{^{65}\mathbf{Cu}}$ for CuTPP doublet) were calculated on the optimised geometries of triplet TPP and doublet CuTPP, and on the geometry of the Zn(II)-substituted heme group extracted from the crystal structure of horse myoglobin dimer (PDB 3VM9), using *Orca* (release version 4.2.0),[108] with the functional B3LYP and the basis sets EPR-II (for H, C, N and O) and Def2-TZVP (for Zn and Cu). The RIJCOSX approximation for Coulomb and Hartree-Fock exchange was used, with the auxiliary basis set Def2/J. The spin-spin contribution to the ZFS tensor was calculated using computed UNO (spin-unrestricted natural orbital) determinants,[139] and no spin-orbit coupling contribution was included.

Orientation-dependent analysis

Simulations of the orientation-dependent datasets for the bis-porphyrin peptides were performed using the *OriDEERsim* algorithm[38] (DEER) or a modified version of it to take into account the ZFS and triplet populations of the two photogenerated porphyrin triplets (LITTER). The spin system parameters obtained from the echo-detected (Figure 3.18 (b)) or trESR (Figure 3.4 (b)) spectra were used to simulate the spectra and resonant fields by means of *EasySpin* functions.[109] The simulations were carried out in the *g*- and ZFS-frames of CuTPP and triplet TPP (Figures 3.20 (b) and 3.3), for DEER and LITTER, respectively, taking into account the calculated spin densities (Figures 3.20 (a) and 3.3). The input orientations were derived from the DFT-optimised structures of **1**-**4**. The position of the pump cen-

tre with respect to the detection centre was defined in terms of the polar angles (ϕ and θ) and a separation r. Geometries in the range $\Delta\phi = \pm 45°$, $\Delta\theta = \pm 45°$ and $\Delta r = \pm 1$ nm (± 0.5 nm for **1**) were sampled around the optimised structures. Dipolar traces were calculated for each orientation at each field position measured. The libraries of simulated traces were fitted to the experimental datasets using the iterative process described in Section 1.4.5[97] until convergence of the RMSD was achieved (RMSD plots in Appendix II). Orientation selection effects due to magnetophotselection of the porphyrin by the pump laser (laser 2) were not included in the simulations as this laser pulse was delivered through an optical fibre and it was assumed that all polarisation was lost within this setup.

The resulting distance distributions were generated from the molecular geometries contributing to the best fits shown in Figures 3.16 (ii) and 3.19 (b), which are represented in the corresponding sphere plots of those figures. For each geometry, a distance distribution was generated as the histogram of pairwise distances between atoms bearing electronic spin density according to DFT calculations, where each pairwise component was weighted by the product of spin densities of the two atoms involved. The distance histograms from all the molecular geometries contributing to the best fit were added together weighted by the number of times each molecular geometry contributes to the fit (represented as the radii of the spheres in Figures 3.16 (iv) and 3.19 (d)). Finally, the distance histograms were displayed as line plots in Figures 3.16 (iii) and 3.19 (c). For direct comparison to the minimum-energy geometries obtained from DFT optimisations, single-molecular geometry distance histograms were generated following the same procedure and were displayed as bar plots.

Orientation-independent analysis

For the orientation-independent analysis of LITTER and DEER, the dipolar traces acquired at different field positions were added together weighted by the corresponding spectral intensities to obtain an averaged form factor,

which was analysed via Tikhonov regularisation using *DeerAnalysis2019*[35] to extract the corresponding distance distribution. A g-factor correction was applied to the distance distribution, as previously described,[38] using the following expression:

$$r_{corrected} = r \left(\frac{g_{pump}^{eff} g_{det}^{eff}}{2.0023^2} \right)^{1/3} \tag{3.21}$$

where g_{pump}^{eff} and g_{det}^{eff} are the effective g-values of the pump and detection spin centres, calculated as averages weighted by the corresponding spectral intensities. This g-factor correction was also applied in the analysis of individual dipolar traces.

Rigid-body docking simulations

All rigid-body docking simulations were carried out using the ClusPro online protein-protein docking server.[140–143] Receptor and ligand were taken to be the crystal dimer structure of myoglobin (PDB: 3VM9)[137] and a crystal monomer structure (PDB: 5ZZE),[144] respectively. From the top 25 models by cluster population, one structure contained a metal-metal distance < 3 nm (2.7 nm), compatible with the short distance obtained from the LITTER and RIDME experiments.

Chapter 4

Two-colour LITTER with non-identical chromophores

Chapter 3 presented the new light-induced triplet-triplet electron resonance (LITTER) technique, which enables the measurement of the dipolar interaction between two photogenerated triplet states. The electron spin-echo detection is performed on a triplet formed by a laser pulse preceding the MW pulse sequence, while the second (pump) triplet is generated by a variable-time laser pulse, switching on the dipolar interaction between the two paramagnetic centres. This technique was used to study the distances and relative orientations of porphyrin chromophores in bis-labelled model peptides, a heme protein dimer and a tetra-porphyrin molecular cage.

LITTER was developed with identical porphyrin chromophores, where both lasers were used at the same wavelength. In that case, the dipolar modulation of the echo intensity was limited by the occurrence of two-chromophore excitation events in the same molecule by the first laser, due to the lack of photoexcitation selectivity, yielding modulation depth values of only 10 %. In addition, relying on identical chromophores limits the applicability of the technique to systems containing the same endogenous photoexcitable groups or systems labelled with the same chromophore.

This chapter reports the development of two-colour LITTER using non-identical chromophores in order to address these limitations. First, the triplet-forming chromophores best suited for two-colour LITTER in combination with TPP are selected, based on optical and ESR characterisation. In synthetic model peptides labelled with TPP and these chromophores, large modulation depth enhancements are achieved with respect to previous one-colour experiments. Finally, these non-identical chromophores are used as dual spin/fluorescent labels to carry out a direct comparison between ESR and FRET distance measurements.

4.1 Identification of suitable chromophores for two-colour LITTER

This section has been adapted from the following book chapter:[60]

A. Bertran, A. Barbon, A. M. Bowen and M. Di Valentin, in *Advances in Biomolecular EPR*, ed. R. D. Britt, Elsevier Inc., 1st edn., 2022, Methods in Enzymology vol. 666, ch. 7, pp. 171–231.

This section reports the results of the spectroscopic characterisation of some chromophores forming photogenerated triplet states and their assessment as potential photoswitchable spin labels for two-colour LITTER: Zn(II) 5-(4-carboxyphenyl)-10,15,20-triphenylporphyrin (ZnTPP), acridine orange (AO), eosin Y (EO), erythrosine B (EB), rose Bengal (RB), Atto Thio12 (AT), crystal violet (CV), toluidine blue-O (TB) and methylene blue (MB). These chromophores have been pre-selected based on published ESR studies.[67,145] The desirable qualities of a photoswitchable triplet spin label are initially discussed for general LiPDS experiments and for LITTER in particular. The typical procedure for the characterisation of a new photoswitchable triplet spin label is then introduced and the results for the aforementioned

candidate chromophores are presented. Finally, the most promising chromophore pairs for two-colour LITTER are selected based on these results.

4.1.1 Desirable qualities of a photoswitchable triplet spin label

A chromophore must have certain spectroscopic properties to perform well as photoswitchable triplet spin label. First of all, it must have a high triplet quantum yield (Φ_T). For organic chromophores, Φ_T can be improved by addition of heavy atoms, such as covalently-linked halogens or coordinated transition metals, which enhance inter-system crossing (ISC).[146] A high extinction coefficient at the wavelength of excitation, ideally within the visible range, is also beneficial but not essential, as it can be compensated by increasing the laser power. Photoexcitation in the UV is often detrimental due to the formation of higher excited states that lead to faster photodegradation of the chromophore.

The resulting triplet state after photoexcitation must have strong and long-lived spin polarisation, together with a long T_1 compared to the duration of the experiment. Short triplet optical lifetime is rarely an issue at the cryogenic temperatures of LiPDS, as typical values are well above the duration of any LiPDS pulse sequence. However, extremely long-lived triplets could limit the maximum repetition rate of the experiment or could reduce signal intensity due to ground-state depletion if very high repetition rates were used. For the triplet state used for spin-echo detection, a long T_m relative to the length of the pulse sequence is also necessary. In addition, a narrow ESR spectrum (small ZFS parameters) for this spin centre is also beneficial to improve the signal intensity, although this usually comes at expenses of orientational resolution if multiple experiments at different spectral positions are carried out. T_m is irrelevant for the second (pump) triplet state in LITTER.

In addition to the aforementioned spectroscopic properties, chromophores

for LiPDS must show good photostability under sustained high-power laser irradiation in degassed frozen solutions, typically for several days. Removing oxygen is important in order to improve the photostability.

When used for structural studies of biomolecules, chromophores should be small, in order not to disrupt the structure and function of the system under investigation. In addition, smaller chromophores can label less exposed sites of the biomolecule, which might be inaccessible with bulky labels. Solubility in water is often a requirement for the labelling process too. Extensive electron spin delocalisation in the triplet state causes additional broadening of the distance distributions obtained; however, this can be taken into account in the analysis and is not necessarily detrimental for the final results.

Finally, it is preferable to use chromophores commercially available in functionalised forms suitable for labelling the biomolecule of interest at the desired site. Functionalised chromophores for biolabelling are often more expensive than their corresponding non-functionalised forms, but given the small amounts required for this type of experiments, price is not critical.

4.1.2 Triplet chromophore characterisation

To assess the suitability of a chromophore for LiPDS, it is useful to perform both optical and ESR spectroscopic characterisation. The UV-Vis absorption spectrum of the chromophore in the ground state will determine the laser excitation wavelength to use in the LiPDS experiments, ideally close to the absorption maximum, and the optimal concentration of chromophore in the sample, which should allow for efficient irradiation of the whole sample volume (sample absorbance < 0.7 at X-band for LITTER with the setup reported in Chapter 4). For two-colour LITTER, the choice of chromophore pairs with complementary absortpion spectra such that photoexcitation can be carried out with high selectivity is critical for the dipolar modulation depth of the experiment. In addition, it is important to take into account that the shape and position of the UV-Vis absorption features might be

solvent- and temperature-dependent. Therefore, a low-temperature UV-Vis absorption measurement in the solvent and at the temperature that will be used for the LiPDS experiments, or at least below the freezing point of the solvent, is recommended whenever possible. For example, for ZnTPP, EO, AT, CV, TB and MB, narrowing and shifts of the absorption bands occur upon cooling (Figure 4.1), while only narrowing occurs for TPP, EB and RB. The triplet state lifetime in those conditions can be determined by transient absorption (TA) spectroscopy (Figure 4.2) and needs to be taken into account if very high repetition rates are used for the LiPDS experiment. This must allow enough time between two consecutive repeats of the experiment for the chromophore to return to the ground state to a reasonable fraction.

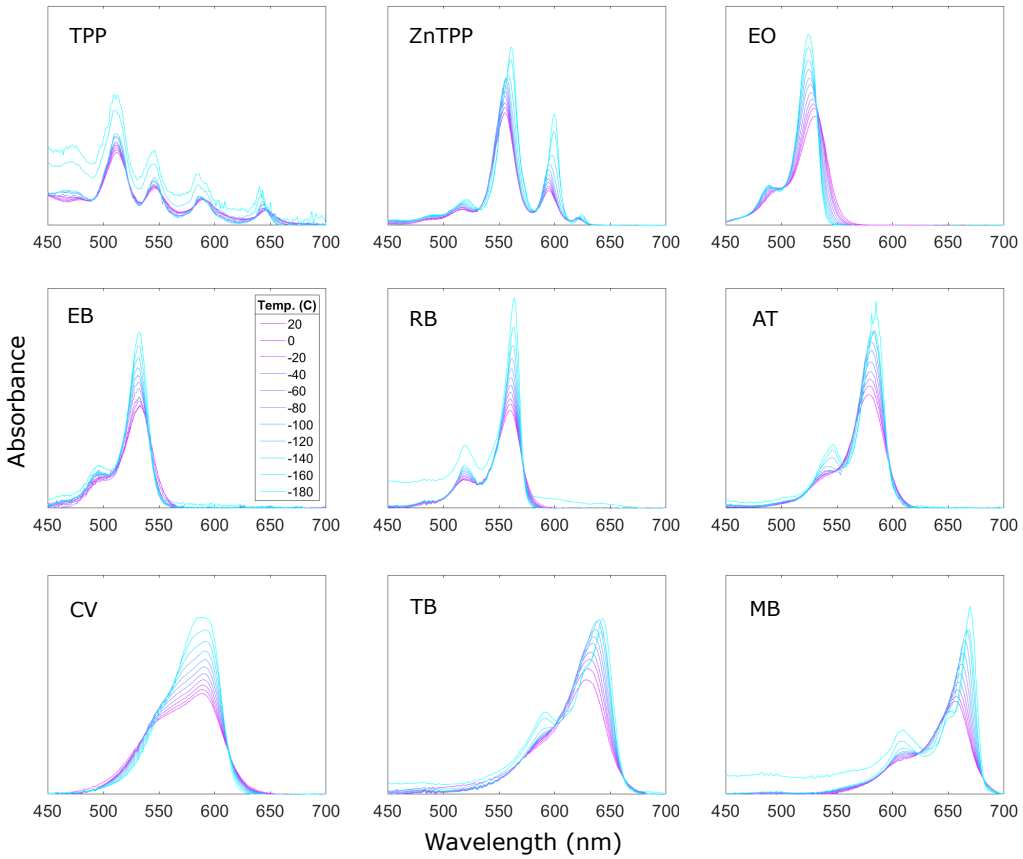


Figure 4.1: Low-temperature optical absorption spectra of the chromophores in ethanol (2-MTHF for ZnTPP). The sudden raise in the baseline of some spectra is due to solvent glass cracking at low temperatures. *Reprinted (adapted) with permission from Bertran, A., Barbon, A., Bowen, A. M., Di Valentin, M. in Advances in Biomolecular EPR, ed. R. D. Britt, Elsevier Inc., 1st edn., 2022, Methods in Enzymology vol. 666, ch. 7, pp. 171–231. doi:10.1016/bs.mie.2022.02.012. Copyright 2022 Elsevier.*[107]

To characterise the ESR spectrum of the photogenerated triplet state, trESR must be used (Figure 4.3 (c)). Simulation and fitting of this spectrum yields the triplet state parameters often needed for the analysis of LiPDS data: g-values, ZFS parameters, triplet sub-level populations, linewidths and strains (Table 4.1). The possibility of selectively forming the triplet state of each chromophore in 1:1 molar mixtures of two chromophores can be assessed by trESR experiments photoexciting at different wavelengths. The

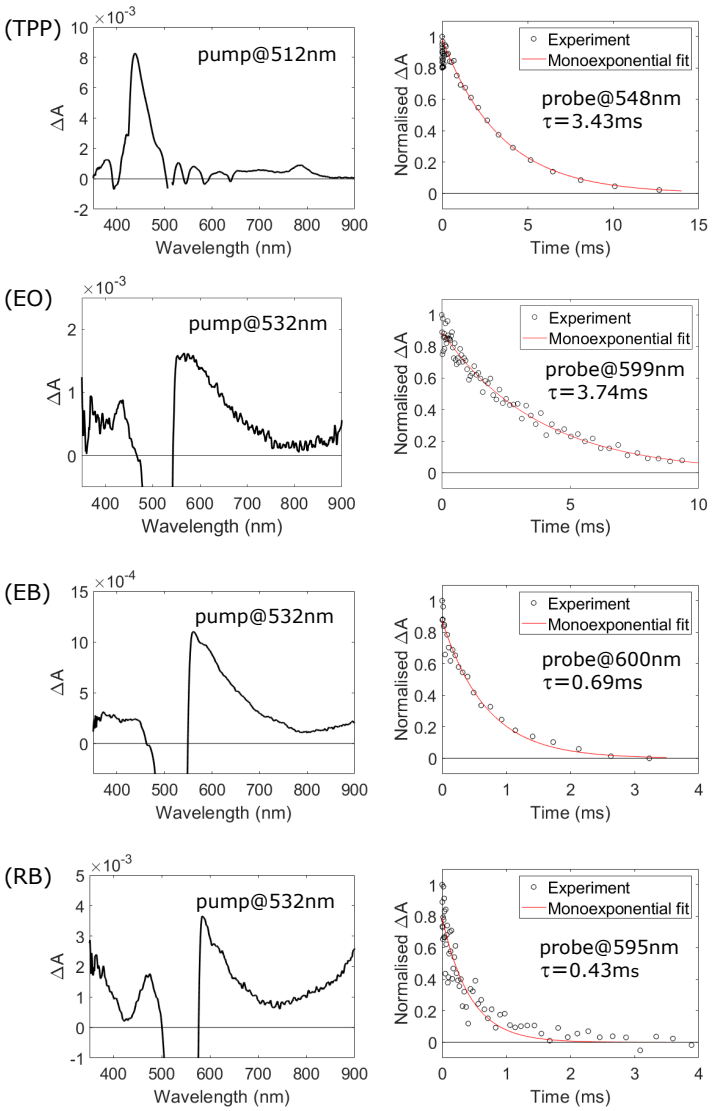


Figure 4.2: Transient absorption spectra of TPP, EO, EB and RB in ethanol at 100 K. (left) Spectra averaged over the first 330 μs and (right) time traces fitted to obtain the triplet state lifetimes. The higher noise level in the RB data is due to its fast photobleaching.

	Φ_T	DAF lifetimes* (ms)	T_m** (μs)	$\lvert D\rvert$ (MHz)	$\lvert E\rvert$ (MHz)	$p_x : p_y : p_z$
TPP	0.88[133]	0.27; 1.56	1.87	1183	228	0.30:0.53:0.17
ZnTPP	0.90[133]	0.17; 1.44	0.84	933	278	0.29:0.30:0.41
AO	0.1[133]	0.22**	0.92	1789	406	0.61:0.35:0.04
EO	0.61[147]	0.36**	1.16	2003	621	0.32:0.62:0.06
EB	0.97[147]	0.01; 0.10	0.35	3486	328	0.40:0.60:0.00
RB	0.93[147]	0.07; 0.89	0.38	3336	278	0.37:0.61:0.02
AT	0.20[a]	0.14; 0.84	0.56	1715	451	0.75:0.00:0.25
CV	0.3[148]	0.16; 0.57	0.63	1605	357	0.08:0.45:0.47
TB		0.46; 1.06	0.61	1530	367	0.21:0.33:0.46
MB	0.52[133]	0.06; 0.34	0.41	1498	284	0.78:0.18:0.04

Table 4.1: Spectroscopic parameters of potential triplet chromophores: triplet quantum yield (Φ_T), delay-after-flash (DAF) lifetimes, phase-memory time (T_m), zero-field splitting parameters (D, E) and triplet sub-level populations (p_x, p_y, p_z). *From biexponential fit. **From monoexponential fit. The DAF and T_m experiments were carried out at the most intense feature of the ESR spectra. See Figures 5.15 and 5.16 in Appendix II for raw data and fits. [a] ATTO-TECH (2021), https://www.atto-tec.com.

ratio of triplet signal intensity from each chromophore can be extracted by spectral fitting and deconvolution. Given that TPP has the most favourable spin relaxation properties to act as detection spin centre (Table 4.1), its photoexcitation selectivity results in mixtures with the other chromophores are shown in Table 4.3. Only the photoexcitation selectivity of laser 1 (i.e. the laser targeting the chromophore to be used as detection centre, chosen to be 512 nm for TPP in this study) is important for the modulation depth of LITTER, as discussed in Section 3.5.2. TPP in combination with EO, AT and CV forms TPP triplet in a very selective manner when photoexcited at this wavelength. The very low fractions of TPP triplet obtained in combination with TB and MB are attributed to an energy transfer process to the latter two chromophores, as they have negligible absorption at 512 nm.

It is also useful to record an echo-detected field-swept spectrum of such triplet state to be used as detection spin centre in LITTER, using a light-induced Hahn-echo pulse sequence with the same delay after flash (DAF) and

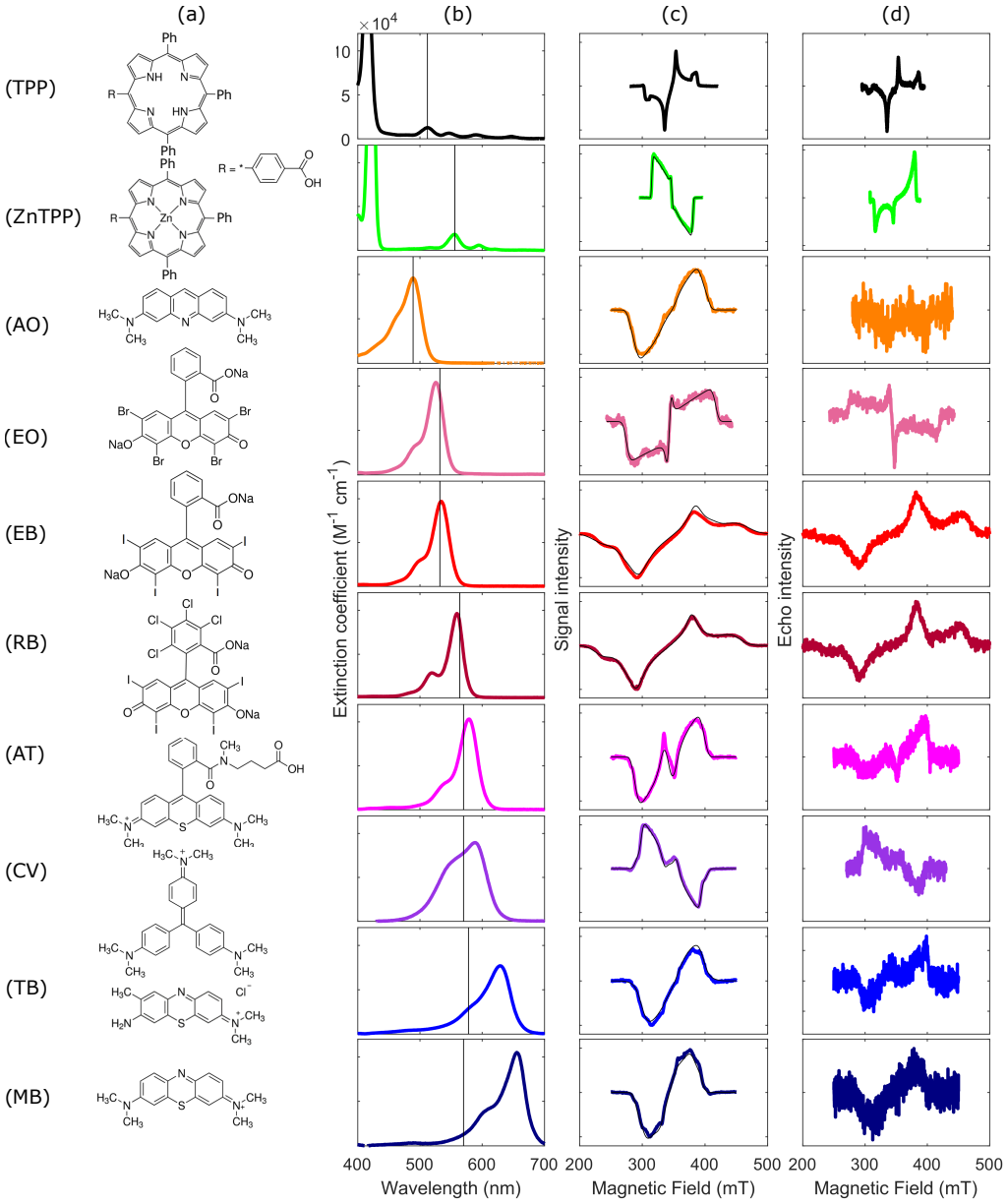


Figure 4.3: Chromophores studied as potential triplet spin labels. (a) Chemical structures. (b) Room-temperature optical absorption spectra in ethanol (2-MTHF for ZnTPP). (c) X-band trESR spectra at 20 K in deuterated ethanol (2-MTHF for ZnTPP) after laser excitation (colour) and simulation using *Easyspin*[109] *pepper* function to extract triplet state parameters (black). (d) X-band pulsed ESR spectra at 20 K in deuterated ethanol (2-MTHF for ZnTPP) after laser excitation *Reprinted (adapted) with permission from Bertran, A., Barbon, A., Bowen, A. M., and Di Valentin, M. (2022). Light-induced pulsed dipolar EPR spectroscopy for distance and orientation analysis, in Advances in Biomolecular EPR, ed. R. D. Britt, Elsevier Inc., 1st edn., 2022, Methods in Enzymology vol. 666, ch. 7, pp. 171–231. doi:10.1016/bs.mie.2022.02.012. Copyright 2022 Elsevier.*[107]

	g-value	linewidth (mT)	D-strain (MHz)	E-strain (MHz)
TPP	2.0054	1.0	59	27
ZnTPP	2.0037	1.5	28	35
AO	2.0242	0.6	292	200
EO	2.0147	2.0	286	0
EB	2.0029	3.0	991	0
RB	2.0383	3.0	789	0
AT	2.0156	3.0	172	200
CV	1.9874	2.0	234	0
TB	1.9995	0.5	404	400
MB	2.0259	1.0	303	200

Table 4.2: Other parameters used for the simulation of the trESR spectra presented in Figure 4.3: g-value, Gaussian linewidth, D-strain and E-strain.

	targeting TPP @ 512 nm	targeting other chromophore
ZnTPP	64:36	11:89
EO	84:16	82:18
EB	64:36	18:82
RB	54:46	14:86
AT	89:11	46:54
CV	79:21	18:82
TB	21:79	9:91
MB	32:68	4:96

Table 4.3: Triplet signal intensity ratios (TPP:chromophore) for 1:1 molar mixtures of TPP with other chromophores. Photoexcitation targeting the second (non-TPP) chromophore was carried out at the wavelengths indicated with vertical lines in Figure 4.3 (b). See Figures 5.15 and 5.16 in Appendix II for raw data and fits.

pulse lengths of the dipolar experiment (flash–DAF–$\frac{\pi}{2}$–τ–π–τ–acquisition, see Figure 1.13), to aid in the choice of field positions for LITTER (Figure 4.3 (d)). The different relative intensities of the spectral features in the echo-detected spectrum with respect to the cw one reflect the different relaxation rates of these features and will determine the intensities of the LITTER traces.

Characterisation of the spin relaxation of the triplet state is key for choosing the optimal experimental parameters in LITTER. The temperature, DAF and inter-pulse delays need to be chosen accordingly. The longitudinal spin relaxation and the decay of spin polarisation due to thermalisation of the non-Boltzmann triplet sub-level populations originated via ISC can be characterised by increasing the DAF stepwise in the previous light-induced Hahn-echo experiment, as explained in Section 1.5.1. A biexponential fit to the echo intensity trace obtained yields a short lifetime dominated by T_1 and thermalisation, and a longer lifetime dominated by triplet decay to the ground state. Similarly, spin-spin relaxation can be characterised by an analogous experiment with fixed DAF and variable τ, and a monoexponential fit to the resulting echo intensity trace yields T_m. In general, in order to use a certain chromophore for LiPDS, the lifetimes obtained from the variable DAF experiment need to be significantly longer than the duration of the LiPDS pulse sequence. For LITTER and other experiments where detection is performed on the triplet, T_m also needs to be longer than the LiPDS pulse sequence. Therefore, detection on a triplet with fast spin relaxation will be limited to short dipolar traces and correspondingly short attainable spin-spin distances. Nevertheless, given that the echo intensity does not always decay monotonically with increasing τ due to electron spin echo envelope modulation (ESEEM), there might be cases where using a longer τ is beneficial for signal intensity. From Table 4.1 it is clear that porphyrins, particularly TPP, have the longest spin relaxation times, making them the best candidates for the detection spin. For the other chromophores, spin relaxation becomes faster when increasing Φ_T, as expected from the heavy-atom effect.

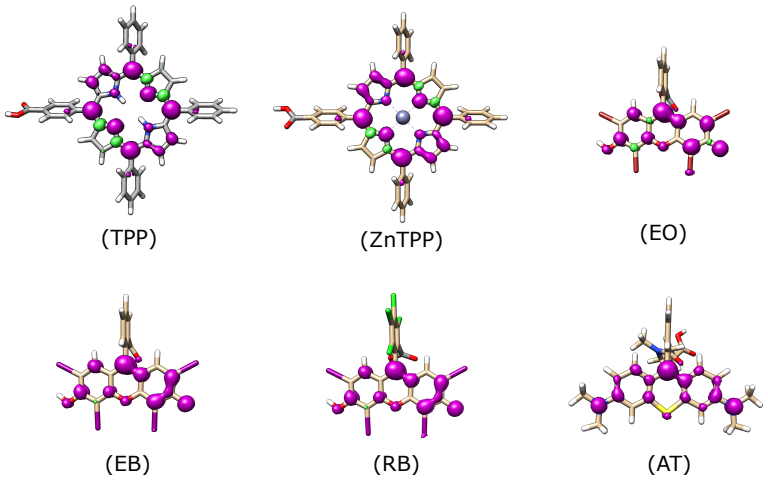


Figure 4.4: Triplet electronic spin density distributions calculated at the DFT level for TPP, ZnTPP, EO, EB, RB and AT. *Reprinted (adapted) with permission from Bertran, A., Barbon, A., Bowen, A. M., and Di Valentin, M. (2022). Light-induced pulsed dipolar EPR spectroscopy for distance and orientation analysis, in Advances in Biomolecular EPR, ed. R. D. Britt, Elsevier Inc., 1st edn., 2022, Methods in Enzymology vol. 666, ch. 7, pp. 171–231. doi:10.1016/bs.mie.2022.02.012. Copyright 2022 Elsevier.*[107]

In addition to spectroscopic characterisation, calculation of the electron spin density distribution in the triplet state prior to experiment is useful to both assess the suitability of the chromophore and aid in the posterior analysis of the dipolar data (Figure 4.4). This can be easily done at DFT level using standard quantum chemistry software such as *Gaussian*[96] or the freely available *Orca*.[108] Triplet states with extensive spatial spin delocalisation (e.g. TPP, ZnTPP and AT in Figure 4.4) will typically lead to broader distributions of dipolar frequency components and might be less suited for the measurement of short spin-spin distances. On the other hand, less spin delocalisation (e.g. EO, EB and RB in Figure 4.4) leads to wider triplet ESR spectra and lower signal intensity at a given spectral position. Electron-nuclear double resonance (ENDOR) spectroscopy on the triplet state can be used to confirm experimentally the mapping of the electron spin density distribution.

4.1.3 Selection of chromophore pairs

From all the triplet chromophores considered, TPP is the best suited to be used as detection centre, due to its high Φ_T, slow spin relaxation and relatively small ZFS parameters. AO yielded extremely weak spin-echo signals owing to its low Φ_T and it was not considered any further. TB and MB were deemed unsuitable for use in combination with TPP due to the energy transfer process observed in TPP:TB and TPP:MB mixtures.

For the second (pump) spin centre, T_m and the size of the ZFS are irrelevant and therefore high Φ_T and low triplet formation when photoexcited at 512 nm were the main selection criteria. In terms of Φ_T, the iodo-derivatives of fluorescein RB and EB are best, closely followed by ZnTPP. Higher Φ_T promises larger modulation depths. However, the 512 nm laser pulse showed the worst photoexcitation selectivity for TPP when combined with these three chromophores. In terms of triplet formation selectivity, AT, EO and CV performed best, yielding 90 to 80 % of TPP triplet after photoexcitation at 512 nm. However, Φ_T for these chromophores, especially for AT and CV, is low, which may be part of the reason why they lead to high TPP triplet formation selectivity.

Given that no candidate pump chromophore clearly stood out from the rest, four different chromophores, representative of the different types investigated, were selected to be tested in two-colour LITTER experiments in combination with TPP: ZnTPP, EB, AT and CV.

ZnTPP constitutes the most natural evolution from the initial porphyrin-porphyrin LITTER work presented in Chapter 3, by introducing Zn(II) inside one of the TPP moieties of the bis-porphyrin model peptides used, and it was exploited as both detection and pump centre for one-colour LITTER in Section 3.3.

EB represents the class of fluorescein-derived dyes, with higher Φ_T than EO and better photostability than RB,[68] and it yielded good ReLaserIMD results for model peptides in Section 2.2.

AT was used in a recent LaserIMD study of a labelled protein.[68] Due to its high price, AT was relegated to the last place in the priority list for two-colour LITTER, in order not to waste precious chromophore in the initial experiment optimisation steps.

Finally, triarylmethyl chromophore triplet states such as that of CV have never been used as spin labels, making this chromophore interesting not only for LITTER, but for the general field of LiPDS. CV is not a chromophore commonly used as biolabel either. However, trityl radical spin labels have recently gathered remarkable interest in the ESR community thanks to their narrow ESR spectra and good stability in reducing environments, such as inside cells.[120,149] Their structural similarities to CV mean that the recent advances in the chemistry and biochemistry of trityl spin labels could be easily transferred to CV and other triarylmethyl dyes. Unfortunately, the synthesis of a CV-TPP model system for LITTER was delayed and only ZnTPP-TPP and EB-TPP systems were available for experiments before the submission of this thesis. These experiments are presented in the following section.

4.2 Two-colour LITTER

This section has been adapted from the following publication:

A. Bertran, C. Dalla Torre, J. Sawyer, L. Morbiato, D. Heyes, S. Hay, C. R. Timmel, M. Di Valentin, M. De Zotti and A. M. Bowen, *J. Am. Chem. Soc.*, *in preparation.*

The molecules used for this study were supplied by Prof. Marta de Zotti (University of Padova, Italy). The FRET data was acquired and analysed by Jack Sawyer, Prof. Sam Hay and Dr. Derren Heyes (University of Manchester, United Kingdom).

This section demonstrates that the modulation depth of LITTER can be greatly enhanced by using non-identical chromophores and two-colour photoexcitation. In synthetic model peptides labelled with TPP and these chromophores, modulation depth improvements corresponding to up to a four-fold reduction of the necessary acquisition times with respect to previous one-colour experiments are achieved. In addition, this shows that LITTER can be performed with non-porphyrin chromophores which are commonly used as biolabels, making the technique directly transferable to structural biology applications. Finally, these chromophores are used as dual spin/fluorescent labels to carry out the first direct comparison between ESR and FRET distance measurements, an important achievement for integrative structural biology which was not possible with conventional spin labels. The obtained distance results are in excellent agreement mutually and with DFT predictions.

4.2.1 Characterisation of the model systems

Bis-labeled model peptides **1** and **2** containing the chromophore pairs ZnTPP-TPP and EB-TPP were synthesised to have rigid α-helical structure resulting from alternating Leu-Aib residues (Figure 4.5). Two important synthetic strategies were applied: firstly, a sarcosine (Sar) linker was used to attach the labels to the N-terminus, avoiding the formation of the colourless EB spirolactam.[106,107] This method is advantageous to previously reported strategies as it uses the more affordable non-derivatised chromophore and introduces a shorter linker.[68] Secondly, Zn(II) complexation inside TPP was carried out with resin-bound TPP-peptide, reducing the number of purification steps compared to the usual complexation in solution.[150]

A two-colour version of LITTER was used in this study (Figure 4.5 (c)). Due to its longer triplet state T_m, TPP was chosen as the detection spin centre, formed by photoexcitation at 512 nm. The selectivity towards formation of TPP triplet state at this wavelength was assessed by trESR in 1:1 molar

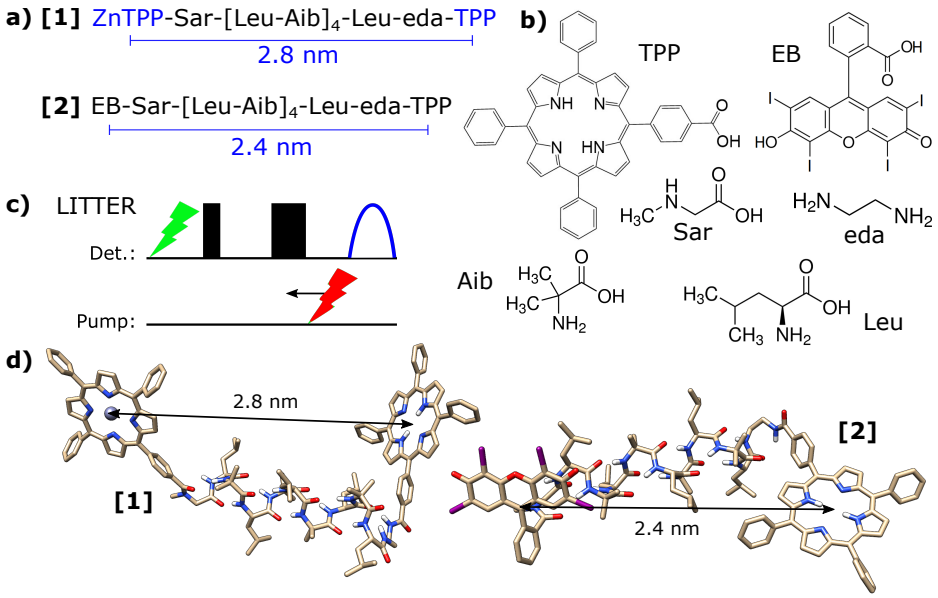


Figure 4.5: (a) Amino acid sequences of molecules **1** and **2**. Key: Sar (sarcosine), Leu (L-leucine), Aib (α-aminoisobutyric acid), Eda (ethylenediamine). (b) Chemical structures of the different building blocks. (c) Two-colour LITTER pulse sequence. (d) DFT-optimised geometries of **1** and **2**, with the chromophore centre-to-centre distances indicated.

mixtures of the free chromophores (Figure 4.6 (a, b)) and in **1** and **2** (Figure 4.6 (c, d)), showing enhanced TPP triplet formation in the labelled peptides, going from 65 % TPP triplet for the free chromophores to 85 % and 100 % for **1** and **2**, respectively. This suggested energy transfer from ZnTPP and EB to TPP in the bis-labeled molecules. Given that the appearance of the TPP triplet spectrum in the trESR experiments was not delayed with respect to the small proportion of ZnTPP and EB triplet, and considering the distances between chromophores predicted by DFT (> 2 nm, see Figure 4.5 (d)), this energy transfer is expected to proceed *via* the singlet-singlet resonant or Förster mechanism, involving the dipole-dipole coupling between the two $S_0 \rightarrow S_1$ transitions.[66] The first excited singlet energies for TPP, ZnTPP and EB in polar solvents are 185, 199 and 212 kJ/mol,[133] meaning that the energy transfer from EB to TPP is more energetically favourable than from ZnTPP. This is consistent with the higher fraction of TPP triplet observed for **2**. The wavelength for the second laser was chosen to be 556 nm and 532 nm for **1** and **2**, respectively, close to the absorption maximum of the pump chromophore and at an absorption minimum of TPP.

4.2.2 Two-colour LITTER

The two-colour LITTER trace (512/556 nm) for **1** yielded a modulation depth of 27 % (Figure 4.7 (b), red), corresponding to a two-fold improvement in modulation-to-noise ratio (MNR) from the one-colour experiments between two TPP chromophores presented in Chapter 3 (from MNR = 7 to MNR = 15, calculated as the modulation depth relative to the noise level at the end of the trace), reducing the acquisition time by a factor of four. The improvement is due to using ZnTPP as pump instead of TPP, which has two beneficial contributions to the modulation depth. First, it provides a higher triplet quantum yield of the pump chromophore, which contributes to an increased modulation depth as already seen with ZnTPP-ZnTPP in Section 3.3.1. Second, in combination with TPP as detection chromophore and targeted two-colour photoexcitation, it decreases the unwanted excitation of the

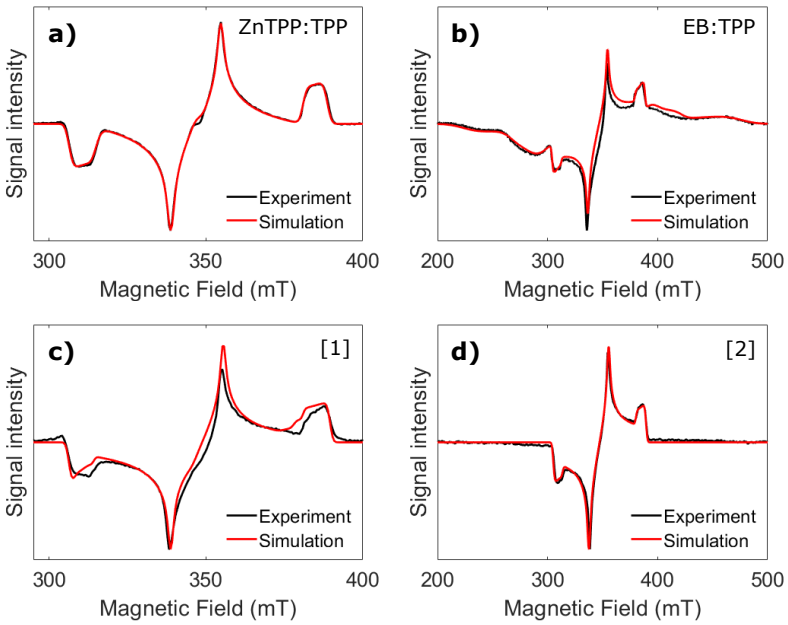


Figure 4.6: Triplet formation selectivity experiments at 512 nm. (a, b) trESR spectra of 1:1 mixtures of ZnTPP:TPP (a) and EB:TPP (b) after laser excitation (black), and simulations using mixtures of the individual triplet spectra in Figure 4.3 (c), performed with *EasySpin pepper* function[109] (red). The fraction of TPP triplet included in the simulations was 65 % in both cases. (c, d) trESR spectra of **1** (c) and **2** (d) after laser excitation (black), and simulations using mixtures of the individual triplet spectra. The fractions of TPP triplet included in the simulations were 85 % (c) and 100 % (d).

pump chromophore by laser 1, which contributes to further increasing the modulation depth. Indeed, the modulation depth is highly sensitive to the wavelength used for laser 2 and the corresponding one-colour LITTER trace (512/512 nm) on **1** resulted in a modulation depth of only 5 % (Figure 4.7 (b), blue) due to the low absorbance of ZnTPP at that wavelength (Figure 4.7 (a), blue).

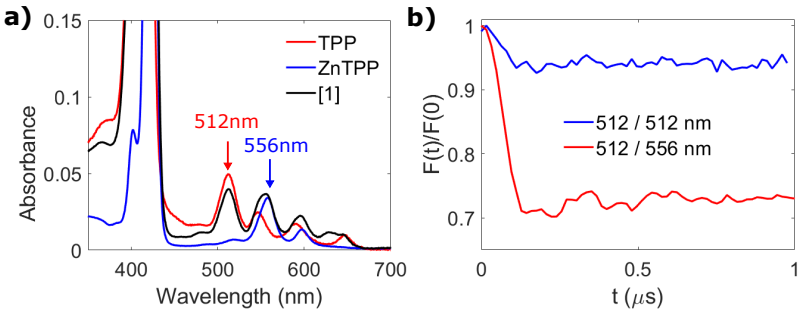


Figure 4.7: (a) Room-temperature optical absorption spectrum of **1** (black), with TPP (red) and ZnTPP (blue) reference spectra. (b) Background-corrected and normalised one-colour (512/512 nm, blue) and two-colour (512/556 nm, red) LITTER traces of 40 μM **1**, acquired on the most intense feature of the TPP triplet ESR spectrum (Figure 4.9 (a), red). The modulation depths are 5 % (one-colour) and 27 % (two-colour).

To investigate the suitability of non-porphyrin chromophores for LITTER, the two-colour experiment was repeated with **2** using the wavelengths 512/532 nm for lasers 1 and 2, respectively. Sample concentration had to be reduced due to the high absorbance of EB at 532 nm (Figure 4.8 (a), blue), in order to avoid excessive attenuation of laser 2 when going through the sample, which would prevent efficient photoexcitation of the complete sample volume by this laser. This yielded a maximum observed modulation depth of 23 % (Figure 4.8 (b), red). The samples of both **1** and **2** had concentrations corresponding to an absorbance of 0.7 through the vertical dimension at the second wavelength. As the sample concentration was controlled by the absorption, the smaller modulation compared to **1** could be attributed to the higher energy transfer efficiency in the EB/TPP pair. MNR was similar to that obtained with **1** (MNR = 14 at 12 μM and MNR = 12 at 40 μM).

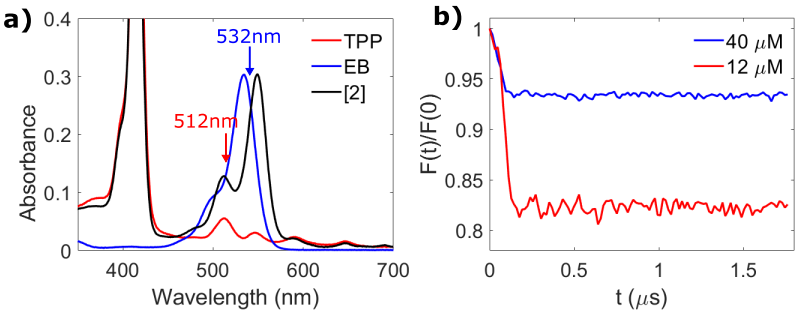


Figure 4.8: (a) Room-temperature optical absorption spectrum of **2** (black), with TPP (red) and EB (blue) reference spectra. (b) Background-corrected and normalised two-colour (512/532 nm) LITTER traces with 40 μM (blue) and 12 μM (red) **2**, acquired on the most intense feature of the TPP triplet ESR spectrum (Figure 4.9 (a), red). The modulation depths are 8 % and 23 %, respectively.

Two-colour LITTER traces were recorded across the Y^- and Z^- turning points for the TPP triplet spectrum (Figure 4.9 (a-c)). Compared to studies on previous systems with two TPP chromophores, little orientation dependence was observed, likely a result of the different geometries of these systems which used both Sar and Eda linkers to attach the porphyrins to the peptide backbone, instead of direct amide bonding at the N-terminus and a trans-1,4-diaminocyclohexane linker at the C-terminus. The isomerism of the protonated states in TPP interconverts the X- and Y-axes of the ZFS-tensor. Thanks to this, averaging two traces measured close to the Y^- turning point and one measured on Z^- yields reasonable orientational averaging, allowing the resultant trace to be analysed using Tikhonov regularisation to extract spin–spin distance distributions for both molecules (Figure 4.9 (d, e)). The main distance features were consistent with the DFT-optimised geometries of [**1**] and [**2**] (Figure 4.5 (d)), and the distribution widths suggested a significant degree of conformational flexibility of the two molecules in solution, which might originate from the unwinding of the α-helix at the peptide termini observed in the optimised geometries.

The large modulation depths obtained with two-colour LITTER constitute a significant improvement with respect to the one-colour experiments reported in Chapter 3. However, they are still far from the values expected

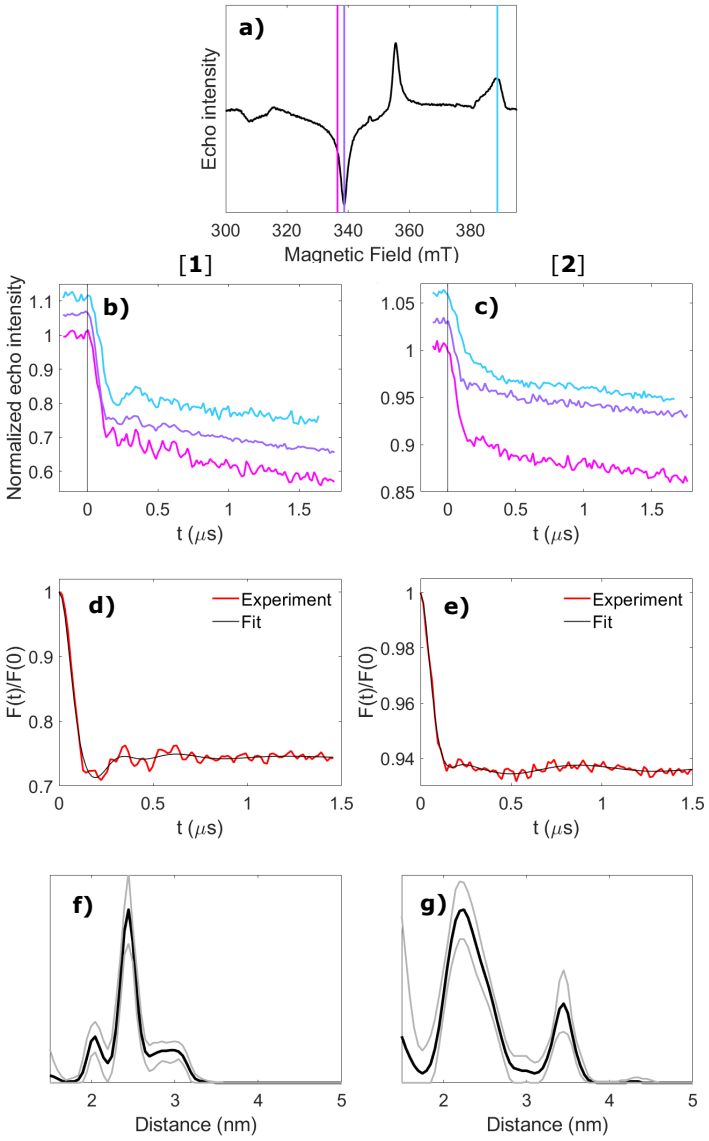


Figure 4.9: (a) Echo-detected field-swept ESR spectrum of **2** acquired after photoexcitation at 512 nm, showing the field values used for LITTER as vertical lines. (b, c) Raw two-colour LITTER traces for 40 μM **1** (512/556 nm) and 40 μM **2** (512/532 nm), respectively. (d, e) Averaged LITTER form factors (red) with fits obtained by Tikhonov regularisation (black). (f, g) Spin-spin distance distributions, with maxima at 2.5 and 2.3 nm, respectively. The 95% confidence bounds on the spin-spin distance distribution as determined using the Comparative DEER Analyser tool are indicated in gray.

for completely photoexcitation-selective experiments according to the analytical expression for the modulation depth derived in Section 3.5.2 (60 and 55 % for **1** and **2**, respectively) This suggests that laser 1 may be exciting a significant fraction of pump chromophores, or that energy transfer may destroy some of the excited states of the pump chromophore, observed as the relative loss of triplet state signal from the EB and ZnTPP with respect to TPP in the trESR experiments (Figure 4.6). Therefore, there is potential room for increasing the modulation depth of LITTER by further reducing the fraction of spectral overlap and unwanted excitations, through better chromophore pair and excitation wavelength choice. More red-shifted chromophores such as CV and AT would be worth testing in combination with TPP.

4.2.3 Direct comparison to FRET

Finally, the energy transfer occurring in the studied chromophore pairs has been exploited to perform ensemble FRET distance measurements between the same labels used for LITTER, which act as both spin centres and fluorophores. FRET is a non-radiative energy transfer process between a donor and an acceptor fluorophore in close proximity (3 to 8 nm), which requires that the fluorescence emission spectrum of the donor overlaps with the absorption spectrum of the acceptor.[151] This process leads to a quenching of the fluorescence of the donor in the presence of the acceptor (I_{DA}), with respect to the fluorescence of the donor alone (I_D). The FRET efficiency (E_{FRET}) can be calculated from these fluorescence intensities as follows:

$$E_{FRET} = 1 - \frac{I_{DA}}{I_D} \tag{4.1}$$

and it can be related to the average distance between the two chromophores (r) through the Förster radius (R_0):

$$E_{FRET} = \left[1 + \left(\frac{r}{R_0}\right)^6\right]^{-1} \tag{4.2}$$

The Förster radius for a given chromophore pair in a given system can be calculated as

$$R_0 = \left(8.79 \times 10^{-5} \frac{\Phi_{fl}^D J \kappa^2}{n^4}\right)^{1/6} \tag{4.3}$$

where n is the refractive index, Φ_{fl}^D is the fluorescence quantum yield of the donor in absence of acceptor, and κ is the orientation factor, which can be assumed to be $\frac{2}{3}$ for systems with short rotational correlation times.[152,153] J is the overlap integral between the emission spectrum of the donor and the absorption spectrum of the acceptor, given by

$$J = \int f_D(\lambda) \epsilon_A(\lambda) \lambda^4 d\lambda \tag{4.4}$$

where $f_D(\lambda)$ is the normalised emission spectrum of the donor and $\epsilon_A(\lambda)$ is the absorption spectrum of the acceptor.

FRET can be performed on liquid samples in physiological conditions, which allows measurements *in vivo* inside cells.[154] In addition, it allows for the study of molecular dynamics in real time down to nanosecond resolution. Therefore, the ability to perform FRET on the exact same system investigated by LITTER complements the study with more biologically-relevant information and acts as a control for potential artefacts due to the frozen-solution nature of PDS.

TPP behaved as the FRET acceptor in **2** (Figure 4.10 (b)), while forwards and backwards FRET was observed in **1** when exciting at different wavelengths (see Figure 5.18 in Appendix II). The occurrence of other photophysical effects in addition to FRET prevented the analysis using TPP as acceptor in **1**, and ZnTPP was used as acceptor instead. The determined FRET distances are shown as intervals in Figure 4.10 (c, d), reflecting the uncertainties in the analysis process. For **1**, the range of distance values arises from the uncertainty in the baseline correction due to the similar fluorescence values at the wavelength used for analysis (Figure 4.10 (a)). For **2**, it arises from the range of Φ_{fl} values reported in the literature for EB.[155] Adsorption of EB on a protein surface has been found to significantly increase Φ_{fl} with respect to the free chromophore. Φ_{fl} of EB in **2** is expected to be between the free and adsorbed chromophore values. The FRET distances obtained can be directly compared to LITTER distance distributions thanks to the use of dual spin/fluorescent labels in this study, which was not possible in previous works comparing FRET to conventional nitroxide–nitroxide DEER.[154,156–158] These distances are in good agreement with LITTER and DFT results (Figure 4.10 (c, d)). Owing to the ensemble character of room-temperature FRET, where numerous conformations of the system of study are likely energetically accessible, the use of molecular dynamic calculations would be preferable over DFT as it could provide detailed structural information of the different conformations sampled by the system at this temper-

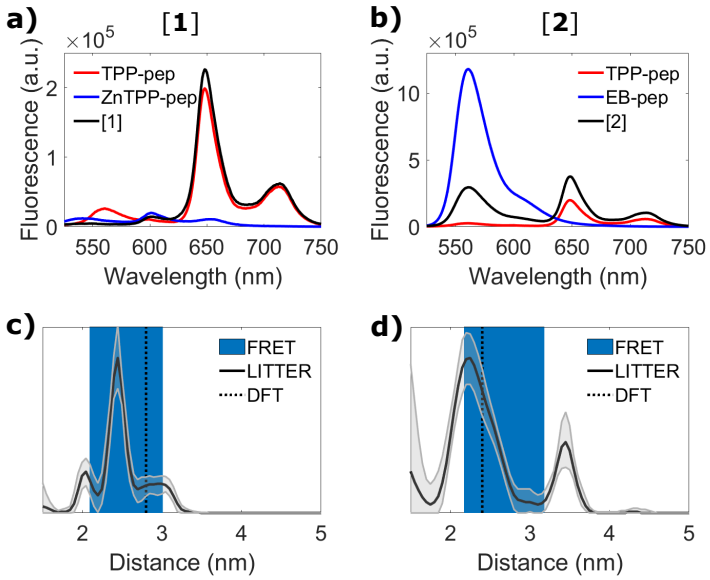


Figure 4.10: Fluorescence spectra of the bis-labelled peptides **1** (a) and **2** (b) (black), and of singly-labelled peptides with each of the chromophores: TPP-peptide **3** (red), ZnTPP-peptide **4** (blue, a), EB-peptide **5** (blue, b). Excitation has been performed at 510 nm. See Figure 5.17 in Appendix II for the amino acid sequences of **3**, **4** and **5**. Comparison of the determined distances for **1** (c) and **2** (d) by FRET (blue), LITTER (solid black line) and DFT (dotted line). The 95% confidence bounds on the spin-spin distance distribution as determined using the Comparative DEER Analyser tool are indicated in gray. FRET analysis was carried out with the fluorescence values at 561 nm (further details are given in Section 4.4.)

ature. These calculations could not be performed before the submission of this thesis due to time constraints, but collaboration on this line is ongoing with Prof. Alberta Ferrarini (University of Padova, Italy).

4.3 Conclusions

In conclusion, this chapter has reported, for the first time, LITTER experiments with non-identical chromophores and two-colour photoexcitation, obtaining larger modulation depths corresponding to a four-fold shortening of the acquisition time with respect to previous one-colour measurements.

Given the high costs associated with PDS measurement time, this achievement is a big step towards making LITTER a more accessible technique. This work has also shown that LITTER can be performed with non-porphyrin chromophores commonly used as biological labels, making the technique directly transferable to structural biology applications. In addition, these dual spin/fluorescent labels have been used to carry out the first parallel distance measurements by ESR and FRET on the exactly the same molecules, allowing for direct comparison between the two techniques and removing the need for preparing different labelled samples.

The selective optical addressability of each chromophore in the presented technique has the potential to enable unambiguous PDS distance determination in systems with more than two labels, without the interference of multi-spin effects.[29,34] Optical orthogonality is easier to achieve and allows a wider choice of labels than ESR orthogonality.[31,32] Therefore, the two-colour LITTER technique offers a promising route to controlling complexity in PDS of multi-spin systems. Finally, the use of only photogenerated triplets as spin labels, which can be formed within cells, makes LITTER suitable for in-cell ESR studies, where conventional nitroxide labels degrade rapidly.[105,119] If combined with fluorescence microscopy, LITTER could provide location-specific structural information for the labelled biomolecules inside the cell.

4.4 Methods

See Appendix I for general instrumentation.

Sample preparation

Bis-labelled and singly-labelled model peptides **1**-**5** were supplied by Prof. Marta de Zotti (University of Padova, Italy).

Samples of the free chromophores were prepared at 1 to 4 μM in spectroscopic grade ethanol ($\geq$ 99 %, Sigma-Aldrich) for optical spectroscopy and at 100 μM in deuterated ethanol (99 % atom D, Sigma-Aldrich) for ESR. For TA, solutions were degassed by freeze-pump-thaw and flame-sealed inside 2 mm glass flat cells. For ESR, solutions were degassed by freeze-pump-thaw and loaded inside 3.9 mm quartz tubes.

Optical spectroscopy

Steady-state optical absorption spectra at room temperature were acquired in 10 mm quartz cuvettes using a UV-Vis spectrophotometer (Cary 60, Agilent Technologies). For low-temperature measurements, a liquid nitrogen cryostat (Oxford Instruments) was fitted inside the spectrometer and 2 mm quartz cuvettes were used.

TA spectra were acquired in sealed 2 mm glass flat cells using a nanosecond transient absorption spectrometer (EOS, Ultrafast systems) after photoexcitation by a Nd:YAG-pumped optical parametric generator (PL2210 and PG403, Ekspla). Triplet spectra were averaged around the signal maximum and time traces taken at specific wavelength were fitted with monoexponential curves to obtain the triplet state lifetimes.

ESR spectroscopy

ESR measurements were performed in a pulsed X-band spectrometer (ElexSys E680, Bruker) using a dielectric resonator (EN 4118XMD5, Bruker), which was critically coupled for trESR and overcoupled for pulsed experiments, and a wet cryostat (Oxford Instruments). The temperature was kept at 20 K using liquid helium.

For trESR, the signal was averaged around the intensity maximum of the time trace and the spectra were simulated using *EasySpin pepper* function[109] to extract spin Hamiltonian parameters for the triplet states.

For pulsed experiments, rectangular MW pulses of 16-32 ns for $\frac{\pi}{2} - \pi$ were used. The laser setups were the same as described in CHAPTER 4, with laser energies of 2 and 3 mJ per flash for laser 1 and laser 2, respectively, a time delay between the two laser pulses of 7 μs and a repetition rate of 20 Hz. Echo-detected field-swept spectra, longitudinal relaxation traces and transverse relaxation traces were acquired using the pulse sequence laser "1 - DAF - $\frac{\pi}{2}$ - τ - π - τ - acquisition" as described in Section 1.5.1. LITTER was performed using the usual pulse sequence "laser 1 - DAF - $\frac{\pi}{2}$ - τ - π - τ' - laser 2 - τ'' - acquisition", with $\tau = \tau' + \tau''$.

The LITTER traces acquired at three different field positions were added together weighted by the corresponding spectral intensities to obtain an averaged trace. A third-order polynomial background correction was applied to yield a form factor that was latter analysed by Tikhonov regularisation using *DeerAnalysis2019*[35] with a regularisation parameter $\alpha = 10$ to extract the corresponding distance distribution.

FRET

Samples for FRET were prepared in ethanol (99.8% analytical reagent grade, Fisher Scientific). Initial stocks of 5 μM of each compound were prepared, from which dilutions gave samples with identical absorbance at the excita-

tion wavelength used. Final concentrations of 0.7 μM for compounds **1**, **3**, and **4**, 1 μM for compound **2**, and 2 μM for compound **5** were prepared. UV-Vis spectra for extinction coefficient and spectral overlap determination were acquired with a Cary 60 UV-Vis spectrometer (Agilent Technologies). Fluorescence emission spectra were recorded at room temperature on an FLS920 series spectrometer (Edinburgh Instruments) equipped with an Xe900 xenon arc lamp (Edinburgh Instruments). An excitation wavelength of 510 nm was used for both FRET pairs, recording emission scans from 525-750 nm in 1 nm steps, and a dwell time of 1 s. An excitation and emission bandwidth of 5 nm was used in all cases.

For **1**, the FRET efficiency was calculated using Equation 4.1 with and without correction for the background signal, giving $E = 0.985$ and 0.864, respectively. This also provides a correction for any emission from the direct excitation of the ZnTPP. Using the values given in Table 4.4, r values calculated from these E with Equation 4.2 are $r = 21.7$ Åand 31.8 Å, which give lower and upper bounds to the estimate of the ZnTPP–TPP distance in **1**.

For **2**, the FRET efficiency was calculated using Equation 4.1 with and without correction for the background signal, giving $E = 0.913$ in both cases due to the negligible background in these measurements. As there is some disagreement over the Φ_{fl} of EB, r values were calculated from this E value using $\Phi_{fl} = 0.02$ and 0.17, giving $r = 20.5$ Åand 29.2 Å, respectively. These values give lower and upper bounds to the estimate of the EB–TPP distance in **2**.

DFT calculations

Initial geometries for the bis-labelled peptides were built using *UCSF Chimera*.[113] Geometry optimisations and spin density calculations were performed *in vacuo* using *Gaussian16* (revision A.03).[96] Ground-state geometry optimisations of the peptides were carried out in the singlet spin state using the PBE1PBE functional and the 6-31g(d) basis set, replacing ZnTPP by TPP

Variable	Value
n of ethanol[133]	1.4
Φ_{fl} of EB[155]	0.2 - 0.17
Φ_{fl} of TPP[159]	0.13
ϵ of TPP	451600 M^{-1} cm^{-1}
ϵ of ZnTPP	511800 M^{-1} cm^{-1}
R_0 for EB-TPP	43.19 Å
R_0 for ZnTPP-TPP	43.31 Å
J for EB-TPP	2.5076×10^{15} M^{-1} cm^{-1} nm^4
J for ZnTPP-TPP	3.3371×10^{15} M^{-1} cm^{-1} nm^4

Table 4.4: Values for the variables used in the analysis of FRET data. R_0 was calculated with Equation 4.3. J was calculated with Equation 4.4.

and the I atoms in EB by H. The geometries of the chromophores were optimised in the triplet state to obtain the electronic spin densities, taken as atomic Mulliken spin densities. These calculations were performed in *Gaussian16* for TPP and ZnTPP (B3LYP; Def2-SVP for H, C, N and O; Def2-TZVP for Zn(II)), and in *Orca*[108] (release version 4.2.0) for EO, EB, RB and AT (BP86; Def2-SVP for H, C, N and O; Def2-TZVP for S, Br and I). The resolution of identity (RI) approximation, with the auxiliary basis set def2/J, was used in the latter cases.

Chapter 5

Conclusions and outlook

The aim of this thesis was the development and application of novel methodologies in the emerging field of light-induced pulsed dipolar spectroscopy (LiPDS), a recently introduced field of electron spin resonance (ESR). In this thesis, LiPDS is particularly focused on elucidating the structures of macromolecular systems that contain endogenous or artificially-added photoexcitable chromophores.

Chapter 1 set the scene for this research work, introducing the theoretical and experimental background of ESR and PDS, and providing a detailed review of the state of the art of the field of LiPDS.

Chapter 2 investigated the orientational effects in previously reported LiPDS techniques, light-induced double electron-electron resonance (LiDEER) and refocused-echo laser-induced magnetic dipole (ReLaserIMD) spectroscopy, and how to exploit them in order to extract additional information on the structure and the conformation of the molecules of study. Using bis-labelled porphyrin-nitroxide model peptides, these techniques were combined to reduce the parameter space required for simulation, simplifying the simulation process and enabling the full characterisation of the relative orientation of the two spin centres. In addition, and a new two-dimensional LiPDS technique,

frequency-correlated ReLaserIMD, was developed to capture the complete orientational dependence of the dipolar interaction with a single experiment, achieving improved frequency resolution and a larger span of frequency offsets. Orientation-dependent analysis of the LiPDS data provided molecular-level geometric structural information of the systems of study, including information on structural distributions, which was validated using DFT calculations. Alternatively, orientational averaging procedures were described, enabling orientation-independent analysis of the dipolar datasets to yield the conventional spin-spin distance distribution.

These newly-developed methodologies were successfully applied to the structural study of bis-labelled chromophore-nitroxide model peptides containing other non-porphyrin chromophores, erythrosin B (EB) and I_2BODIPY, which had never been reported for PDS before. Their excellent spectroscopic properties, small size, biocompatibility and commercial availability in functionalised forms for biolabeling make them ideal candidates for biological applications.

Finally, the feasibility of LiPDS experiments with EB above liquid nitrogen temperatures was demonstrated, removing the need for expensive liquid helium or cryogen-free cryostats, which often restricts the accessibility of these techniques to institutions and researchers with reduced funding. In addition, decoupling these techniques from the use of helium, which is a finite resource becoming scarce, makes LiPDS studies more sustainable.

Rigidly embedded endogenous spin centres, such as native cofactors which are either present in a paramagnetic state or can be photoexcited to form a suitable triplet state, are of significant interest for the PDS study of unmodified protein systems, in particular for investigations in near-native environments where conventional spin labels, such as nitroxides, may degrade.[105] While the rigidity of the binding site within the protein structure may result in narrow distance distributions enabling more accurate reporting of protein structural changes, the likely orientation selection of PDS experiments on such systems necessitates careful analysis. Consequently, the combined

approaches presented here for the PDS experiments measured between a photogenerated and a permanent paramagnetic centres will likely prove useful in the analysis of endogenous PDS studies. These methods offer the ability either to obtain geometric information on the structure of macromolecules, beyond the distance distribution, or to reduce the complexity of the measurements such that orientation-independent analysis of the dipolar trace can be confidently performed. Although orientational information can also be obtained in PDS of metal-containing systems,[27,38,40,47,115] photogenerated triplet states have proven to be superior for detection owing to their strong spin polarisation and more favourable relaxation properties.[72]

When generalising to the study of any protein system, which may not contain suitable endogenous chromophores, the variety of choice in photoswitchable spin labels is critical for the expansion of LiPDS to become a widespread and complementary methodology to conventional PDS. This work takes an important step in this direction by introducing new photoswitchable triplet spin labels.

Chapter 3 tackled the challenge of measuring the dipolar interaction between two photogenerated triplet states, thereby removing the need for having any permanent spin centre in order to perform PDS. A new LiPDS technique was developed for this purpose, light-induced triplet-triplet electron resonance (LITTER) spectroscopy, which combined the concepts of LiDEER and LaserIMD to use photogenerated triplet states for both detection and pump. Following proof-of-concept experiments, an in-depth conformational study was performed on a spectroscopic molecular ruler consisting in bis-porphyrin model peptides with different porphyrin-porphyrin distances and relative orientation. Exploiting the orientational effects in LITTER, originating from the large anisotropy of the triplet ZFS-tensor, information on the conformational distribution of the molecules in frozen solution was extracted using orientation-dependent simulations and fits, in good agreement with density functional theory (DFT) predictions. Direct comparison to conven-

tional DEER between Cu(II) centres showed that LITTER is advantageous in allowing data to be recorded in a shorter amount of time and at a higher temperature thanks to the strong spin polarisation and longer T_m of the photogenerated porphyrin triplet state. In addition, being a single-frequency technique, LITTER removes the limitations of DEER in terms of available resonator bandwidths with regard to spectral width, and its orientational resolution does not require the use of high fields as it originates from the triplet zero-field splitting (ZFS), unlike for conventional spin-half centres. This highly anisotropic ZFS offers orientational resolution comparable or exceeding that of typical metal centres with large g-anisotropy, such as Cu(II) and Fe(III). Alternatively, the orientational averaging procedure presented in Chapter 2 was shown to work well with LITTER datasets too, enabling a computationally faster orientation-independent analysis that can be used when orientational information is not required.

The novel LITTER technique was applied to the structural study of more complex molecular systems, such as a dimeric heme protein and a supramolecular porphyrin tetramer, with the aim of demonstrating its potential for real structure determination problems. In the Zn(II)-substituted dimeric heme protein myoglobin, LITTER allowed the study protein oligomerisation and the structure of the oligomers without need for any labelling, which is unusual in conventional PDS and was not possible with previous LiPDS techniques. The obtained results were in partial agreement with the reported crystallographic structure of myoglobin dimer and suggested the presence of some trimer that is suspected to be the source of the additional short distance observe in the data. This was supported by mass spectrometry and relaxation-induced dipolar modulation enhancement (RIDME) experiments, and rigid-body docking simulations. In the tetra-porphyrin molecular host, LITTER confirmed and quantified the conformational change caused by the complexation of the C_{60} guest molecule suggested by nuclear magnetic resonance (NMR) and computational studies.

Finally, an analytical treatment of LITTER was provided, with a density-

operator description of the experiment and analytical expressions for the dipolar modulation depth as a function of chromophore photoexcitation efficiencies and triplet quantum yields. This exposed the limitations of this new technique arising from the use of identical chromophores and one-colour photoexcitation, reducing the modulation depth of the dipolar traces and restricting its applicability to unmodified homodimeric systems or systems labelled with the same chromophore.

LITTER removes the restriction, recurrent in all previous LiPDS techniques, of having to use one stable paramagnetic centre to perform distance measurements. By accessing the dipolar interaction between two photogenerated triplet states, LITTER has the potential to allow the determination of distance distributions and relative orientations in unmodified macromolecular systems containing endogenous photoexcitable moieties, such as light-harvesting proteins, heme proteins and flavoproteins, or systems modified with several photoexcitable triplet spin labels. The use of photogenerated triplets as spin probes makes this technique a strong candidate for performing structural studies in the cellular environment, as triplets can be formed within cells.[117] Removing the need to have a permanent paramagnetic centre, such as a nitroxide spin label, known to be unstable and rapidly degraded inside cells,[118,119] is a key point for the success of in-cell structural studies. This also mitigates the need to use more complex spin labels such as trityl radicals or Gd(III) complexes.[120–122]

Chapter 4 tackled the limitations of one-colour LITTER by generalising the technique to non-identical chromophores using two-colour laser excitation. Focusing on addressing the lack of selectivity in triplet state formation arising from the one-colour nature of the original experiment, a range of new chromophores were spectroscopically screened as potential triplet labels for a two-colour LITTER. The best candidate chromophores were incorporated into model peptides and proof-of-concept two-colour experiments were carried out, yielding larger modulation depths corresponding to a four-fold

shortening of the acquisition time with respect to previous one-colour measurements. Given the high costs associated with PDS measurement time, this achievement is a big step towards making LITTER a more accessible technique. In addition, this showed that LITTER can be performed with non-porphyrin chromophores commonly used as biological labels, making the technique directly transferable to structural biology applications.

The energy transfer and fluorescence properties of the chromophore pairs chosen for the study make them dual spin/fluorescent labels, enabling FRET distance measurements on exactly the same molecules studied by LITTER and therefore direct comparison between the two techniques. The results were consistent between the two techniques and in agreement with DFT predictions. This type of parallel study exploits the complementarity of the two techniques, with LITTER yielding distance distributions in frozen solution and Föster resonance energy transfer (FRET) providing information in room-temperature liquid state and potentially with nanosecond time resolution if single-molecule techniques are used.[154] In addition, the fact of using dual spin/fluorescent labels removes the need for preparing different labelled samples.

The selective optical addressability of each chromophore in two-colour LITTER has the potential to enable unambiguous PDS distance determination in systems with more than two labels, without the interference of multi-spin effects.[29,34] Optical orthogonality is easier to achieve and allows a wider choice of labels than spin-label orthogonality.[31–33] Therefore, this technique offers a promising route to controlling complexity in PDS of multi-spin systems. Finally, the use of only photogenerated triplets as spin labels, which can be formed within cells, makes two-colour LITTER suitable for in-cell dual ESR/FRET studies. If combined with fluorescence microscopy, LITTER could provide location-specific structural information for the labelled biomolecules inside the cell. It must be noted, however, that FRET requires chromophores with high fluorescence quantum yield and therefore low triplet quantum yield, while high triplet quantum yields and correspondingly low

fluorescence yields are necessary for LITTER. High triplet yields might lead to high generation of singlet oxygen by sensitisation inside cells, resulting in a significant amount of photobleaching. Potential solutions to this problem are discussed in the Outlook section.

Although FRET might be the technique of choice for the majority of structural biology studies, LITTER can be advantageous in certain cases. Un-modified systems containing endogenous chromophores are unlikely to have the correct energetics for FRET, especially for oligomeric systems where each of the monomers contains the same chromophore. LITTER, on the other hand, can access the inter-chromophore distance in such systems as demonstrated in this thesis. This capability also allows to use the same chromophore when labelling multiple sites of a system for LITTER, with the same chemistry, while FRET would normally require different labels and orthogonal labelling chemistries. Finally, LITTER is better suited for the study of multi-labelled systems, where the energy transfer processes between more than two chromophores could become to complicated to perform FRET. Using chromophores with well-separated optical spectra in order to avoid energy transfer, pairwise distance measurements could be carried out by LITTER employing selective laser excitation.

In conclusion, photogenerated triplet states are promising spin centres for PDS, thanks to being photoswitchable, having remarkable spectroscopic properties, and being endogenous to many biological systems of interest. This thesis has provided further support for the widespread application of photogenerated triplet spin centres and LiPDS techniques to the structural study of macromolecular biological systems, introducing new triplet spin labels, improving existing techniques, developing new experiments and analysis methods, and combining them with other experimental tools for integrative structural biology.

It must be pointed out that the model systems used in this thesis have

been found to be more conformationally flexible in solution than originally anticipated, often leading to a wide spread of spin-spin distances and relative spin centre orientations determined by LiPDS. This flexibility therefore makes these systems not optimal models for the purpose of this thesis: to test new techniques on molecules of known and well-defined conformations. Peptide-based systems were originally chosen for their higher relevance for future biological applications of the techniques compared to other synthetic chemical systems. In addition, this choice of model systems was conditioned by the synthetic collaborators in this project, with expertise in peptide chemistry. More rigid molecules with planar insaturated spacers would have been preferable for the studies presented in this thesis; however, those could not be obtained from collaborators.

Outlook

Despite the advances made in this thesis, several aspects would require further research in order to unlock the full potential of LiPDS for molecular structural studies.

Firstly, the phase-memory time (T_m) of most photogenerated triplet states studied in this work is too short for them to be used as detection spin in LiPDS, which restricts detection to porphyrin triplets. This is a strong limitation especially for spin labelling studies, as porphyrins are not a common label used in biological applications. In addition, it makes combination with other triplet chromophores for LITTER more challenging. Further research is needed to identify or develop other photogenerated triplet spin labels with T_m values of at least several microseconds at cryogenic temperatures while keeping triplet quantum yield (Φ_T) close to unity. The brominated derivative of fluorescein eosin Y (EO) has $T_m \sim 1\mu$s and reasonable $\Phi_T = 0.6$, despite lower than its iodinated counterparts erythrosin B (EB) and rose Bengal (RB), suggesting that a trade-off between T_m and Φ_T can be achieved in spin-orbit coupling (SOC)-enhanced inter-system crossing (ISC) triplets by

the heavy-atom effect.

For LiPDS techniques using a single triplet state, such as LiDEER and LaserIMD, it is necessary to investigate alternative spin centres to nitroxides, with good long-term stability in reducing environment, to enable in-cell applications. Some initial steps have recently been taken in this direction, demonstrating the feasibility of LiDEER measurements between a C_{60} triplet and a triarylmethyl (trityl) radical,[69] and LaserIMD between a porphyrin triplet and a Gd(III) complex.[160] Both trityl radicals and Gd(III) complexes are know to be stable under reducing conditions. The different combinations of reported photogenerated triplet labels with trityl radicals and Gd(III) and other metal complexes (such as Cu(II)) would need to be tested in order to identify the best performing pairs. Nevertheless, these techniques have now reached the stage of being ready for proof-of-concept in-cell studies, where the enhanced sensitivity provided by the hyperpolarised triplet state could make a big difference with respect to existing in-cell PDS technologies.

In-cell applications of LiPDS bring new issues that had been avoided in the model studies reported so far, namely the potential photodegradation of the chromophore and the system of study by singlet oxygen generated via photosensitisation from the photogenerated triplet state, as oxygen removal from the sample may not be a viable option in the case of cells. Faster photodegradation was observed when samples were not thoroughly degassed in the experiments presented in this thesis. A singlet-oxygen quencher could be added to limit photodegradation.[161,162] Alternatively, chromophores with triplet state energies below that of triplet oxygen to avoid sensitisation (such as carotenoids) could be used as triplet spin labels. In that case, however, the carotenoid triplet would need to be populated via energy transfer from a higher-energy triplet, as Φ_T of carotenoids is very low.[133] Photoswitchable spin labels should then be designed in a dyad fashion mimicking the photoprotection mechanisms of plants,[163] with a high-Φ_T higher-energy triplet chromophore (e.g. porphyrin) in close proximity to the carotenoid, such that the initial triplet is preferentially quenched by the carotenoid rather than

by triplet oxygen. The carotenoid triplet could then act as spin centre for LiPDS, as already demonstrated.[78]

Besides photodegradation, another challenge for in-cell applications of LiPDS concerns the introduction of the labelled biomolecules inside the cells. Electric shock is a well-established technique for this purpose,[164] consisting in an application of a short high-voltage pulse that drastically increases the permeability of the cell membrane and favours the uptake of molecules from the extracellular medium. If the biomolecule of interest cannot be labelled externally prior to introduction into the cell, the labelling could be performed inside the cell following the introduction of the chromophore by electric shock, using, for instance, the well-established bio-orthogonal labelling strategies based on click chemistry.[165] In-cell fluorescence spectroscopy and microscopy have greatly benefited from the use of genetically-encoded fluorophores, such as fluorescent proteins.[166,167] Similar proteins could potentially be engineered to contain chromophores with high triplet quantum yield and low fluorescence quantum yield, for ESR. However, the size of the protein scaffold (4.2 x 2.4 nm cylinder for the popular green fluorescent protein[168]) would need to be reduced significantly in order to become suitable for LiPDS applications, where only spin-spin distances up to 6 nm have been shown to be measurable accurately so far.[72]

Sensitivity is another concern for in-cell applications, where the concentration of the labelled biomolecule of study would be in the low μM range. However, several examples of in-cell DEER have recently been reported using non-Boltzmann populated spin centres, yielding dipolar traces with good enough SNR for analysis.[169,170] If similar in-cell concentrations of chromophore-labelled biomolecules can be achieved, techniques such as LiDEER or LITTER, for which the sensitivity benefits from the strong spin polarisation of the photogenerated detection spin centre, are expected to yield better results.

Regarding the novel LITTER technique, further improvement of the triplet formation selectivity by the first laser pulse is highly desirable and would lead

to even larger modulation depths than those of the two-colour experiments reported in Chapter 4. Already in that chapter, potentially better chromophores for triplet formation selectivity in combination with TPP were identified, namely ATTO Thio12 (AT), EO and crystal violet (CV), and these should be tested in the near future.

In terms of the illumination setup for LITTER, the setup described in Chapter 3 and used for the experiments in this thesis would need to be modified to improve the laser geometrical overlap if maximum modulation depth is to be achieved. As explained in Section 3.1, the perpendicular geometry of the laser beams at the sample leads to sub-optimal laser overlap and to attenuation of the second laser beam by the dead volume at the top of the sample. A parallel geometry would address these issues. This could be realised either by delivering both lasers through optical fibres directly inserted into the sample tube, or by overlapping the two perpendicular laser beams using a 50:50 beam-splitting cube. The latter option promises the best laser overlap, as both beams could be made collinear at the exit of the beam-splitting cube, but comes at the expense of laser power due to 50 % of each beam being diverted away.

Once these issues have been addressed, it would be necessary to further investigate the distance range of applicability of LITTER, in particular the upper distance limit measurable with this technique, which was not reached with the molecular spectroscopic ruler studied in Chapter 3. The experiments on Zn(II) myoglobin (ZnMG) dimer reported in Section 3.3 demonstrated that porphyrin-porphyrin distances up to 4-5 nm can be captured by LITTER, although the length of the dipolar traces was limited by the short T_m of the Zn(II) proto-porphyrin IX (ZnPP) triplet. An extended LITTER ruler study on free-base porphyrin model compounds exploring the distance range > 5 nm would provide valuable insight into the upper distance limit achievable with optimal triplet chromophores.

In regards to two-colour LITTER and its possible combination with FRET, as demonstrated in Section 4.2.3, it must be pointed out that the observation

of energy transfer between the chromophores studied in the model peptides was serendipitous and that the chromophore pairs had not been chosen with FRET measurements in mind. Therefore, chromophore pair selection for future dual LITTER/FRET studies should take both ESR and fluorescence properties into account. For instance, toluidine blue-o (TB) and methylene blue (MB), which already showed strong energy transfer with tetraphenylporphyrin (TPP) as free chromophores in solution in the screening studies reported in Section 4.1, and were discarded for LITTER for this reason, could lead to very efficient FRET and may be worth investigating further. In addition, they were the chromophores that showed optical absorption furthest away from TPP, which makes them good candidates for improving photoexcitation selectivity.

Finally, moving towards more complex macromolecular systems, where inclusion of multiple (> 2) spin labels would be of interest, the optical addressability of the different chromophores would need to be exploited in order to avoid multi-spin effects. Not only in LITTER, but also in all the other LiPDS techniques, the selection of ESR-active label pairs, and therefore pairwise dipolar interactions, by appropriately choosing the laser excitation wavelengths can avoid the experimental or post-processing complications associated with conventional PDS of multi-spin systems.

Looking further into the future of LiPDS, several ideas come to mind that would be beneficial for the development of the field, the first of them being the combination of experimental structural studies with molecular dynamics (MD) simulations. The distance and orientation distributions obtained from LiPDS studies so far have been compared to computationally predicted molecular geometries by *in-vacuo* DFT optimisation. Although often indicative of the preferential conformation of the molecules in solution, DFT structures do not inform on their conformational flexibility and therefore are not the most adequate to validate the distributions obtained from LiPDS. MD simulations, on the other hand, allow the conformational space that the

molecules can sample at a given temperature to be defined, and can include the effects of the solvent more accurately than DFT, making them a better validation tool not only for the main distances, but also for the shape of the distance distributions obtained from LiPDS. Work in this direction is already ongoing in collaboration with Prof. Alberta Ferrarini (University of Padova).

The combination with other experimental techniques would also broaden the scope and relevance of LiPDS studies. The use of chromophores as spin centres offers unique opportunities in this direction, which were not available to standard PDS. The combination of LITTER with FRET could be pursued a step further by using single-molecule FRET techniques, which would allow for the time-resolved study of conformational changes in physiological conditions down to the nanosecond time-scale,[154] complementing the static conformational distributions obtained by LITTER. Further combination with fluorescence microscopy in cells would allow to relate this information to the intracellular location of the biomolecules studied, providing further insight into structure-function relationships.

Going beyond molecular structure determination, LiPDS techniques, especially LITTER, could shed further light into the photophysical processes underlying solar energy harvesting by molecular materials. Photogenerated paramagnetic states, in particular triplets, are known to play an important role in these materials, being involved in processes such as singlet fission and triplet-triplet annihilation.[171] LITTER could be used to determine the distribution of relative positions and orientations of the triplet excitons, providing further information on the mechanisms of the solar energy harvesting process by these materials.

This thesis has focused on the use of photogenerated triplet states as spin centres, but there are other approaches to photoswitchable spin centres for PDS. One of these approaches is the use of labels with photo-removable protecting groups that allow the formation of an ESR-active radical after photocleavage, as recently reported with a photocaged nitroxide.[172] Radi-

cal labels may be in some cases desirable over triplet states because of the absence of ZFS, leading to narrow ESR linewidths. However, the photoswitching of these labels is irreversible, after which they behave as regular nitroxide spin labels. A more promising approach to photoswitchable radical labels is afforded by the one-electron reduction of the photoexcited states of certain chromophores by electron donors, to form semistable radicals with lifetimes of several minutes in degassed liquid solutions at room temperature.[173] Reversibility in this case is enabled by the oxidation of the radical after exposition of the sample to oxygen, to return the chromophore to is closed-shell ground state. This strategy combines the advantages of radical spin labels and reversible photoswitchability. In addition, many standard fluorescent labels and stains used routinely in biological studies undergo this photoreduction process in the presence of thiols as one-electron donors, making the methodology easily transferable to structural biology laboratories. Initial work following this approach has been carried out over the course of this DPhil, using the model chromophore Rhodamine 6G (R6G), and its compatibility with permanent spin labels has been assessed. Preliminary results are presented in Appendix III, and this research line is being continued in the group.

Appendices

I. Instrumentation

This appendix provides a more detailed description of the instruments and setups used to carry out the experiments reported in this thesis.

I.1. ESR instrumentation

The ESR spectrometers used in this thesis are commercial cw/pulsed spectrometers (Bruker) equipped with SpinJet Arbitrary Waveform Generators (AWGs), SpecJetIII, PatternJetII, and wet cryostats and temperature-controlling units (Oxford Instruments) allowing for experiments down to liquid He temperatures to be performed. The dual X/Q-band system ELEXYS-E580 was used for the Q-band measurements reported in this thesis, with resonators ER-5106QT2 for light-induced experiments and EN-5107D2 for DEER experiments. X-band measurements were performed using the dual X/W-band ELEXYS-E680 system, with the resonator EN-4118XMD5. All resonators have optical windows to allow for direct laser excitation.

I.2. Laser instrumentation

The pulsed tunable lasers used in this thesis are class-4 Nd:YAG-pumped Optical Parametric Oscillators (OPOs), running at 20 Hz. Both flash lamp (FL) and Q-switch (QS) of the pump laser are triggered using an external pulse-delay generator, with the optimal FL-QS delay for each laser, yielding the maximum output power, in order to minimise power jittering. The same pulse-delay generator is also used to trigger the SpecJet (for trESR) or the PatternJet (for pulsed ESR) of the ESR spectrometer, allowing for synchronisation of the different instruments. For LITTER experiments, where both Laser 1 and Laser 2 are used at the same time, two external pulse-delay generators are used, each to trigger one of the lasers. One of the delay generators acts as the master clock for the experiment, triggering the other delay generator and the spectrometer in addition to the laser. Whenever one single

laser was used, this was Laser1.

Laser 1 is an OPOlette 355 (Opotek), with tunable output in the range of 410-2200 nm, maximum visible output power of 8.5 mJ, pulse length of 7 ns and beam diameter of 3.4 mm. The optical setup used with this laser (Figure 5.1) is inside a purpose-built laser enclosure of anodised aluminium on a mobile optical table, with covers that can be removed in sections to access different parts of the setup for alignment. The tunable output of the OPO is attenuated by rotating the waveplate ($\lambda/2$) with respect to the following Glan-Taylor prism linear polariser (P). The second and third harmonics of the YAG are stopped by beam dumps. The attenuated beam is directed into the ESR resonator by three dielectric mirrors at 45°with the beam (MI, MII and MII), on x-y adjustable mounts, and is passed through a depolariser (D). The beam is focussed through a beam tube into the resonator using a convergent lens (L, f = 1 m), such that the focus occurs slightly past the sample position. The beam tube fits tightly around the window of the cryostat, and its length can be adjusted to fit the gap between the laser enclosure on the mobile optical table and the cryostat. A shutter (S) can be placed between the laser enclosure and the beam tube to stop the laser going into the resonator. The full power going into the cryostat can be measured by temporarily placing a power meter (W) after L. The alignment into the resonator is adjusted with the help of a purpose-built circular alignment card holder that fits tightly on the window of the cryostat.

Laser 2 is a GWU/UVScan (VersaScan), with tunable output in the range of 213-2800 nm, maximum visible output power of 50 mJ, pulse length of 2-3 ns and beam diameter of 7.9 mm. The optical setup used with this laser (Figure 5.2) is inside a purpose-built laser enclosure of anodised aluminium on a fixed optical table, with covers that can be removed in sections to access different parts of the setup for alignment. The laser (YAG + OPO) is separated from the rest of the setup by another wall, to allow for alignment without being exposed to the YAG beam. The tunable output of the OPO is attenuated by rotating the waveplate ($\lambda/2$) with respect to the following

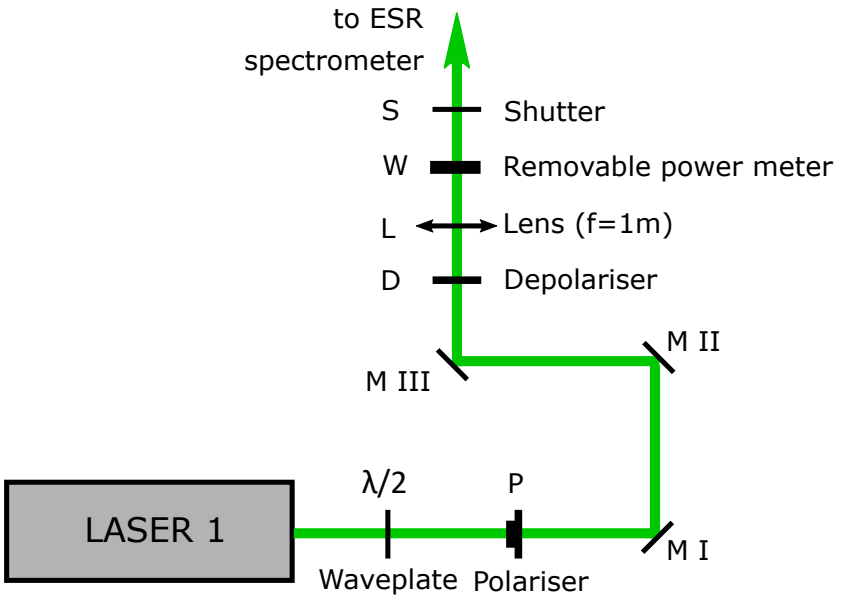


Figure 5.1: Optical setup for Laser 1. Legend: waveplate ($\lambda/2$), Glan-Taylor linear polariser (P), dielectric mirrors (MI, MII and MII), depolariser (D), 1 m focal convergent lens (L), powermeter (W) and shutter (S).

Glan-Taylor prism linear polariser (P). The degree of attenuation is monitored with a removable power meter (WI) inserted after P. The attenuated beam is directed into the fibre by two dielectric mirrors at 90°with respect to each other and 45°with the beam (MI and MII), on x-y adjustable mounts. A 10% reflection beam splitter (BS) allows for constant power monitoring by placing a power meter (WII) at 90°with the beam. The beam is passed through an iris (I) and focussed slightly before the tip of the fibre using a convergent lens (L, f = 30 cm). The bare end of the fibre is held in place by a fibre mound with x-y-z position screws that allow for fine adjustment of the coupling. The fibre tip is enclosed into a beam tube to dump any scattered light. A short support tube at the other end of the fibre mount helps keep the fibre in place. The cladded fibre is taken out of the laser enclosure and the other bare end is threaded through a sample rod (tightly sealed with o-rings and teflon tape) and inserted into the sample tube. A shutter (S) is placed after L to allow for safe sample insertion/extraction while the laser is running. The laser power going into the sample is measured placing a power

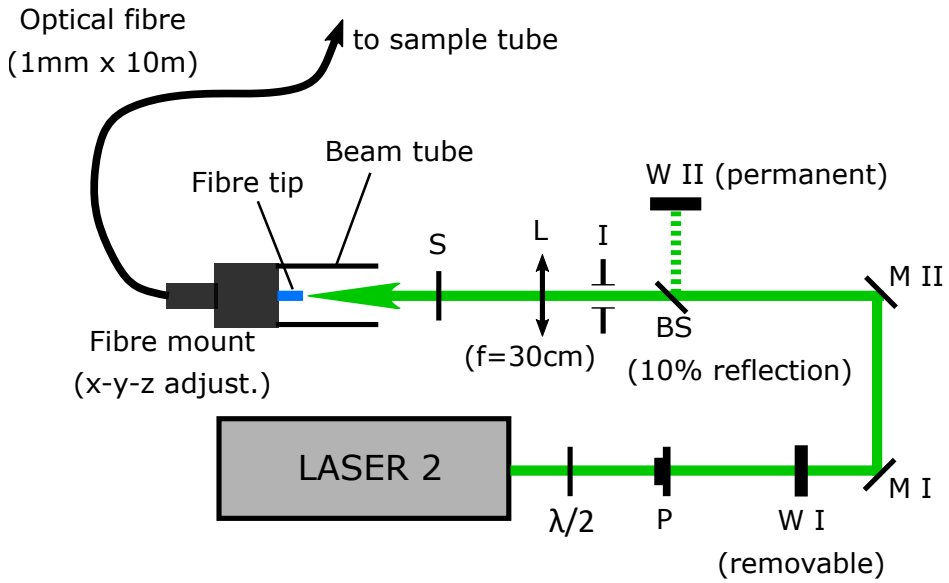


Figure 5.2: Optical setup for Laser 2. Legend: waveplate ($\lambda/2$), Glan-Taylor linear polariser (P), dielectric mirrors (MI and MII), power meters (WI and WII), 10% beam splitter (BS), iris (I), 30 cm focal convergent lens (L) and shutter (S).

meter at the end of the fibre, before inserting it into the sample tube. This operation is carried out inside the laser enclosure once the fibre is coupled.

I.3. Optical spectroscopy instrumentation

Steady-state absorption spectra were recorded in a commercial UV-Vis spectrometer (Cary 60, Agilent Technologies), equipped with a Xe flash lamp source and allowing for measurements in the wavelength range of 190-1100 nm. All spectra were acquired with solvent baseline correction (100% transmittance). For low-temperature measurements, a liquid N_2 cryostat with two quartz windows (Oxford Instruments) and a custom-made temperature-controlling unit was fitted into the spectrometer using a custom-made mount.

TA spectra were acquired using a nanosecond transient absorption spectrometer (EOS, Ultrafast Systems) after photoexcitation by a class-4 Nd:YAG-pumped OPO (PL2210 and PG403, Ekspla). The laser provides a tunable output in the range of 410-26000 nm, maximum visible output power of 50

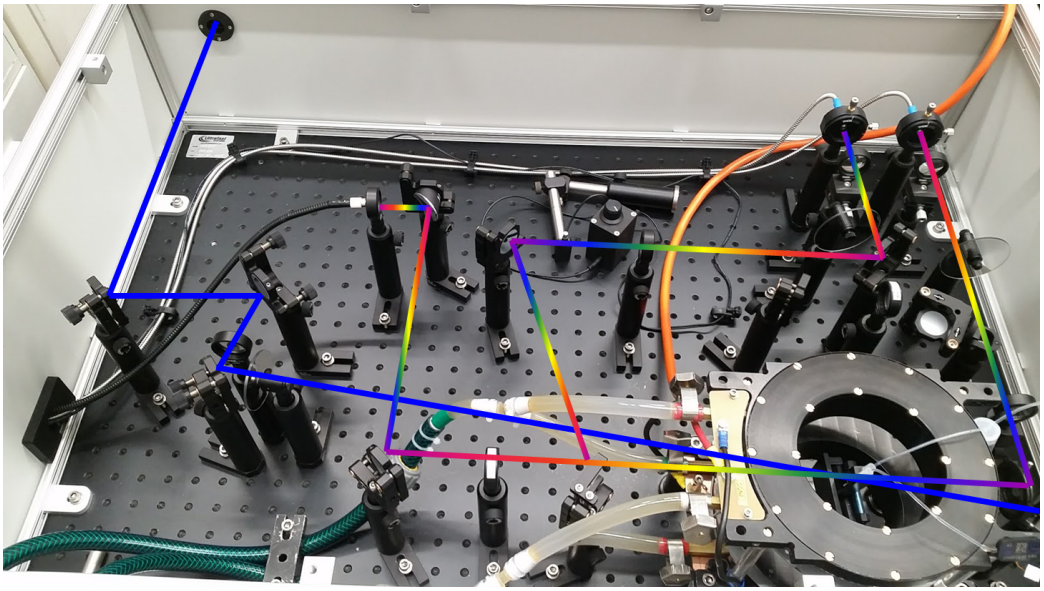


Figure 5.3: Optical setup for TA. The paths for the pump (blue) and probe (rainbow) beams are indicated. The liquid N_2 cryostat has been removed for clarity.

μJ, pulses at 1 kHz frequency with lengths of 15 ps and beam diameter of 3 mm. The spectrometer contains a 2 kHz Supercontinuum white light laser (Leukos) providing 1 ns pulses for probe.

The optical setup for TA is shown in Figure 5.3. The sample cell is placed at the centre of the Helmholtz coils, which were not used in this thesis. The pump beam (blue) is directed to towards the sample using mirrors, attenuated with a variable neutral-density filter and focused with a convergent lens. The white-light probe beam (rainbow) is split in two using a beam splitter. The transmitted beam is passed through the sample and directed to a diode detector. The reflected beam is directed to another diode detector, for reference. Both white-light beams can be independently attenuated to optimise detection. For low-temperature measurements, a liquid N_2 cryostat with four quartz windows and temperature controlling unit (Oxford Instruments) can be fitted inside the Helmholtz coils.

II. Supplementary data

II.1 Supplementary data for Chapter 2

II.1.1 Supplementary data for Section 2.1

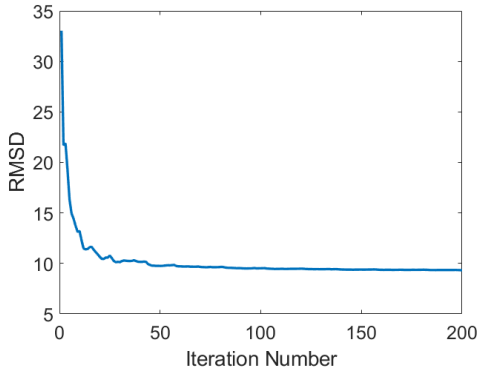


Figure 5.4: RMSD plot for the iterative process leading to the fits shown in Figure 2.4

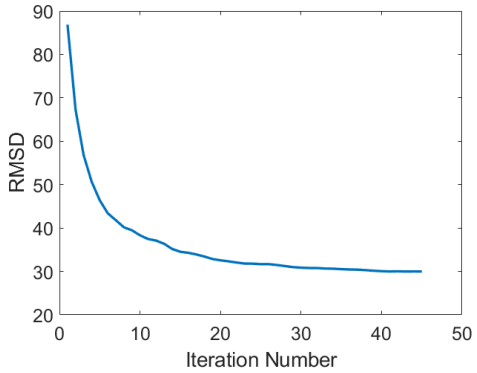


Figure 5.5: RMSD plot for the iterative process leading to the fits shown in Figure 2.8

II.1.2 Supplementary data for Section 2.2

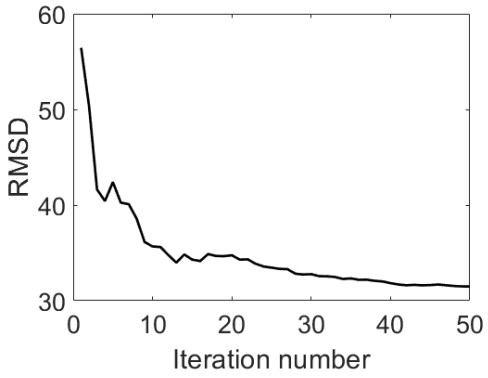


Figure 5.6: RMSD plot for the iterative process leading to the fits shown in Figure 2.14

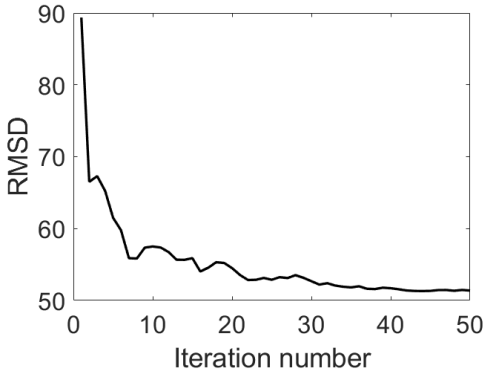


Figure 5.7: RMSD plot for the iterative process leading to the fits shown in Figure 2.15

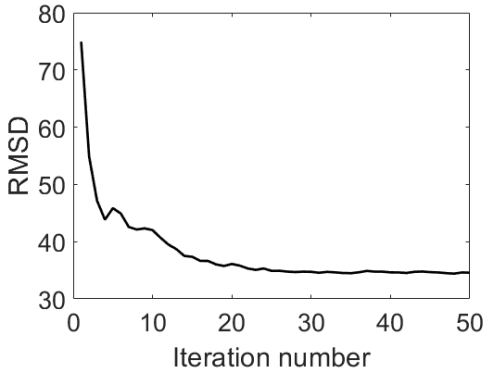


Figure 5.8: RMSD plot for the iterative process leading to the fits shown in Figure 2.17

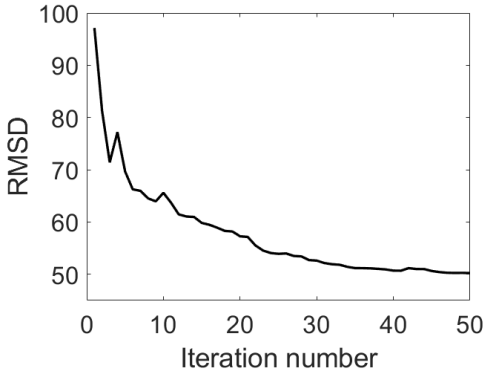


Figure 5.9: RMSD plot for the iterative process leading to the fits shown in Figure 2.18

II.2 Supplementary data for Chapter 3

II.2.1 Supplementary data for Section 3.2

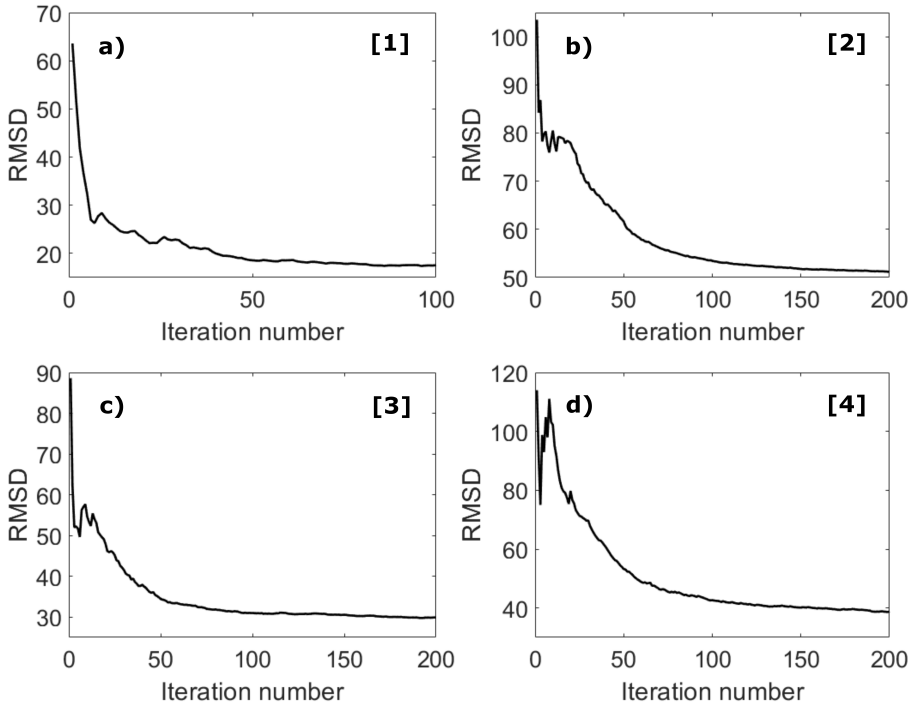


Figure 5.10: RMSD plot for the iterative process leading to the fits shown in Figure 3.16

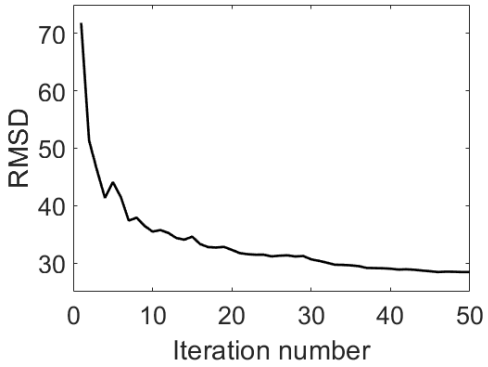


Figure 5.11: RMSD plot for the iterative process leading to the fits shown in Figure 3.19

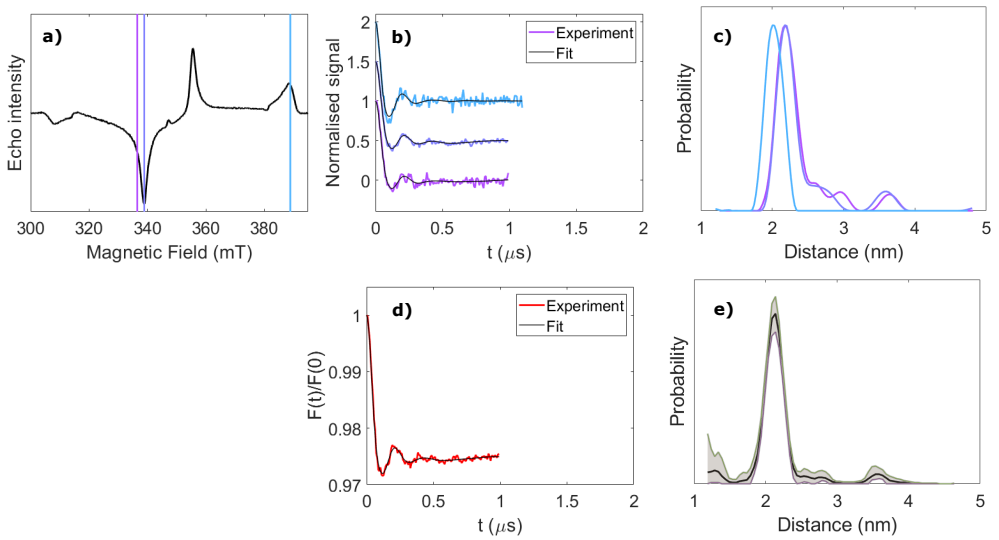


Figure 5.12: Orientation-independent analysis of LITTER with **1**. (a) Echo-detected field-swept ESR spectrum of **1** measured after 512 nm laser flash. The field positions used to record the LITTER traces are indicated with vertical lines. (b) Background-corrected and modulation depth-normalised LITTER traces acquired at the different field positions (colour) and corresponding orientation-independent fits by Tikhonov regularization using DeerAnalysis (black). (c) Spin–spin distance distributions obtained from the analysis shown in (b). (d) Averaged LITTER trace (red) and corresponding orientation-independent fit by Tikhonov regularization (black). (e) Spin–spin distance distributions obtained from the analysis shown in (d), showing the 95% confidence intervals estimated using the Comparative DEER Analyser (CDA) tool in *DeerAnalysis2022*.[125–127]

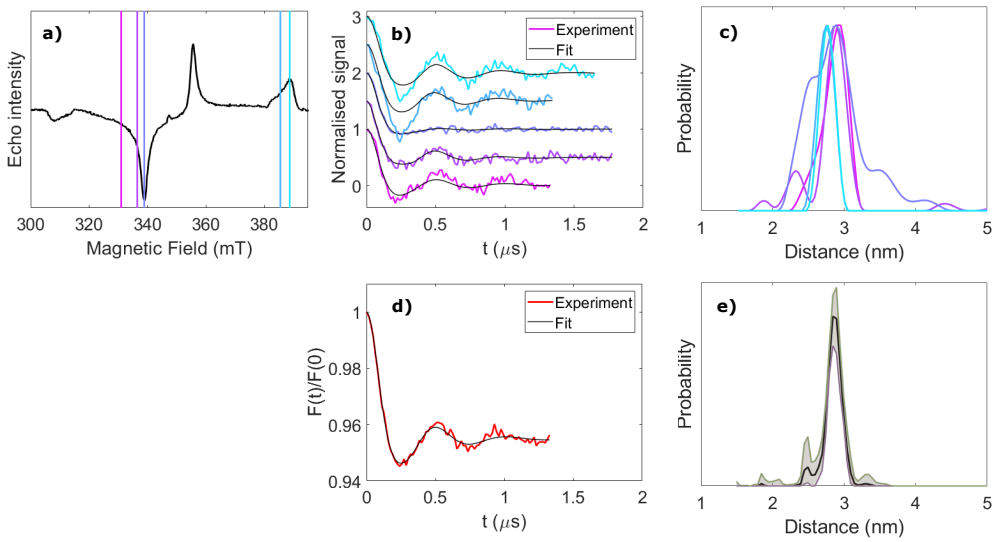


Figure 5.13: Orientation-independent analysis of LITTER with **2**. (a) Echo-detected field-swept ESR spectrum of **2** measured after 512 nm laser flash. The field positions used to record the LITTER traces are indicated with vertical lines. (b) Background-corrected and modulation depth-normalised LITTER traces acquired at the different field positions (colour) and corresponding orientation-independent fits by Tikhonov regularization using DeerAnalysis (black). (c) Spin–spin distance distributions obtained from the analysis shown in (b). (d) Averaged LITTER trace (red) and corresponding orientation-independent fit by Tikhonov regularization (black). (e) Spin–spin distance distributions obtained from the analysis shown in (d), showing the 95% confidence intervals estimated using the Comparative DEER Analyser (CDA) tool in *DeerAnalysis2022*.[125–127]

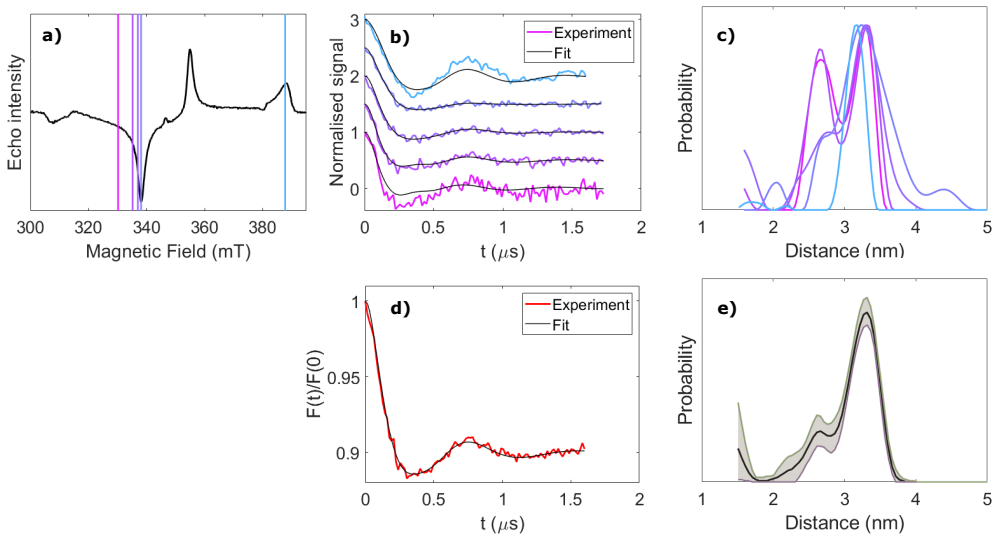


Figure 5.14: Orientation-independent analysis of LITTER with **4**. (a) Echo-detected field-swept ESR spectrum of **4** measured after 512 nm laser flash. The field positions used to record the LITTER traces are indicated with vertical lines. (b) Background-corrected and modulation depth-normalised LITTER traces acquired at the different field positions (colour) and corresponding orientation-independent fits by Tikhonov regularization using DeerAnalysis (black). (c) Spin–spin distance distributions obtained from the analysis shown in (b). (d) Averaged LITTER trace (red) and corresponding orientation-independent fit by Tikhonov regularization (black). (e) Spin–spin distance distributions obtained from the analysis shown in (d), showing the 95% confidence intervals estimated using the Comparative DEER Analyser (CDA) tool in *DeerAnalysis2022*.[125–127]

II.3 Supplementary data for Chapter 4

II.3.1 Supplementary data for Section 4.1

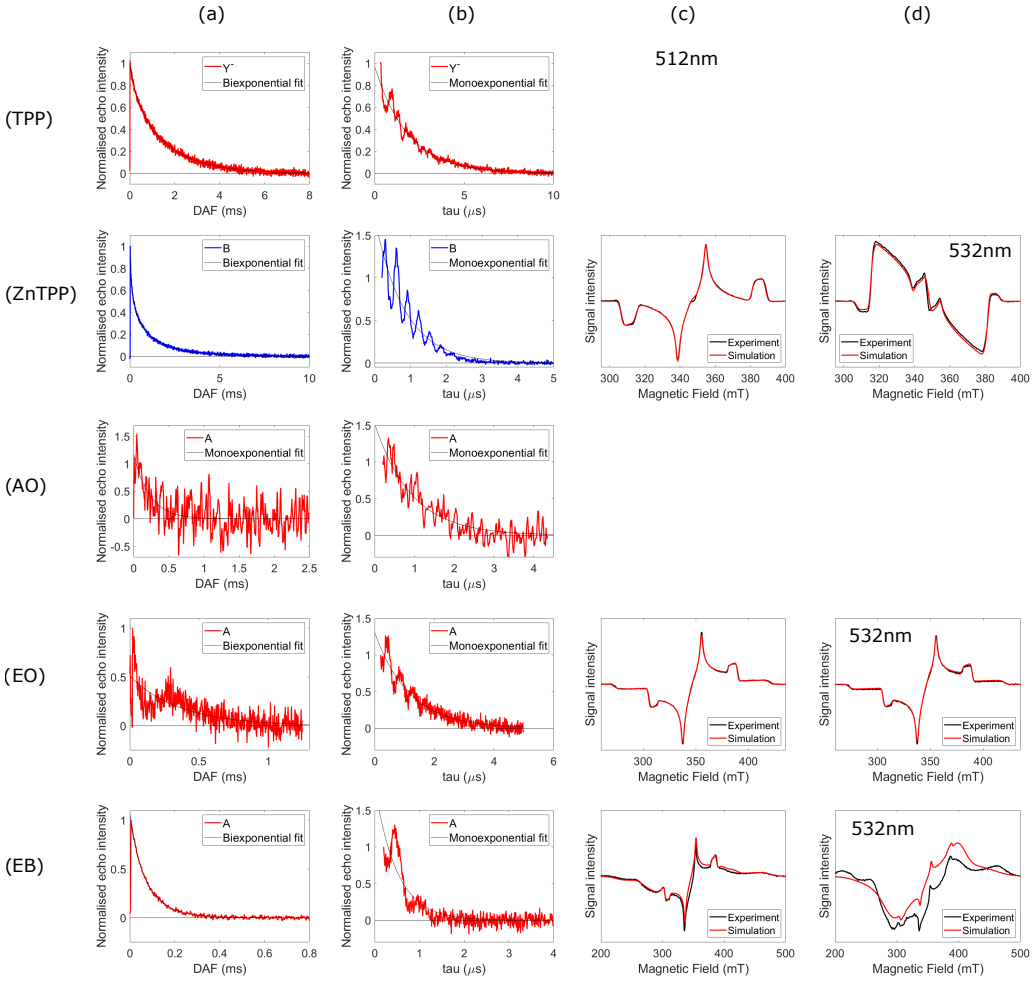


Figure 5.15: ESR triplet state characterisation of the free chromophores studied in this work. (a) DAF experiments (red) and biexponential fits (black) to extract the lifetimes. (b) Phase-memory experiments (red) and monoexponential fits (black) to extract T_m. (c) trESR spectra of 1:1 molar mixtures with TPP after 512 nm excitation (black) and simulation with *EasySpin pepper* function (red) for deconvolution. (d) Same as c, but at the indicated wavelength. Continued in Figure 5.16

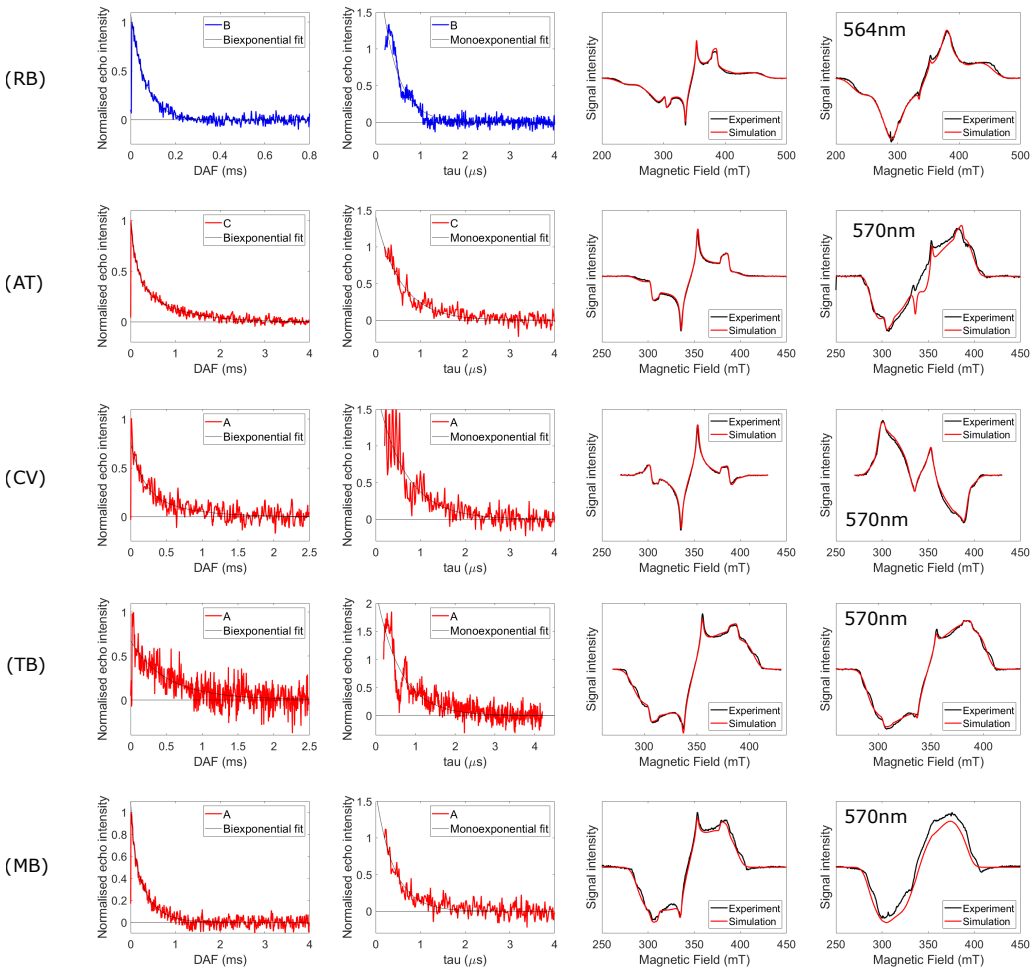


Figure 5.16: Continuation of Figure 5.15.

II.3.2 Supplementary data for Section 4.2

[**1**]	TPP(Zn)-Sar-Leu-Aib-Leu-Aib^{5}-Leu-Aib-Leu-Aib-Leu^{10}-NH-CH_2-CH_2-NH-TPP
[**2**]	EB-Sar-Leu-Aib-Leu-Aib^{5}-Leu-Aib-Leu-Aib-Leu^{10}-NH-CH_2-CH_2-NH-TPP
[**3**]	TPP-Sar-Leu-Aib-Leu-Aib^{5}-Leu-Aib-Leu-Aib-Leu^{10}-NH-Cyclohexyl-COOH
[**4**]	TPP(Zn)-Sar-Leu-Aib-Leu-Aib^{5}-Leu-Aib-Leu-Aib-Leu^{10}-NH-CH_2-CH_2-NH_2
[**5**]	EB-Sar-Leu-Aib-Leu-Aib^{5}-Leu-Aib-Leu-Aib-Leu^{10}-NH-CH_2-CH_2-NH_2

Figure 5.17: Peptide sequences studied in this work.

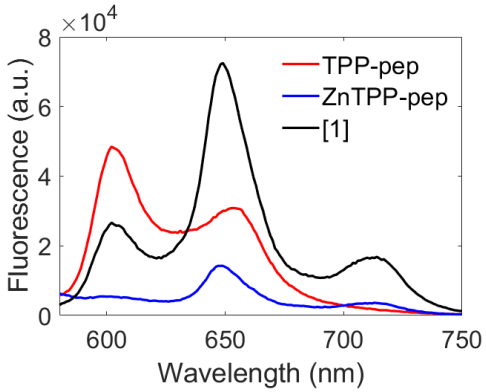


Figure 5.18: Fluorescence spectra of **1** (black) and the singly-labeled TPP-peptide **3** (red) and ZnTPP-peptide **4** (blue), all at 1 μM in ethanol. Excitation was performed at 567 nm.

III. Photoswitchable radical labels for PDS

Triplet states are not the only type of photoswitchable paramagnetic centre with potential as spin label for PDS. The photoexcited states of certain dyes can undergo one-electron reduction by electron donors to form semistable radicals (Figure 5.19), with lifetimes of several minutes in degassed solution.[173] Exposition to oxygen quickly oxidises the radical, restoring the singlet ground state population of the dye and making the photoswitching of the spin label reversible. The concept of semi-stable radicals has never been used for PDS before.

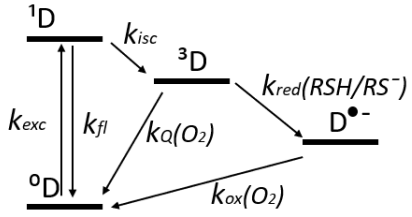


Figure 5.19: Jablonski diagram for the formation of a semi-stable rhodamine radical ($D^{\bullet-}$) by reduction with a thiol (RSH/RS^-). ^{1}D, ^{1}D* and ^{3}D are the ground singlet, first excited singlet and first triplet states of the dye, respectively. k_{exc}, k_{fl}, and k_{isc} are the rate constants for the optical excitation, fluorescence and inter-system crossing (ISC) processes, respectively. $k_{red}(RSH/RS^-)$ corresponds to the reduction of the triplet state to form the dye radical, and $k_Q(O_2)$ and $k_{ox}(O_2)$ are the decay processes of the triplet state and the radical, respectively, both mediated by oxygen.

Building on preliminary work carried out by the former part II student in the group Charles Larminie, the compatibility of semi-stable Rhodamine 6G (R6G) radicals with conventional spin labels for a potential PDS experiment (eg. nitroxide radicals (2,2,6,6-Tetramethylpiperidine 1-oxyl (TEMPO)) and Gd(III) complexes (Gd(III) 1,4,7,10-tetraazacyclododecane-N,N',N",N"'-tetraacetate (Gd-DOTA)) was investigated by cwESR (Figure 5.20 (a, b)).

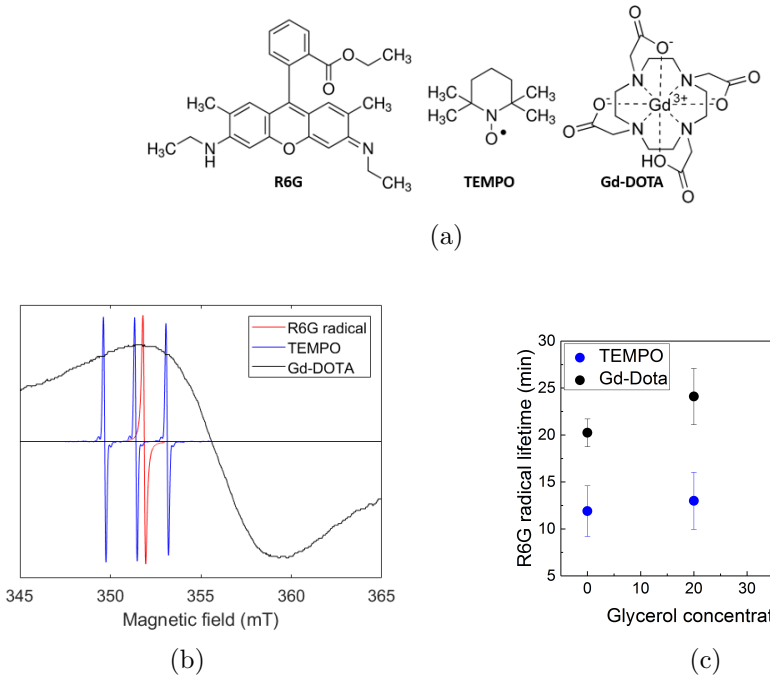


Figure 5.20: (a) Chemical structures of R6G, TEMPO and Gd-DOTA. (b) Room-temperature X-band cwESR spectra of R6G radical, TEMPO and Gd-DOTA in aqueous solution. (c) R6G radical lifetimes in the presence of TEMPO and Gd-DOTA and variable concentrations of glycerol. The lifetimes have been determined from the fast component of a biexponential fit to the decay trace of the R6G ESR second integral in the dark after illumination at > 455 nm.

The measurements were carried out in aqueous solutions at room temperature and X-band, in an EMX-Micro cwESR spectrometer with an X-band Super High Sensitivity Probehead resonator (both Bruker), using a Xe arc lamp with appropriate filters as the light source. β-mercaptoethylamine (cysteamine) was used as reducing agent, acting as a one-electron donor to form the R6G radical. The lifetime of this radical in the presence of TEMPO or Gd-DOTA, with different concentrations of glycerol, was determined from the fast component of the ESR signal decay after illumination. Water/glycerol mixtures are normally used to stabilise biomolecules for low temperature ESR measurements. Glycerol also changes the viscosity of the solution and may affect the kinetics of radical formation and decay. R6G radical lifetimes increased with glycerol concentration (Figure 5.20 (c)). However, the

increase between 20% and 50% was not significant and a slight reduction in signal intensity was observed. For these reasons, 20% glycerol was used in subsequent experiments.

The formation of the R6G radical was found to be insensitive to the presence of Gd-DOTA (Figure 5.20 (c)), but a reaction between R6G and TEMPO occurred under illumination (a correlated decay of the nitroxide signal intensity with the appearance of the R6G radical, Figure 5.21 (a)). A systematic study of this nitroxide degradation process was carried out in order to identify the optimal conditions that maximise the concentration of both radicals (Figure 5.22 (a-c)): pH, concentration of reducing agent (cysteamine) and illumination wavelength (Figure 5.21 (b)). The coordinates of the crossover point between the ESR intensity time traces for the two radical species (i.e. the illumination time at which the nitroxide and R6G radicals reach the same concentration, and this concentration value, Figure 5.21 (a)) are indicative of the kinetics of the process and were used to identify the optimal conditions for radical generation for a PDS measurement, as detailed below.

- **Changing pH:** the R6G radical formation / TEMPO degradation process became slower when decreasing the pH of the solution, which also reduced the radical concentration at the crossover point (Figure 5.22 (a)). Indeed, thiol groups act as reducing agents in their deprotonated form,[174] and the concentration of S-deprotonated cysteamine is reduced when decreasing the pH.

- **Changing cysteamine concentration:** The decrease of the concentration of reducing agent had the expected effect of slowing down the process, without changing the concentration at the crossover point (Figure 5.22 (a)).

- **Changing illumination wavelength:** Red-shifting the illumination cut-on wavelength only had some negative effect on the crossover time and concentration when a significant fraction of the R6G absorption

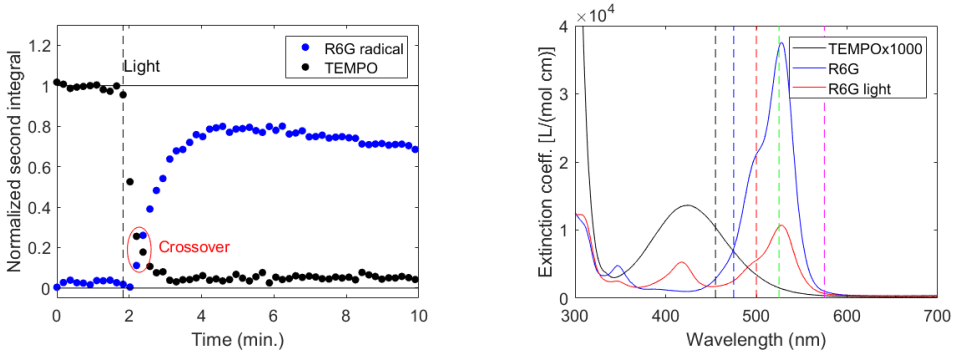


Figure 5.21: (a) Example of a R6G/TEMPO compatibility measurement, with 100 μM R6G, 100 μM TEMPO, 200 mM cysteamine and 20% glycerol in water at pH 9.0, under $>$ 455 nm illumination. The data has been normalized to the initial TEMPO signal, and the crossover point is indicated. (b) UV-Vis spectra of TEMPO (x1000) and a R6G/cysteamine mixture before and after illumination with blue light. The cut-on wavelengths of the long pass filters used for the wavelength-dependant study are indicated with vertical dotted lines (from left to right: 455, 475, 500, 525 and 575 nm).

spectrum was left outside the illumination range (eg. $>$ 525 nm, Figure 5.22 (c)). No R6G radical was detected for the illumination cut-on of 575 nm.

The optimal conditions for a PDS measurement with R6G and nitroxide are pH$\geq$9 and illumination cut-on wavelength between 455 and 475 nm. However, high pH values tend to cause problems with protein systems, so the pH for the measurement should be as high as possible within the stability range of the system of study. The concentration of reducing agent is not a critical parameter as long as it is kept at a reasonably high value ($\geq$ 20 mM cysteamine). On one hand, prolonged illumination times (low cysteamine concentrations) increase the risk of sample photodamage. On the other hand, when the formation of the R6G radical is very fast (high cysteamine concentrations), the relative radical concentration becomes more sensitive to illumination time, making it more difficult to stop illumination at the crossover point. For these reasons, an intermediate cysteamine con-

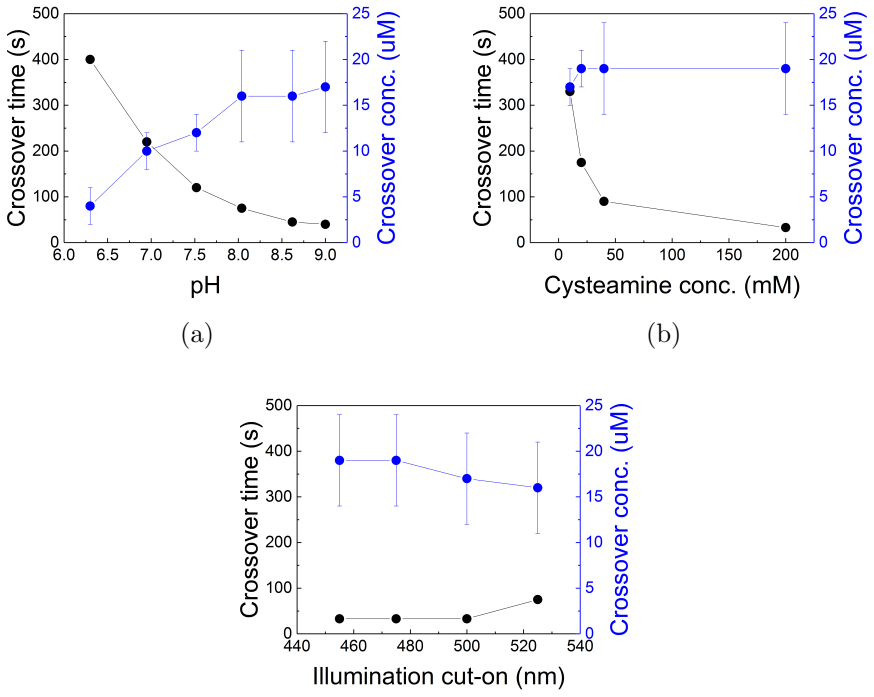


Figure 5.22: Times and concentrations at the crossover point for the R6G/TEMPO compatibility studies as a function of (a) pH, (b) concentration of reducing agent (cysteamine) and (c) illumination cut-on wavelength (as indicated in Figure 5.21). The values of the parameters not explicitly indicated were: [R6G] = 100 μM, [TEMPO] = 100 μM, [cysteamine] = 200 mM, 20% glycerol, pH $\approx$ 9 and illumination cut-on = 455 nm.

centration (eg. $\approx$ 50 mM) is preferable.

Despite the optimisation of conditions, the results indicate that the concentration of spin-active nitroxide in a sample after R6G radical formation would be approximately 20% of the initial value, which might not be high enough to detect dipolar interactions by PDS. Although this concentration is likely to be higher in a labelled macromolecule, where R6G and nitroxide are held apart, Gd(III) complexes are more suitable spin labels to use in combination with R6G semistable radicals.

The preliminary work on the synthesis of model peptide systems for proof-of-concept PDS experiments using R6G radicals, under the supervision of Prof. Marina Gobbo (Univeristy of Padova), encountered the problem of colourless spiro forms already discussed in Section 2.2. In this case, conditions for the recovery of the coloured form of R6G attached to a peptide via amide bond were identified by lowering the pH (see Figure 2.9), but were found to be incompatible with the formation of the R6G semistable radical. The alternative labelling strategy developed by Prof. Marta de Zotti (Univeristy of Padova) for triplet chromophores, presented in Section 2.2, which makes use of a sarcosine linker to avoid the formation of the colourless spirolactam, is also applicable to these systems and should allow efficient formation of R6G radical while attached to a peptide. Research in this direction is ongoing in the group.

Bibliography

[1] G. Jeschke, *Emerg. Top. Life Sci.*, 2018, **2**, 9–18.

[2] D. Goldfarb, *J. Magn. Reson.*, 2019, **306**, 102–108.

[3] M. G. Dal Farra, S. Ciuti, M. Gobbo, D. Carbonera and M. Di Valentin, *Mol. Phys.*, 2019, **117**, 2673–2687.

[4] H. Schmidt-Böcking, L. Schmidt, H. J. Lüdde, W. Trageser, A. Templeton and T. Sauer, *Eur. Phys. J. H*, 2016, **41**, 327–364.

[5] V. Chechik, E. Carter and D. Murphy, *Electron Paramagnetic Resonance*, Oxford University Press, Oxford, 1st edn., 2015.

[6] A. Schweiger and G. Jeschke, *Principles of pulse electron paramagnetic resonance*, Oxford University Press, Oxford, 1st edn., 2001.

[7] P. Gast and E. J. Groenen, in *EPR Spectrosc. Fundam. Methods*, ed. D. Goldfarb and S. Stoll, John Wiley and Sons, Inc., Chichester, 1st edn., 2018, ch. 2, pp. 17–28.

[8] M. Bennati, in *EPR Spectrosc. Fundam. Methods*, ed. D. Goldfarb and S. Stoll, John Wiley and Sons, Inc., Chichester, 1st edn., 2018, ch. 5, pp. 63–80.

[9] J. Tesler, in *EPR Spectrosc. Fundam. Methods*, ed. D. Golfarb and S. Stoll, John Wiley and Sons, Inc., Chichester, 1st edn., 2018, ch. 3, pp. 29–62.

[10] S. Richert, C. E. Tait and C. R. Timmel, *J. Magn. Reson.*, 2017, **280**, 103–116.

[11] C. Hintze, U. E. Steiner and M. Drescher, *ChemPhysChem*, 2017, **18**, 6–16.

[12] A. van der Est, in *EPR Spectrosc. Fundam. Methods*, ed. D. Goldfarb and S. Stoll, John Wiley and Sons, Inc., Chichester, 1st edn., 2018, ch. 1, pp. 3–16.

[13] S. Weber, in *EPR Spectrosc. Fundam. Methods*, ed. D. Goldfarb and S. Stoll, John Wiley and Sons, Inc., Chichester, 1st edn., 2018, ch. 10, pp. 195–214.

[14] S. Stoll, in *EPR Spectrosc. Fundam. Methods*, ed. D. Goldfarb and S. Stoll, John Wiley and Sons, Inc., Chichester, 1st edn., 2018, ch. 11, pp. 215–234.

[15] P. E. Spindler, P. Schöps, A. M. Bowen, B. Endeward and T. F. Prisner, *eMagRes*, 2016, **5**, 1477–1492.

[16] S. S. Eaton and G. R. Eaton, in *EPR Spectrosc. Fundam. Methods*, ed. D. Goldfarb and S. Stoll, John Wiley and Sons, Inc., Chichester, 1st edn., 2018, ch. 9, pp. 175–192.

[17] M. Pannier, S. Veit, A. Godt, G. Jeschke and H. W. Spiess, *J. Magn. Reson.*, 2000, **142**, 331–340.

[18] P. P. Borbat and J. H. Freed, in *EPR Spectrosc. Fundam. Methods*, ed. D. Goldfarb and S. Stoll, John Wiley and Sons, Inc., Chichester, 1st edn., 2018, ch. 20, pp. 425–462.

[19] G. Jeschke, *ChemPhysChem*, 2002, **3**, 927–932.

[20] G. Jeschke, A. Koch, U. Jonas and A. Godt, *J. Magn. Reson.*, 2002, **155**, 72–82.

[21] A. D. Milov, A. G. Maryasov and Y. D. Tsvetkov, *Appl. Magn. Reson.*, 1998, **15**, 107–143.

[22] J. E. Lovett, B. W. Lovett and J. Harmer, *J. Magn. Reson.*, 2012, **223**, 98–106.

[23] G. Jeschke and Y. Polyhach, *Phys. Chem. Chem. Phys.*, 2007, **9**, 1895–1910.

[24] O. Schiemann, C. A. Heubach, D. Abdullin, K. Ackermann, M. Azarkh, E. G. Bagryanskaya, M. Drescher, B. Endeward, J. H. Freed, L. Galazzo, D. Goldfarb, T. Hett, L. Esteban Hofer, L. Fábregas Ibáñez, E. J. Hustedt, S. Kucher, I. Kuprov, J. E. Lovett, A. Meyer, S. Ruthstein, S. Saxena, S. Stoll, C. R. Timmel, M. Di Valentin, H. S. Mchaourab, T. F. Prisner, B. E. Bode, E. Bordignon, M. Bennati and G. Jeschke, *J. Am. Chem. Soc.*, 2021, **143**, 17875–17890.

[25] P. E. Spindler, P. Schops, A. M. Bowen, B. Endeward and T. F. Prisner, in *EPR Spectrosc. Fundam. Methods*, ed. D. Goldfarb and S. Stoll, John Wiley and Sons, Inc., Chichester, 1st edn., 2018, ch. 21, pp. 463–482.

[26] A. M. Bowen, C. E. Tait, C. R. Timmel and J. R. Harmer, in *Struct. Inf. from Spin-Labels Intrinsic Paramagn. Centres Biosci.*, ed. C. R. Timmel and J. R. Harmer, Springer, Berlin, Heidelberg, 1st edn., 2013, ch. 7, pp. 283–328.

[27] A. Giannoulis, K. Ackermann, P. E. Spindler, C. Higgins, D. B. Cordes, A. M. Slawin, T. F. Prisner and B. E. Bode, *Phys. Chem. Chem. Phys.*, 2018, **20**, 11196–11205.

[28] G. Jeschke, *Prog. Nucl. Magn. Reson. Spectrosc.*, 2013, **72**, 42–60.

[29] G. Jeschke, M. Sajid, M. Schulteb and A. Godt, *Phys. Chem. Chem. Phys.*, 2009, **11**, 6580–6591.

[30] B. E. Bode, D. Margraf, J. Plackmeyer, G. Dürner, T. F. Prisner and O. Schiemann, *J. Am. Chem. Soc.*, 2007, **129**, 6736–6745.

[31] A. M. Bowen, R. Schuldais, J. Plackmeyer, S. Sigurdsson and T. F. Prisner, EUROMAR, Warsaw, 2017, p. 147.

[32] Z. Wu, A. Feintuch, A. Collauto, L. A. Adams, L. Aurelio, B. Graham, G. Otting and D. Goldfarb, *J. Phys. Chem. Lett.*, 2017, **8**, 5277–5282.

[33] C. J. Rogers, D. Asthana, A. Brookfield, A. Chiesa, G. A. Timco, D. Collison, L. S. Natrajan, S. Carretta, R. E. P. Winpenny and A. M. Bowen, *Angew. Chemie*, 2022, **134**, year.

[34] T. Von Hagens, Y. Polyhach, M. Sajid, A. Godt and G. Jeschke, *Phys. Chem. Chem. Phys.*, 2013, **15**, 5854–5866.

[35] G. Jeschke, V. Chechik, P. Ionita, A. Godt, H. Zimmermann, J. Banham, C. R. Timmel, D. Hilger and H. Jung, *Appl. Magn. Reson.*, 2006, **30**, 473–498.

[36] J. L. Baber, J. M. Louis and G. M. Clore, *Angew. Chemie*, 2015, **127**, 5426–5429.

[37] G. Jeschke, G. Panek, A. Godt, A. Bender and H. Paulsen, *Appl. Magn. Reson.*, 2004, **26**, 223–244.

[38] J. E. Lovett, M. Hoffmann, A. Cnossen, A. T. Shutter, H. J. Hogben, J. E. Warren, S. I. Pascu, C. W. Kay, C. R. Timmel and H. L. Anderson, *J. Am. Chem. Soc.*, 2009, **131**, 13852–13859.

[39] A. Marko, V. Denysenkov and T. F. Prisner, *Mol. Phys.*, 2013, **111**, 2834–2844.

[40] D. Abdullin and O. Schiemann, *Chempluschem*, 2020, **85**, 353–372.

[41] A. V. Astashkin, in *Electron Paramagn. Reson. Investig. Biol. Syst. by Using Spin Labels, Spin Probes, Intrinsic Met. Ions, Part A*, ed. P. Z. Qin and K. Warncke, Elsevier, Waltham, San Diego, Oxford, London., 1st edn., 2015, ch. 10, pp. 251–284.

[42] G. Hagelueken, D. Abdullin and O. Schiemann, *MtsslSuite: Probing biomolecular conformation by spin-labeling studies*, Elsevier Inc., 1st edn., 2015, vol. 563, pp. 595–622.

[43] T. Schmidt, M. A. Wälti, J. L. Baber, E. J. Hustedt and G. M. Clore, *Angew. Chemie - Int. Ed.*, 2016, **55**, 15905–15909.

[44] C. Altenbach, S. L. Flitsch, H. G. Khorana and W. L. Hubbell, *Biochemistry*, 1989, **28**, 7806–7812.

[45] J. P. Klare and H.-J. Steinhoff, in *Electron Paramagn. Reson. Investig. Biol. Syst. by Using Spin Labels, Spin Probes, Intrinsic Met. Ions, Part B*, ed. P. Z. Qin and K. Warncke, Elsevier, Waltham, San Diego, Oxford, London., 1st edn., 2015, ch. 11, pp. 315–347.

[46] A. A. Kuzhelev, O. A. Krumkacheva, M. Y. Ivanov, S. A. Prikhod'Ko, N. Y. Adonin, V. M. Tormyshev, M. K. Bowman, M. V. Fedin and E. G. Bagryanskaya, *J. Phys. Chem. B*, 2018, **122**, 8624–8630.

[47] B. E. Bode, J. Plackmeyer, T. F. Prisner and O. Schiemann, *J. Phys. Chem. A*, 2008, **112**, 5064–5073.

[48] J. Sarver, K. I. Silva and S. Saxena, *Appl. Magn. Reson.*, 2013, **44**, 583–594.

[49] I. Kaminker, M. Bye, N. Mendelman, K. Gislason, S. T. Sigurdsson and D. Goldfarb, *Phys. Chem. Chem. Phys.*, 2015, **17**, 15098–15102.

[50] D. Akhmetzyanov, J. Plackmeyer, B. Endeward, V. Denysenkov and T. F. Prisner, *Phys. Chem. Chem. Phys.*, 2015, **17**, 6760–6766.

[51] M. Ezhevskaya, E. Bordignon, Y. Polyhach, L. Moens, S. Dewilde, G. Jeschke and S. Van Doorslaer, *Mol. Phys.*, 2013, **111**, 2855–2864.

[52] D. Abdullin, F. Duthie, A. Meyer, E. S. Müller, G. Hagelueken and O. Schiemann, *J. Phys. Chem. B*, 2015, **119**, 13539–13542.

[53] C. L. Motion, J. E. Lovett, S. Bell, S. L. Cassidy, P. A. Cruickshank, D. R. Bolton, R. I. Hunter, H. El Mkami, S. Van Doorslaer and G. M. Smith, *J. Phys. Chem. Lett.*, 2016, **7**, 1411–1415.

[54] D. Abdullin, H. Matsuoka, M. Yulikov, N. Fleck, C. Klein, S. Spicher, G. Hagelueken, S. Grimme, A. Lützen and O. Schiemann, *Chem. - A Eur. J.*, 2019, **25**, 8820–8828.

[55] I. Kaminker, H. Yagi, T. Huber, A. Feintuch, G. Otting and D. Goldfarb, *Phys. Chem. Chem. Phys.*, 2012, **14**, 4355–4358.

[56] M. Yulikov, P. Lueders, M. Farooq Warsi, V. Chechik and G. Jeschke, *Phys. Chem. Chem. Phys.*, 2012, **14**, 10732–10746.

[57] P. Lueders, H. Jäger, M. A. Hemminga, G. Jeschke and M. Yulikov, *J. Phys. Chem. B*, 2013, **117**, 2061–2068.

[58] M. Di Valentin, M. Albertini, E. Zurlo, M. Gobbo and D. Carbonera, *J. Am. Chem. Soc.*, 2014, **136**, 6582–6585.

[59] A. Bieber, D. Bücker and M. Drescher, *J. Magn. Reson.*, 2018, **296**, 29–35.

[60] A. Bertran, A. Barbon, A. M. Bowen and M. Di Valentin, in *Adv. Biomol. EPR*, ed. R. D. Britt, Elsevier Inc., 1st edn., 2022, vol. 666, ch. 7, pp. 171–231.

[61] M. Di Valentin, C. Büchel, G. M. Giacometti and D. Carbonera, *Biochem. Biophys. Res. Commun.*, 2012, **427**, 637–641.

[62] S. Ciuti, A. Barbon, M. Bortolus, A. Agostini, E. Bergantino, C. Martin, M. Di Valentin and D. Carbonera, *Appl. Magn. Reson.*, 2021, **53**, pages1031–1042.

[63] B. M. Hoffman, *J. Am. Chem. Soc.*, 1975, **97**, 1688–1694.

[64] M. G. Dal Farra, S. Richert, C. Martin, C. Larminie, M. Gobbo, E. Bergantino, C. R. Timmel, A. M. Bowen and M. Di Valentin, *ChemPhysChem*, 2019, **20**, 931–935.

[65] D. Nohr, R. Rodriguez, S. Weber and E. Schleicher, *Front. Mol. Biosci.*, 2015, **2**, 1–16.

[66] N. J. Turro, V. Ramamurthy and J. C. Scaiano, *Modern Molecular Photochemistry of Organic Molecules*, University Science Books, Mill Valley, California, 2010.

[67] K. Serrer, C. Matt, M. Sokolov, S. Kacprzak, E. Schleicher and S. Weber, *Mol. Phys.*, 2019, **117**, 2688–2699.

[68] L. Williams, S. Tischlik, A. Scherer, J. W. A. Fischer and M. Drescher, *Chem. Commun.*, 2020, **56**, 14669–14672.

[69] O. A. Krumkacheva, I. O. Timofeev, L. V. Politanskaya, Y. F. Polienko, E. V. Tretyakov, O. Y. Rogozhnikova, D. V. Trukhin, V. M. Tormyshev, A. S. Chubarov, E. G. Bagryanskaya and M. V. Fedin, *Angew. Chemie*, 2019, **131**, 13405–13409.

[70] N. E. Sannikova, I. O. Timofeev, A. S. Chubarov, N. S. Lebedeva, A. S. Semeikin, I. A. Kirilyuk, Y. P. Tsentalovich, M. V. Fedin, E. G. Bagryanskaya and O. A. Krumkacheva, *Photochem. Photobiol.*, 2020.

[71] I. O. Timofeev, L. V. Politanskaya, E. V. Tretyakov, Y. F. Polienko, V. M. Tormyshev, E. Bagryanskaya, O. A. Krumkacheva and M. V. Fedin, *Phys. Chem. Chem. Phys.*, 2022, **24**, 4475–4484.

[72] M. Di Valentin, M. Albertini, M. G. Dal Farra, E. Zurlo, L. Orian, A. Polimeno, M. Gobbo and D. Carbonera, *Chem. - A Eur. J.*, 2016, **22**, 17204–17214.

[73] P. E. Spindler, P. Schöps, W. Kallies, S. J. Glaser and T. F. Prisner, *J. Magn. Reson.*, 2017, **280**, 30–45.

[74] M. G. Dal Farra, S. Richert, C. Martin, C. Larminie, M. Gobbo, E. Bergantino, C. R. Timmel, A. M. Bowen and M. Di Valentin, *ChemPhysChem*, 2019, **20**, 931–935.

[75] C. Hintze, D. Bücker, S. Domingo Köhler, G. Jeschke and M. Drescher, *J. Phys. Chem. Lett.*, 2016, **7**, 2204–2209.

[76] A. Doll, M. Qi, A. Godt and G. Jeschke, *J. Magn. Reson.*, 2016, **273**, 73–82.

[77] P. E. Spindler, S. J. Glaser, T. E. Skinner and T. F. Prisner, *Angew. Chemie - Int. Ed.*, 2013, **52**, 3425–3429.

[78] M. Di Valentin, M. G. Dal Farra, L. Galazzo, M. Albertini, T. Schulte, E. Hofmann and D. Carbonera, *Biochim. Biophys. Acta - Bioenerg.*, 2016, **1857**, 1909–1916.

[79] A. M. Bowen, A. Bertran, K. B. Henbest, M. Gobbo, C. R. Timmel and M. Di Valentin, *J. Phys. Chem. Lett.*, 2021, **12**, 3819–3826.

[80] D. Goldfarb, in *Struct. Inf. from Spin-Labels Intrinsic Paramagn. Centres Biosci.*, ed. C. R. Timmel and J. R. Harmer, Springer-Verlag Berlin Heidelberg, Berlin, 2013, ch. 4, pp. 163–204.

[81] M. Ji, S. Ruthstein and S. Saxena, *Acc. Chem. Res.*, 2014, **47**, 688–695.

[82] Z. Yang, M. Ji, T. F. Cunningham and S. Saxena, *Methods Enzymol.*, 2015, **563**, 459–481.

[83] D. Abdullin and O. Schiemann, *Dalt. Trans.*, 2021, **50**, 808–815.

[84] A. M. Bowen, E. O. Johnson, F. Mercuri, N. J. Hoskins, R. Qiao, J. S. McCullagh, J. E. Lovett, S. G. Bell, W. Zhou, C. R. Timmel, L. L. Wong and J. R. Harmer, *J. Am. Chem. Soc.*, 2018, **140**, 2514–2527.

[85] I. M. C. V. Amsterdam, M. Ubbink, G. W. Canters and M. Huber, *Angew. Chem. Int. Ed*, 2003, **42**, 62–64.

[86] C. W. Kay, H. El Mkami, R. Cammack and R. W. Evans, *J. Am. Chem. Soc.*, 2007, **129**, 4868–4869.

[87] C. Elsässer, M. Brecht and R. Bittl, *J. Am. Chem. Soc.*, 2002, **124**, 12606–12611.

[88] M. M. Roessler, M. S. King, A. J. Robinson, F. A. Armstrong, J. Harmer and J. Hirst, *Proc. Natl. Acad. Sci. U. S. A.*, 2010, **107**, 1930–1935.

[89] A. V. Astashkin, H. Hara and A. Kawamori, *J. Chem. Phys.*, 1998, **108**, 3805–3812.

[90] M. Di Valentin, C. E. Tait, E. Salvadori, L. Orian, A. Polimeno and D. Carbonera, *Biochim. Biophys. Acta - Bioenerg.*, 2014, **1837**, 85–97.

[91] C. W. Kay, M. Di Valentin and K. Möbius, *Sol. Energy Mater. Sol. Cells*, 1995, **38**, 111–118.

[92] W. Lubitz, F. Lendzian and R. Bittl, *Acc. Chem. Res.*, 2002, **35**, 313–320.

[93] C. E. Tait, P. Neuhaus, H. L. Anderson and C. R. Timmel, *J. Am. Chem. Soc.*, 2015, **137**, 6670–6679.

[94] A. Barbon, M. G. Dal Farra, S. Ciuti, M. Albertini, L. Bolzonello, L. Orian and M. Di Valentin, *J. Chem. Phys.*, 2020, **152**, 034201.

[95] A. Savitsky, A. A. Dubinskii, M. Plato, Y. A. Grishin, H. Zimmermann and K. Möbius, *J. Phys. Chem. B*, 2008, **112**, 9079–9090.

[96] M. J. Frisch, G. W. Trucks, H. B. Schlegel, G. E. Scuseria, M. A. Robb, J. R. Cheeseman, G. Scalmani, V. Barone, G. A. Petersson, H. Nakatsuji, X. Li, M. Caricato, A. Marenich, J. Bloino, B. G. Janesko, R. Gomperts, B. Mennucci, H. P. Hratchian, J. V. Ortiz, A. F. Izmaylov, J. L. Sonnenberg, D. Williams-Young, F. Ding, F. Lipparini, F. Egidi, J. Goings, B. Peng, A. Petrone, T. Henderson, D. Ranasinghe,

V. G. Zakrzewski, J. Gao, N. Rega, G. Zheng, W. Liang, M. Hada, M. Ehara, K. Toyota, R. Fukuda, J. Hasegawa, M. Ishida, T. Nakajima, Y. Honda, O. Kitao, H. Nakai, T. Vreven, K. Throssell, J. A. Montgomery, J. E. Peralta, F. Ogliaro, M. Bearpark, J. J. Heyd, E. Brothers, K. N. Kudin, V. N. Staroverov, T. Keith, R. Kobayashi, J. Normand, K. Raghavachari, A. Rendell, J. C. Burant, S. S. Iyengar, J. Tomasi, M. Cossi, J. M. Millam, M. Klene, C. Adamo, R. Cammi, J. W. Ochterski, R. L. Martin, K. Morokuma, O. Farkas, J. B. Foresman and D. J. Fox, *Gaussian 09*, 2009.

[97] A. Marko and T. F. Prisner, *Phys. Chem. Chem. Phys.*, 2013, **15**, 619–627.

[98] V. Monaco, F. Formaggio, M. Crisma, C. Toniolo, P. Hanson, G. Millhauser, C. George, J. R. Deschamps and J. L. Flippen-Anderson, *Bioorganic Med. Chem.*, 1999, **7**, 119–131.

[99] B. Joseph, V. M. Tormyshev, O. Y. Rogozhnikova, D. Akhmetzyanov, E. G. Bagryanskaya and T. F. Prisner, *Angew. Chemie - Int. Ed.*, 2016, **55**, 11538–11542.

[100] S. Milikisyants, F. Scarpelli, M. G. Finiguerra, M. Ubbink and M. Huber, *J. Magn. Reson.*, 2009, **201**, 48–56.

[101] G. Jeschke, M. Pannier, A. Godt and H. W. Spiess, *Chem. Phys. Lett.*, 2000, **331**, 243–252.

[102] A. Doll and G. Jeschke, *Phys. Chem. Chem. Phys.*, 2016, **18**, 23111–23120.

[103] A. M. Bowen, N. Erlenbach, P. van Os, L. S. Stelzl, S. T. Sigurdsson and T. F. Prisner, *Appl. Magn. Reson.*, 2018, **49**, 1355–1368.

[104] I. Ritsch, H. Hintz, G. Jeschke, A. Godt and M. Yulikov, *Phys. Chem. Chem. Phys.*, 2019, **21**, 9810–9830.

[105] A. P. Jagtap, I. Krstic, N. C. Kunjir, R. Hänsel, T. F. Prisner and S. T. Sigurdsson, *Free Radic. Res.*, 2015, **49**, 78–85.

[106] A. Bertran, L. Morbiato, S. Aquilia, L. Gabbatore, M. De Zotti, C. R. Timmel, M. Di Valentin and A. M. Bowen, *Molecules*, 2022, **27**, 7526.

[107] A. Bertran, A. Barbon, A. M. Bowen and M. Di Valentin, *Methods Enzymol.*, 2022, **666**, 171–231.

[108] F. Neese, *Wiley Interdiscip. Rev. Comput. Mol. Sci.*, 2012, **2**, 73–78.

[109] S. Stoll and A. Schweiger, *J. Magn. Reson.*, 2006, **178**, 42–55.

[110] G. Jeschke, H. Zimmermann and A. Godt, *J. Magn. Reson.*, 2006, **180**, 137–146.

[111] V. Meyer, M. A. Swanson, L. J. Clouston, P. J. Boratyński, R. A. Stein, H. S. McHaourab, A. Rajca, S. S. Eaton and G. R. Eaton, *Biophys. J.*, 2015, **108**, 1213–1219.

[112] A. Savitsky, M. Plato and K. Möbius, *Appl. Magn. Reson.*, 2010, **37**, 415–434.

[113] E. F. Pettersen, T. D. Goddard, C. C. Huang, G. S. Couch, D. M. Greenblatt, E. C. Meng and T. E. Ferrin, *J. Comput. Chem.*, 2004, **25**, 1605–1612.

[114] A. Bertran, K. B. Henbest, M. De Zotti, M. Gobbo, C. R. Timmel, M. Di Valentin and A. M. Bowen, *J. Phys. Chem. Lett.*, 2021, **12**, 80–85.

[115] S. Ghosh, M. J. Lawless, H. J. Brubaker, K. Singewald, M. R. Kurpiewski, L. Jen-Jacobson and S. Saxena, *Nucleic Acids Res.*, 2020, **48**, e49.

[116] S. Padilla-Parra and M. Tramier, *BioEssays*, 2012, **34**, 369–376.

[117] M. Geissbuehler, T. Spielmann, A. Formey, I. Märki, M. Leutenegger, B. Hinz, K. Johnsson, D. Van De Ville and T. Lasser, *Biophys. J.*, 2010, **98**, 339–349.

[118] A. P. Jagtap, I. Krstic, N. C. Kunjir, R. Hänsel, T. F. Prisner and S. T. Sigurdsson, *Free Radic. Res.*, 2015, **49**, 78–85.

[119] K. Singewald, M. J. Lawless and S. Saxena, *J. Magn. Reson.*, 2019, **299**, 21–27.

[120] N. Fleck, C. A. Heubach, T. Hett, F. R. Haege, P. P. Bawol, H. Baltruschat and O. Schiemann, *Angew. Chemie - Int. Ed.*, 2020, **59**, 9767–9772.

[121] Y. Yang, F. Yang, Y. J. Gong, T. Bahrenberg, A. Feintuch, X. C. Su and D. Goldfarb, *J. Phys. Chem. Lett.*, 2018, **9**, 6119–6123.

[122] D. Goldfarb, *Phys. Chem. Chem. Phys.*, 2014, **16**, 9685–9699.

[123] S. Oancea, F. Formaggio, S. Campestrini, Q. B. Broxterman, B. Kaptein and C. Toniolo, *Biopolymers*, 2003, **72**, 105–115.

[124] A. M. Bowen, M. W. Jones, J. E. Lovett, T. G. Gaule, M. J. McPherson, J. R. Dilworth, C. R. Timmel and J. R. Harmer, *Phys. Chem. Chem. Phys.*, 2016, **18**, 5981–5994.

[125] L. F. Ibáñez, G. Jeschke and S. Stoll, *Magn. Reson.*, 2020, **1**, 209–224.

[126] J. Keeley, T. Choudhury, L. Galazzo, E. Bordignon, A. Feintuch, D. Goldfarb, H. Russell, M. J. Taylor, J. E. Lovett, A. Eggeling, L. Fábregas, K. Keller, M. Yulikov, G. Jeschke and I. Kuprov, *J. Magn. Reson.*, 2022, **338**, 107186.

[127] S. G. Worswick, J. A. Spencer, G. Jeschke and I. Kuprov, *Sci. Adv.*, 2018, **4**, 1–18.

[128] D. Abdullin, G. Hagelueken, R. I. Hunter, G. M. Smith and O. Schiemann, *Mol. Phys.*, 2015, **113**, 544–560.

[129] M. Tramier and M. Coppey-Moisan, *Methods Cell Biol.*, 2008, **85**, 395–414.

[130] S. Nagao, H. Osuka, T. Yamada, T. Uni, Y. Shomura, K. Imai, Y. Higuchi and S. Hirota, *Dalt. Trans.*, 2012, **41**, 11378–11385.

[131] A. Jozeliūnaitė, A. Neniškis, A. Bertran, A. M. Bowen, M. Di Valentin, S. Raišys, P. Baronas, K. Kazlauskas, L. Vilčiauskas and E. Orentas, *J. Am. Chem. Soc.*, 2023, **145**, 455–464.

[132] J. E. Banham, C. M. Baker, S. Ceola, I. J. Day, G. H. Grant, E. J. Groenen, C. T. Rodgers, G. Jeschke and C. R. Timmel, *J. Magn. Reson.*, 2008, **191**, 202–218.

[133] S. L. Murov, I. Carmichael and G. L. Hug, *Handbook of Photochemistry*, Marcel Dekker, Inc., New York, 2nd edn., 1993, p. 432.

[134] N. M. Barbosa Neto, D. S. Correa, L. De Boni, G. G. Parra, L. Misoguti, C. R. Mendonça, I. E. Borissevitch, S. C. Zílio and P. J. Gonçalves, *Chem. Phys. Lett.*, 2013, **587**, 118–123.

[135] Y. Kamata, K. Akiyama, S. Tero-Kubota and M. Tabata, *Appl. Magn. Reson.*, 2003, **23**, 409–420.

[136] F. W. Teale, *BBA - Biochim. Biophys. Acta*, 1959, **35**, 543.

[137] S. Nagao, H. Osuka, T. Yamada, T. Uni, Y. Shomura, K. Imai, Y. Higuchi and S. Hirota, *Dalt. Trans.*, 2012, **41**, 11378–11385.

[138] I. Guryanov, A. Moretto, S. Campestrini, Q. B. Broxterman, B. Kaptein, C. Peggion, F. Formannio and C. Toniolo, *Biopolymers*, 2006, **82**, 482–490.

[139] S. Sinnecker and F. Neese, *J. Phys. Chem. A*, 2006, **110**, 12267–12275.

[140] I. T. Desta, K. A. Porter, B. Xia, D. Kozakov and S. Vajda, *Structure*, 2020, **28**, 1071–1081.e3.

[141] D. Kozakov, D. R. Hall, B. Xia, K. A. Porter, D. Padhorny, C. Yueh, D. Beglov and S. Vajda, *Nat. Protoc.*, 2017, **12**, 255–278.

[142] S. Vajda, C. Yueh, D. Beglov, T. Bohnuud, S. E. Mottarella, B. Xia, D. R. Hall and D. Kozakov, *Proteins Struct. Funct. Bioinforma.*, 2017, **85**, 435–444.

[143] D. Kozakov, D. Beglov, T. Bohnuud, S. E. Mottarella, B. Xia, D. R. Hall and S. Vajda, *Proteins Struct. Funct. Bioinforma.*, 2013, **81**, 2159–2166.

[144] M. Kitahara, S. Fudo, T. Yoneda, M. Nukaga and T. Hoshino, *Cryst. Growth Des.*, 2019, **19**, 6004–6010.

[145] S. Noimark, E. Salvadori, R. Gómez-Bombarelli, A. J. MacRobert, I. P. Parkin and C. W. Kay, *Phys. Chem. Chem. Phys.*, 2016, **18**, 28101–28109.

[146] C. M. Marian, *Annu. Rev. Phys. Chem.*, 2020, **72**, 617–640.

[147] M. V. Encinas, A. M. Rufs, S. G. Bertolotti and C. M. Previtali, *Polymer (Guildf).*, 2009, **50**, 2762–2767.

[148] M. L. Herz, *J. Am. Chem. Soc.*, 1975, **97**, 6777–6785.

[149] Y. Yang, B. B. Pan, X. Tan, F. Yang, Y. Liu, X. C. Su and D. Goldfarb, *J. Phys. Chem. Lett.*, 2020, **11**, 1141–1147.

[150] M. Sibrian-Vazquez, T. J. Jensen, F. R. Fronczek, R. P. Hammer and M. G. H. Vicente, *Bioconjug. Chem.*, 2005, **16**, 852–863.

[151] J. R. Lakowicz, *Principles of Fluorescence Spectroscopy*, Springer, New York, 3rd edn., 2006.

[152] B. Hellenkamp, P. Wortmann, F. Kandzia, M. Zacharias and T. Hugel, *Nat. Methods*, 2017, **14**, 176–182.

[153] B. Hellenkamp, S. Schmid, O. Doroshenko, O. Opanasyuk, R. Kühnemuth, S. Rezaei Adariani, B. Ambrose, M. Aznauryan, A. Barth, V. Birkedal, M. E. Bowen, H. Chen, T. Cordes, T. Eilert, C. Fijen, C. Gebhardt, M. Götz, G. Gouridis, E. Gratton, T. Ha, P. Hao, C. A. Hanke, A. Hartmann, J. Hendrix, L. L. Hildebrandt, V. Hirschfeld, J. Hohlbein, B. Hua, C. G. Hübner, E. Kallis, A. N. Kapanidis, J. Y. Kim, G. Krainer, D. C. Lamb, N. K. Lee, E. A. Lemke, B. Levesque, M. Levitus, J. J. McCann, N. Naredi-Rainer, D. Nettels, T. Ngo, R. Qiu, N. C. Robb, C. Röcker, H. Sanabria, M. Schlierf, T. Schröder, B. Schuler, H. Seidel, L. Streit, J. Thurn, P. Tinnefeld, S. Tyagi, N. Vandenberk, A. M. Vera, K. R. Weninger, B. Wünsch, I. S. Yanez-Orozco, J. Michaelis, C. A. Seidel, T. D. Craggs and T. Hugel, *Nat. Methods*, 2018, **15**, 669–676.

[154] M. F. Peter, C. Gebhardt, R. Mächtel, G. G. Muñoz, J. Glaenzer, A. Narducci, G. H. Thomas, T. Cordes and G. Hagelueken, *Nat. Commun.*, 2022, **13**, 1–19.

[155] N. V. Sablin, M. A. Gerasimova and E. V. Nemtseva, *Russ. Phys. J.*, 2016, **58**, 1797–1803.

[156] D. Grohmann, D. Klose, J. P. Klare, C. W. Kay, H. J. Steinhoff and F. Werner, *J. Am. Chem. Soc.*, 2010, **132**, 5954–5955.

[157] D. Klose, J. P. Klare, D. Grohmann, C. W. Kay, F. Werner and H. J. Steinhoff, *PLoS One*, 2012, **7**, year.

[158] D. Klose, A. Holla, C. Gmeiner, D. Nettels, I. Ritsch, N. Bross, M. Yulikov, F. H. Allain, B. Schuler and G. Jeschke, *Biophys. J.*, 2021, **120**, 4842–4858.

[159] M. Taniguchi, J. S. Lindsey, D. F. Bocian and D. Holten, *J. Photochem. Photobiol. C Photochem. Rev.*, 2021, **46**, 100401.

[160] A. Scherer, X. Yao, M. Qi, M. Wiedmaier, A. Godt and M. Drescher, *J. Phys. Chem. Lett.*, 2022, **13**, 10958 – 10964.

[161] M. Le Bechec, T. Pigot and S. Lacombe, *ChemPhotoChem*, 2018, **2**, 622–631.

[162] Z. Jiang, Y. Huang, Z. Zhu, S. Gao, Q. Lv and F. Li, *Proc. Natl. Acad. Sci. U. S. A.*, 2022, **119**, 6–11.

[163] A. Pinnola and R. Bassi, *Biochem. Soc. Trans.*, 2018, **46**, 467–482.

[164] T. Y. Tsong, *Biophys. J.*, 1991, **60**, 297–306.

[165] K. Lang and J. W. Chin, *Chem. Rev.*, 2014, **114**, 4764–4806.

[166] B. Hochreiter, A. P. Garcia and J. A. Schmid, *Sensors (Switzerland)*, 2015, **15**, 26281–26314.

[167] M. Fernández-Suárez and A. Y. Ting, *Nat. Rev. Mol. Cell Biol.*, 2008, **9**, 929–943.

[168] R. Y. Tsien, *Annu. Rev. Biochem.*, 1998, **67**, 509–544.

[169] G. Karthikeyan, A. Bonucci, G. Casano, G. Gerbaud, S. Abel, V. Thomé, L. Kodjabachian, A. Magalon, B. Guigliarelli, V. Belle, O. Ouari and E. Mileo, *Angew. Chemie - Int. Ed.*, 2018, **57**, 1366–1370.

[170] P. Widder, J. Schuck, D. Summerer and M. Drescher, *Phys. Chem. Chem. Phys.*, 2020, **22**, 4875–4879.

[171] B. T. Luppi, D. Majak, M. Gupta, E. Rivard and K. Shankar, *J. Mater. Chem. A*, 2019, **7**, 2445–2463.

[172] A. Kugele, B. Silkenath, J. Langer, V. Wittmann and M. Drescher, *ChemBioChem*, 2019, **20**, 2479–2484.

[173] S. Van De Linde, I. Krstić, T. Prisner, S. Doose, M. Heilemann and M. Sauer, *Photochem. Photobiol. Sci.*, 2011, **10**, 499–506.

[174] A. Mirzahosseini and B. Noszál, *Sci. Rep.*, 2016, **6**, 1–11.